Microscopic and macroscopic modeling of particle formation processes in spray fluidized beds

Dissertation
Zur Erlangung des akademischen Grades

Doktoringenieur
(Dr.-Ing.)

von M.Sc. Christian Rieck
geb. am 7. April 1989 in Magdeburg

genehmigt durch die Fakultät für Verfahrens- und Systemtechnik
der Otto-von-Guericke-Universität Magdeburg

Promotionskommission: Prof. Dr.-Ing. habil. Ulrich Krause (Vorsitz)
Prof. Dr.-Ing. habil. Evangelos Tsotsas (Gutachter)
Prof. Dr.-Ing. Andreas Bück (Gutachter)
Prof. Dr.-Ing. Themis Matsoukas (Gutachter)

eingereicht am 15. April 2020

Promotionskolloquium am 11. August 2020

Abstract

Spray fluidized bed processes are often used in agriculture, as well as the chemical, pharmaceutical and food industries to produce particulate products from solid containing liquid raw materials such as solutions, suspensions, or melts. The transformation of liquids into a solid form offers advantages regarding transportation, handling, preservation, and subsequent process steps. Examples of such products are fertilizers, detergents, coated tablets, and instant food powders.

In a spray fluidized bed, the liquid is sprayed on a particle bed fluidized by a hot gas stream. By cooling (melts) or evaporation (suspensions and solutions), the sprayed liquid is transformed into solid material remaining on the particles. Different types of size enlargement processes can be performed in spray fluidized beds: coating, layering granulation, and agglomeration. In coating and layering granulation, the sprayed material forms a solid layer around the particles. In case of coating, the focus lies on applying a solid layer with a certain function (e.g., a protective layer), while in layering granulation size enlargement is the main purpose. Agglomeration denotes the formation of clusters consisting of several particles sticking together by binding forces. Agglomeration can also be observed when pure water is sprayed on amorphous particles since sticky spots may be created on the particle surface due to glass transition. Generally, both size enlargement mechanisms may occur simultaneously in a spray fluidized bed. Depending on the application of the product, only one mechanism should be dominant since the properties of the resulting particles differ significantly. Process design requires detailed knowledge about the relationship between the resulting product properties and operating conditions, material parameters, and equipment design, which can be obtained by experimental work and mathematical modeling.

The present work deals with modeling of particle formation in batch spray fluidized bed processes, using different methods. First, two process models for coating and layering granulation as well as agglomeration of amorphous particles based on a Monte Carlo method are presented. This method offers great advantages over common modeling approaches. In case of coating and layering granulation, a more detailed description of product properties and their distributions can be obtained. For the first time, the process kinetics for agglomeration of amorphous particles can be described while the influence of process and material parameters is directly taken into account. The presented Monte Carlo models describe layering and agglomeration as a result of processes occurring on the single particle scale such as droplet deposition, binary collisions, droplet drying, size enlargement, and breakage. The influence of operating conditions and material parameters is discussed and the models are validated using theoretical approaches and experimental data. Second, a process model based on population balances and a heat and mass transfer model for spray fluidized beds

is presented. This model is used to characterize the border between layering and agglomeration by combining the Stokes criterion and a new dynamic model describing the wet surface fraction of the particles. The influence of operating conditions and material parameters on the dominant size enlargement mechanism is presented in a simulation study. Further simulations and experimental data are used to provide a new classification of the size enlargement mechanisms based on the probability of successful collisions.

Kurzzusammenfassung

Sprühwirbelschichtprozesse werden häufig in der Landwirtschaft sowie der chemischen, pharmazeutischen, und Lebensmittelindustrie genutzt,um partikuläre Produkte aus feststoffhaltigen Flüssigkeiten, z.B. Lösungen, Suspensionen, oder Schmelzen, herzustellen. Die Umwandlung vom flüssigen in den festen Zustand bietet Vorteile hinsichtlich Transport, Handhabung, Konservierung und nachfolgender Prozessschritte. Beispiele solcher Produkte sind Düngemittel, Waschmittel, beschichtete Tabletten, und lösliche Lebensmittelpulver.

In Sprühwirbelschichten wird die Flüssigkeit auf eine Partikelschüttung, die durch einen heißen Gasstrom fluidisiert wird, gesprüht. Die Flüssigkeit wird dabei entweder durch Abkühlung (Schmelze) oder Verdunstung (Lösung, Suspension) in einen Feststoff umgewandelt, der auf den Partikeln verbleibt. In Sprühwirbelschichten können unterschiedliche Prozesse realisiert werden: Coating, Granulation und Agglomeration. Coating und Granulation bezeichnen das Aufbringen einer Feststoffschicht auf der Oberfläche der fluidisierten Partikel. In Coatingprozessen liegt der Schwerpunkt auf der Bildung einer funktionalen Schicht, z.B. mit einer Schutzwirkung, wobei Granulation hauptsächlich auf Vergrößerung der Partikel abzielt. Agglomeration beschreibt das Zusammenführen mehrerer Partikel zu Agglomeraten, die durch Bindekräfte aneinander haften. Dies kann auch erreicht werden, indem reines Wasser auf amorphe Partikel gesprüht wird. In diesem Fall können durch Glasübergang klebrige Stellen auf der Partikeloberfläche erzeugt werden, die zur Bildung von Agglomeraten führen. Im Allgemeinen finden in Sprühwirbelschichtprozessen sowohl Schichtwachstum als auch Agglomeration gleichzeitig statt. Da sich aber die erzielten Produkteigenschaften erheblich unterscheiden können, sollte abhängig von der Anwendung des Produktes nur ein Wachstumsmechanismus dominieren. Die Auslegung dieser Prozesse erfordert detailliertes Wissen über den Zusammenhang zwischen den erzeugten Produkteigenschaften und den Prozessbedingungen, Materialeigenschaften sowie konstruktiven Merkmalen verwendeter Anlagen. Dies kann über experimentelle Untersuchungen sowie mathematische Modellierung erreicht werden.

Die vorliegende Arbeit beschäftigt sich mit der Modellierung von Partikelbildung in absatzweise betriebenen Sprühwirbelschichten mit unterschiedlichen Methoden. Zunächst werden zwei Modelle für Coating und Granulation sowie Agglomeration amorpher Materialien unter Verwendung einer Monte-Carlo Methode vorgestellt. Diese Methode bietet Vorteile gegenüber herkömmlichen Ansätzen. Mit dem präsentierten Modell für Schichtwachstumsprozesse ist eine detailliertere Beschreibung der erzeugten Produkteigenschaften und deren Verteilungen möglich. Zusätzlich kann die Prozesskinetik bei der Agglomeration amorpher Partikel zum ersten Mal beschrieben werden,

wobei der Einfluss von Prozess- und Materialparametern direkt berücksichtigt wird. Die vorgestellten Modelle beschreiben Schichtwachstum und Agglomeration als Folge von Prozessen, die auf der Einzelpartikelebene ablaufen, wie z.B. Tropfenabscheidung, binäre Kollisionen, Tropfentrocknung, Partikelvergrößerung und Bruch. Der Einfluss der Prozessbedingungen und Materialeigenschaften wird präsentiert und beide Modelle werden mit theoretischen Ansätzen und experimentellen Daten validiert. Anschließend wird ein weiteres Prozessmodell bestehend aus Populationsbilanzen und einem Wärme- und Stoffübertragungsmodell für Sprühwirbelschichten vorgestellt. Mit diesem Modell kann die Grenze der unterschiedlichen Wachstumsmechanismen beschrieben werden, indem das Stokes-Kriterium und ein neuer Ansatz für die Berechnung des Benetzungsgrades kombiniert werden. Der Einfluss der Prozess- und Materialparameter auf den dominanten Wachstumsmechanismus wird im Rahmen einer Simulationsstudie diskutiert. Basierend auf weiteren Simulationen und experimentellen Daten wird eine neue Klassifizierung der Wachstumsmechanismen mit Hilfe der Wahrscheinlichkeit erfolgreicher Kollisionen vorgeschlagen.

Contents

Nomenclature

Latin symbols

a	coefficient	–
A	surface area	m^2
A_{spray}	contact area between spray cone and bed	m^2
A_V	surface area per volume	$m^2\,m^{-3}$
Ar	Archimedes number	–
B_0	birth rate of particles with smallest size	s^{-1}
B_{agg}	birth rate of agglomerates	$m^{-3}\,s^{-1}$
B_{gt}	constant in Williams-Landel-Ferry equation	K
c	specific heat capacity	$J\,kg^{-1}\,K^{-1}$
$c'_{n,p}$	number concentration of particles	m^{-3}
C_{gt}	constant in Williams-Landel-Ferry equation	–
$C_{V,inter}$	inter-particle coefficient of variation	–
$C_{V,intra}$	intra-particle coefficient of variation	–
d	diameter	m
d_{10}	number-based mean diameter	m
d_{32}	Sauter mean diameter	m
D_{agg}	death rate of agglomerates	$m^{-3}\,s^{-1}$
e	external coordinate	m
$\mathbf{e}$	vector of external coordinates	m
e'	coefficient of restitution	–
E	Young's modulus	Pa
f	frequency	s^{-1}
F_{coll}	factor for scaling collision frequency	–
FN	flux-number	–
g	gravitational acceleration	$m\,s^{-2}$
G	growth rate	$m\,s^{-1}$
h	height	m
Δh_{evap}	specific enthalpy of evaporation at 0 °C	$J\,kg^{-1}$
H	enthalpy	J
$\dot{H}$	enthalpy flow rate	$J\,s^{-1}$
$\overline{\dot{H}}$	mean enthalpy flow rate	$J\,s^{-1}$
i	internal coordinate	various
$\mathbf{i}$	vector of internal coordinates	various
k	Gordon-Taylor constant	–
K_{gt}	constant	$g\,K\,mol^{-1}$
K_{max}	maximum coordination number	–
L	length	m
Le	Lewis number	–

m	exponent	–
M	mass	kg
$\widetilde{M}$	molar mass	kg kmol^{-1}
$\dot{M}$	mass flow rate	kg s^{-1}
$\overline{\dot{M}}$	mean mass flow rate	kg s^{-1}
$n(x)$	number density function for size	m^{-1}
$n(v)$	number density function for volume	m^{-3}
$\dot{n}_{12}$	number density function flow rate from spraying zone to drying zone	m^{-1} s^{-1}
$\dot{n}_{21}$	number density function flow rate from drying zone to spraying zone	m^{-1} s^{-1}
N	number	–
N'_p	number of particles coated per coating trial	–
N'_{pos}	number of positions coated per coating trial	–
Nu	Nusselt number	–
Nu′	apparent Nusselt number	–
p_{sat}	saturation vapor pressure	Pa
P	probability	–
P_{tot}	total pressure	Pa
Pr	Prandtl number	–
$q_0(x)$	normalized number density function	m^{-1}
Q_0	normalized cumulative distribution	–
$\dot{Q}$	heat flow rate	J s^{-1}
$\overline{\dot{Q}}$	mean heat flow rate	J s^{-1}
r	random number (uniformly distributed)	–
r_n	random number (normally distributed)	–
r'	gradient	–
R	particle radius	m
$\widetilde{R}$	molar gas constant	J mol^{-1} K^{-1}
Re	Reynolds number	–
Re$_\varepsilon$	Reynolds number divided by porosity	–
s	layer thickness	m
$\bar{s}$	mean layer thickness	m
S	scaling factor	–
S_{max}	maximum pore saturation	–
Sc	Schmidt number	–
Sh	Sherwood number	–
Sh′	apparent Sherwood number	–
St$_{crit}$	critical Stokes number	–
St$_{def}$	deformation Stokes number	–
St$_v$	viscous Stokes number	–
t	time	s
Δt	time step	s
Δt_{dry}	drying time	s
T	temperature	°C
u	velocity	m s^{-1}
v, v'	particle volume	m^3
V	volume	m^3
w	mass fraction	–

x	particle size	m
x_j	boundary value of j-th particle size interval or control volume	m
$\bar{x}_j$	center of j-th particle size interval or control volume	m
Δx_j	size of j-th particle size interval or control volume	m
X, Y	moisture content	$\mathrm{kg_{liquid}/kg_{dry\ matter}}$
Y'	yield stress	Pa

Greek symbols

α	heat transfer coefficient	$\mathrm{W\,m^{-2}\,K^{-1}}$
β	mass transfer coefficient	$\mathrm{m\,s^{-1}}$
$\beta'(t, v, v')$	agglomeration kernel	$\mathrm{s^{-1}}$
$\beta'(v, v')$	agglomeration kernel (size dependent part)	various
β'_0	agglomeration efficiency	depending on $\beta'(v, v')$
γ	surface tension	$\mathrm{N\,m^{-1}}$
δ	diffusion coefficient	$\mathrm{m^2\,s^{-1}}$
ε	porosity	–
ζ	dimensionless height	–
$\Delta\zeta_j$	size of j-th dimensionless height interval	–
η	viscosity	Pa s
θ	contact angle	°
Θ	elasticity parameter	$\mathrm{Pa^{-1}}$
κ	adjustable parameter	–
λ	thermal conductivity	$\mathrm{W\,m^{-1}\,K^{-1}}$
Λ	coefficient	–
μ_k	k-th moment of a distribution	$\mathrm{m^k}$
ν	kinematic viscosity	$\mathrm{m^2\,s^{-1}}$
ν'	Poisson's ratio	–
$\dot{\nu}$	dimensionless drying rate	–
ξ	number fraction	–
Π	dimensionless elasticity parameter	–
ϱ	density	$\mathrm{kg\,m^{-3}}$
σ_{M_c}	standard deviation of coating mass distribution	m
σ_s	standard deviation of layer thickness distribution	m
σ_u	standard deviation of velocity distribution	$\mathrm{m\,s^{-1}}$
σ_x	standard deviation of particle size distribution	m
τ	residence time	s
φ	spray zone volume fraction	–
ϕ	limiter function	–
Ψ_c	coated surface fraction	–
Ψ_{wet}	wet surface fraction	–
Ω	property space	–

Subscripts

0	smallest size considered, initial value
a	asperities
as	adiabatic saturation
agg	agglomerate
bed	bed
break	breakage
c	coating
class	classes
coll	collision
contact	contact
core	core particle
crit	critical
depos	deposition
diff	diffusion
drop	droplet
dry	dry
e	external
elu	elutriation
eq	equilibrium
evap	evaporation
exp	experimental
free	free
g	gas, gas phase
gl	gas-liquid
gp	gas-particle
gt	glass transition
i	internal
in	inlet
imb	imbibition
I	first drying stage
j	index
k	index
l	liquid, liquid phase
lam	laminar
layer	coating layer
max	maximum
mf	minimal fluidization
min	minimum
MC	Monte Carlo
p	particle, particle phase
pl	particle-liquid
pos	position
pp	primary particle
r	random
real	real
s	solid
sec	sector

sel	selection
spray	spray
sprayed	sprayed
suc	successful
tab	tablet
tot	total
turb	turbulent
v	water vapor
w	water
wet	wet

Abbreviations

2D	two dimensional
3D	three dimensional
aq.	aqueous
γ-Al_2O_3	alumina
CFD	computational fluid dynamics
CNMC	constant number Monte Carlo
CVMC	constant volume Monte Carlo
DE	dextrose equivalent
DEM	discrete element method
HPMC	hydroxypropyl methylcellulose
MC	Monte Carlo
MPT	magnetic particle tracking
NaB	sodium benzoate
NaCl	sodium chloride
NH_3	ammonia
PEPT	positron emission particle tracking
PIV	particle image velocimetry
PTV	particle tracking velocimetry

Chapter 1

Introduction

1.1 Motivation

Particulate products represent the majority of all chemical products manufactured in industry. Estimates of the relative amount vary between 60 % for bulk solids according to Schulze [1] and up to 80 % when liquid and solid mixtures, aerosols, and materials that contain gas bubbles are further taken into account, see Merkus [2]. Particles play an important role in many fields such as agriculture, and the chemical, pharmaceutical, and food industries. Examples of particulate products manufactured in these fields are fertilizers, catalysts, detergents, tablets containing an active pharmaceutical ingredient, cosmetics, milk powder, soup and beverage powders.

Particulate goods can be produced from liquids containing solid material, which may be solutions, suspensions, or melts. This process step is performed to reduce transportation costs, simplify handling and post-processing, and to prolong shelf life in comparison to the liquid state of the material.

The end-use properties and performance of the product are defined by the particle properties. Usually, the particle size and its distribution is considered to be the most important property. In general, the particle size distribution should be as narrow as possible to ensure defined properties and the amount of dust (particle size below approx. 100 µm [3]) should be as small as possible. Since inter-particle adhesion forces increase compared to their weight force for smaller particles, the flowability may be diminished. Beyond that, the presence of dust may lead to mass loss, dust explosions, and poses a health risk if the material is toxic.

Another important property is the particle porosity, which relates the void volume and the total volume of a particle. If the desired application involves dissolution (e.g., in case of fertilizers, pharmaceuticals, and beverage powders), the dissolution rate is significantly influenced by porosity. Generally, a high porosity leads to faster dissolution rates. The porosity also has an effect on the mechanical strength of the particles, which should be high enough to withstand stress during packaging, transport, and storage without breakage or dust formation due to abrasion. A high porosity lowers the mechanical strength of the particles. Additionally, porosity directly influences the bulk density of

the product: if the porosity is small, the bulk density will be high and vice versa, affecting packaging and transport of the product.

The product properties are further influenced by the moisture content. If it is too high, the flowability may be diminished due to adhesion forces or the particles may stick together during storage, forming a product, which may not be usable for the intended purpose. The moisture content influences the growth rate of microorganisms, potentially leading to spoilage and a reduced shelf life, which is especially important for foodstuffs. A reduction of the moisture content can be reached by drying, which can be realized during the particle production process or in a subsequent process step. An upper limit of the moisture content is usually given by product specifications. Drying far below this limit directly increases the production costs.

Several processes exist to produce particulate products from liquid raw materials such as crystallization, spray drying, and spray granulation. In crystallization, particles are formed from liquids by solvent evaporation or cooling. In spray drying, a liquid is atomized into droplets, which are in contact with a hot gas. Evaporation of the liquid then produces solid particles. In contrast to crystallization and spray drying, where particles are directly formed from liquid materials, spray granulation aims for size enlargement and adjusting further properties of already existing particles. In this case, the liquid is sprayed onto an agitated particle bed. Several methods exist to realize agitation of the particles such as mechanical agitation in mixers, rotating drums, or pans and pneumatic agitation in fluidized beds. The term granulation can be further categorized based on the size enlargement mechanism and the purpose of the process. If the particles grow by applying a layer of the sprayed solid material around the initial particles, the size enlargement mechanism is called layering. The process is called layering granulation if size enlargement is the main objective. However, if the solid layer is intended to have a function (e.g., a protective layer) and the materials of the solid layer and the particles are different, the process is called coating. The size enlargement mechanism and the process are named agglomeration if particle clusters connected by adhesion forces are created. If the particles are amorphous, spraying pure water may also lead to agglomeration, as sticky spots may be formed on the particle surface due to glass transition. Generally, particle size enlargement by layering and agglomeration can occur simultaneously, but depending on the intended product application only one mechanism should be dominant.

The present dissertation deals with spray fluidized bed processes such as coating, layering granulation, and agglomeration induced by spraying a solution or suspension onto a fluidized particle bed. In this type of equipment, particle formation and drying can be realized in either batch or continuous mode in a single process step with generally high heat and mass transfer rates. Design of such processes requires detailed knowledge of the relationship between operating conditions, material parameters, equipment design, and the final product properties. This can be achieved by extensive experimental work as well as mathematical modeling of the underlying phenomena (i.e., particle formation and heat and mass transfer). For this purpose, different computational methods exist, ranging between macroscopic and microscopic approaches. Macroscopic methods are usually simplified based on assumptions and fast, while microscopic approaches tend to be more detailed,

e.g., by considering each particle individually. At the same time, the increase in resolution leads to higher computational cost, limiting their application for systems at industrial scale.

In this dissertation, both microscopic and macroscopic modeling of batch spray fluidized bed processes is presented. Two microscopic models based on a Monte Carlo method are developed for coating and layering granulation, and agglomeration in spray fluidized beds. Modeling layering using a microscopic approach provides the possibility to describe product properties and their distributions in greater detail compared to previously published models based on macroscopic approaches. Modeling spray fluidized bed agglomeration by means of solid containing liquid using a Monte Carlo method has already been presented in literature. It has been shown to provide a more straightforward method of modeling agglomeration kinetics compared to macroscopic approaches. This dissertation aims at applying this technique to model spray fluidized bed agglomeration of amorphous particles since no model for this process has been published in literature until now. Additionally, a macroscopic method for estimating the dominant size enlargement mechanism in spray fluidized bed processes is presented. This method combines the Stokes criterion, which is usually used in microscopic modeling of agglomeration processes, with a macroscopic process model, enabling the investigation of the border between both size enlargement mechanisms.

1.2 Outline of the thesis

This thesis consists of five main chapters covering a detailed literature survey on particle formation in spray fluidized beds, microscopic modeling using a Monte Carlo method, presenting simulation results for coating and layering granulation and binder-less agglomeration of amorphous particles, and a macroscopic approach for estimating the dominant size enlargement mechanism.

Chapter 2 focuses on the state of the art of spray fluidized bed processes and the theory necessary to understand the present dissertation. First, the fundamentals of fluidization and spray fluidized bed processes are given, and the underlying processes occurring on the single particle scale are discussed. The relevant properties influencing the product performance and established methods describing the border of the size enlargement mechanisms are discussed. Finally, the state of the art of modeling spray fluidized bed processes is presented.

In Chapter 3, a detailed description of the Monte Carlo method used to model both coating and layering as well as binder-less agglomeration is given. At first, the scaling procedure, event selection, time step calculation, and discretization of the particle surface are discussed. Then, modeling of the micro-processes and events occurring in the considered processes such as deposition of droplets, binary particle collisions, droplet drying, size enlargement, and breakage is shown. Additionally, the assumptions used in modeling the micro-processes and events are summarized.

Chapter 4 shows how coating and layering granulation in spray fluidized beds can be modeled based on the events and processes on the single particle scale, described in the previous chapter. A detailed simulation study, including theoretical validation of the model and an investigation of the influence

of various parameters on product properties, is presented. Furthermore, the model is validated with experimental data. The used experimental setup is described before comparing results from simulations and experiments.

In Chapter 5, the Monte Carlo model for binder-less agglomeration of amorphous particles is presented. The description of the structure of the algorithm is followed by the presentation of a simulation study investigating the influence of process conditions and material parameters on the microscopic agglomeration behavior. The governing agglomeration behavior on the macroscopic scale is explained using experimental data, after the experimental setup is described. Additionally, the results from experiments are compared to simulation results.

Chapter 6 covers the macroscopic model for estimating the border between layering and agglomeration. First, the process model is described in detail, including relevant probabilities as well as the used heat and mass transfer and growth model. The solution of the used equations is explained and the applied model assumptions are summarized. The influence of process and wetting parameters on the dominant size enlargement mechanism is investigated by means of a simulation study. Additionally, a new description of the border between layering and agglomeration is proposed based on further simulations and experiments published in literature.

The main results and corresponding conclusions of this dissertation are summarized in Chapter 7 along with an outlook on future research.

Chapter 2

Particle formation in spray fluidized beds

This chapter presents a detailed literature review about particle formation in spray fluidized beds. At first, the phenomenon of fluidization is explained, and the fundamentals of spray fluidized beds are given. Afterwards, micro-processes (i.e., processes occurring on the single particle scale), size enlargement mechanisms, properties of the formed particles, and the border between different size enlargement mechanisms are discussed. Macroscopic and microscopic modeling concepts for the discussed processes are presented before the goals of this dissertation are formulated based on the presented literature survey.

2.1 Fluidized beds

2.1.1 Fluidization

A fluidized bed apparatus consists of a process chamber, a distributor plate, and a bed of particles in the fluid-like or fluidized state. Fluidization is achieved by a fluid flow (gas or liquid) passing through the particle bed. The distributor plate ensures an even distribution of the fluid over the cross sectional area of the apparatus. As particle formation in gas-solid fluidized beds is to be investigated in this work, the focus lies on gas-solid fluidized beds in the following sections. Depending on the flow rate of the gas, different stages of fluidization can be observed, see Kunii and Levenspiel [4]. The main stages of fluidization in gas-solid fluidized beds are shown in Figure 2.1. At a very low flow rate of the gas, the particles remain in contact and a fixed bed is present. If the flow rate is increased to the point where the particles begin to float and move stochastically, the so-called point of minimum fluidization is reached. At this point, equilibrium between the force of resistance between particle and gas, buoyancy, and the weight force of the particles is established [5]. Compared to the fixed bed, height and porosity of the bed are larger. Increasing the flow rate above minimum fluidization results in further expansion of the bed height, a higher bed porosity, and instabilities with bubbling and channeling of the gas. This stage is called bubbling fluidization. A further increase of the flow rate eventually leads to pneumatic transport or elutriation of the particles. In this case, the solids are carried out of the bed along with the gas. According to Mörl et al. [6], the range of existence of a

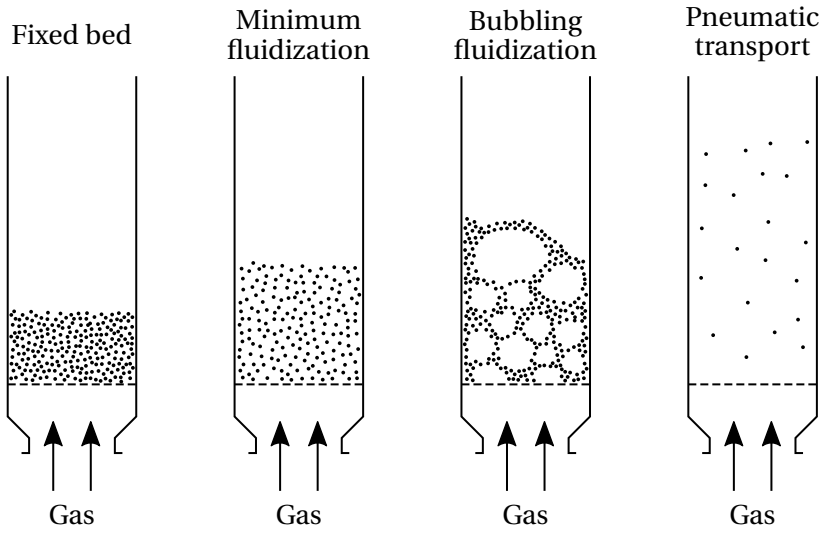

Figure 2.1: Selected fluidization regimes for gas-solid fluidized beds (adapted from Kunii and Levenspiel [4]).

fluidized bed lies between minimum fluidization and elutriation. The correlations used to determine these two points in this work are summarized in Appendix B.

Geldart [7] investigated the influence of particle properties (i.e., the density difference between solid material and gas, and the particle size) on the fluidization behavior. Based on published literature and own experimental work, he identified four groups of particles, which are shown in Figure 2.2 and described below:

- *Group A*: The particles have a small mean size (50 µm to 200 µm according to Mörl et al. [6]) and a density below 1400 kg m^{-3}. After minimum fluidization, a considerable bed expansion is observed before bubbling commences.
- *Group B*: Particle size is typically between 40 µm and 500 µm, and the density ranges between 1400 kg m^{-3} and 4000 kg m^{-3}. In this group, bubbles start to form slightly above the minimum fluidization velocity and the bed expansion is rather small.
- *Group C*: This group includes particles which are cohesive and very hard to fluidize, since the inter-particle forces are stronger than those exerted by the gas flow. This may occur as a result of a very small particle size (smaller than 50 µm [6]), electrostatic forces, or the presence of liquid or sticky material in the bed. Mechanical stirrers, vibration of the apparatus, and pulsation of the gas can be used to improve the fluidization behavior [6].
- *Group D*: Particles falling into this group are rather large and/or very dense. Deep beds of these particles are difficult to fluidize, large exploding bubbles and channeling is observed. Fluidization of particles showing such behavior is usually done in shallow beds or spouted beds [4].

In general, a fluidized bed shows the following advantages and disadvantages [4, 8]:

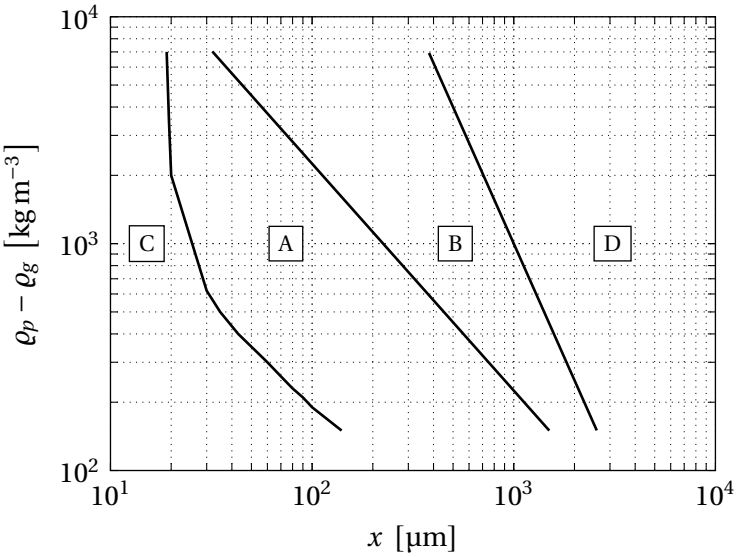

Figure 2.2: Geldart classification for fluidization by ambient air (adapted from Geldart [7]).

- high heat- and mass transfer rates,
- high surface area,
- suitable for large-scale and continuous operations, and
- easy handling of the solids.

Disadvantages are:

- abrasion of the solid material,
- erosion of pipes and vessels,
- possible segregation for wide particle size distributions (elutriation of fines), and
- non-uniform residence time distributions in continuous operations resulting in non-uniform product properties.

Fluidized bed technology is widely used in industry for different chemical and physical processes [6, 9]. Chemical processes comprise gas-gas reactions, in which particles act as a catalyst, and gas-solid reactions, where the solid material is transformed. Examples are cracking of hydrocarbons and combustion or gasification, respectively. Examples of physical processes are mixing, classifying, adsorption, heating/cooling, drying, coating, layering granulation, and agglomeration.

2.1.2 Spray fluidized beds

The main parts of a spray fluidized bed are shown in Figure 2.3. The fluidization gas enters the gas inlet chamber, passes through the gas distributor, and fluidizes the particle bed in the process chamber. In the exhaust chamber, filter elements are often used to remove dust from the gas before

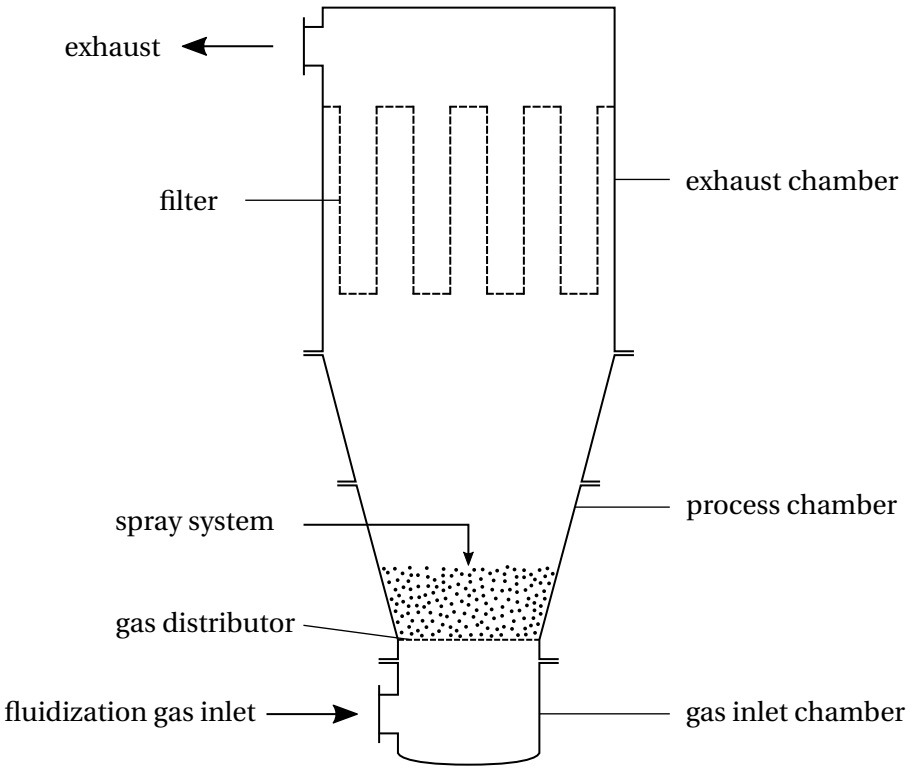

Figure 2.3: Main parts of a spray fluidized bed used for particle formation (adapted from Jacob [10]).

it flows out of the apparatus. In the process chamber, liquid containing solid material is added to the particle bed using a spray system (feed lines and one or several nozzles). Solutions, suspensions, and melts may be sprayed to induce growth of the particles by different mechanisms. In case of solutions and suspensions, the liquid part evaporates and is removed along with the gas, while the solid part remains on the particles. When melts are sprayed, the liquid is transformed into solid material by cooling.

Fluidized bed equipment can be used for batch or continuous processes and is available in various designs such as process chambers with circular or rectangular cross-sections, which may be constant or expanding in the vertical direction. A detailed overview regarding different design options of spray fluidized beds is given by Jacob [10]. Furthermore, different processing options concerning the nozzle orientation are available, which influence the product properties. The main processing options are briefly described below [10]:

- *Top-spray*: The spray nozzle is located in the upper part of the process chamber and the liquid is sprayed on top of the fluidized particles. The tendency for spray drying and nozzle caking is increased compared to other options. This configuration is typically used for coating and producing agglomerates with low and medium bulk densities.
- *Bottom-spray*: The spray nozzle is located in the lower part of the process chamber and sprays upward into the bed. The tendency for spray drying is reduced. Due to a "cleaning effect" of the particle bed, nozzle caking is reduced as well. Bottom-spray is typically used for coating,

layering granulation and agglomeration (medium and high bulk densities).

- *Tangential-spray*: The spray nozzle is installed at the wall of the process chamber and sprays tangentially into the particle bed. The tendency for spray drying and nozzle caking is reduced. This option is typically used for coating and layering granulation.

Based on these processing options, two specialized options have been developed [10]:

- *Wurster processing*: The Wurster process was developed in the 1950s and 1960s [11] based on the bottom-spray option. In this case, the process chamber is divided into two regions using a tube and in combination with a segmented gas distributor, a more controlled circulation of the particles is obtained. Typical applications are coating of fine particles and layering granulation.
- *Rotor processing*: This process was developed based on the tangential-spray option. A rotating disk is used in the lower part of the process chamber instead of a gas distributor. The fluidization gas enters via a ring gap between the rotor and the wall of the apparatus. This option is typically used to produce very compact particles by layering granulation and agglomeration.

In the following sections, the underlying processes leading to different size enlargement mechanisms in top-spray fluidized beds using solutions or suspensions are described.

2.2 Size enlargement of particles in spray fluidized beds

2.2.1 Micro-processes

Particle growth in spray fluidized beds is the result of a complex network of processes occurring on the single particle scale, so-called micro-processes. Several attempts have been made in literature to summarize the network of micro-processes for spray fluidized bed processes, see Tan et al. [12] for melt granulation, Guignon et al. [13] and Werner et al. [14] for coating, and Terrazas-Velarde [15] for agglomeration. Based on these works, a simplified network of micro-processes categorized into single droplet drying, particle-droplet collisions, particle-particle collisions, and deposited droplet processes is shown in Figure 2.4.

The spray nozzle creates single droplets with a size and velocity distribution entering the fluidized bed. The droplets start to dry and their size is reduced in the first drying stage, where the drying rate is controlled by external heat and mass transfer [16]. Depending on the conditions and the used materials, drying increases the solid concentration in the droplet until a solid shell or crust is formed at the surface of the droplet while the interior of the droplet is still wet. The solid crust formation represents the beginning of a second drying stage and adds a heat and mass transfer resistance leading to a slower drying process of the droplets [16]. As drying continues, a solid dust particle is formed eventually. This phenomenon is called spray drying. It is also referred to as overspray in the context of spray fluidized bed processes, where it is generally unwanted, since it produces dust. Additional phenomena such as inflation, deflation, and particle rupture, influencing the morphology

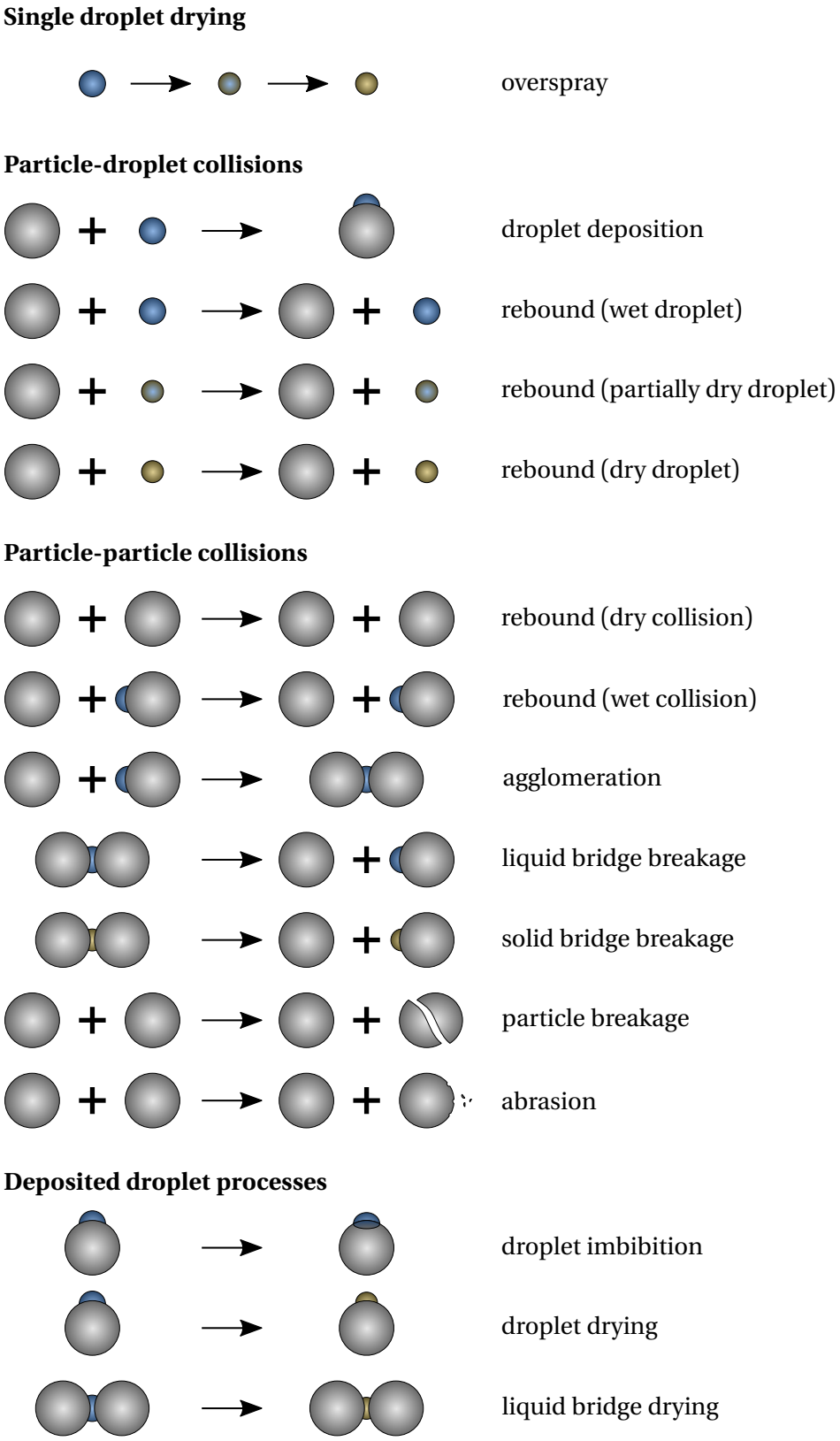

Figure 2.4: Simplified network of micro-processes occurring in spray fluidized bed processes.

of the resulting dust particles have been reported, see Tran et al. [16], Walton [17], and Handscomb et al. [18], which are omitted in Figure 2.4.

Collisions between particles and droplets occur due to their movement in the fluidized bed. The result of such a collision can either be adherence and subsequent spreading of the droplet on the particle surface (droplet deposition) or rebound of the droplet. In a spray fluidized bed, droplets and particles collide mainly due to interception (passage of droplets close to the particle surface) and inertia (particle surface is on the trajectory of the droplets), see Guignon et al. [13]. According to Werner et al. [14], adherence of the droplets is influenced by a number of parameters such as the collision parameters (angle of the collision as well as momentum of droplets and particles), liquid and interfacial properties, and the surface structure of the particles. A collision may result in rebound if the droplet recoil velocity after impact is too high or significant droplet drying has occurred prior to the collision.

Inter-particle collisions occur in spray fluidized bed processes as well. A collision is called a dry collision if no wet droplet is present at the contact point of the colliding particles, resulting in rebound. Consequently, a wet droplet must be present at the contact point during a wet collision. A wet collision results either in adherence (agglomeration) of the particles and subsequent formation of a liquid bridge or in rebound. The outcome of a wet collision depends strongly on the parameters of the collision and properties of the liquid and solid material. Collisions may also lead to different types of breakage such as breakage of bridges (liquid and solid bridges in agglomerates), breakage of single particles, and abrasion of the material present on the particle surface (particle material or solidified droplets).

If the particle material exhibits an interconnected pore system, a deposited droplet may be imbibed into the porous structure. At the same time, drying of deposited droplets occurs. Both processes lead to a reduction of the droplet height. Similar to the above described case of spray drying, deposited droplets containing solid material may show crust formation during drying before the deposited droplet solidifies completely. Additionally, liquid bridges in agglomerates dry and solidify as well, transforming them into solid bridges.

The above described micro-processes imply that the droplet size is smaller than the particle size. However, if the droplet size is larger than the particle size, the interactions between particles and droplets are different, see Abberger et al. [19], Seo et al. [20], and Boerefijn and Hounslow [21]. In this case, a droplet can wet the surface of multiple particles at once. The result is an agglomerate consisting of several particles connected by liquid bridges. Collisions between these agglomerates lead to compaction and further agglomeration, see Iveson et al. [22] and Hapgood et al. [23]. Since this work focuses on systems with small droplets compared to the particle size, a detailed discussion of these phenomena is omitted.

2.2.2 Coating and layering granulation

In coating and layering granulation, the main goal is the production of single particles consisting of a core particle covered by a solid layer. The solid layer is built around the core particles by repeated deposition and drying of droplets, see Figure 2.4. In both processes, the size enlargement mechanism is identical and called layering. Overspray and particle-particle collisions leading to agglomeration are generally undesired. Continuous layering granulation is an exception since the particles produced by overspray serve as new seed particles in this process. In coating and batch layering granulation, overspray is considered as material loss and may impair the product quality. According to Nienow [24], typical growth rates of coating and layering granulation are in the range of 10 µm h^{-1} (coating) to 100 µm h^{-1} (layering granulation). Figure 2.5 shows a schematic representation of particle growth by layering.

In case of coating, the material of the core particles and the added solid material are different. The thickness of the added solid layer is relatively small since the main purpose of this process is a functionalization of the particles and not a change of the particle size [25]. In layering granulation, the material of the core particles and the added solid material are the same. The change of the particle size distribution is the main goal, resulting in larger layer thicknesses compared to coating.

Applications of coating can be found in the pharmaceutical, chemical, agricultural, and food industries with varying objectives. Sustained release coatings are applied to pharmaceuticals and fertilizers, which control the start and duration of release of active ingredients [26–28]. In the chemical industry the properties of catalysts can be enhanced by membrane coating of catalyst particles [29]. Coatings are also used to add flavor [30], mask bad taste and odor [13, 30, 31], and to protect ingredients from environmental influences (water/moisture, acid, oxygen) [13, 32, 33]. Further applications are improvement of appearance [27, 30, 34] and reducing abrasion or sticking [13, 33]. Applications of layering granulation can be found in the agricultural industry, where it is used to produce solid pesticides [35] and fertilizers (e.g., urea [36, 37], and ammonium sulfate [38, 39]).

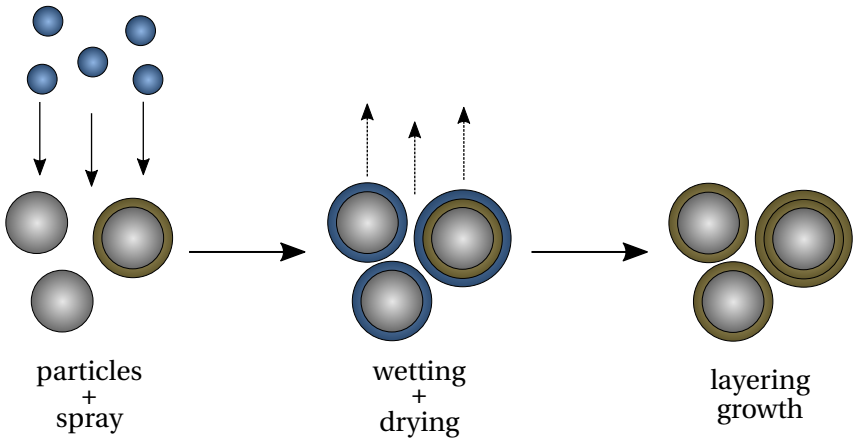

Figure 2.5: Schematic representation of particle size enlargement by layering.

2.2.3 Agglomeration

In agglomeration, small powder particles are transformed into larger particles called agglomerates. They consist of several primary particles bound together by different mechanisms. The fundamentals of binding mechanisms between primary particles in agglomerates have been presented by Rumpf [40]. An overview regarding the major binding mechanisms is given by Bück et al. [25] and Schubert [41], see Figure 2.6. Particles can be bound together by material bridges. Solid material bridges can be formed due to sintering, chemical reactions, cooling of molten binders, and crystallization of binder solutions due to drying at contact points. Liquid material bridges comprise adhesion due to highly viscous binder and capillary forces. Particles may also stick together without material bridges. These mechanisms are divided into van der Waals and electrostatic forces. Interlocking may also play a role for fibrous particles. For industrial agglomeration, mostly van der Waals forces and material bridges are relevant [42].

In spray fluidized bed processes, agglomerates are formed by repeated droplet deposition, wet collisions, and liquid bridge drying, see Figure 2.4. Overspray and layering are undesired since in both cases material for generating liquid and solid bridges is lost. Typical growth rates are in the range of 100 µm h^{-1} to 1000 µm h^{-1} [24] exceeding by far the growth rates of coating and layering granulation. A schematic representation of size enlargement by agglomeration is shown in Figure 2.7.

Depending on the molecular structure of the particle material, different mechanisms leading to agglomeration can be observed, see Palzer [42, 43]. Especially in food systems, two different supramolecular structures can be found: amorphous and crystalline systems. In amorphous systems the molecules are in disorder, while in crystalline systems the atoms and molecules are highly ordered. As the free volume of a system is linked to its degree of order, the free volume of amorphous structures is generally higher than in equivalent crystalline structures at a given temperature. Amorphous structures are meta-stable, which means they transform into crystalline structures over time. Amorphous structures can be produced by transforming a melt or liquid into a solid by either fast cooling or rapid removal of solvent. Solids can also be converted into the amorphous state by grinding, which is called solid state amorphization [42, 44, 45]. If amorphous materials and liquids with similar polarity come into contact, solvent molecules can migrate into the solid matrix and increase the mobility of the matrix molecules, acting as a plasticizer while solid molecules may migrate into the liquid droplet. This is observed in various agglomeration processes used in the food industry, where water or aqueous solutions are sprayed on moving, water-soluble amorphous particles [42]. The migration of water from deposited droplets into the amorphous matrix leads to a locally decreased glass transition temperature. If the temperature of the material is near the glass transition temperature, the viscosity of the material decreases. The result is a sticky, rubbery material, which is able to form viscous bridges when particles collide at these spots [42, 45]. Drying then generates solid bridges connecting the primary particles. If a water-soluble crystalline material comes into contact with water, the material dissolves, but almost no water migrates into the crystalline structure. Therefore, the viscosity of the wet spots remains moderate [42]. Depending on the materials, other substances need to be included in the binder to increase viscosity and generate liquid bridges between colliding

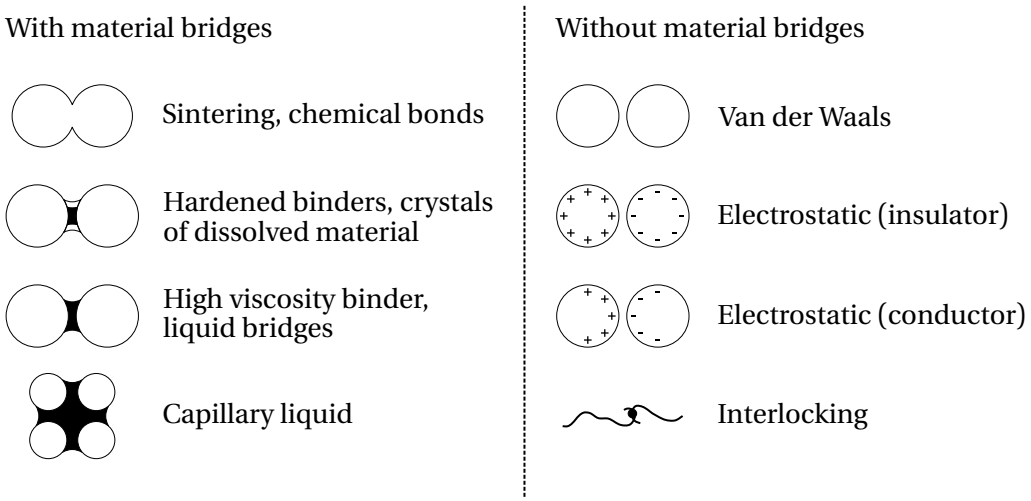

Figure 2.6: Major binding mechanisms in agglomerates (adapted from Bück et al. [25] and Schubert [41]).

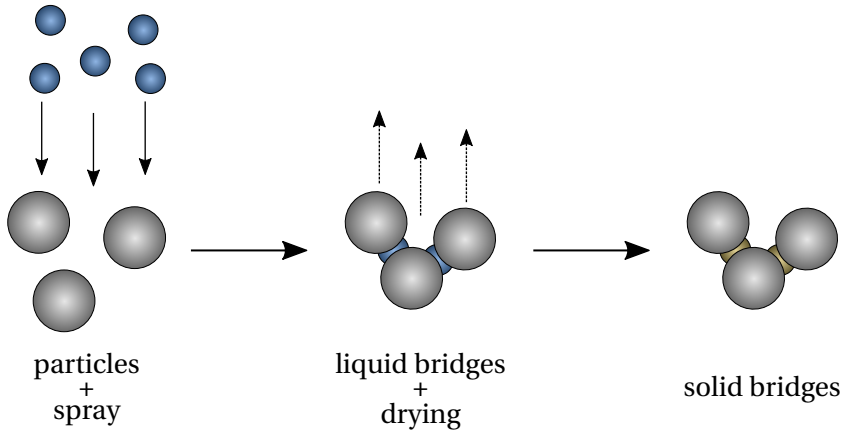

Figure 2.7: Schematic representation of particle size enlargement by agglomeration.

particles. Solid bridges are formed by drying and re-crystallization in this case.

Depending on the process conditions, several growth regimes can be observed in agglomeration processes. Iveson and Litster [46] and Iveson et al. [47] developed a growth regime map for liquid-bound agglomerates, indicating the type of agglomeration depending on a Stokes deformation number St_{def} and the maximum pore saturation S_{max}. These parameters are defined as:

$$\mathrm{St}_{def} = \frac{\varrho_p u_{coll}^2}{2Y'}, \tag{2.1}$$

$$S_{max} = \frac{\varrho_p X \left(1 - \varepsilon_{p,min}\right)}{\varrho_l \varepsilon_{p,min}}. \tag{2.2}$$

In these equations, ϱ_p is the density of the particles (or agglomerates), u_{coll} is the collision velocity, Y' is the yield stress of the particles, X is the liquid content of the particles, ϱ_l is the density of the liquid, and $\varepsilon_{p,min}$ is the minimum porosity of the particles for the given process conditions. The growth regime map is shown in Figure 2.8. The identified types of agglomerate growth are:

- *Steady growth*: The average agglomerate size increases steadily with time. This is typical for easily deformable agglomerates. Increasing the liquid content increases the growth rate.
- *Induction growth*: At the beginning of the process, a period of little or no agglomeration is observed, followed by a period of rapid agglomeration. Increasing the liquid content decreases the length of the first period. This is typical for less deformable agglomerates.
- *Nucleation*: Small agglomerates are formed by spraying of liquid. Further agglomeration is not possible due to insufficient liquid content.
- *Crumb*: The formed agglomerates are too weak and cannot form stable bonds, leading to breakage.
- *Slurry/over-wet mass*: Too much liquid is added and the particles form an oversaturated slurry.
- *Dry, free-flowing powder*: The particles will remain as a dry powder since the amount of added liquid is insufficient to form agglomerates.

Applications of agglomeration can be found in several industries such as food, chemical, and pharmaceutical industry. The main objective is to increase the particle size and improve properties for the respective application. In the food industry, the manufacturing of several products such as dairy powders (milk or whey powders), dehydrated convenience foods (instant soups, sauces, seasonings), or beverage powders (soluble coffee, cocoa, sugar-based beverage powders) [42, 43] involves an agglomeration step. In the chemical industry, products such as detergent powders [48–50] or fine chemicals (e.g., vitamin mixes) [42] are agglomerated. Pharmaceutical and detergent powders undergo an agglomeration step prior to tableting [42, 51, 52] or in combination with spheronizing when producing spherical agglomerates [53].

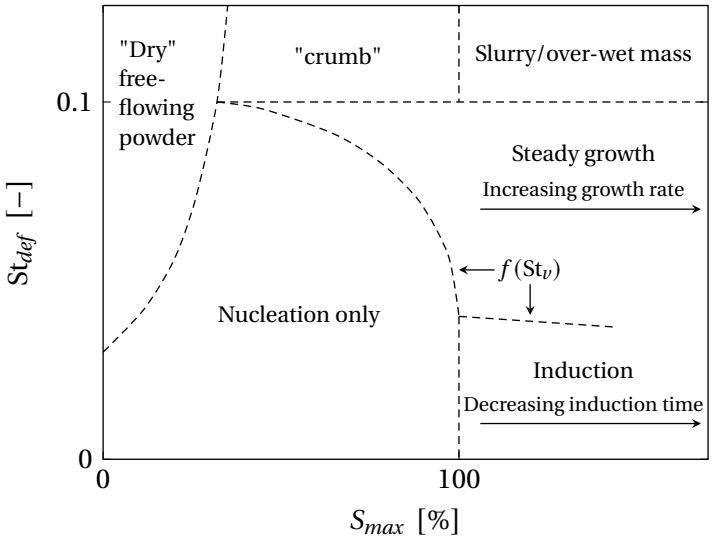

Figure 2.8: Growth regime map derived by Iveson and Litster [46] and Iveson et al. [47] indicating the types of agglomerate growth.

2.2.4 Product properties

Important properties defining the product quality of particles produced by coating, layering granulation, and agglomeration are the particle size distribution, shape, density, porosity, flowability, strength, redispersion behavior, and the moisture content [25]. To ensure intended product performance, these properties have to be within certain specifications. Below, the influence of the properties on the product performance is briefly discussed.

Important properties of coated particles are coating mass uniformity and the morphology of the coating [27, 33]. Coating mass uniformity refers to the variation of coating mass among individual particles and is therefore called an inter-particle property. The variation of the coating mass is especially important when applying active ingredients in the coating. Coating morphology refers to the distribution of the coating thickness on individual particles, which is an intra-particle property. The morphology is further characterized by coating layer porosity and the existence of fissures or gaps. Beyond that, surface coverage is an important property. These properties also influence product performance when the coating is applied for a sustained release application or as a protective layer.

The main property of particles produced by layering granulation, influencing product performance is the particle size distribution, see Cotabarren et al. [36]. In case of fertilizers, usually a narrow size distribution is preferred to ensure uniform distribution of the fertilizer on the field. Additionally, segregation effects are minimized when producing mixtures of fertilizers [36]. The dissolution behavior depends on the size and porosity of the particles. The porosity should be relatively low to achieve a certain strength minimizing abrasion [36] and to ensure slow dissolution behavior [25].

Important properties of agglomerates are the particle size distribution, redispersion behavior, and compressibility. Fundamentals of redispersion of agglomerates have been stated by Pfalzer et al. [54]. The process of redispersion can be divided into wetting, sinking, and breakup of the agglomerates

into their primary particles. In order to achieve fast and complete redispersion, agglomerates should consist of a large number of bridges characterized by relatively weak strength. The bridges should be weak to facilitate dissolution, while a large number of bridges ensures mechanical stability of the agglomerates, e.g., during transport or packaging. Powders are agglomerated prior to tableting to improve compactibility and the strength of the resulting tablets [42, 55]. The flowability of the agglomerates needs to allow accurate dosing when tableting particles including active ingredients and minimize segregation prior to tableting to ensure tablet uniformity [52].

Tsotsas [56] states that particle formation in spray fluidized beds is strongly influenced by the drying conditions. For layering granulation and coating it is shown that the surface structure of the resulting particles depends on the drying conditions: at low spraying rates and high temperatures smooth particles are obtained, while high spraying rates and low temperatures lead to rough particles. Rieck et al. [57] show that not only the surface structure, but also the porosity of the solid layer is changed accordingly. An influence of layer porosity on the process kinetics is shown as well. Since in these studies a solution crystallizing during drying was used for coating, the influence of drying on crystallization is assumed to be the reason for the change in surface structure and porosity. The kinetics of agglomeration and the agglomerate structure depend on the drying conditions as well. However, the structure of agglomerates is much more complex than the structure of particles produced by layering. As a result, a variety of morphological descriptors such as radius of gyration, fractal dimension and pre-factor, agglomerate porosity, coordination number distribution, and coordination angle distribution are available [56]. Dadkhah and Tsotsas [58] investigated the influence of operating conditions on such descriptors by creating 3D images of agglomerates using X-ray micro-tomography. It was found for non-porous primary particles that a higher agglomeration rate leads to denser agglomerates (higher fractal dimension and coordination number, lower porosity) and a lower agglomeration rate leads to a looser, fluffier product (lower fractal dimension and coordination number, higher porosity).

2.2.5 Border between layering and agglomeration

In particle formation processes in spray fluidized beds, usually both size enlargement mechanisms (layering and agglomeration) occur simultaneously. However, in order to achieve the required product quality, only one mechanism depending on the application of the product is desired. In this case, the material properties as well as the process parameters need to be adjusted to favor either layering or agglomeration. The amount of properties and parameters influencing the dominating mechanism opens up a wide field of investigation.

Many studies investigating the border of the size enlargement mechanisms experimentally can be found in literature. Some investigations focus on the detection of defluidization [59, 60] occurring when agglomeration leads to very large particles and the mass flow rate of the fluidization gas cannot maintain the fluidized state. Others deal with the direct measurement of the mass fraction of agglomerated particles [34, 37, 61, 62]. In any case, these studies are focused on coating experiments, where agglomeration is undesired and should be avoided. According to the mentioned works,

agglomeration is more pronounced if particle size, bed temperature, mass flow rate, and evaporation capacity of the fluidization gas are decreased and the spraying rate and droplet size are increased.

Theoretical studies regarding the border of layering and agglomeration are also available in the literature. Below, the criteria presented by Akkermans et al. [63], Davis et al. [64] and Barnocky and Davis [65] are discussed.

Akkermans et al. [63] presented a criterion predicting the dominant size enlargement mechanism for the production of detergent agglomerates. A dimensionless number called Flux-number FN was introduced, which is defined as:

$$\mathrm{FN} = \log\left(\frac{\varrho_p\left(u_g - u_{mf}\right)A_{spray}}{\dot{M}_{spray}}\right). \tag{2.3}$$

In this equation, ϱ_p is the density of the particles, $u_g - u_{mf}$ is the difference between the gas velocity and the minimum fluidization velocity (also known as excess gas velocity), $\dot{M}_{spray}$ is the mass flow rate of the spray, and A_{spray} is the contact area between each spray cone and the particle bed. A classification of the size enlargement mechanisms based on the works of Wasserman et al. [49] and Akkermans et al. [63] is given by Boerefijn and Hounslow [21] and Boerefijn et al. [50]:

- *Flooding*: Flooding will occur if FN < 2. The result is rapid agglomeration leading to defluidization.
- *Agglomeration*: In order to achieve agglomeration without defluidization, the condition $2 \leq$ FN ≤ 3.5 must be fulfilled.
- *Layering*: Particle growth by layering will occur if FN > 3.5.

Hede et al. [61] suggest that higher values for the Flux-number are needed to ensure size enlargement by layering since they found layering to be the dominant size enlargement mechanism for FN $\geq$ $4.5 \ldots 4.7$.

Further investigations focus on the description of binary, normal collisions between particles in spray fluidized beds. In these studies, two spherical particles with a radius R approaching each other with a velocity u_{coll} and covered with a liquid layer of thickness h_l and viscosity η are considered. Davis et al. [64] consider particles with a smooth surface (no surface roughness). Upon collision, the approaching particles are slowed down due to viscous forces of the liquid. A large pressure develops in the liquid, which may additionally lead to elastic deformation of the particles. Barnocky and Davis [65] consider two colliding spherical particles with a surface roughness h_a covered by a liquid layer, based on a theory presented by Davis [66]. In this case, the particles are also slowed down by the liquid layer. When the particles come into contact at the surface roughness elements, they may also deform elastically. In both cases, particles will stick together and agglomerate if their kinetic energy is dissipated during the collision. Otherwise, rebound will occur.

In both approaches, the particles are characterized by their viscous Stokes number St_v. The condition for rebound is met if a critical value St_{crit} is exceeded. Therefore, the general condition for successful

agglomeration can be expressed as:

$$\mathrm{St}_v \leq \mathrm{St}_{crit}. \tag{2.4}$$

The viscous Stokes number is defined as:

$$\mathrm{St}_v = \frac{2}{3}\frac{M_p u_{coll}}{\pi \eta R^2}, \tag{2.5}$$

where M_p is the mass of the colliding particles, u_{coll} is the collision velocity, η is the viscosity of the liquid layer, and R is the radius of the colliding particles. If size and mass of colliding particles are not equal, the harmonic mean values of the individual masses and radii can be used as shown in literature, see Terrazas-Velarde [15] and Tardos et al. [67]. The definition of the critical viscous Stokes number depends on the morphology of the particles (smooth or rough surfaces). For smooth surfaces, St_{crit} becomes [68]:

$$\mathrm{St}_{crit} = \frac{2}{5}\ln\left(\frac{4\sqrt{2}}{3\pi\Pi}\right). \tag{2.6}$$

In this equation, Π is a dimensionless elasticity parameter, which is defined as:

$$\Pi = \frac{4\Theta\eta u_{coll} R^{3/2}}{h_l^{5/2}} \quad \text{with} \quad \Theta = \frac{1-\nu_1'^2}{\pi E_1} + \frac{1-\nu_2'^2}{\pi E_2}. \tag{2.7}$$

The parameter Θ can be calculated using Poisson's ratio ν' and the Young's modulus E of particle 1 and 2. For rough surfaces, St_{crit} becomes [65]:

$$\mathrm{St}_{crit} = \left(1 + \frac{1}{e'}\right)\ln\left(\frac{h_l}{h_a}\right). \tag{2.8}$$

In this equation, e' is the coefficient of restitution of the particles and h_a is the height of the surface asperities (surface roughness).

The criterion for the collision of two particles with rough surfaces was later used by Ennis et al. [69] two derive a classification of the size enlargement mechanisms:

- *Noninertial regime*: In this regime $\mathrm{St}_v/\mathrm{St}_{crit} \rightarrow 0$. This means that St_v is always smaller than St_{crit} and consequently all collisions lead to agglomeration as long as a liquid layer is present. The distribution of the liquid controls the agglomeration process.
- *Inertial regime*: The largest Stokes numbers equal the critical value ($\mathrm{St}_{v,max} \approx \mathrm{St}_{crit}$). The kinetic energy of the particles and the layer viscosity start to play a role.
- *Coating regime*: The average Stokes number equals the critical value ($\overline{\mathrm{St}}_v \approx \mathrm{St}_{crit}$). Particle growth by agglomeration is not achieved since coalescence and rebound compensate each other. Instead, the particles grow only by layering.

An extended criterion taking plastic deformation of the colliding particles into account has been presented by Liu et al. [70]. However, the present work focuses on non-deformable, elastic particles, which is why a detailed discussion of the model by Liu et al. [70] is omitted.

In contrast to theoretical approaches dealing with normal collisions described above, Donahue et al. [71, 72] present theoretical and experimental work on oblique collisions between particles. They have found that the above shown Stokes criterion (derived for normal collisions) is able to describe the outcome of oblique collisions as well. However, when a certain impact angle is exceeded, particles may separate after successful agglomeration, although the Stokes criterion is met. This observation is attributed to centrifugal forces arising from rotation of the agglomerate, leading to breakage of the liquid bridge. A dimensionless number (i.e., the centrifugal number) is proposed to characterize the influence of centrifugal forces.

The above shown criteria allow an estimation of the dominant size enlargement mechanism based on parameters on the single particle level. The decision whether a collision is successful depends on the properties of the particles (i.e., size, density, surface roughness, velocity, elasticity) and the liquid film (i.e., height and viscosity). As shown by Tsotsas [56], drying influences the liquid film properties, but also the area covered by deposited droplets. The latter also plays a role since wet spots must be present at the contact points for agglomeration to occur. In this way, drying influences not only the kinetics of the particle formation process, but also which size enlargement mechanism dominates.

Both criteria (Flux-number and Stokes criterion for normal collisions) have been tested experimentally in the frame of spray fluidized bed layering granulation by Hede et al. [61] and Villa et al. [73] using urea and sodium sulfate, respectively. In both cases, layering was the desired size enlargement mechanism, which was also predicted by both criteria. However, in some cases high percentages of agglomerates were measured, indicating that more complex criteria are required. For example, the wet particle surface also plays a role as discussed above and should therefore be included in such an extended criterion.

2.3 Modeling of particle formation

2.3.1 Particle size distribution

A particulate product or a population of particles is characterized by its properties such as size, shape, temperature, or moisture content. Usually, such properties are distributed and cannot be sufficiently described solely by a mean value. In order to characterize such property distributions, the number density function can be used. According to Ramkrishna [74], the number density function n is defined as:

$$N_{p,tot}(t) = \int_{\Omega_e} \int_{\Omega_i} n(t, \mathbf{i}, \mathbf{e}) \, \mathrm{d}V_i \, \mathrm{d}V_e. \tag{2.9}$$

In this equation, $N_{p,tot}$ is the total number of particles in the population, the vectors **i** and **e** refer to the internal and external coordinates, Ω_i and Ω_e represent the domain of internal and external coordinates, respectively. The variables $\mathrm{d}V_i$ and $\mathrm{d}V_e$ are then infinitesimal volume measures of Ω_i and Ω_e. External and internal coordinates are used to characterize the state of a particle. External coordinates represent the spatial position and are limited to a number of three. Internal coordinates represent the properties of a particle such as size, shape, temperature, or moisture content. The number of internal coordinates is not limited. The unit of the number density function depends on the units of the properties. In general, the unit of n can be described as:

$$[n] = \frac{1}{\prod_i [e_i] \prod_j [i_j]}. \tag{2.10}$$

If the particle properties do not depend on the spatial position of the particle, external coordinates can be neglected and Equation (2.9) simplifies to:

$$N_{p,tot}(t) = \int_{\Omega_i} n(t, \mathbf{i})\, \mathrm{d}V_i. \tag{2.11}$$

In this case, $n(t, \mathbf{i})$ describes the number of particles being in the same property interval at time t.

An important example is the number density distribution of the particle size x. Here, external coordinates are neglected and only one internal coordinate (i.e., the particle size x) is used. Usually, a normalized number density function q_0 is used:

$$q_0(x) = \frac{n(x)}{\int_0^\infty n(x)\,\mathrm{d}x} = \frac{n(x)}{N_{p,tot}} \quad \text{with} \quad [n] = [q_0] = \frac{1}{[x]}. \tag{2.12}$$

The unit of both $n(x)$ and $q_0(x)$ depends on the unit of x. The normalization of $n(x)$ with the total number of particles $N_{p,tot}$ leads to:

$$\int_0^\infty q_0(x)\,\mathrm{d}x = 1. \tag{2.13}$$

In addition to the normalized number density function q_0, a cumulative form Q_0 can be used to describe a size distribution:

$$Q_0(x) = \int_0^x q_0(x)\,\mathrm{d}x. \tag{2.14}$$

In the above shown equations, the subscript of q_0 and Q_0 indicates that the distribution with respect to the particle number is used. In general, other types of distributions are also available such as the distribution with respect to the particle volume or mass [75]. However, in this work the distribution with respect to the particle number is used in all cases.

Important parameters such as different mean values can be obtained from moments of the number density function. The k-th moment μ_k of a number density function $n(x)$ is defined as [76]:

$$\mu_k = \int_0^\infty x^k n(x)\,\mathrm{d}x. \tag{2.15}$$

Depending on the value of k, different physical interpretations of the corresponding moments are possible such as the total number, length, surface area, and volume of the particles:

$$N_{p,tot} = \mu_0, \tag{2.16}$$

$$L_{p,tot} = \mu_1, \tag{2.17}$$

$$A_{p,tot} = \pi\mu_2, \tag{2.18}$$

$$V_{p,tot} = \frac{\pi}{6}\mu_3. \tag{2.19}$$

Note that the shape factors used for the total surface area and the total volume are valid for spherical particles. If the shape of the particles is different, other shape factors need to be applied.

In addition to the physical interpretations, moments can be used to calculate mean values characterizing a size distribution. Often used parameters are the mean diameter d_{10}, the Sauter mean diameter d_{32}, and the standard deviation σ_x [77]. The mean diameter d_{10} represents the arithmetic mean diameter of the number density function and can be calculated from the total length of the particles $L_{p,tot}$ and the total number $N_{p,tot}$:

$$d_{10} = \frac{L_{p,tot}}{N_{p,tot}} = \frac{\mu_1}{\mu_0}. \tag{2.20}$$

The Sauter mean diameter d_{32} corresponds to the diameter of a sphere with the same ratio between its volume and surface area as the particle system:

$$d_{32} = 6\frac{V_{p,tot}}{A_{p,tot}} = \frac{\mu_3}{\mu_2}. \tag{2.21}$$

The standard deviation is defined as the square root of the variance (mean quadratic variation) with d_{10} being the expected value:

$$\sigma_x = \left(\int_0^\infty (x - d_{10})^2 q_0(x)\,\mathrm{d}x\right)^{1/2} = \left(\frac{\mu_2}{\mu_0} - \left(\frac{\mu_1}{\mu_0}\right)^2\right)^{1/2}. \tag{2.22}$$

A high σ_x indicates large variations of the particle size, while a small value implies that only minor variations exist. In the limit ($\sigma_x \to 0$) all particles have the same size.

When dealing with discrete data from measurements, the particle size x is divided into a certain number of size classes. For each class j a value of Q_0 is obtained. The corresponding normalized

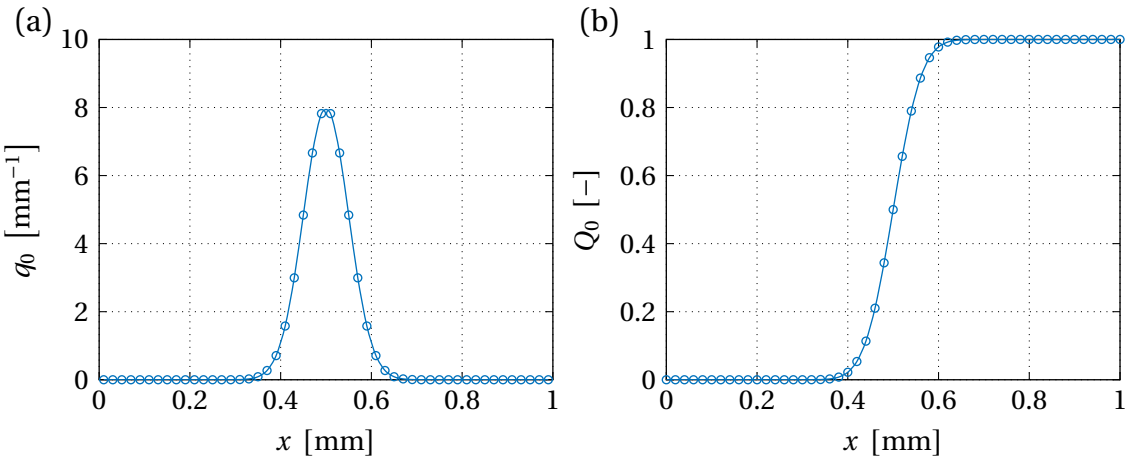

Figure 2.9: Example of a particle size distribution in the form of a normalized number density function q_0 (a) and a normalized cumulative distribution Q_0 (b).

number density q_0 is then calculated as follows:

$$q_0(\bar{x}_j) = \frac{Q_0(x_{j+1}) - Q_0(x_j)}{x_{j+1} - x_j} \quad \text{with} \quad \bar{x}_j = \frac{x_{j+1} + x_j}{2}. \tag{2.23}$$

In a graphical representation Q_0 is plotted vs. the boundary of each class, while q_0 represents a mean value of the interval $\left[x_j, x_{j+1}\right]$ and is plotted vs. the center $\bar{x}_j$ of each class. In case of discrete values, the calculation of the moments and corresponding mean values can be performed as follows:

$$\mu_k \approx \sum_{j=1}^{N_{class}} \bar{x}_j^k \, n(\bar{x}_j) \, \Delta x_j. \tag{2.24}$$

Examples of q_0 and Q_0 (normal distribution with $d_{10} = 0.5\,\text{mm}$ and $\sigma_x = 0.05\,\text{mm}$) are shown in Figure 2.9.

2.3.2 Macroscopic models

In macroscopic models, usually the transient behavior of a property distribution (e.g., the particle size distribution) due to different particulate processes is modeled. A well-established concept used to model the change of property distributions is the population balance introduced by Hulburt and Katz [78]. This concept is widely used to model particle formation processes such as crystallization, see Randolph and Larson [76] and Gerstlauer et al. [79], layering granulation and coating, see Heinrich et al. [80], Vreman et al. [81], and Silva et al. [82], and agglomeration, see Hounslow et al. [83], Kumar et al. [84], and Peglow et al. [85]. Burgschweiger and Tsotsas [86] modeled a continuous drying process using population balances, where the residence time is used as the internal coordinate. Applications of population balance models are the prediction of property distributions, the design of operating conditions to achieve a desired property distribution, and control of particulate processes [87].

A general form of a population balance for a batch process is given by Randolph and Larson [76], assuming that external coordinates can be neglected. Changes of the number density function $n(t, \mathbf{i})$ can then be described by the following equation:

$$\frac{\partial n(t,\mathbf{i})}{\partial t} = -\nabla(Gn) + B - D. \tag{2.25}$$

In this equation, $\nabla(Gn)$ is a term representing the convection of n with a velocity G along the internal coordinates. B and D are birth and death terms describing phenomena leading to production or disappearance of particles. Depending on the dominant size enlargement mechanism, different forms of Equation (2.25) can be derived, which are discussed below.

Layering

In coating and layering granulation processes, the particles grow by repeated droplet deposition, drying, and solidification of the droplets, leading to a layer-wise growth. Usually, this phenomenon is described by the convection term with the particle size x being the internal coordinate, while no birth and death terms are used. Equation (2.25) then simplifies to:

$$\frac{\partial n(t,x)}{\partial t} = -\frac{\partial(Gn)}{\partial x}. \tag{2.26}$$

In this case, the growth rate G is defined as:

$$G = \frac{\mathrm{d}x}{\mathrm{d}t}, \quad [G] = \mathrm{m\,s^{-1}}. \tag{2.27}$$

In order to solve Equation (2.26), a mathematical formulation for G must be found. A general formulation is given by Rieck et al. [57] considering that the distribution of the sprayed liquid is related to an arbitrary moment μ_k of the number density function n:

$$G_k = \frac{2w_s\dot{M}_{spray}}{\varrho_s\pi\left(1-\varepsilon_{layer}\right)}\frac{x^{k-2}}{\mu_k}. \tag{2.28}$$

In this equation, $\dot{M}_{spray}$ is the spraying rate of the liquid, w_s is the mass fraction of the solid material in the sprayed liquid, ϱ_s is the density of the solid material in the liquid (without pores), and ε_{layer} is the porosity of the solid layer. If $\varepsilon_{layer} = 0$, the solid layer is compact and Equation (2.28) is equal to the formulation given by Peglow et al. [88]. The total growth rate can be calculated from:

$$G = \sum_j \Lambda_j G_j \quad \text{with} \quad \sum_j \Lambda_j = 1. \tag{2.29}$$

The values of Λ_j can lie between 0 and 1. The sum of all Λ_j must equal unity to ensure mass conservation. A selection of $\Lambda_2 = 1$ leads to the well-known formulation given by Mörl et al. [6]. In this case, the distribution of the liquid is related to the total surface area of the particles. This leads to a growth rate, which is independent of the particle size. As a result, all particles grow with the same velocity

and the shape of the number density function n is preserved.

According to Peglow et al. [88], experimental results show that the shape of the number density function may change during a layering process, depending on the apparatus. In order to describe this effect, different values for Λ_j (other than $\Lambda_2 = 1$) can be used. Additionally, this phenomenon can be modeled by introducing compartment models. In such models, the apparatus is divided into at least two coupled zones and each zone is described by its own population balance. Examples where the apparatus is divided into a spraying zone and a drying zone are given by Silva et al. [82], Sherony [89], Wnukowski and Setterwall [90], and Li et al. [91], who use the coating mass or volume as the internal coordinate and Rieck et al. [57], Hampel et al. [92], and Neugebauer et al. [93], who use the particle size as the internal coordinate. Maronga and Wnukowski [94] introduce a third zone to account for the influence of stagnant regions on the number density function. In case of two coupled zones, the system of two population balance equations reads:

$$\frac{\partial n_1(t,x)}{\partial t} = -\frac{\partial (G n_1)}{\partial x} - \dot{n}_{12} + \dot{n}_{21}, \tag{2.30}$$

$$\frac{\partial n_2(t,x)}{\partial t} = \dot{n}_{12} - \dot{n}_{21}. \tag{2.31}$$

In these equations, n_1 and n_2 are the number density functions of the spraying zone (index 1) and the drying zone (index 2), respectively. The particles grow in the spraying zone, while no size enlargement occurs in the drying zone, see Figure 2.10. The zones are coupled, which means that particles can be exchanged between the zones. This is taken into account by introducing number flow rates $\dot{n}_{12}$ and $\dot{n}_{21}$ in Equation (2.30) and Equation (2.31), which are calculated using the residence time τ of the particles in the respective zone and the corresponding number density function:

$$\dot{n}_{12} = \frac{n_1}{\tau_1}, \quad \dot{n}_{21} = \frac{n_2}{\tau_2}. \tag{2.32}$$

In order to ensure mass conservation, the residence times of both zones must fulfill the following condition:

$$\frac{\tau_1}{\tau_2} = \frac{\varphi}{1-\varphi}. \tag{2.33}$$

In this equation, φ denotes the relative volumetric fraction of the spray zone. If either φ or τ_1 (or both) are large, the influence of the drying zone is small and the two-zone model behaves like the one-zone model (cf. Equation (2.26)) in terms of dispersion of the number density function. Experimental studies regarding the size of the spray zone and the residence times of the particles in both zones have been presented by Börner et al. [95].

Population balance models can be used to calculate particle size or coating mass distributions for batch or continuous processes. However, a more detailed description of particle properties such as intra-particle layer thickness distributions or information about the surface coverage of the coating has not been presented in literature with this approach.

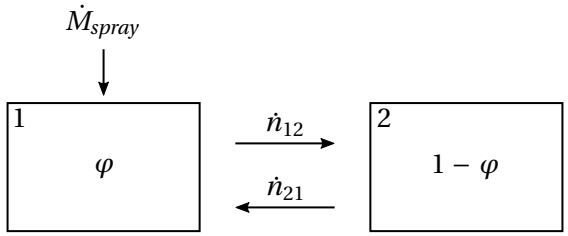

Figure 2.10: Schematic representation of a two compartment model, where the fluidized bed is divided into a spraying zone (index 1) and a drying zone (index 2).

Agglomeration

In order to describe agglomeration processes, usually birth and death terms are used. Layering, which may occur simultaneously, is often neglected since its influence on the kinetics is small (cf. typical growth rates given by Nienow [24] in Section 2.2). The complexity of the birth and death terms depends on the number of micro-processes, which need to be included. For agglomeration, Equation (2.25) can be simplified to:

$$\frac{\partial n(t,v)}{\partial t} = B_{agg} - D_{agg}. \tag{2.34}$$

In this equation, B_{agg} and D_{agg} describe birth and death of particles of a certain size due to binary agglomeration. These terms are often described using the particle volume as internal coordinate due to its additivity: if two particles with volumes v and v' agglomerate, a particle with volume $v+v'$ is formed. The birth and death terms are then defined as [83]:

$$B_{agg}(t,v) = \frac{1}{2}\int_0^v \beta'(t,v-v',v')\, n(t,v-v')\, n(t,v')\, \mathrm{d}v', \tag{2.35}$$

$$D_{agg}(t,v) = n(t,v)\int_0^\infty \beta'(t,v,v')\, n(t,v')\, \mathrm{d}v'. \tag{2.36}$$

In Equation (2.35), the pre-factor $1/2$ ensures that collisions between two particles are not counted twice. The parameter $\beta'(t,v,v')$ is called agglomeration kernel (also aggregation kernel or coalescence kernel) and describes the kinetics of the process. It can be split into two factors [96]:

$$\beta'(t,v,v') = \beta'_0(t)\beta'(v,v'). \tag{2.37}$$

The time-dependent part $\beta'_0(t)$ is called agglomeration efficiency and varies with particle properties (other than size or volume), material properties, and process conditions [87]. For the description of the volume-dependent part $\beta'(v,v')$, several approaches are reported in literature, which can be divided into empirical and mechanistic approaches. A brief overview is given in Table 2.1. A more thorough summary is presented by Hussain [97]. The above shown Equations (2.34) to (2.36) represent the population balance for agglomeration for one compartment (spray zone). A two-

Table 2.1: A brief summary of agglomeration kernels proposed in the literature.

Name	Equation	Reference
Constant	$\beta'(v,v') = 1$	Scott [102]
Brownian	$\beta'(v,v') = \left(v^{1/3} + v'^{1/3}\right)\left(v^{-1/3} + v'^{-1/3}\right)$	Smoluchowski [103] (found in [104])
Shear	$\beta'(v,v') = \left(v^{1/3} + v'^{1/3}\right)^3$	Smoluchowski [103] (found in [104])
Sum	$\beta'(v,v') = v + v'$	Golovin [105]
Product	$\beta'(v,v') = vv'$	Scott [102]
Sastry	$\beta'(v,v') = \left(v^{2/3} + v'^{2/3}\right)\left(v^{-1} + v'^{-1}\right)$	Sastry [96]
Kapur	$\beta'(v,v') = \left(v + v'\right)^a \left(vv'\right)^{-b}$	Kapur [100]
EME	$\beta'(v,v') = \left(v^{1/3} + v'^{1/3}\right)^2 \left(v^{-2} + v'^{-2}\right)^{1/2}$	Hounslow [106]
EKE	$\beta'(v,v') = \left(v^{1/3} + v'^{1/3}\right)^2 \left(v^{-1} + v'^{-1}\right)^{1/2}$	Hounslow et al. [107]

compartment model similar to the one shown in Figure 2.10 has been presented by Hussain et al. [98] for agglomeration.

In contrast to layering, the agglomeration kinetics cannot be directly calculated from process parameters and particle properties as shown by the mathematical formulations of agglomeration kernels given in Table 2.1. Instead, one of the existing kernels has to be selected, which still remains a difficult problem since a single kernel considering all governing factors does not yet exist [87]. As a result, one has to rely on experimental data fitting to extract numerical values for either $\beta'_0(t)$ (see Hampel et al. [99]), or adjustable parameters of $\beta'(v,v')$ in empirical formulations (e.g., the kernel given by Kapur [100] in Table 2.1). This issue is also known as the inverse problem in literature. Empirical kernels may provide an acceptable level of model prediction [101], but the obtained values are restricted to the used material, experimental setup, and process parameters.

In a more recent publication, Hussain et al. [108] presented a method to model the agglomeration kernel as a result of process conditions and material parameters. Assuming a size-independent aggregation process (i.e., $\beta'(v,v') = 1$), the following expression was obtained:

$$\beta' = \beta'_0 = f_{coll} P_{coll,wet,suc} \frac{N_{p,wet}}{N_{p,tot}^2} \left(\frac{2\left(N_{p,tot} - N_{p,wet}\right)}{N_{p,tot} - 1} P_{coll,wd} + \frac{N_{p,wet} - 1}{N_{p,tot} - 1} P_{coll,ww} \right). \tag{2.38}$$

In this equation, f_{coll} is the collision frequency, $N_{p,wet}$ and $N_{p,tot}$ are the number of wet particles and the total particle number, respectively. In order to calculate $N_{p,wet}$ and $N_{p,tot}$, the one-dimensional population balance model was extended by corresponding differential equations. Additional parameters were introduced such as the probability of successful wet collisions $P_{coll,wet,suc}$ (probability that the kinetic energy is dissipated during a wet collision), as well as $P_{coll,wd}$ and $P_{coll,ww}$ representing the probability of a collision at a wet spot in a wet-dry collision (a wet particle colliding with a dry particle) and in a wet-wet collision (two wet particles colliding with each other), respectively. Hussain et al. [108] show that these parameters can be derived based on the wet surface fraction (ratio between wet particle surface area and total particle surface area) and the Stokes criterion, which are directly

influenced by process parameters and material properties.

In order to solve the population balances, several methods are available. Analytical solutions are only possible in very few cases (simple kernels and initial conditions), e.g., using Laplace transforms [87]. However, usually numerical approaches have to be used to obtain an approximate solution. According to Abberger [87], several techniques may be used for the numerical solution of population balance equations: finite difference, finite volume (see also LeVeque [109]), finite elements, and spectral methods (see also Bück et al. [110]). If agglomeration or breakage need to be included, more advanced methods such as pivotial methods (fixed or moving pivot) [111, 112] or the cell-average method [84] need to be applied. As a result, the partial differential equations are transformed into a system of ordinary differential equations and can be solved numerically (e.g., using Runge-Kutta methods) yielding the transient behavior of the number density function. For discretization of the partial differential equations, different types of grids can be used (i.e., equidistant or geometric grids). The former provides accurate solutions, but requires high computational cost resulting from the large number of grid cells. Geometric grids can reduce the number of grid cells, but may lead to problems conserving mass [84]. Other methods reducing the calculation times are moment methods yielding the transient behavior of the moments of the number density function, see Marchisio et al. [113] and Marchisio and Fox [114].

2.3.3 Microscopic models

Microscopic models describe the particle formation processes as a result of phenomena occurring on the single particle level. No grid or discretization is needed as the particles are treated as discrete entities. Two well-known methods are discrete element methods (DEM), often coupled with computational fluid dynamics (CFD), and Monte Carlo (MC) methods. Both approaches are discussed below.

In a DEM, the motion of each individual particle is described by Newton's second law of motion. Forces resulting from gravity, particle-particle or particle-wall contacts, particle-fluid interaction, and non-contact forces can be taken into account. DEMs are used to study particle packing, transport properties, hopper flow, mixing, and granulation. Coupled with CFD, in which the gas phase is described by volume-averaged Navier-Stokes equations, complex multiphase flows (e.g., occurring in fluidized beds or pneumatic conveying equipment) can be described [115, 116]. Particle formation in spray fluidized beds has been studied using CFD-DEM simulations by Goldschmidt et al. [117] and Fries [118]. Goldschmidt et al. [117] presented a CFD-DEM model for agglomeration, directly taking into account the increasing particle size and steric hindrance during collisions. Since the used binder is a liquid melt, drying is not considered, but solidification of the binder due to cooling is accounted for. However, it is assumed that every collision at a wet spot leads to agglomeration. Fries [118] focused on particle and collision dynamics in different fluidized bed equipment. Partially wet particles were taken into account and the influence of the liquid film properties (wet surface fraction, film thickness and viscosity) on the particle and collision dynamics was investigated. However, the properties of the liquid film were fixed values and not related to the process conditions. The resulting

size of the agglomerates was not investigated, as the focus lay on particle velocities and collision frequencies. Since CFD-DEM models are computationally expensive, the simulated process time is short and ranged between 2.5 s and 10 s in the above discussed studies. The application of CFD-DEM models for simulating real process times in the range of minutes or hours is therefore not yet possible. Nevertheless, they can be used to extract important properties such as residence time distributions, collision frequencies, or particle velocities for macroscopic models.

Another way of discrete modeling of particulate processes is given by Monte Carlo methods. Metropolis and Ulam [119] introduced this method, which is essentially a statistical approach to study differential equations. The connection between this method and the population balance approach has been established by Ramkrishna [120]. The solution is in this case performed by a stochastic sampling experiment involving random numbers [121]. Monte Carlo methods have been used to model different particulate processes such as agglomeration during crystallization [121], agglomeration of droplets in clouds [122], agglomeration of particles in spray fluidized beds [108, 123, 124], twin-screws [125], high-shear granulators [126], and coating in spray fluidized beds (Wurster) [127] and pan coaters [128]. In comparison to population balances, this simulation method offers several advantages. No mathematical formulation of the macroscopic process kinetics is needed and the discretization of the property domain is unnecessary. The consideration of several internal coordinates or properties can be easily performed, while in case of macroscopic modeling a multidimensional population balance must be solved, which may lead to large computation times, see Barrasso and Ramachandran [129]. In order to use a Monte Carlo method to model particle formation in spray fluidized beds, the processes occurring on the single particle level (see Figure 2.4) need to be modeled. They are then applied sequentially to a sample of the particle population changing its properties over time.

A classification of Monte Carlo methods is given by Zhao et al. [130]. Monte Carlo methods can be divided into time-driven and event-driven methods based on the treatment of the time step. In time-driven methods a fixed time step is specified and all possible events are executed within this time step. In event-driven methods only one event per time step is executed and the length of the time step corresponds to the frequency or probability of the event. In this context, event refers to a specific action involving particles such as agglomeration or breakage of particles or agglomerates, and deposition of droplets on the particle surface [130]. They are also termed Markov jump events, as they evolve the simulation in time [125]. According to Zhao et al. [130], event-driven methods show better accuracy and performance than time-driven methods. However, if a Monte Carlo model is coupled with a process model performing explicit integrations over time, a time-driven method is more suitable due to the fixed time-step. Monte Carlo methods can be further categorized into constant number (CNMC) and constant volume (CVMC) methods based on the regulation of the sample size, sometimes referred to as simulation box. The sample size (i.e., the number of particles considered in the simulation) needs to be regulated since agglomeration or breakage lead to a decreasing and increasing number of particles or agglomerates, respectively. If the sample size is too small, it will not be statistically representative, while a high sample size leads to large computation times. In a constant number method the sample size is regulated in each time step, while periodic regulation is

applied in a constant volume method. Smith and Matsoukas [131] point out that in case of a constant volume method the sample size may be too large (a smaller number would be sufficient to guarantee statistical accuracy) or too small depending on the number concentration in the simulation box. As a result, the statistical error oscillates about a constant value between successive regulations of the sample size. Considering a simplified case of spray fluidized bed agglomeration, Hussain et al. [108] compared the results of two Monte Carlo models (CNMC and CVMC) to an analytical solution. The results indicate a higher accuracy of the CNMC approach.

The foundation for the Monte Carlo methods derived in this thesis has been presented in the works of Terrazas-Velarde [15], Dernedde [132], and Hussain [97]. All of them considered spray fluidized bed agglomeration by spraying a binder solution. Terrazas-Velarde [15] introduced an event-driven CVMC method to model spray fluidized bed agglomeration. It is the first model being able to describe the influence of drying conditions on the kinetics of the process without fitting agglomeration kernels. Instead, this behavior arises due to combined modeling of heat and mass transfer and agglomeration on the single particle scale. Dernedde [132] created an extended CNMC model based on the work of Terrazas-Velarde [15] and introduced a three-dimensional description of the particle structure, eliminating simplifying assumptions made in the previous work. However, an increase in computation time was observed. Hussain [97] used a CNMC model based on Terrazas-Velarde [15] and focused on developing a population balance model in which the kernel is modeled by introducing additional differential equations describing the number of wet particles (cf. Equation (2.38)). The resulting population balance model is able to describe the influence of drying conditions on agglomeration.

The above mentioned dissertations focused on spray fluidized bed agglomeration with a binder solution. However, Monte Carlo modeling of agglomeration of amorphous particles due to glass transition as well as layering in spray fluidized beds have not been addressed. Publications concerning these processes are briefly discussed below.

In case of agglomeration due to glass transition, many articles deal with experimental investigations. The measurement of the glass transition temperature is often addressed, see Roos and Karel [133], Aguilera et al. [134], Descamps et al. [135], and Paterson et al. [136]. Investigations regarding agglomeration of amorphous materials in fluidized beds are presented by Palzer [137] and Avilés-Avilés et al. [138]. It was found by Palzer [137] that the agglomeration process is strongly influenced by the distribution of the moisture in the bed. In case of a more or less equal distribution of the moisture, the fluidized bed will collapse due to excessive agglomeration if the process temperature is near the glass transition temperature. This behavior was shown in experiments, in which humid fluidization air was used instead of spraying water. If the fluidization air is dry and the water is sprayed on the particles, only a fraction of the particles is wetted leading to a more controlled agglomeration process. Avilés-Avilés et al. [138] investigated the influence of operating parameters (spraying rate and temperature) and the material (amorphous maltodextrin DE 12 and DE 21) on agglomeration. An increasing spraying rate led to larger agglomerates for DE 12, but did hardly influence the DE 21 particles. A higher temperature of the fluidization air led to larger agglomerates for DE 12 and smaller ones in case of DE 21. Theoretical investigations of agglomeration of amorphous particles are rarely

found in literature. According to Palzer [43], the Frenkel equation can be used to calculate the growth of material bridges due to sintering. However, Dopfer et al. [45] state that agglomeration of amorphous powders due to sintering may only take place in a static agglomeration process, e.g., during storage. Since in dynamic agglomeration processes such as fluidized bed agglomeration the contact times during particle collisions are short, it is assumed that the development of a sinter bridge is not possible. A process model describing the dynamic agglomeration process of amorphous materials in spray fluidized beds has not been introduced.

Monte Carlo modeling of layering growth has been presented by KuShaari et al. [127] and Pandey et al. [128]. KuShaari et al. [127] developed a model for tablet coating in a Wurster fluidized bed. The model focused on the description of particle movement and the increase in tablet mass during the process. The model yields the number density function of the coating mass by tracking the mass increase of each tablet. Pandey et al. [128] used a Monte Carlo model to calculate the variability of the coating mass of tablets in a pan coater. The movement of the particles was experimentally investigated with a camera, yielding distributions of the circulation time and the velocity of the tablets. These distributions were then used in the model to simulate the process. The coating mass of each tablet was tracked and used to calculate its inter-particle variability for different operating conditions. Drying was not considered in either model. A Monte Carlo model for spray fluidized bed layering, which is able to describe several property distributions such as distribution of the particle size, coating mass, and layer thickness (inter-particle and intra-particle), provide information about the surface coverage of the coating, and includes the influence of drying has not been presented in literature.

2.3.4 Heat and mass transfer

Heat and mass transfer in fluidized beds depends strongly on the complex multiphase flow emerging from the interaction between the gas, particles, and droplets. An overview regarding the modeling approaches for multiphase flows is given by van Annaland et al. [116] along with the corresponding length-scale that can be resolved. One example is the above mentioned CFD-DEM. However, for systems at engineering scale the required number of particles and the corresponding calculation times would become very large. Such systems can be modeled more efficiently with the continuum approach, where gas and particle phase are modeled as interpenetrating continua. The properties of the particles such as concentration and velocities are then averaged over control volumes [139]. Other approaches use empirical engineering models to treat the multiphase flow, which are relatively simple, fast, and able to handle large systems [116]. Two examples of such models are discussed below.

In the approach presented by Burgschweiger et al. [140] for fluidized bed drying, a two-phase model dividing the fluidized bed into a suspension phase and a bubble phase is used to account for bypassing effects. The suspension phase is the part of the gas flow containing the particles, while the bubble phase contains no particles (cf. Figure 2.1). Heat and mass can be exchanged between both phases. Additionally, the wall of the apparatus is considered in the heat transfer equations. The gas flow

is approximated by plug flow, which is a common assumption for fluidized bed models, see also Heinrich and Mörl [141] and Ronsse et al. [142]. The particle phase is assumed to be ideally mixed. As a result, particle properties do not depend on the spatial location. Since a plug flow model does not incorporate backmixing of the gas, it is introduced in the kinetics as proposed by Groenewold and Tsotsas [143]. The model considers transport resistances within particles using the concept of a normalized drying rate introduced by van Meel [144] as well as sorption equilibrium. In this concept, the normalized drying rate $\dot{\nu}$ is used, which is defined as the ratio between the actual evaporation rate $\dot{M}_{evap}$ and the evaporation rate in the first drying stage $\dot{M}_{evap,I}$:

$$\dot{\nu} = \frac{\dot{M}_{evap}}{\dot{M}_{evap,I}}. \tag{2.39}$$

During the first drying stage transport resistances within the particles are negligible compared to gas-side resistances. For non-hygroscopic materials the evaporation rate in the first drying stage is constant, while for hygroscopic material it depends on the solid moisture content. Hygroscopicity is introduced in the model by building the driving force with the sorptive equilibrium $Y_{eq}(X, T_p)$:

$$\dot{M}_{evap} \sim Y_{eq}(X, T_p) - Y. \tag{2.40}$$

In this equation, $Y_{eq}(X, T_p)$ is the equilibrium moisture content of the gas calculated using sorption isotherms at moisture content X and temperature T_p of the particles. Y is the moisture content of the bulk gas. Peglow et al. [85] applied the model to describe drying during spray fluidized bed agglomeration. An extension was presented by Burgschweiger and Tsotsas [86] to account for residence time distributions in continuous drying processes.

Heinrich and Mörl [141] proposed a model for layering granulation, assuming plug flow for the gas phase (without further division into suspension and bubble phase) and taking into account axial and radial dispersion of the particle phase. They assume that the sprayed liquid forms a coherent film with arbitrary thickness (model parameter) around the particles. Neither imbibition of liquid and a corresponding transport resistance within the particles nor hygroscopicity is considered. They introduce a wet surface fraction Ψ_{wet} characterizing the ratio between the wet particle surface area $A_{p,wet}$ and the total particle surface area $A_{p,tot}$, which is incorporated in the evaporation rate similarly to Equation (2.39):

$$\Psi_{wet} = \frac{A_{p,wet}}{A_{p,tot}} = \frac{\dot{M}_{evap}}{\dot{M}_{evap,I}}. \tag{2.41}$$

Since no hygroscopicity is considered, the driving force is built with the moisture content of the gas at adiabatic saturation Y_{as}:

$$\dot{M}_{evap} \sim Y_{as} - Y. \tag{2.42}$$

Particle growth by layering is taken into account by a simple model based on mean values.

The wet surface fraction does not only control the evaporation rate, but also influences the border between the size enlargement mechanisms along with further liquid film properties (height and viscosity) as discussed in Section 2.2.5. Since the height of the liquid film is a free parameter and not related to the process conditions and material properties in the model of Heinrich and Mörl [141], it cannot be used to investigate the border between agglomeration and layering. However, droplet geometry models such as the one used in a Monte Carlo model by Terrazas-Velarde [15], enable to calculate droplet properties (i.e., height and covered surface area) depending on the droplet volume and the wetting characteristics of the liquid and particle material.

2.4 Goal of the thesis

Previous investigations have shown that discrete modeling of particle formation based on a Monte Carlo method has certain advantages compared to macroscopic modeling using population balance equations. In the discrete approach, a more detailed description of particle properties is possible and no macroscopic process kinetics needs to be derived. Instead, kinetics is modeled as a result of a complex network of phenomena occurring on the single particle level. The studies laying the groundwork for this thesis [15, 97, 132] focused on spray fluidized bed agglomeration with a binder solution. Monte Carlo modeling of layering and agglomeration of amorphous material due to glass transition have not been treated. Therefore, in this thesis two process models based on a Monte Carlo method dealing with layering, as well as with agglomeration of amorphous material are presented. The model for layering is expected to provide valuable property distributions and information about the surface coverage of the coating, which has not been achieved using macroscopic modeling approaches. Since a process model treating agglomeration of amorphous material due to glass transition in spray fluidized beds does not exist yet, this thesis aims at closing this gap by deriving a corresponding process model based on previous Monte Carlo models for agglomeration, including the influence of process and material parameters on the agglomeration kinetics. For each model a simulation study is performed, investigating the influence of selected process parameters on the kinetics and particle properties. Additionally, theoretical approaches and experimental data obtained in lab-scale fluidized beds are used to validate the presented models.

The border between size enlargement by layering and agglomeration is of great interest since both phenomena may occur simultaneously in spray fluidized bed processes and the properties of the resulting particles differ significantly. Therefore, only one of these mechanisms should be dominant. Experimental studies indicate that current criteria may fail in predicting the dominant size enlargement mechanism. As discussed above, existing criteria take particle properties (size, density, surface roughness, velocity, elasticity) and liquid properties (height, viscosity) into account, but do not consider the wet surface fraction (ratio of wet particle surface area and total particle surface area), which also plays a role according to Tsotsas [56]. Therefore, in this thesis an extended criterion describing the border between layering and agglomeration for spray fluidized bed processes is presented. The dominant size enlargement mechanism is classified based on the probability of

successful collisions. This parameter is calculated from the probability of wet collisions and the probability of successful wet collisions (in terms of dissipation of kinetic energy), which have been used to model the agglomeration kernel in a previous study by Hussain et al. [108]. A new dynamic model for the wet surface fraction based on a droplet geometry model is derived, which is used to calculate the probability of wet collisions. In order to incorporate the influence of drying conditions, a spray fluidized bed drying model using the wet surface fraction to calculate the evaporation rate is derived. Additionally, a new method to include the Stokes criterion is presented, which is used to derive the probability of successful wet collisions. A simulation study is performed to investigate the influence of operating conditions and material parameters on the dominant size enlargement mechanism. Based on experimental data and further simulation results, a classification of the size enlargement mechanism using the probability of successful collisions is proposed.

Chapter 3

Micro-scale modeling using a Monte Carlo method

This chapter is an extended version of Rieck et al. [145, 146]. At first, an overview of the general structure of the used Monte Carlo algorithm is given. Scaling of the particle system, micro-scale event selection, calculation of the time step, and the concept of positions are discussed. Afterwards, details of the events and micro-processes used in both models are presented and the corresponding assumptions are summarized.

3.1 General structure

3.1.1 Flow chart

As discussed in the previous chapter, event-driven methods and constant number approaches show better accuracy and performance than time-driven methods [130] and constant volume approaches [108]. As a result, an event-driven, constant number Monte Carlo algorithm is used in this work.

A general flow chart of the Monte Carlo algorithm is shown in Figure 3.1. After initializing the required variables and process parameters, the real particle system is scaled down. Then, the Markov jump event evolving the simulation in time is selected and the time step is calculated. Afterwards, the selected event is executed and the properties of all wet droplets in the system are changed due to drying. Then, particle properties such as layer thickness, coated surface fraction, size, and number of primary particles per agglomerate are updated. If necessary, the scaling factor is updated as well, in order to re-scale the system in the following time step. The simulation will continue until a defined process time is reached. Then, the particle system is scaled up again and the data is saved.

3.1.2 Scaling and regulation of the sample size

As discussed in Chapter 2, Monte Carlo models consider a sample from a real particle population. Therefore, the real particle system is scaled down using a scaling factor S. Scaling reduces the number of particles considered in the simulation, but the properties such as size distribution are identical.

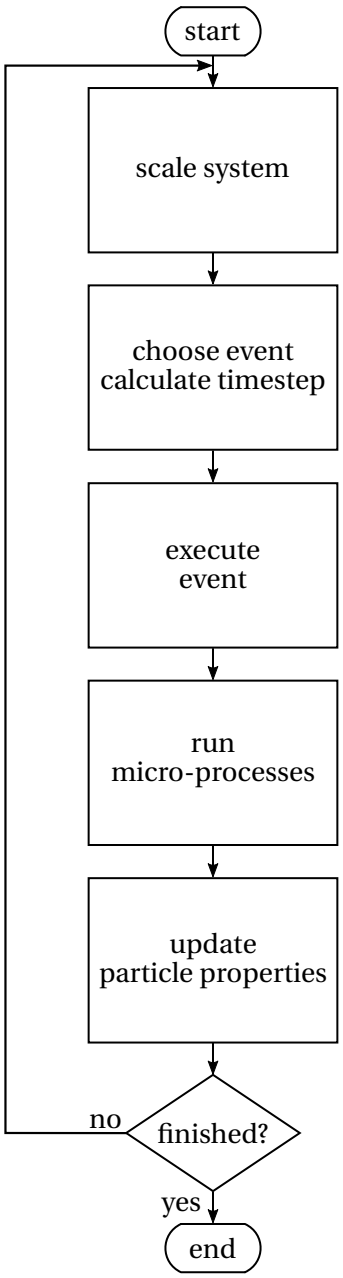

Figure 3.1: General flow chart of the Monte Carlo algorithm used in this work.

Table 3.1: Overview of constant and variable parameters for layering and agglomeration processes in reality and the simulation.

Parameter	Layering		Agglomeration	
	real	MC	real	MC
N_{pp}	–	–	const.	$f(t)$
N_p	const.	const.	$f(t)$	const.
S	const.		$f(t)$	

Using S, any parameter changing with the size of the particle system can be scaled from the real system to the sample system and vice versa. In previous works focusing on agglomeration, see Terrazas-Velarde [15], Hussain [97], and Dernedde [132], the scaling factor is defined based on the number of primary particles in the sample and in the real system, respectively. In case of layering processes, the distinction between particles and primary particles is, though, unnecessary and therefore the scaling factor is calculated from the number of particles. The scaling factor for both processes is thus defined as:

$$S = \begin{cases} \dfrac{N_{p,MC}}{N_{p,real}} & \text{layering,} \\ \dfrac{N_{pp,MC}}{N_{pp,real}} & \text{agglomeration.} \end{cases} \tag{3.1}$$

As the presented simulation method is a constant number Monte Carlo algorithm, the size of the sample system must be regulated if the particle number changes during the simulation to ensure statistical accuracy and reasonable computation times. In a real layering process, the number of particles is constant if overspray and breakage of particles are neglected. As a result, once the real system is scaled down, the sample size and the scaling factor stay constant over time and no regulation is needed. However, in a real agglomeration process the number of primary particles stays constant, while the number of particles changes due to agglomeration and breakage of bridges. In this case, the term “particle” comprises single primary particles and agglomerates. In the simulation the number of particles is held constant by randomly deleting a particle in case of a breakage event, which would otherwise increase the number of particles by one. In case of an agglomeration event, which decreases the number of particles by unity, one randomly selected particle is copied. This leads to a constant number of particles and a variable number of primary particles in the simulation. As a result, the scaling factor changes over time and must be re-calculated in each time step. Table 3.1 gives an overview of constant and variable parameters in agglomeration and layering processes.

In case of agglomeration, the number of primary particles $N_{pp,MC}$ in the simulation used in Equation (3.1) is equal to the number of particles at the beginning of the simulation since no agglomerates exist at this stage. As the simulation proceeds, $N_{pp,MC}$ changes and is accessible by counting the number of primary particles of all agglomerates in the sample system. The number of primary

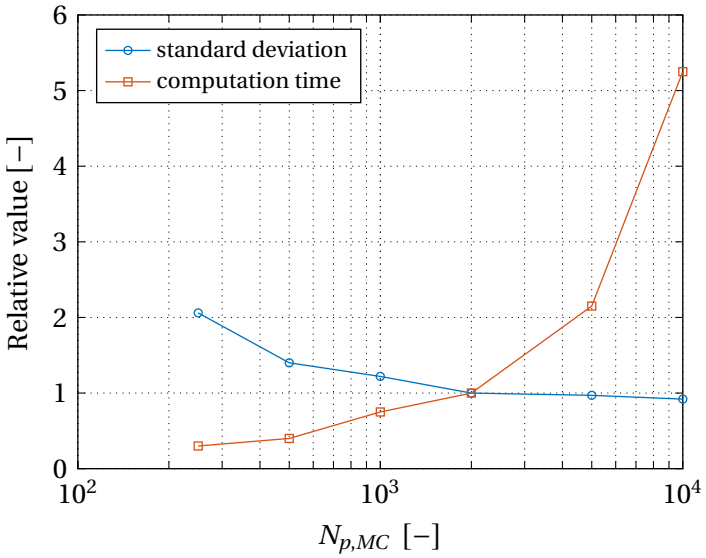

Figure 3.2: Influence of the number of particles considered in the simulation on the relative standard deviation and computation time. The values are normalized to the simulation results, in which a number of 2000 particles were used. The data is taken from Terrazas-Velarde et al. [147].

particles $N_{pp,real}$ in the real system is constant and can be calculated using the bed mass, particle density, and the initial particle size distribution, assuming spherical particles:

$$N_{pp,real} = \int_0^\infty n \, \mathrm{d}x \quad \text{with} \quad n = \frac{6M_{bed}}{\pi \varrho_p} \frac{q_0}{\int_0^\infty x^3 q_0 \, \mathrm{d}x}. \tag{3.2}$$

In case of layering, the number of particles $N_{p,MC}$ in the simulation in Equation (3.1) stays constant. The number of particles in the real system stays constant as well and can also be calculated using Equation (3.2).

The remaining parameter, which must be set, is the size of the sample system. The size of the sample can be adjusted by the number of particles considered in the simulation. In order to guarantee statistical accuracy, this value should not be too small and, at the same time, it should not exceed a certain value to prevent long computation times. An investigation regarding the influence of the number of particles in the simulation on both the results and the computation times has been performed by Terrazas-Velarde et al. [147]. Several simulations with different sample sizes were performed. The computation time and standard deviation characterizing the variation of the simulation results compared to the case with the highest accuracy (i.e., the largest number of particles) were evaluated. The results, which are normalized to the values for the case of 2000 particles, are shown in Figure 3.2. Based on these results, Terrazas-Velarde et al. [147] suggest that the number of particles in the simulation should lie between 1000 and 2000 particles to ensure accuracy and reasonable computation times. Zhao et al. [130] also recommend a sample size in the order of 1000 particles. As a result, the number of particles considered in the simulation is set to 1000 in this thesis.

Mass conservation

For agglomeration the combination of sample size regulation and the definition of the scaling factor in Equation (3.1) only ensures mass conservation if the primary particles are equally sized. However, if the primary particle size is distributed, mass conservation is not fulfilled and the scaling factor needs to be re-defined, as shown in the following example.

In this example, an amount of 1000 single particles (no agglomerates) is considered and no agglomeration or breakage takes place. Particles are only randomly copied and deleted, ensuring a constant number of particles. This is done for equally sized primary particles as well as distributed primary particle sizes. The parameters used in this example are given in Table 3.2. In case of distributed primary particle sizes, a normal distribution of particle diameter is used, which is created as shown in Appendix C. In case of equally sized particles, every time a particle replaces another the total mass of the sample stays constant. However, in case of distributed primary particle sizes, a smaller particle may replace a larger one or vice versa. As a result, the total mass of the sample changes, while particle number is still constant. This effect increases with increasing variation in particle size. In Figure 3.3, the evolution of the relative sample mass (total mass of the primary particles in the sample divided by its initial value) for an increasing number of sample size regulations (copying and deleting) is shown. If the particles are equally sized, mass is conserved, while mass is lost in case of the distributed primary particle sample. In this example, approximately 2 % of the initial mass is lost after 1000 sample size regulations. Therefore, information about the number of primary particles in the sample system is not sufficient to ensure mass conservation since the size of the primary particles plays a role.

As Equation (3.1) only relies on the number of the primary particles, this effect will lead to errors in the simulation. A solution is to re-define the scaling factor and directly use the total mass of the primary particles:

$$S = \frac{M_{pp,tot,MC}}{M_{pp,tot,real}}. \tag{3.3}$$

In this way, mass conservation is fulfilled even if the primary particle size is distributed. The total mass of the primary particles in the real system corresponds to the bed mass and the total mass of the primary particles in the simulation is calculated using the size and density of each primary

Table 3.2: Simulation parameters used in the example to investigate mass conservation of the sample system.

Parameter	Value	Unit
Mean particle diameter d_{10}	0.6	mm
Standard deviation σ_x	0 and 0.06	mm
Particle density ϱ_p	2500	kg m^{-3}
Number of particles $N_{p,MC}$	1000	–

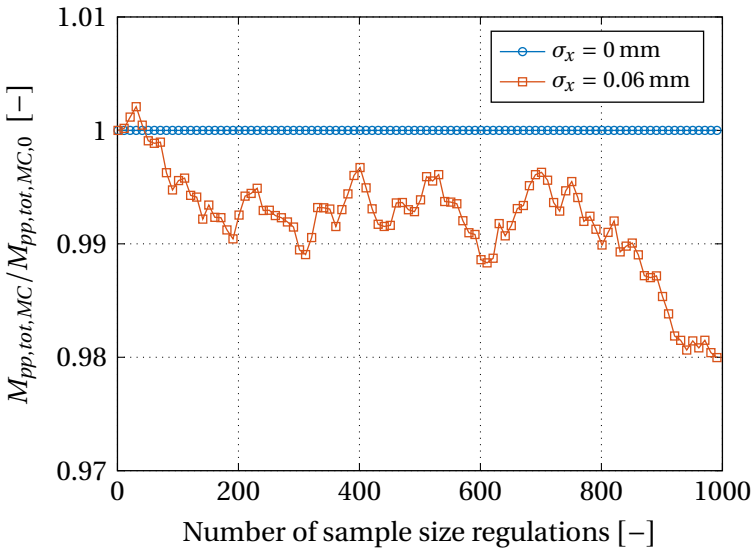

Figure 3.3: Evolution of the relative sample mass depending on the number of sample size regulations for equally sized particles ($\sigma_x = 0$ mm) and distributed particle sizes ($\sigma_x = 0.06$ mm).

particle. Since in case of layering the regulation of the sample size is not necessary, Equation (3.1) may still be used even if the initial particle size is distributed. In this work, Equation (3.1) is used in the Monte Carlo model for layering and Equation (3.3) is used for the agglomeration model.

3.1.3 Event selection

After scaling the particle system, a Markov jump event evolving the simulation in time needs to be selected. In contrast to micro-processes, which run in time, such events are considered to occur instantaneously. In previous works [15, 97, 132], two micro-scale events have been identified to change the state of the particle sample for the considered processes: droplet deposition and binary collisions. In order to correlate the simulation with real time, frequencies of these events can be used. The calculation of these frequencies is given in Section 3.2.1 and 3.2.2, respectively.

The selection of an event based on its frequency can be performed using a uniformly distributed random number r from the open interval $(0, 1)$ and the total event frequency $f_{tot,MC}$ (sum of all event frequencies):

$$\text{event} = \begin{cases} \text{collision} & r f_{tot,MC} \leq f_{coll,MC}, \\ \text{droplet deposition} & f_{coll,MC} < r f_{tot,MC} \leq f_{tot,MC}. \end{cases} \tag{3.4}$$

This approach is depicted in Figure 3.4. The total event frequency is composed of the frequencies of the individual events. Using a random number r, a value between 0 and $f_{tot,MC}$ is drawn. If this number lies between 0 and $f_{coll,MC}$, the selected event will be “collision”. If it lies between $f_{coll,MC}$ and $f_{tot,MC}$, the selected event will be “droplet deposition”. This method can easily be extended to an arbitrary number of events. In this way, the number of times each event is selected corresponds

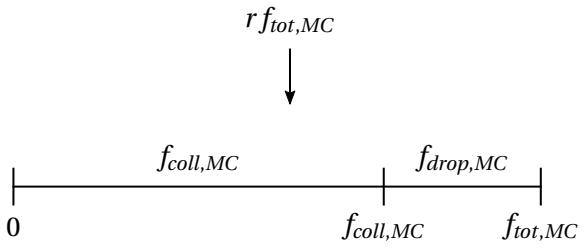

Figure 3.4: Schematic representation of the method used for event selection.

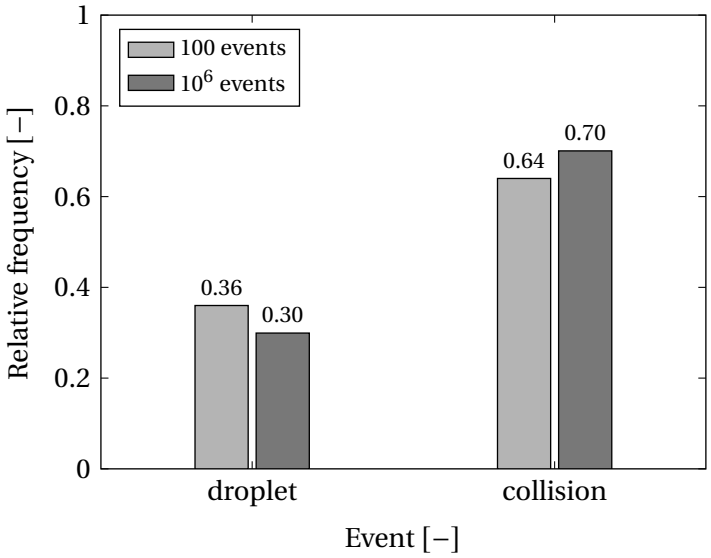

Figure 3.5: Relative frequencies of the two events "droplet deposition" and "collision" for 100 events and 10^6 events, respectively. The event frequencies are $f_{coll,MC} = 7\,\mathrm{s}^{-1}$ and $f_{drop,MC} = 3\,\mathrm{s}^{-1}$.

to its individual fraction of the total frequency for a sufficiently large number of event selections. This is shown in the following example, in which $f_{coll,MC} = 7\,\mathrm{s}^{-1}$ and $f_{drop,MC} = 3\,\mathrm{s}^{-1}$. Both events are selected according to Equation (3.4). The expected relative frequencies should therefore be 0.7 (collision) and 0.3 (droplet deposition). The results are shown in Figure 3.5 for 100 events and 10^6 events, respectively. In case of 100 events, the expected values are only approximately met, while the obtained relative frequencies and the expected values match for 10^6 events.

3.1.4 Calculation of the time step

In an event-driven Monte Carlo method, each event evolves the simulation in time by a certain time step Δt. The simulated process time is then approximated by the sum of these time steps. In many approaches, see Hussain [97], McGuire et al. [125], Dernedde [132], and Fichthorn and Weinberg [148], the time step is treated as an exponentially distributed parameter. According to these works, the time step can be calculated using the following equation based on the inverse method proposed by Gillespie [149]:

$$\Delta t = -\frac{1}{f_{tot,MC}} \ln r. \tag{3.5}$$

In this equation, r is a uniformly distributed random number from the open interval $(0, 1)$. For a sufficiently large number of time steps, the average time step $\overline{\Delta t}$ becomes

$$\overline{\Delta t} = \frac{1}{f_{tot,MC}}. \tag{3.6}$$

3.1.5 Concept of positions

The concept of positions was first introduced by Terrazas-Velarde [15] and divides the surface of a particle into sectors, which are additionally subdivided into smaller surfaces called “positions”. Each position can hold one deposited droplet. This concept is used in the model to easily describe partial wetting and binary collisions including steric effects. Dernedde et al. [124] extended this approach and enabled a more detailed description of the steric accessibility of droplets. In this thesis, the concept of positions is further extended, firstly, by taking a size distribution of the initial particles into account (for both layering and agglomeration) and secondly, by considering a growing number of positions per single particle for layering processes. The approach used in this thesis is described below.

The number of sectors is assumed to be equal to a maximum coordination number K_{max}. This parameter represents the number of neighbors a primary particle can have at most within an agglomerate. Following previous studies [15, 97, 124], a maximum coordination number equal to six will be used in this thesis. Dadkhah et al. [150] showed by investigating agglomerates of different sizes using X-ray micro-tomography that the mean coordination number is in the range of four. Consequently,

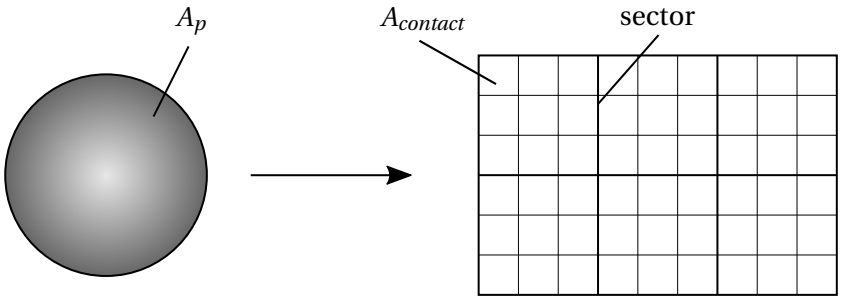

Figure 3.6: Division of the particle surface into sectors and positions.

the assumed maximum coordination number is considered to be appropriate. Figure 3.6 shows a particle, which is divided into 6 sectors and 9 sub-surfaces (positions) per sector.

The number of positions per sector $N_{pos,sec}$ is calculated from the particle surface A_p, the contact area between a deposited droplet and the particle surface $A_{contact}$, and the maximum coordination number K_{max}:

$$N_{pos,sec} = \text{nint}\left(\frac{A_p}{A_{contact}}\frac{1}{K_{max}}\right). \tag{3.7}$$

The obtained value is then rounded to the nearest integer. Consequently, the number of positions for a primary particle can be calculated using

$$N_{pos} = N_{pos,sec} K_{max}. \tag{3.8}$$

It is assumed that droplets instantaneously take the form of a spherical cap after deposition, see Figure 3.7. Meric and Erbil [151] provide equations for several geometrical parameters of deposited droplets:

$$A_{drop} = \frac{\pi}{2}\frac{d_{contact}^2}{1+\cos\theta}, \tag{3.9}$$

$$V_{drop} = \pi h_{drop}^3\left[\frac{1}{1-\cos\theta} - \frac{1}{3}\right], \tag{3.10}$$

$$d_{contact} = 2\left[\frac{3V_{drop}}{\pi}\frac{\sin^3\theta}{2-3\cos\theta+\cos^3\theta}\right]^{1/3}. \tag{3.11}$$

In these equations, A_{drop} is the curved surface area of the droplet, V_{drop} is the droplet volume, h_{drop} is the droplet height, $d_{contact}$ is the diameter of the contact area, and θ is the contact angle. The contact area then follows from:

$$A_{contact} = \frac{\pi}{4} d_{contact}^2. \tag{3.12}$$

As a result, a position vector can be assigned to each particle, which is used to store information for each position such as presence or absence of a droplet, droplet state (wet or dry), presence of a bridge, and the steric accessibility of the position. As shown by Dernedde et al. [124], this information

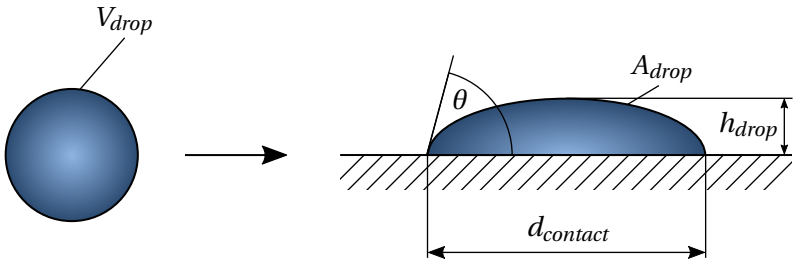

Figure 3.7: Illustration of a droplet before and after deposition on a particle surface.

can be stored by assigning integer values to each position (labeling). The meaning of the used labels is summarized in Table 3.3.

Assigning a position vector for each particle enables to store the information in form of a matrix. An example showing this matrix for three particles of equal size is given in Figure 3.8. In this example, each particle has three sectors, each consisting of three positions. Note that this example is simplified to avoid an oversized illustration. As stated above, in the simulation 1000 particles with six sectors per particle are used. Figure 3.8 shows that the first particle does not have any wet droplets, see Table 3.3. The second particle holds a wet droplet on the second position of sector 1 and a dry droplet on the first position of sector 3. The first position of particle three holds a droplet used as a bridge. As a result, the whole sector is blocked and no droplets can be deposited on the empty, blocked positions. The second sector is blocked as well due to another bridge located on the second position. The first and third position of this sector hold a wet and a dry droplet, respectively. The wet droplet may not become a bridge, unless the existing bridge breaks before the droplet has dried.

Blocking sectors and deactivating the corresponding positions is a way to account for steric effects in agglomerates and has been introduced by Terrazas-Velarde [15]. Such effects are illustrated in Figure 3.9, where two particles collide and agglomerate both at the second position of the colliding sectors. Both particles hold additional wet droplets, which are, however, inaccessible for other colliding particles after agglomeration. At the same time, the remaining free positions may not receive any droplets. Unless the bridge breaks, the positions of the colliding sectors stay blocked, the free positions remain empty, and the droplet states change only due to drying.

In previous works using the concept of positions [15, 97], only monodisperse primary particles were considered. The model from Dernedde [132] is able to take a size distribution of the initial particles into account. However, the type of the distribution is restricted to a normal distribution and the concept of positions was not used in this case. Therefore, the concept of positions is extended to consider an arbitrary size distribution of the initial particles in the present work. In Appendix C, an algorithm is presented, which is used in the present thesis to create a set of particle diameters according to an arbitrary size distribution. Necessary changes to the concept of positions when distributed initial particle diameters are taken into account are presented below.

If monodisperse primary particles are considered, the particle diameter and the number of positions (both $N_{pos,sec}$ and N_{pos}) are identical for each particle. In order to extend the concept of positions,

Table 3.3: Meaning of the possible position labels used in the presented algorithm (adapted from Dernedde et al. [124]).

Label	Position state	Sterical accessibility	Presence of droplet	Droplet state
0	inactive	–	–	–
1	active	+	–	no droplet
2	active	+	+	wet
3	active	–	–	no droplet
4	active	–	+	wet
5	active	–	+	bridge
6	active	+	+	dry
7	active	–	+	dry
8	active	+	–	no droplet

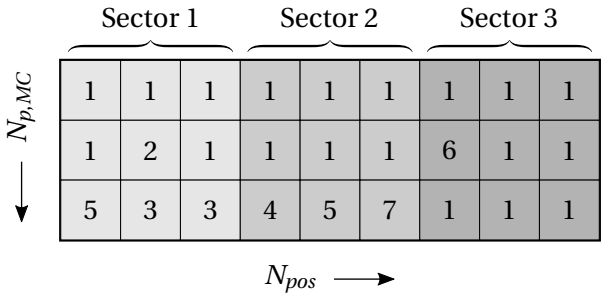

Figure 3.8: Schematic representation of the matrix used to store information about the droplet states for each position of each particle. For simplification, three equally sized particles with three sectors, each consisting of three positions, are shown.

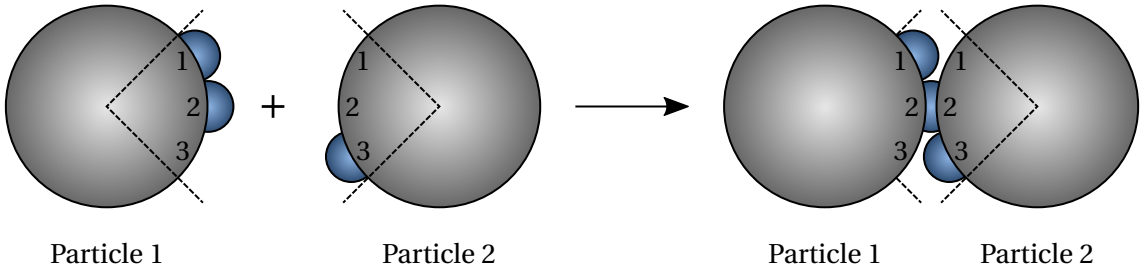

Figure 3.9: Illustration of two agglomerating particles. In this example, agglomeration results in two blocked wet droplets, which are inaccessible for further collisions due to steric hindrance (adapted from Terrazas-Velarde [15]).

enabling size distributions of primary particles, $N_{pos,sec}$ and N_{pos} need to correspond to the diameter of each particle, following Equation (3.7) and Equation (3.8). Note that independently of the particle size, the maximum coordination number K_{max} is still assumed to be six. As a result, a minimum particle diameter $d_{p,min}$ exists, which can be considered using this approach. For a particle with a size equal to $d_{p,min}$, the number of positions per sector $N_{pos,sec}$ equals unity and the corresponding number of positions N_{pos} is six. A particle diameter smaller than $d_{p,min}$ cannot be considered in the simulation without changing the maximum coordination number. The minimum particle diameter depends on the maximum coordination number and the contact area between the droplet and the particle $A_{contact}$; it can be calculated by rearranging Equation (3.7) and setting $N_{pos,sec}$ to unity:

$$d_{p,min} = \left(\frac{K_{max} A_{contact}}{\pi} \right)^{1/2}. \tag{3.13}$$

Figure 3.10 shows the behavior of $d_{p,min}$ depending on the droplet diameter d_{drop}, which is used to calculate the droplet volume, assuming spherical droplets in Equation (3.11). The minimum particle diameter changes linearly with increasing droplet diameter. For example, if the droplet diameter is equal to 40 µm, the smallest particle diameter that can be considered with $K_{max} = 6$ and $\theta = 40°$ is approximately 94 µm.

Since each particle has a different number of positions (both $N_{pos,sec}$ and N_{pos}), the length of the corresponding position vector is also different. In order to save the droplet state for each position in a matrix as shown in Figure 3.8, the label "0"(see Table 3.3) is used, representing an inactive position. An example is shown in Figure 3.11. The first particle in this example is the largest with three positions per sector. Particle two is smaller with two positions per sector and the third particle is the smallest one is this example with only one position per sector. As stated above, the positions labeled with "0" are inactive and only used to fill the matrix. They are not involved in droplet deposition and collision events. In this way, size distributions of primary particles can be included into the concept of positions.

A simplification can be made in case of layering. Since the particles grow layer-wise and not by agglomeration, the introduction of sectors is unnecessary. Therefore, the particle surface is only divided into positions. The number of positions per particle can then be calculated using the following

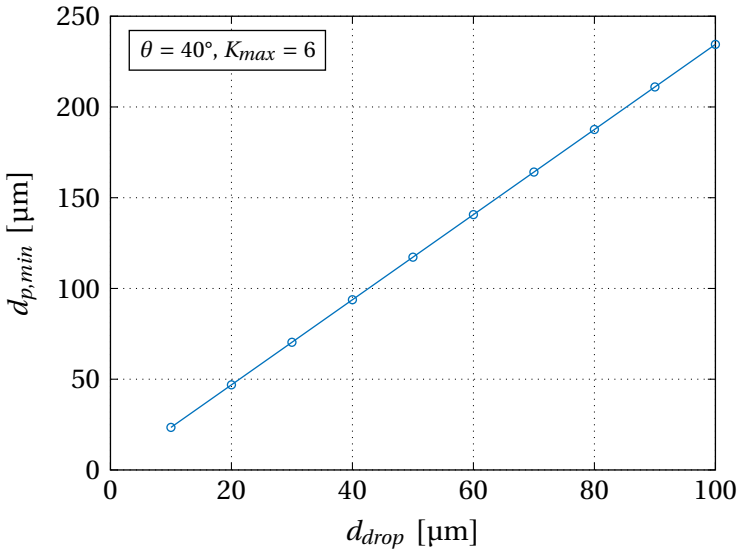

Figure 3.10: Influence of the droplet diameter on the minimum particle diameter for a contact angle of 40° and a maximum coordination number equal to 6.

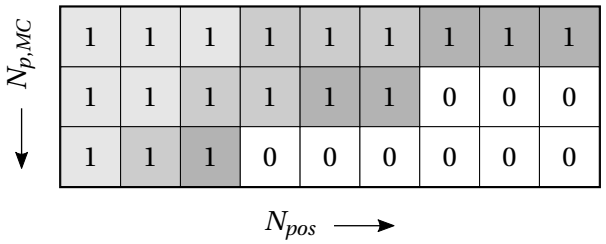

Figure 3.11: Schematic representation of the matrix used to store information about the droplet states for the case of distributed particle sizes.

equation:

$$N_{pos} = \text{nint}\left(\frac{A_p}{A_{contact}}\right). \tag{3.14}$$

A distribution of the particle size and the corresponding number of positions can be taken into account in the same way as described above.

Layer-wise particle growth implies an enlargement of the surface of single particles. Correspondingly, the number of positions per particle should be adjusted during the layering process. A detailed description of this procedure is given in Section 3.2.4. This adjustment may also be necessary for agglomeration processes if a binder solution is used since undesired layering may take place and lead to growth of the primary particles. However, in previous works [15, 97, 124], this effect has not been taken into account. In this thesis, the focus lies on agglomeration due to glass transition. Since in these processes pure water is sprayed and no solid material is present in the liquid to induce layering, the adjustment of the number of positions per particle is only taken into account in the simulations for layering processes. However, an increasing number of positions due to agglomeration is certainly taken into account and described in Section 3.2.5.

3.2 Micro-processes and events

3.2.1 Droplet deposition

The frequency of the droplet deposition event can be directly calculated from the mass flow rate of sprayed droplets. This parameter scales with the size of the particle system, and therefore the scaling factor needs to be used. Assuming monodisperse and spherical droplets, the frequency of the droplet deposition event in the simulation $f_{drop,MC}$ can be calculated as follows:

$$f_{drop,MC} = S\dot{N}_{drop} = S\frac{6\dot{M}_{spray}}{\pi\varrho_{drop}d_{drop}^3}. \tag{3.15}$$

If this event is selected to occur in a time step, a particle and a position must be randomly selected to deposit a droplet. As stated in Chapter 2, Mörl et al. [6] presented a mathematical formulation of the process kinetics for layering processes, assuming that droplet deposition is related to the surface area of the particles. A particle having a large diameter and consequently a large surface area is more likely to receive a droplet than a small particle. The generalization proposed by Peglow et al. [88] (droplet deposition can be related to an arbitrary moment of the particle size distribution) can also be adapted in the Monte Carlo algorithm as described below.

One way to select a particle for a droplet deposition event, is to select it based on its number. Since in this thesis 1000 particles are considered in the simulation, a particle can be selected by randomly choosing an integer number between 1 and 1000. However, it is also possible to select the particle

Table 3.4: Properties and selection probabilities of the set of three particles used in the example to test the particle selection methods in the droplet deposition algorithm.

No.	d_p [mm]	A_p [mm^2]	V_p [mm^3]	$P_{sel}(\Lambda_0 = 1)$ [−]	$P_{sel}(\Lambda_1 = 1)$ [−]	$P_{sel}(\Lambda_2 = 1)$ [−]	$P_{sel}(\Lambda_3 = 1)$ [−]
1	0.4	0.5027	0.0335	0.3333	0.3333	0.2857	0.2222
2	0.2	0.1257	0.0042	0.3333	0.1667	0.0714	0.0278
3	0.6	1.1310	0.1131	0.3333	0.5000	0.6429	0.7500
$\sum$	1.2	1.7593	0.1508	1	1	1	1

based on physical properties, e.g., length (diameter), surface area, or volume. The procedure and the influence of the particle selection on the particle formation process is illustrated in the following example.

Consider three particles with different diameters, surface areas and volumes, see Table 3.4. If the particles are selected based on their number, a random integer between unity and three would be necessary in the current example. In this case, each particle has the same probability to be selected. However, the selection probability is not equal if the particles are selected based on physical properties. The procedure is shown in Figure 3.12 for the selection based on the diameter, but is identical for other properties. A random number from the interval $(0, d_{p,tot})$ is drawn, where $d_{p,tot}$ is the sum of all individual diameters and equals 1.2 mm in this example. Figure 3.12 shows that the size of the intervals corresponds to the value of the diameter. The number of the selected particle can then be obtained by the interval, in which the random number lies:

$$\text{particle} = \begin{cases} 1 & r\,d_{p,tot} \leq 0.4, \\ 2 & 0.4 < r\,d_{p,tot} \leq 0.6, \\ 3 & 0.6 < r\,d_{p,tot} \leq 1.2, \end{cases} \quad \text{with} \quad d_{p,tot} = \sum_j d_{p,j}. \tag{3.16}$$

In this case, the selection probability is not equal for each particle. In fact, it depends on the property itself and corresponds to the normalized size of the interval. For the case depicted in Figure 3.12, the interval of the third particle occupies half of the total range and its selection probability is therefore 0.5. Particles 1 and 2 are smaller and their selection probabilities are $1/3$ and $1/6$, respectively. Table 3.4 lists the selection probabilities depending on the used property.

In case of layering, the different methods of particle selection for droplet deposition described above directly correspond to the macroscopic growth kinetics given in Equation (2.29). If the particles are selected based on their number, the kinetics correspond to $G = \Lambda_0 G_0$ with $\Lambda_0 = 1$. If the particles are selected according to their length, $G = \Lambda_1 G_1$ with $\Lambda_1 = 1$ and so on. If values other than unity are used for Λ_j, mixtures of these kinetics are obtained. The selection property in a specific time step can

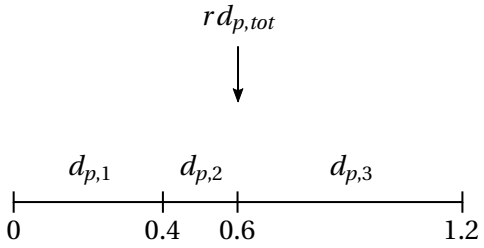

Figure 3.12: Schematic representation of the method used to select particles for droplet deposition. In this example, selection based on particle diameter is shown.

be determined randomly with a uniformly distributed random number r from the interval $(0, 1)$:

$$\text{property} = \begin{cases} \text{number} & r \leq \Lambda_0, \\ \text{length} & \Lambda_0 < r \leq \Lambda_0 + \Lambda_1, \\ \text{surface area} & \Lambda_0 + \Lambda_1 < r \leq \Lambda_0 + \Lambda_1 + \Lambda_2, \\ \text{volume} & \Lambda_0 + \Lambda_1 + \Lambda_2 < r \leq 1. \end{cases} \tag{3.17}$$

In the simulations presented in this thesis the particles are selected based on their surface area by setting Λ_2 to unity.

The described selection algorithm was tested using the set of particles listed in Table 3.4. The particles were selected for droplet deposition based on their number, diameter, surface area, and volume and the number of droplets each particle received was counted. The results are shown in Figure 3.13 for 100 and 10^6 droplets, respectively. Figure 3.13a shows that the probability for each particle to be selected is identical if the selection is based on their number. If the selection property is the particle diameter, particle number 3, being the largest particle in this example, receives half of the droplets, while the other two receive significantly less droplets. This effect increases if the surface area or the volume are used as the selection property. It can also be seen that the relative droplet number each particle receives changes with the number of droplets. For the case of 10^6 droplets, the relative droplet numbers match the selection probabilities in Table 3.4.

The example shown in Figure 3.13 illustrates that the way particles are selected for droplet deposition influences the distribution of droplets within the sample system and therefore the behavior of the particle formation process. The influence of droplet deposition on layering and agglomeration is addressed in the frame of simulation studies in Section 4.2.2 and Section 5.2.1, respectively.

Once a particle has been selected, a position of this particle is randomly chosen and the droplet is deposited. The position is selected based on the number of positions of the specific particle by drawing a random number from the interval $(1, N_{pos})$. The label of the position is changed according to Table 3.3. Additionally the time of droplet deposition is stored and later used to calculate the progress of drying during the simulation, see Section 3.2.3.

In the Monte Carlo models presented by Terrazas-Velarde [15] and Hussain [97], particles were selected for droplet deposition based on their surface area as well, which corresponds to the case

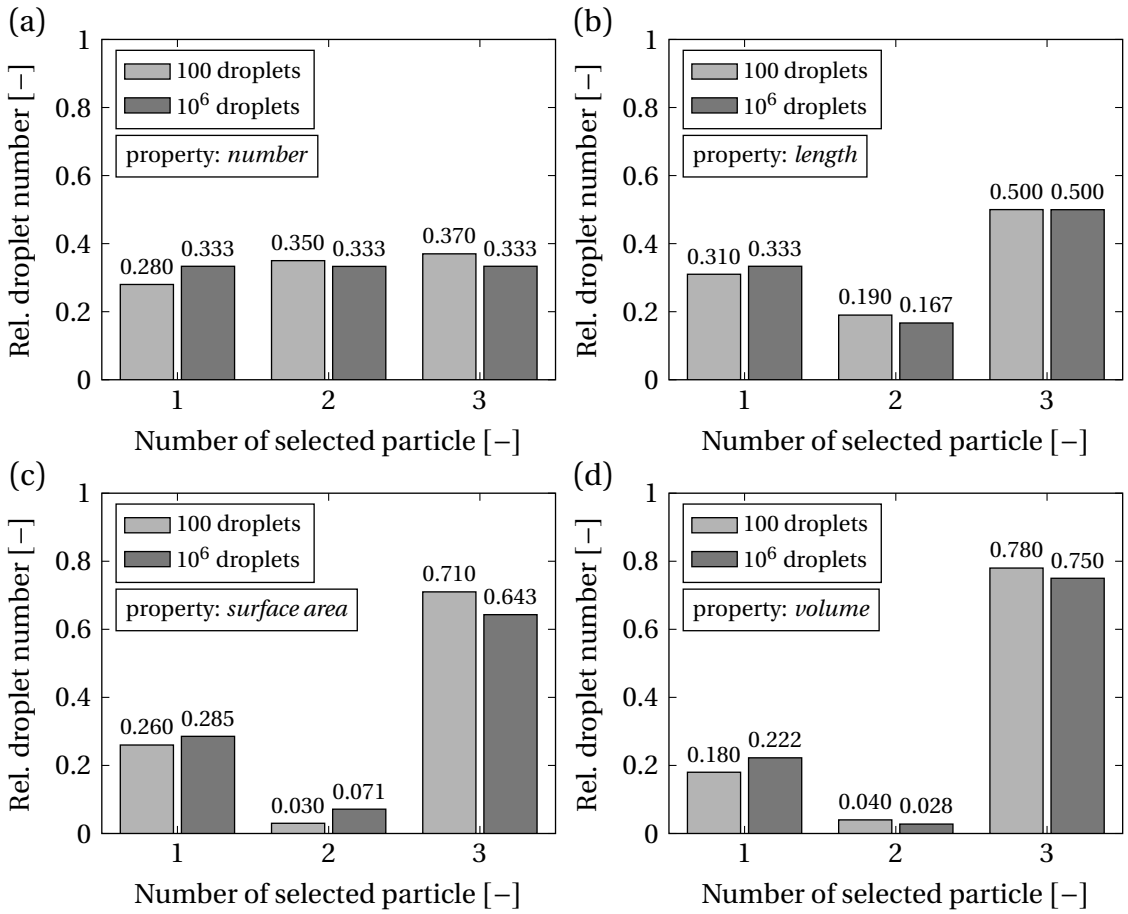

Figure 3.13: Relative droplet number received by the particles (example of Table 3.4) for different selection properties: number (a), length (b), surface area (c), volume (d).

given in Figure 3.13c and Equation (3.17) (with $\Lambda_2 = 1$). Dernedde [132] picked the particles randomly by their number, which corresponds to the case shown in Figure 3.13a. In comparison to the current thesis, small particles are preferred in the selection for droplet deposition in the model by Dernedde [132].

3.2.2 Particle collisions

The frequency of the collision event $f_{coll,MC}$ is calculated using the collision frequency per single particle in the real particle system f_{coll} and the number of particles in the simulation:

$$f_{coll,MC} = \frac{1}{2} f_{coll} N_{p,MC}. \tag{3.18}$$

The pre-factor $1/2$ follows from the assumption of binary collisions. The collision frequency per single particle f_{coll} is an important parameter and depends on the complex multiphase flow in the fluidized bed. This parameter is accessible either by CFD-DEM modeling, see Fries [118], or experimental methods such as different particle tracking techniques comprising PTV (particle tracking

velocimetry), MPT (magnetic particle tracking), and PEPT (positron emission particle tracking), see Jiang et al. [152]. Previous modeling approaches by Terrazas-Velarde [15] and Hussain [97] calculated f_{coll} using an empirical model presented by Buffière and Moletta [153] based on hydrophone measurements in an inverse three-phase fluidized bed. Dernedde [132] used a theoretically developed expression presented by Oesterle and Petitjean [154] in combination with an empirical correlation for the relative particle velocity obtained by experiments in a pseudo-2D fluidized bed. The calculated value of f_{coll} needed to be adjusted with a constant pre-factor, in order to reduce the calculated collision frequency in the models of Terrazas-Velarde [15] and Hussain [97] as well as in the work of Dernedde [132]. Otherwise, the large number of collisions associated with a high collision frequency leads to the situation that liquid bridges are formed shortly after droplet deposition. This leads to a negligible influence of droplet drying on the agglomeration process, which has been, however, observed experimentally. The adjusted collision frequency is then considered to be an effective collision frequency in the sense of agglomeration [15]. In this thesis, the approach presented by Dernedde [132] is used to calculate f_{coll} and explained below.

The collision frequency of a particle j can be calculated according to Oesterle and Petitjean [154] using the following equation:

$$f_{coll,j} = \sqrt{2}\,\pi \left(R_j + R_0\right)^2 c'_{n,p} \left|u_{p,j} - u_{p,0}\right|. \tag{3.19}$$

In this equation, R_j and $u_{p,j}$ are the radius and velocity of particle j and R_0 and $u_{p,0}$ represent the mean radius and the mean velocity of the surrounding particles. The parameter $c'_{n,p}$ is the number concentration of particles in the fluidized bed. Assuming monodisperse particles, a mean velocity of the particles in the fluidized bed $\overline{u}_p$, and that the surrounding particles move with a small velocity equal to minimum fluidization velocity, Dernedde [132] simplified Equation (3.19) to:

$$f_{coll} = F_{coll} \sqrt{2}\,\pi\, d_p^2\, c'_{n,p}\, \overline{u}_p. \tag{3.20}$$

In this equation, F_{coll} is the constant pre-factor used to scale the collision frequency. Dernedde [132] obtained $F_{coll} = 0.1$ by fitting his simulation results to experimental data. The number concentration $c'_{n,p}$ is defined as the number of particles per bed volume:

$$c'_{n,p} = \frac{N_{p,real}}{V_{bed}} = \frac{1 - \varepsilon_{bed}}{V_p} \quad \text{with} \quad V_p = \frac{\pi}{6} d_p^3. \tag{3.21}$$

In this equation, ε_{bed} is the porosity of the fluidized bed and V_p is the volume of a single particle. The mean relative particle velocity is calculated according to an empirical correlation based on PIV (particle image velocimetry) measurements in a pseudo-2D fluidized bed presented by Dernedde [132]:

$$\overline{u}_p = -0.00001669\,\mathrm{Re}^2 + 0.00444290\,\mathrm{Re} \quad \text{with} \quad \mathrm{Re} = \frac{u_g d_p}{\nu_g}. \tag{3.22}$$

Since in the simulations a particle size distribution is considered, the above shown equations in

which monodisperse particles are assumed, are evaluated with the number-based mean particle size.

If the event “collision” is selected to occur in a time step, two particles have to be selected randomly. In contrast to droplet deposition, the particles are selected only based on their numbers. In this way, the probability for each particle to be selected is identical, which follows from the assumption that the fluidized bed is well mixed. However, a selection based on physical properties as shown above for droplet deposition would be possible. Once two particles have been chosen, the colliding positions are selected based on their numbers as well, which accounts for a random orientation of the particles during collisions. Subsequently, the agglomeration criteria described later in Section 3.2.5 need to be checked to determine the outcome of the collision.

3.2.3 Droplet drying

Once a droplet has been deposited on a particle, the corresponding position is labeled accordingly and the droplet starts to dry. The purpose of the droplet drying algorithm is to provide the drying time of the deposited droplets, depending on the process conditions. In combination with the deposition time of the droplet, the droplet state (wet or dry) can be checked as follows:

$$\text{droplet state} = \begin{cases} \text{dry} & t \geq t_{depos} + \Delta t_{dry}, \\ \text{wet} & \text{otherwise.} \end{cases} \tag{3.23}$$

In this equation, t is the process time in the simulation, t_{depos} is the time of droplet deposition, which is stored for each droplet, and Δt_{dry} is the drying time of the droplet. If a droplet has dried completely, the corresponding position is labeled according to Table 3.3.

In the following, the drying models for coating and layering as well as binder-less agglomeration are presented separately.

Drying model for coating and layering

In case of coating and layering, drying of deposited droplets containing solid material is considered. Similar to spray drying (cf. Section 2.2.1), evaporation of the liquid causes shrinkage of the sessile droplet as well as crust formation, see Sondej et al. [155], who investigated drying of sessile solution droplets. These stages are shown in Figure 3.14. In previous Monte Carlo approaches focusing on agglomeration using binder droplets, drying of deposited droplets has been modeled. Terrazas-Velarde [15] and Hussain [97] used a model calculating the reduction of the droplet height during drying, assuming a constant contact angle. This assumption is based on observations from single droplet drying experiments. Terrazas-Velarde [15] also considered crust formation by calculating a critical droplet height, which corresponds to the maximum concentration of the solid material in the droplet. Droplets smaller than this value, are considered to be dry. A drying model for the stage after crust formation was not presented. The model has been validated using deposited droplet drying

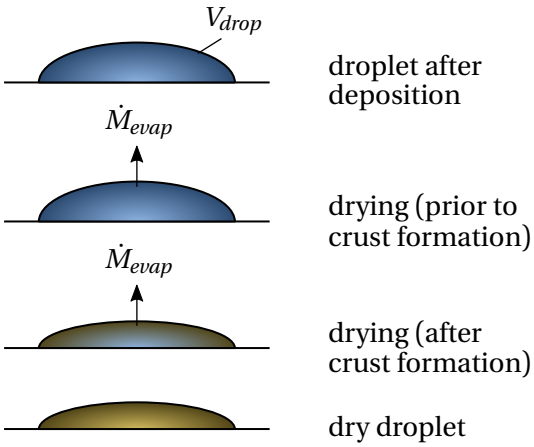

Figure 3.14: Schematic representation of the stages during drying of a deposited droplet.

experiments and showed good agreement in case of pure water droplets at lower temperatures. In case of elevated temperatures and binder droplets (aqueous hydroxypropyl methylcellulose (HPMC) solution), the model overestimates the drying kinetics. Hussain [97] neglected crust formation and considered droplets to be dry if their height equals zero. Dernedde [132] calculated the reduction of the droplet mass due to drying and additionally modified the driving force by multiplying the moisture content at adiabatic saturation with the mean mass fraction of water in the droplet to account for an increasing mass transfer resistance during drying. The resulting drying times are larger and closer to values estimated from experimental data on the mean moisture content of particle samples taken from spray fluidized bed agglomeration experiments. However, in some cases, the drying times calculated by the model exceed the values obtained from the experimental data.

In this thesis a relatively simple approach is used to calculate drying times of deposited droplets. Neglecting shrinkage, the drying time follows from the liquid mass of the droplet and the evaporation rate:

$$\Delta t_{dry} = \frac{M_{drop}(1 - w_s)}{\dot{M}_{evap}}. \tag{3.24}$$

Assuming gas-side controlled drying (neglecting an increased mass transfer resistance due to crust formation), the mass flow rate of evaporation is calculated based on the following equation:

$$\dot{M}_{evap} = \beta \varrho_g A_{drop}(Y_{as} - Y). \tag{3.25}$$

In this equation, β is the mass transfer coefficient calculated as shown in Appendix B, ϱ_g is the density of the fluidization gas, A_{drop} is the curved surface area of the droplet following from Equation (3.9), and $Y_{as} - Y$ is the driving force of the drying process. The driving force is calculated from the moisture content of the fluidization gas at adiabatic saturation Y_{as} and the moisture content of the bulk gas Y. The moisture content at adiabatic saturation is calculated as shown in Appendix A. Similar to Terrazas-Velarde [15], Hussain [97], and Dernedde [132], the moisture content of the bulk gas is

calculated, assuming that the sprayed water evaporates completely:

$$Y = Y_{in} + \frac{\dot{M}_{spray}(1 - w_s)}{\dot{M}_{g,dry}} \quad \text{with} \quad \dot{M}_{g,dry} = \frac{\dot{M}_g}{1 + Y_{in}}. \tag{3.26}$$

In this equation, Y_{in} is the inlet moisture content of the fluidization gas, w_s is the solid mass fraction of the sprayed liquid, $\dot{M}_{spray}$ and $\dot{M}_{g,dry}$ are the mass flow rates of the sprayed liquid and the dry fluidization gas, respectively.

Drying model for binder-less agglomeration

In case of binder-less agglomeration, pure water droplets are sprayed on fluidized amorphous particles. It is assumed that each droplet is instantaneously and fully imbibed into the amorphous particle, creating a cylindrical wet region (puddle) beneath the original contact area between the droplet and the particle. The puddle has a depth (or height) of h_{imb} and a rough bottom with a height of asperities equal to h_a. During drying, the geometry of the puddle (height and cross section) stays constant. However, the mass fraction of water w_w, which is used to determine the local glass transition temperature as explained in Section 3.2.5, decreases. Figure 3.15 shows a schematic representation of formation and drying of the wet regions.

In reality, wetting can be the result of different mechanisms such as capillarity in case of porous substrates or matrix diffusion in case of macroscopically non-porous substrates, or a combination of both. Pashminehazar et al. [156] investigated the internal 3D structure of amorphous material using the example of maltodextrin, which is also used in the present work as described in detail in Chapter 5. X-ray tomography was used to measure the internal porosity of maltodextrin single particles. The results show that maltodextrin particles are porous with porosity values ranging between 0.19 and 0.29. The results also indicate that the porosity appears mainly in the form of inclusions, which are not interconnected to each other. These findings favor the non-capillary imbibition mechanism in case of maltodextrin, but the substrate is formally considered as porous with a certain porosity in the present work. Since droplet imbibition is considered to be instantaneous (see Figure 3.15) this assumption has no kinetic influence in the model. Below, the equations of the drying model are derived.

Once a droplet has been deposited, a wet region V_{imb} with a porosity corresponding to the primary particle porosity ε_{pp} is created (see Figure 3.15), which contains solid volume V_s and liquid volume V_w:

$$V_{imb} = \frac{V_w}{\varepsilon_{pp}} = \frac{V_s}{1 - \varepsilon_{pp}}. \tag{3.27}$$

Note that at the time of deposition, the volume of water in the wet region V_w is equal to the droplet volume V_{drop}, which is calculated from the droplet diameter. The depth or height of the wet region,

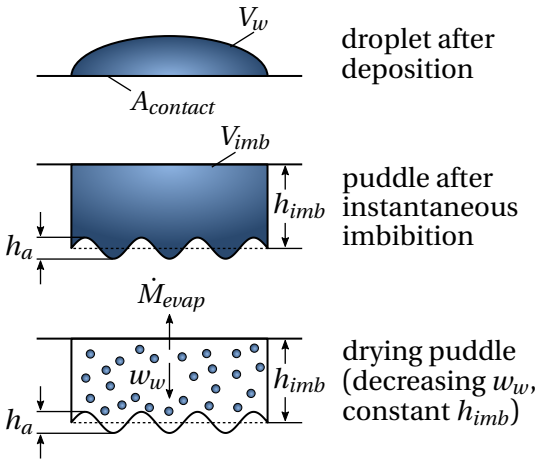

Figure 3.15: Schematic representation of formation and drying of wet regions in the model for binderless agglomeration.

which is constant during drying, can be obtained to:

$$h_{imb} = \frac{V_{drop}}{\varepsilon_{pp} A_{contact}}. \tag{3.28}$$

The mass fraction of water in the wet region is defined as:

$$w_w = \frac{M_w}{M_w + M_s} = \frac{\varrho_w V_w}{\varrho_w V_w + \varrho_s V_s}, \tag{3.29}$$

where M_w, M_s, and ϱ_w, ϱ_s are the masses and densities of water and solid material (without pores), respectively. Combining Equations (3.27) and (3.29), the mass fraction of water in the wet region can be calculated as follows:

$$w_w = \frac{\varrho_w \varepsilon_{pp}}{\varrho_w \varepsilon_{pp} + \varrho_s (1 - \varepsilon_{pp})} + w_{w,0}. \tag{3.30}$$

The mass of the water droplet M_w decreases during drying due to the evaporation mass flow rate:

$$\frac{\mathrm{d}M_w}{\mathrm{d}t} = -\dot{M}_{evap}. \tag{3.31}$$

The equation for the evaporation mass flow rate is formally equal to the formulation given in Equation (3.25) (gas-side controlled drying, no hygroscopicity), but in this case the evaporation rate is calculated with the (constant) footprint of the droplet (contact area between the droplet and the particle) (see Equation (3.12)) instead of the curved surface area of the droplet:

$$\dot{M}_{evap} = \beta \varrho_g A_{contact} (Y_{as} - Y). \tag{3.32}$$

The moisture content of the fluidization gas at adiabatic saturation and the mass transfer coefficient are calculated as shown in Appendices A and B, respectively. Combining Equations (3.31) and (3.32)

and integrating the resulting equation, the change in droplet mass over time is obtained:

$$\int_{M_{w,0}}^{M_w(t)} \frac{\mathrm{d}M_w}{\mathrm{d}t}\mathrm{d}t = \int_{t=0}^{t} -\beta\varrho_g A_{contact}(Y_{as}-Y)\mathrm{d}t, \tag{3.33}$$

$$M_w(t) = M_{w,0} - \beta\varrho_g A_{contact}(Y_{as}-Y)t. \tag{3.34}$$

The value of the mass fraction of water in the wet region $w_w(t)$ can be obtained by inserting $M_w(t)$ into Equation (3.29). The drying time of the imbibed water droplet is then calculated using:

$$\Delta t_{dry} = \frac{M_{w,0}}{\dot{M}_{evap}}, \tag{3.35}$$

where $M_{w,0}$ is the initial water mass of the wet region, which is equal to the mass of the water droplet.

3.2.4 Size enlargement in coating and layering

If one or several droplets have dried in a time step according to Equation (3.23), the height of the resulting solid material needs to be calculated. This height or layer thickness can be calculated for each position of each particle and varies with the number of droplets deposited on a position over time and the volume of one solidified droplet. The calculation of the layer thickness in the presented Monte Carlo model is described below.

Freireich and Wassgren [157] suggest to calculate the layer thickness assuming that the radius of curvature of the particle can be neglected (layer thickness is small compared to the particle radius). In this case, the layer thickness generated by a dry droplet for a position follows from the volume of a dry droplet and the contact area between droplet and particle:

$$s_{drop,dry} = \frac{V_{drop,dry}}{A_{contact}}. \tag{3.36}$$

In the present work, an approach taking the particle radius into account when calculating the layer thickness of solidified droplets is used. Considering a particle with a uniform solid layer, the layer thickness s_{layer} can be calculated using a simple volume balance:

$$V_{layer} = V_p - V_{core} = \frac{\pi}{6}\left(d_{core}+2s_{layer}\right)^3 - \frac{\pi}{6}d_{core}^3. \tag{3.37}$$

Expanding, Equation (3.38) is obtained:

$$0 = s_{layer}^3 + \frac{3}{2}d_{core}s_{layer}^2 + \frac{3}{4}d_{core}^2 s_{layer} - \frac{3}{4}\frac{V_{layer}}{\pi}. \tag{3.38}$$

Equation (3.38) can be solved analytically yielding an expression for the layer thickness:

$$s_{layer} = \left(\frac{d_{core}^3}{8} + \frac{3}{4} \frac{V_{layer}}{\pi} \right)^{1/3} - \frac{d_{core}}{2}. \tag{3.39}$$

Equation (3.39) can be used to calculate the thickness of a uniform layer if the volume of the layer V_{layer} and the diameter of the core particle d_{core} are known. Note that the calculated layer thickness depends on the particle size (i.e., it increases for smaller particle diameters).

In case of a non-uniform solid layer, the layer thickness must be calculated for each position individually. Equation (3.39) must be modified using the idea illustrated in Figure 3.16 before it can be used in this case. When the layer thickness for one position needs to be calculated (left hand-side particle), Equation (3.39) may be used if the solid volume is virtually placed on each position of the particle (right hand-side particle), as indicated in Figure 3.16. In this way, the calculation of the layer thickness generated by a dry droplet $s_{drop,dry}$ on a position is reduced to the above discussed case of a uniform solid layer and Equation (3.39) can be used. The volume of the (virtual) layer V_{layer} can then be calculated from the number of positions of the considered particle in the specific time step and the volume of a single dry droplet:

$$V_{layer} = N_{pos} V_{drop,dry}. \tag{3.40}$$

The volume of the dry droplet depends on the amount of solid mass in the droplet, calculated from the droplet mass M_{drop} and the solid mass fraction w_s, the density of the solid material without pores ϱ_s and the porosity of the dry droplet $\varepsilon_{drop,dry}$, which is a model parameter and needs to be set in the simulation:

$$V_{drop,dry} = \frac{M_{drop} w_s}{\varrho_s (1 - \varepsilon_{drop,dry})}. \tag{3.41}$$

The described method allows to calculate the layer thickness for each position on each particle during the layering process. The increase in particle diameter can be calculated using the initial diameter $d_{p,0}$ and the mean layer thickness $\bar{s}$ of each particle:

$$d_p = d_{p,0} + 2\bar{s} \quad \text{with} \quad \bar{s} = \frac{1}{N_{pos}} \sum_{j=1}^{N_{pos}} s_j. \tag{3.42}$$

In addition to the layer thickness and the particle size, the coating mass of single particles is an important parameter. The coating mass M_c of a particle can be calculated from its number of dry droplets, which is tracked during the simulation and the amount of solid mass in a droplet:

$$M_c = N_{drop,dry} M_{drop} w_s. \tag{3.43}$$

By computing histograms, different layer thickness distributions can be obtained: intra-particle layer thickness distribution for each particle, which describes the distribution of the layer thickness on

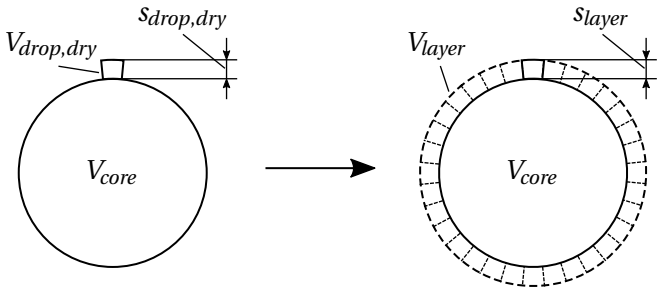

Figure 3.16: Schematic representation of the method used to calculate the layer thickness of a solidified droplet.

single particles, and the inter-particle layer thickness distribution describing the distribution of the mean layer thickness in the population. Additionally, the distribution of the particle size and the coating mass in the population can be calculated.

As the particles grow, their surface area increases over time as well. As a result, the number of positions for each particle needs to be adjusted. Each time the diameter of a particle increases, the number of positions is re-calculated using Equation (3.14). If the number of positions increases, more positions will be activated, which are then available for droplet deposition. This approach is shown in Figure 3.17, where a particle is represented by five positions. In this example, a wet droplet is present on the first position, dried droplets are located on positions two to four, and the fifth position is still inactive (left hand-side). Assuming the number of positions to increase by one, a sixth position is enabled (right hand-side) and the label changes from "0" to "8", see Table 3.3. This label represents an empty position, which does not belong to the initial particle. In this way, information about the surface coverage of the coating can be obtained as described below. Subsequently a layer thickness value other than zero must be assigned to this position since otherwise the value of the mean layer thickness of the particle (see Equation (3.42)) would decrease due to activating this position. In this approach, the mean layer thickness of the particle (before activating the position) is assigned to the activated position.

If the purpose of the layering process is coating, information about the surface coverage of the coating is important. This property is described by the coated surface fraction Ψ_c, which can be calculated using the labeling system in Table 3.3. The coated surface fraction is defined as the ratio between the coated surface area and the total surface area of a particle, which can be written as:

$$\Psi_c = \frac{A_p - A_{p,free}}{A_p} = \frac{N_{pos} - N_{pos,free}}{N_{pos}}. \tag{3.44}$$

In this approach, Ψ_c is directly calculated from the corresponding number of positions. The number of free positions (positions without any droplet) $N_{pos,free}$ is then obtained by counting the number of positions labeled "1". Once a particle is completely coated (i.e., the coated surface fraction equals unity and the number of free positions is equal to zero) the time is stored in the simulation. This parameter represents the coating time of a particle, which is used to calculate the distribution of the coating time in the population.

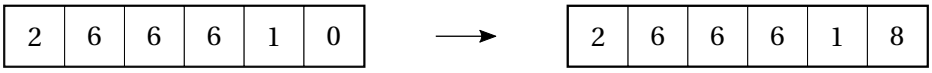

Figure 3.17: Adjustment of the number of positions during layering: if the number of positions of a particle must be increased due to growth, additional positions are activated and labeled according to the introduced labeling system, see Table 3.3.

3.2.5 Size enlargement in binder-less agglomeration

In case of binder-less agglomeration, particles grow by forming agglomerates that consist of several (at least two) primary particles. The size of agglomerates depends on the number, size and spatial arrangement of the primary particles within the agglomerate. In this thesis, an equivalent diameter is used to represent the size of agglomerates based on the diameters of the primary particles and a mean agglomerate porosity. The same equivalent diameter has been used in previous works [15, 97] for monodisperse primary particles:

$$d_{agg} = \left(\frac{N_{pp} d_{pp}^3}{1 - \varepsilon_{agg}} \right)^{1/3} . \tag{3.45}$$

In this equation, N_{pp} is the number of primary particles within an agglomerate, d_{pp} is the primary particle diameter, and ε_{agg} is the porosity of the agglomerate. In case of polydisperse primary particles, Equation (3.45) needs to be modified, leading to:

$$d_{agg} = \left(\frac{\sum_{j}^{N_{pp}} d_{pp,j}^3}{1 - \varepsilon_{agg}} \right)^{1/3} . \tag{3.46}$$

In this approach, Equation (3.46) is used to calculate the equivalent diameter of agglomerates consisting of at least two primary particles (i.e., it is not applied for single particles). The agglomerate porosity is a model parameter and needs to be set in the simulation. This parameter depends on process parameters and on the number of primary particles an agglomerate consists of, see Dadkhah and Tsotsas [58]. Depending on the mentioned parameters, the porosity values obtained by X-ray micro-tomography range between 0.3 and 0.8 for agglomerates consisting of non-porous glass particles produced in a spray fluidized bed. A similar study by Pashminehazar et al. [156] which investigated agglomerates consisting of maltodextrin particles shows porosities between 0.4 and 0.85, depending on the evaluation method (convex hull, dilation, or radius of gyration). The value for ε_{agg} is therefore set to 0.5 in all simulations.

If two particles (single primary particles or agglomerates) collide successfully according to the criteria described below, they form an agglomerate consisting of the colliding particles. This growth behavior needs to be reflected in the number of positions of the resulting agglomerate. As shown by an example in Figure 3.18, the position vector of the agglomerate is obtained by merging the position vectors of the colliding particles. In this simplified example, two particles consisting of three sectors and six

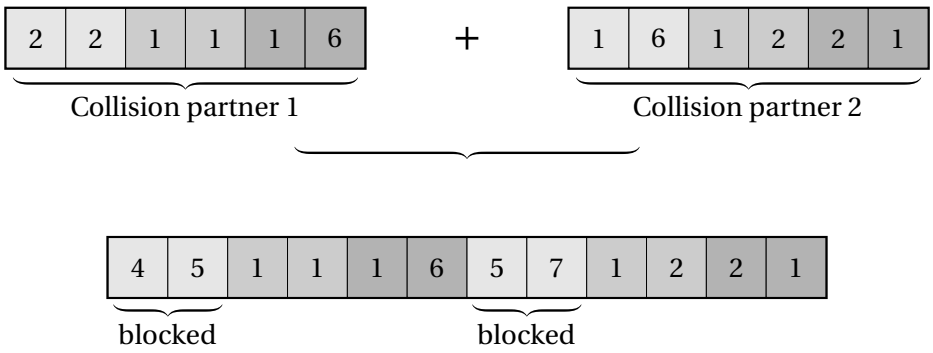

Figure 3.18: Adjustment of the number of positions during agglomeration: if two particles collide successfully they form an agglomerate consisting of the colliding particles. The resulting position vector of the agglomerate is obtained by merging the position vectors of the colliding particles. Additionally, re-labeling according to Table 3.3 to represent bridges and sterically inaccessible positions is performed.

positions agglomerate. Position two of the first particle and position one of the second particle are selected for collision. After merging the position vectors, the corresponding sectors are blocked and re-labeled according to Table 3.3. The information of the other positions is left unchanged. Since both collision partners do not exist anymore as individual entities, they are deleted from the sample. The resulting agglomerate is added to the sample and another randomly selected particle is copied and added to the sample as well to ensure a constant number of particles. The scaling factor is then adjusted according to Equation (3.3). An increasing number of positions due to layering as described in Section 3.2.4 is not considered here, as in binder-less agglomeration only pure water is sprayed. Below, the agglomeration criteria used in the presented model are described.

Glass transition

Upon droplet deposition, a wet region is formed as shown in Figure 3.15. Water migrates from the droplet into the amorphous matrix and decreases the glass transition temperature locally. If the temperature of the material is near its glass transition temperature, the viscosity of the material decreases and a sticky spot is created at that position. As described in Section 3.2.3, the wet region is subjected to drying. As a result, the water content decreases until it reaches zero. During the lifetime of the droplet, glass transition may occur and create an agglomerate upon particle-particle collision. If the wet region has dried completely, the sticky material has re-solidified and collisions involving this position cannot result in agglomeration anymore. Re-wetting of such spots may, however, induce glass transition again.

The glass transition temperature of the material in a wet region can be calculated using the Gordon-Taylor equation [158]:

$$T_{gt} = \frac{(1 - w_w)T_{gt,s} + k w_w T_{gt,w}}{(1 - w_w) + k w_w}. \tag{3.47}$$

In this equation, k is a constant, and $T_{gt,s}$ and $T_{gt,w}$ represent the glass transition temperatures of the dry solid and water, respectively. Equation (3.47) shows that the local glass transition temperature also depends on the water mass fraction of the wet region. As described in Section 3.2.3, this parameter changes during droplet drying and therefore connects drying to stickiness and possible agglomeration in the model. Values of $T_{gt,s}$ and $T_{gt,w}$ can be found in the literature, see Palzer [43]. If no value for $T_{gt,s}$ can be found, it can be estimated using an equation given by Roos and Karel [159]:

$$T_{gt,s} = T_{gt}(\infty) - \frac{K_{gt}}{\widetilde{M}_s}. \tag{3.48}$$

In this equation, $\widetilde{M}_s$ is the molar mass of the material, $T_{gt}(\infty)$ is the limiting glass transition temperature at a high molar mass, and K_{gt} is a material specific constant. For maltodextrins, which are used in this thesis, $T_{gt}(\infty) = 243\,°\mathrm{C}$ and $K_{gt} = 52\,800\,\mathrm{g\,K\,mol^{-1}}$ [159]. If the molar mass is unknown, a method presented by Dokic et al. [160] and Castro et al. [161] can be used to estimate it based on the DE value:

$$\widetilde{M}_s = \frac{18000}{\mathrm{DE}} + 18, \quad \left[\widetilde{M}_s\right] = \mathrm{g\,mol^{-1}}. \tag{3.49}$$

Figure 3.19a shows the decrease of the glass transition temperature with increasing water mass fraction, calculated using Equation (3.47) for the example of maltodextrin DE 10 and water ($T_{gt,s} = 160\,°\mathrm{C}$, $k = 7$, $T_{gt,w} = -135\,°\mathrm{C}$, values taken from Palzer [43]).

The change in viscosity η associated with glass transition can be estimated using the Williams-Landel-Ferry equation [43, 162]:

$$\log \frac{\eta}{\eta_{gt}} = \frac{C_{gt}\left(T_s - T_{gt}\right)}{B_{gt} + \left(T_s - T_{gt}\right)}. \tag{3.50}$$

The constants in this equation have the values $B_{gt} = 51.6\,\mathrm{K}$ and $C_{gt} = -17.4$ for most polymers. The parameters T_s and η_{gt} represent the temperature of the solid material and its viscosity at the glass transition temperature, respectively. In the literature [163, 164], it is often assumed that $\eta_{gt} = 10^{12}\,\mathrm{Pa\,s}$, while a recent study by Paterson et al. [136] reports a higher value in the range of $10^{14}\,\mathrm{Pa\,s}$. A value of $10^{12}\,\mathrm{Pa\,s}$ is used in the simulations presented in this thesis. Figure 3.19b shows the decrease in viscosity for an increasing water mass fraction, calculated using Equation (3.47) and Equation (3.50) for the same example (maltodextrin DE 10 and water) at $T_s = 20\,°\mathrm{C}$. Note that in this example glass transition sets in at a water mass fraction of approximately 0.11. The viscosity at water mass fractions lower than this threshold is therefore set to $10^{12}\,\mathrm{Pa\,s}$.

As stated above, glass transition leads to soft, sticky spots on the particle surface, which may cause agglomeration. However, according to Palzer [42] and Descamps et al. [164], the viscosity of the material must in fact be lower than $10^8\,\mathrm{Pa\,s}$ to enable stickiness and therefore agglomeration. If the viscosity is higher, the formation of viscous bridges will not be possible. In literature, this point is referred to as the sticky point with a corresponding sticky point temperature, which lies about 10 K to 30 K above the glass transition temperature. In this thesis, a temperature difference of 20 K is used.

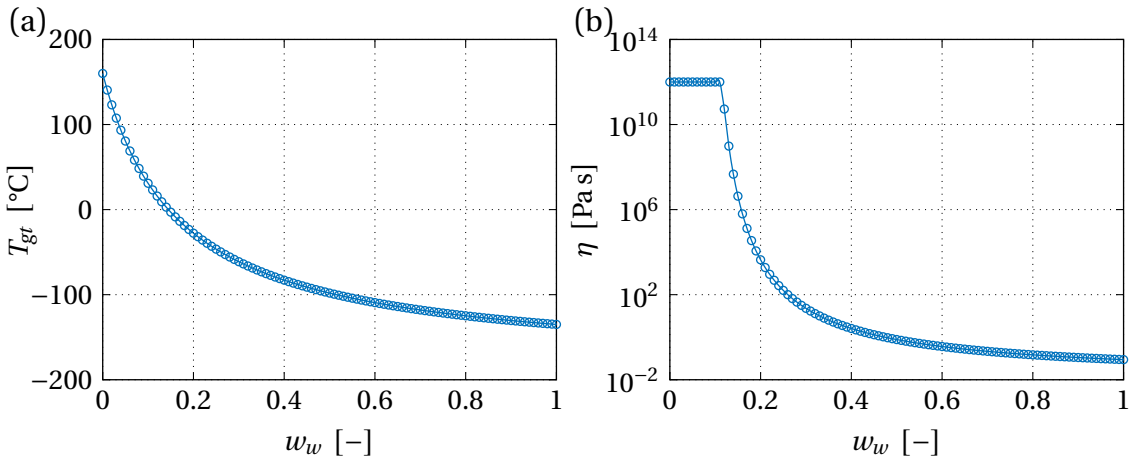

Figure 3.19: Example of a decreasing glass transition temperature (a) and viscosity (b) with an increasing water mass fraction for maltodextrin DE 10 and water at a solid temperature of 20 °C.

Agglomeration criteria

In this modeling approach, a series of criteria is used to determine whether a binary particle-particle collision leads to the formation of a viscous bridge or to rebound. First, if two particles collide, at least one wet position must be involved in the collision to reduce both the glass transition temperature and the viscosity of the material. If no wet droplet is present at the colliding positions, the corresponding glass transition temperatures are equal to the values of the dry solid $T_{gt,s}$, which is always above the temperature in the fluidized bed in the investigated parameter range of this thesis. Consequently, a collision of two dry particles will always result in rebound.

Second, the temperature of the particles needs to be higher than the local sticky point temperature lying 20 K above the glass transition temperature as described above. This condition can be expressed as:

$$T_s \geq T_{gt} + 20\,\mathrm{K}. \tag{3.51}$$

The temperature of the solid material is assumed to be equal to the outlet temperature of the gas, which can be approximated using an energy balance derived for a well-mixed fluidized bed and constant process parameters (spraying rate, gas inlet conditions):

$$T_s = \frac{T_{g,in}\left(c_g + Y_{in}c_v\right) + (Y_{in} - Y)\Delta h_{evap}}{c_g + Y c_v}. \tag{3.52}$$

In this equation, $T_{g,in}$ and Y_{in} represent the temperature and moisture content of the fluidization gas at the inlet. Y is the moisture content of the bulk gas, c_g and c_v are the specific heat capacities of the fluidization gas and vapor, and Δh_{evap} is the specific enthalpy of evaporation of water at 0 °C.

If conditions one and two are met, the Stokes criterion is additionally checked, see Equations (2.4),

(2.5), and (2.8). If this condition is met as well, the colliding particles agglomerate as described in Section 3.2.5, otherwise they rebound and the simulation proceeds without agglomeration in the specific time step.

In order to calculate the viscous Stokes number St_v, the masses and radii of the colliding particles as well as the collision velocity and the viscosity of the layer need to be known. The masses of the colliding particles (single particles or agglomerates) follow from the sum of the masses of the primary particles in each collision partner. The radii can be deduced from the diameters, which are calculated using Equation (3.46). As described in Section 2.2.5, the harmonic mean values of the masses and radii are then used when calculating the viscous Stokes number. The viscosity of the sticky layer is given by Equation (3.50) and depends on the changing water mass fraction of the wet spot. If the particles collide at two wet spots, the highest of the two viscosity values is used to calculate St_v. In order to estimate the collision velocity, an approach presented by Dernedde [132] is used. In this approach, the collision velocity depends on the individual velocities of the colliding particles:

$$u_{coll} = u_{p,1} + u_{p,2}. \tag{3.53}$$

The velocities of the colliding particles are calculated, assuming normally distributed velocities:

$$u_{p,j} = \left|\overline{u}_p + \sigma_{u_p} r_{n,j}\right| \quad \text{with} \quad \sigma_{u_p} = 10\,\overline{u}_p. \tag{3.54}$$

The mean value of the velocity distribution is given by the empirical correlation given in Equation (3.22). Dernedde [132] suggests that the standard deviation of the distribution σ_{u_p} is equal to $10\,\overline{u}_p$ to account for distinct variations of the measured velocities observed in the PIV experiments, which are the basis for Equation (3.22).

In the Monte Carlo model, the collision velocity is calculated based on the mean particle velocity with the above shown equations in each collision event. As a result, the distribution of collision velocity is not a parameter that needs to be set explicitly in the simulation. Instead, it follows from Equation (3.53) and Equation (3.54). However, the distribution of collision velocity can be visualized by calculating a large number of collision velocities and computing a corresponding histogram. The parameters used in the simulation study shown in Chapter 5 lead to a mean particle velocity equal to $0.018\,\mathrm{m\,s^{-1}}$. The collision velocity distribution is then obtained by calculating 10^6 collision velocities (requiring $2 \cdot 10^6$ normally distributed random numbers). It can be characterized by a mean value of $0.29\,\mathrm{m\,s^{-1}}$ and a standard deviation of $0.15\,\mathrm{m\,s^{-1}}$, see Figure 3.20. A study presented by Jiang et al. [152] shows collision velocities measured using particle tracking velocimetry (PTV) in a pseudo-2D fluidized bed. The values vary between $0.1\,\mathrm{m\,s^{-1}}$ and $0.25\,\mathrm{m\,s^{-1}}$ and are in the same range as the collision velocities calculated with the approach used in this thesis.

To calculate the critical Stokes number St_{crit}, the coefficient of restitution, the height of the viscous layer and the height of asperities at the bottom of the wet spot must be known. The height (or depth) of the viscous layer follows from Equation 3.28 and is constant during drying. Both the coefficient of restitution and the height of asperities are model parameters and must be set in the simulation.

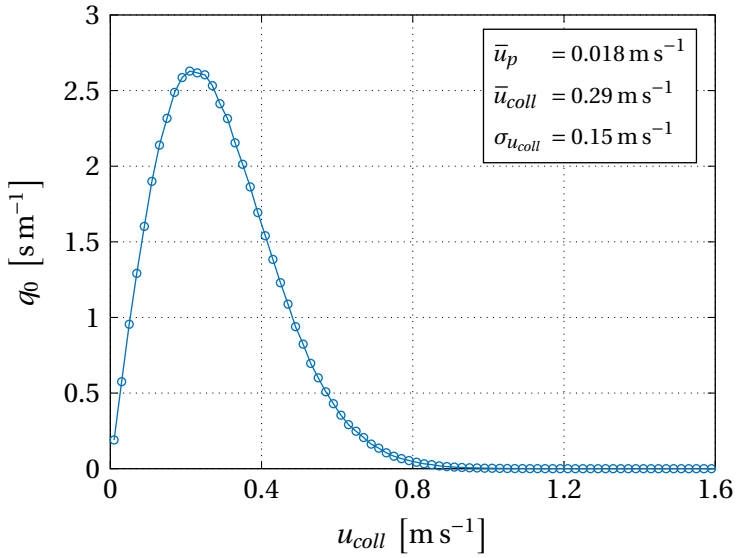

Figure 3.20: Normalized distribution of the collision velocity for the conditions in the simulation study in Chapter 5. The mean and standard deviation characterizing the distribution are 0.29 m s^{-1} and 0.15 m s^{-1}, respectively.

3.2.6 Breakage

Breakage may occur if the kinetic energy of the collision partners cannot be dissipated by a viscous layer. This may occur when either no wet droplet is present at the colliding positions, or the Stokes criterion predicts rebound. In this thesis, breakage is taken into account in terms of breakage of wet and solid bridges. Abrasion or breakage of the primary particles is not considered (cf. Figure 2.4). The used breakage algorithm defines a fixed fraction of unsuccessful collisions leading to a breakage event. The value of this fraction is 0.002 (0.2 %). It is an empirical value, which was obtained by visually fitting simulation results to experimental results for experiment 17, see Chapter 5. The obtained value was then used in each simulation. If a breakage event happens, one randomly picked bridge (wet or dry) in the first collision partner breaks when the selected particle is actually an agglomerate. Otherwise, no breakage will occur. The details of the breakage algorithm and the changes made to the position vector in case of a breakage event are described below.

If a bridge (wet or dry) breaks, the corresponding droplet is assigned to the same particle and position it was deposited on before the collision. The state of the droplet is then checked using Equation (3.23) and the position vector is labeled accordingly. An example is shown in Figure 3.21, where an agglomerate consisting of three primary particles has been selected for breakage. The bridge is randomly chosen based on its number, using a uniformly distributed random number. In this example, depending on the bridge selected for breakage, different particles are formed: if the first bridge breaks, a single particle (former first primary particle) and an agglomerate (former second and third primary particles) are created. The single particle holds two wet spots: one is created by the droplet which used to be the bridge, and another wet spot becomes available due to the blocking of the corresponding sector being revoked. If the second bridge breaks, an agglomerate (former first

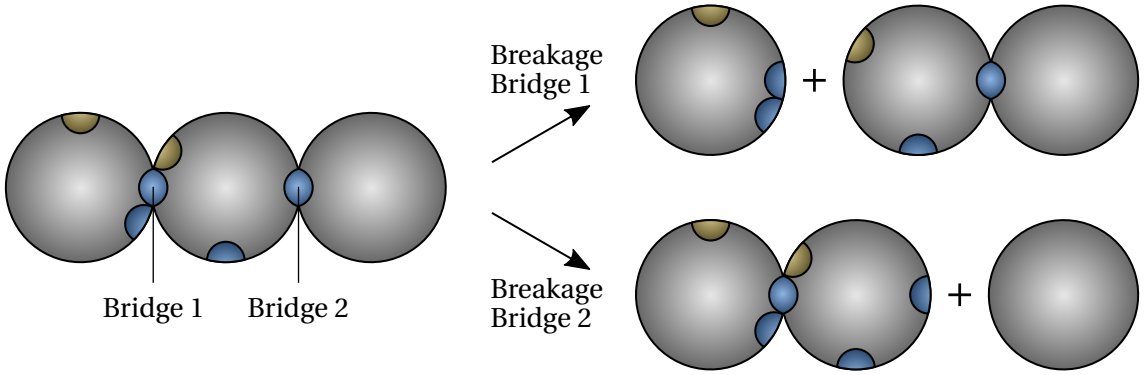

Figure 3.21: Breakage of an agglomerate consisting of three primary particles: one bridge is randomly selected to break. Depending on the selection of the bridge, different particles are created. The information stored in the position vectors (presence and state of droplets and bridges) for each primary particle is preserved and transferred to the newly created particles.

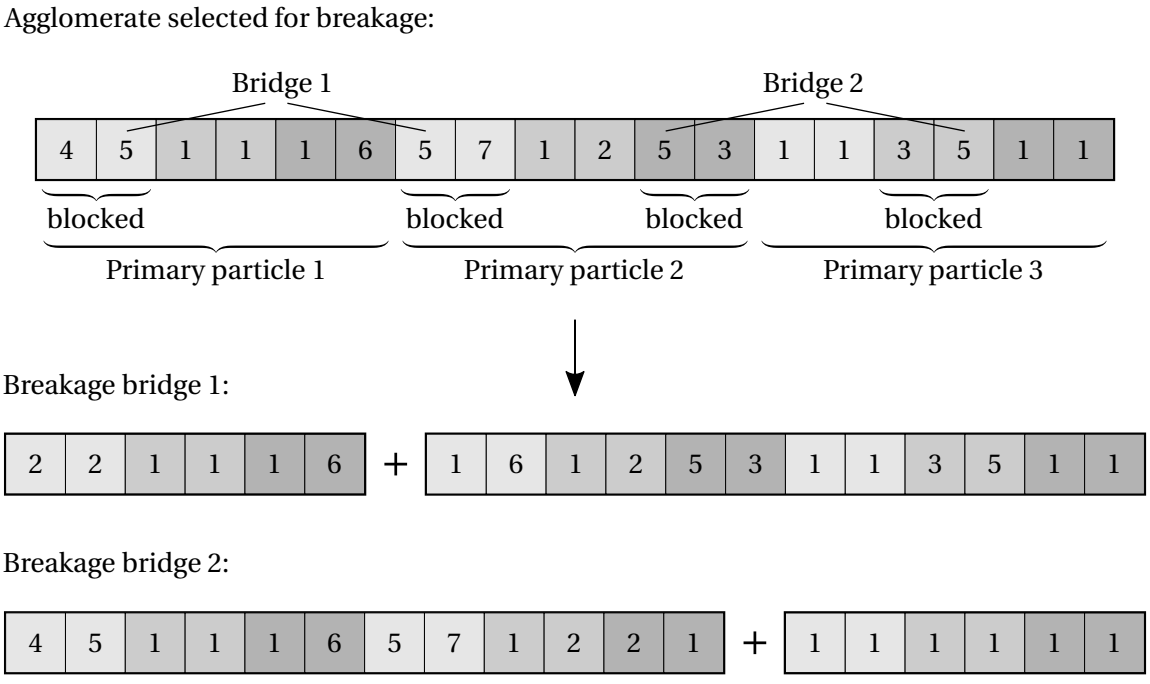

Figure 3.22: Breakage of an agglomerate consisting of three primary particles: detailed illustration of the changes made to the position vectors depending on the bridge selected for breakage. For simplification, only three sectors per primary particle are used in this example.

and second primary particles) and a single particle (former third primary particle) are created as well. In this case, the single particle does not hold any wet spot and must therefore collide with a wetted particle or receive a wet droplet prior to another collision to agglomerate again. Figure 3.22 shows the changes made to the position vectors for the same example as in Figure 3.21. The result of any breakage event is an increase of the number of particles in the simulation box. After breakage, the first newly created particle replaces the former agglomerate and the second particle replaces another randomly selected particle in the sample. In this way, the number of particles is kept constant. Then, the scaling factor is re-calculated using Equation (3.3).

3.3 Summary of model assumptions

The assumptions used in the Monte Carlo models for coating and layering granulation as well as for binder-less agglomeration are summarized below.

Assumptions used in both models:

- well mixed fluidized bed,
- no division into compartments (e.g., spraying and drying zone),
- no overspray,
- sprayed droplets are monodisperse and spherical,
- droplets attain spherical cap geometry instantly after deposition,
- no overlapping or coalescence of deposited droplets,
- spherical particles,
- gas-side controlled drying,
- complete evaporation of sprayed liquid,
- deposition of droplets related to particle surface,
- exponentially distributed time steps.

Assumptions used in Monte Carlo model for coating and layering granulation:

- geometry of added solid layer is assumed to be a spherical shell,
- porosity of dry droplets is equal to the porosity of the complete layer,
- no imbibition of deposited droplets,
- neglecting shrinkage of deposited droplets when calculating the drying time.

Assumptions used in Monte Carlo model for binder-less agglomeration:

- only binary collisions are considered,
- constant collision frequency,
- particle velocity is normally distributed,
- constant agglomerate porosity (independent of agglomerate size),
- maximum coordination number equal to 6 (independent of particle size),
- sticky point temperature 20 K above glass transition temperature,
- particle temperature is equal to gas outlet temperature,
- constant probability of unsuccessful collisions leading to breakage,
- after deposition, instantaneous and full imbibition of droplets,
- droplet drying with constant height and cross section of the wet region and varying water mass fraction.

Chapter 4

Monte Carlo model for coating and layering granulation

This chapter is an extended version of Rieck et al. [145]. Here, the structure of the Monte Carlo model for coating and layering granulation is described. A simulation study is presented, investigating the influence of the droplet deposition mechanism as well as inlet gas temperature, spraying rate, coating layer porosity, solid mass fraction, droplet size, and the contact angle on selected particle properties. Additionally, the presented model is validated by comparing simulation results to analytical models and experimental data.

4.1 Structure of the algorithm

A schematic representation of the micro-processes and events used to model coating and layering granulation is shown in Figure 4.1. In order to model particle growth by layering, only one micro-scale event, the deposition of droplets on the particle surface, needs to be included. Subsequently, the deposited droplets dry and leave a solidified droplet behind. Repeated deposition of droplets and solidification then builds a layer around the initial particles.

The structure of the Monte Carlo algorithm for coating and layering granulation is shown in Figure 4.2. After initializing the variables and scaling of the particle system, which is done only once at the beginning as the sample size is constant over time, the simulation starts by calculating the length of the first time step. The only considered event in this process is droplet deposition, which is executed as described in Section 3.2.1. Then, drying of all deposited droplets is calculated in each time step by updating the droplet states according to Equation (3.23). Subsequently, if droplets have dried in a time step, the layer thickness of the corresponding positions is increased, the position number of the corresponding particle is updated as described in Section 3.2.4, and the coated surface fraction is calculated. The process time in the simulation is compared to a pre-defined value: if this value is reached, the simulation will stop. Otherwise, it will continue for another time step. Since a large number of time steps will be executed in the simulation, the results are stored in total at 50 uniformly distributed points in time during the simulation to reduce the amount of generated data.

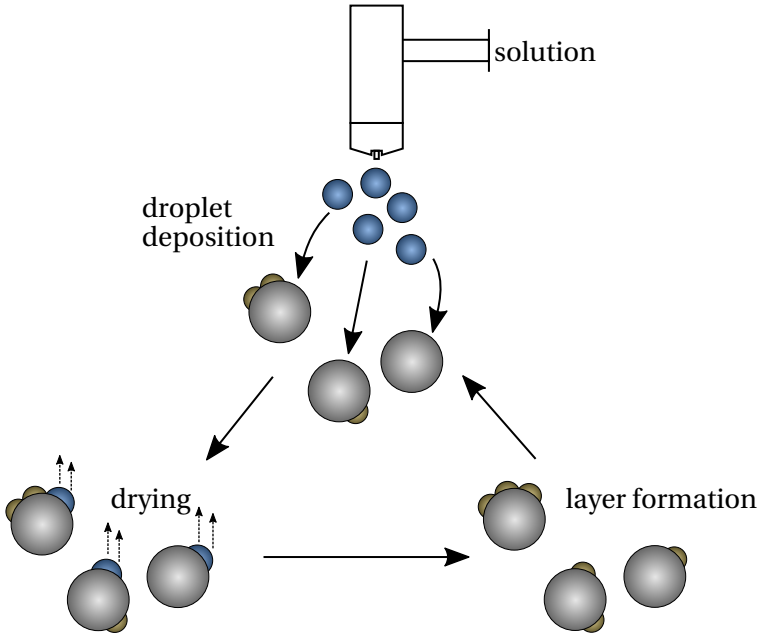

Figure 4.1: Network of the micro-processes and events used to model coating and layering granulation.

4.2 Simulation study

A simulation study is performed to show the influence of process parameters on selected particle properties during a coating process. Firstly, the reference case of the simulation study is used to present the particle properties, which can be extracted from the Monte Carlo simulation, including intra-particle and inter-particle layer thickness distributions, distributions of the particle size, coating mass, and coating time, and the transient behavior of the coated surface fraction. Then, the simulation results of the reference case are compared with analytical models. The simulation parameters correspond to a batch coating process in a lab-scale fluidized bed, in which non-porous glass particles are coated with a sodium benzoate solution, and are given in Table 4.1. The chosen parameters lead to full surface coverage of the particle system. The simulation time is set to 3600 s in the reference case, leading to a sprayed solid mass of 150 g. In the simulations varying the spraying rate and the solid mass fraction of the solution, the simulation time is adjusted to achieve the same mass of sprayed solid material.

4.2.1 Theoretical validation

The results of the reference case simulation (bold parameters in Table 4.1) are shown in Figure 4.3. Figure 4.3a shows intra-particle and inter-particle layer thickness distributions, which can be extracted from the simulation. As described above, intra-particle layer thickness distributions indicate the variation of the layer thickness on a single particle. These distributions can be obtained for each particle considered in the simulation. Since all of them cannot be shown, the intra-particle layer

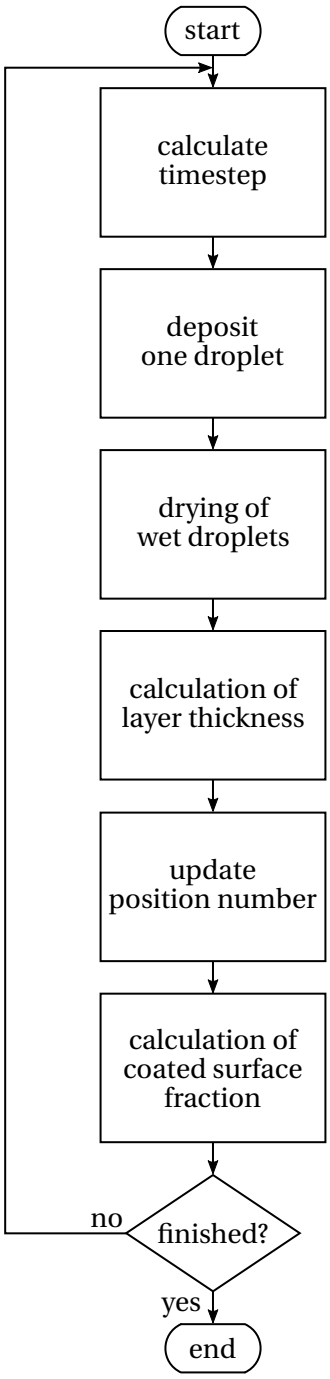

Figure 4.2: Flow chart of the Monte Carlo algorithm for coating and layering granulation.

Table 4.1: Simulation parameters used in the Monte Carlo simulations for coating (simulation study).

Parameter	Value	Unit
Particle material	glass	
Sprayed solid material	NaB	
Sprayed liquid material	water	
Bed diameter d_{bed}	0.15	m
Bed mass M_{bed}	0.5	kg
Mean particle diameter d_{10}	0.6	mm
Standard deviation σ_x	0.06	mm
Particle density ϱ_p	2500	$\mathrm{kg\,m^{-3}}$
Solid density of coating material ϱ_s	1440	$\mathrm{kg\,m^{-3}}$
Spraying rate $\dot{M}_{spray}$	0.25, **0.5**, 0.75	$\mathrm{kg\,h^{-1}}$
Droplet diameter d_{drop}	25, **50**, 75	µm
Contact angle θ	20, **40**, 60	°
Solid mass fraction of the solution w_s	0.2, **0.3**, 0.4	–
Porosity of the coating layer $\varepsilon_{drop,dry}$	0.1, **0.3**, 0.5	–
Inlet temperature of the fluidization gas $T_{g,in}$	50, **70**, 95	°C
Inlet moisture content of the fluidization gas Y_{in}	1	$\mathrm{g\,kg^{-1}}$
Mass flow rate of the fluidization gas $\dot{M}_g$	120	$\mathrm{kg\,h^{-1}}$
Sprayed solid mass $M_{s,sprayed}$	150	g
Number of particles in the MC simulation $N_{p,MC}$	1000	–

thickness distributions of three particles are selected: the particles with the smallest (58.5 µm), average (61.6 µm), and largest (65 µm) mean layer thickness in the simulation. They show that the layer thickness varies approximately between 30 µm and 90 µm on single particles. The inter-particle layer thickness distribution indicates the variation of the mean layer thickness in the population. It can be seen that this distribution is much narrower than the intra-particle layer thickness distributions, indicating that the mean layer thickness hardly varies in the population. This effect directly follows from the assumptions made in the droplet deposition algorithm described in Section 3.2.1: since the fraction of sprayed material a particle receives during the coating process is assumed to depend on its surface area, all particles grow with the same velocity in terms of $\mathrm{mm\,s^{-1}}$. As a result, the differences of the mean layer thicknesses in the population are very small. Figure 4.3b shows the particle size distribution at the beginning ($t = 0$) and at the end of the coating process. As mentioned above, all particles grow with the same velocity, leading to a shift of the particle size distribution towards larger particle sizes, while maintaining the shape of the distribution. The mean particle size increased from 0.60 mm to 0.72 mm. Figure 4.3c depicts the distribution of the coating mass in the population. It shows that the mass of solid material on the particles varies between approximately 40 µg and 140 µg with a mean coating mass of 86.5 µg. Figure 4.3d shows the coating time distribution

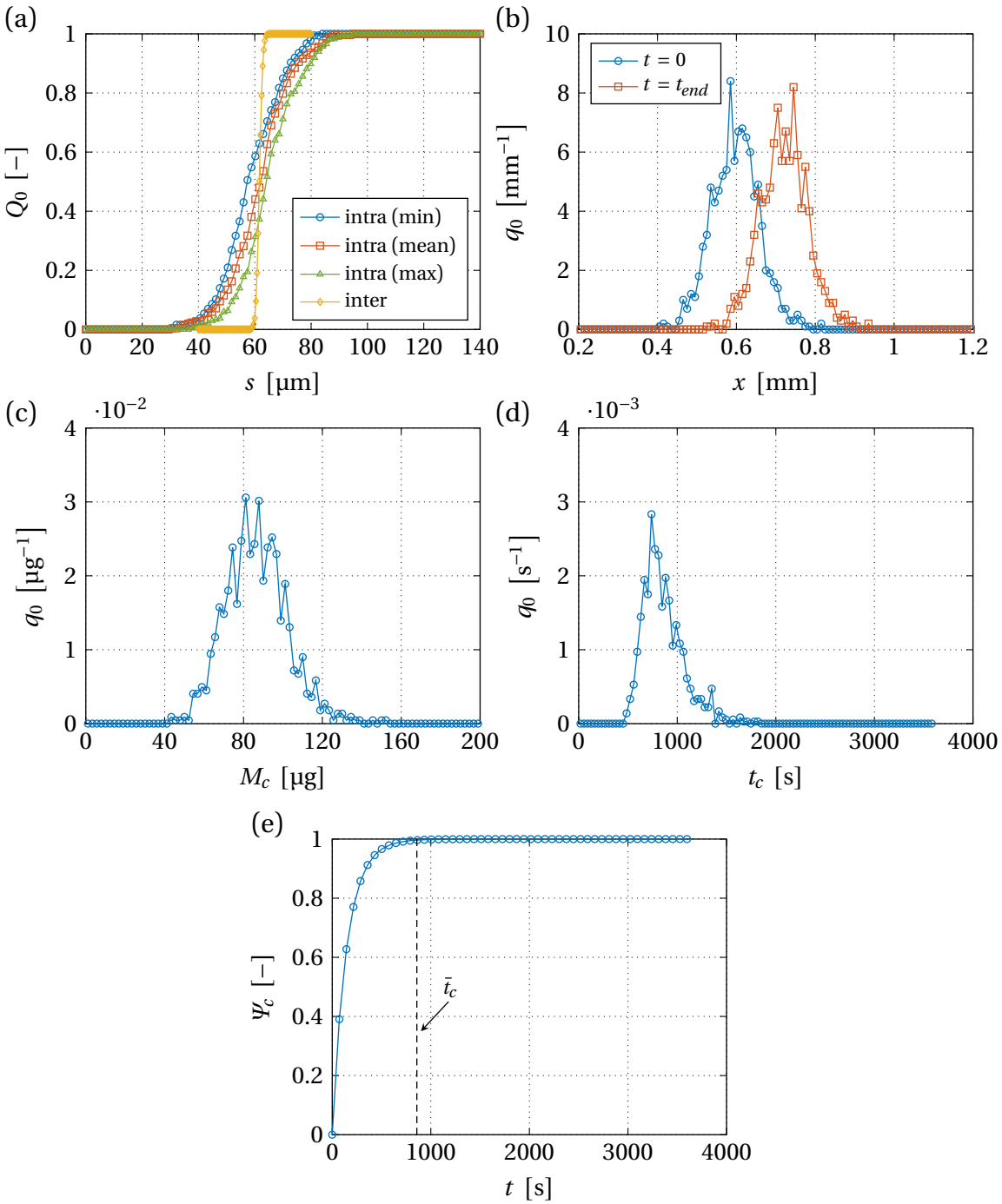

Figure 4.3: Simulation results of the reference case: intra-particle and inter-particle layer thickness distributions (a), particle size distribution before and after the coating process (b), coating mass distribution (c), coating time distribution (d), and transient behavior of the coated surface fraction (averaged over the population) (e).

indicating that the coating times vary between 500 s and 1800 s with a mean value of 858 s. Figure 4.3e shows the transient behavior of the coated surface fraction (averaged over the population) during the coating process. The coated surface fraction at $\bar{t}_c$, which is the mean coating time obtained from the coating time distribution shown in Figure 4.3d, is 0.996. Note that the coated surface fraction at $\bar{t}_c$ does not equal unity since some particles are still not fully coated as indicated by the coating time distribution. The particles are completely coated after 1800 s (i.e., after the last position labeled "1" received a droplet) in this simulation. Below, the results of the Monte Carlo simulations are validated by comparison to analytical models using the example of the reference case.

Assuming a constant particle surface area, the behavior of the coated surface fraction during a coating process can be calculated by a differential equation, which has an analytical solution as presented in detail in Appendix C. Based on the contact area $A_{contact}$, the total surface area of the particles $A_{p,tot}$, and the number flow rate of droplets $\dot{N}_{drop}$, the coated surface fraction can be calculated using:

$$\Psi_c = 1 - \exp\left(-\frac{A_{contact}}{A_{p,tot}}\dot{N}_{drop}t\right). \tag{4.1}$$

Figure 4.4 shows the transient behavior of the coated surface fraction from Equation (4.1) and two Monte Carlo simulations performed with parameters corresponding to the reference case. The first simulation (labeled MC) is performed with the algorithm described above and the second simulation (labeled MC (no position update)) is performed without the update of the number of positions during the coating process, which corresponds to the assumption of a constant particle surface area used in the analytical model. Figure 4.4a shows the evolution of the coated surface fraction during the complete simulation time and Figure 4.4b shows an enlarged version of the same plot. The results from the analytical model and the Monte Carlo simulation without the position update agree well. The coated surface fraction from the Monte Carlo simulation including the position update is slightly smaller. This is a result of a reduced probability of a single position to be hit by a droplet since more positions are available in this case. However, the influence of the position update on the coated surface fraction is small.

Additionally, theoretical work on the intra-particle layer thickness distribution has been presented by Freireich and Wassgren [157]. Their model does not calculate the distribution, but yields the corresponding coefficient of variation $C_{V,intra}$. In general, the coefficient of variation is defined as the ratio between the standard deviation and the mean value of a distribution. According to Freireich and Wassgren [157], the coefficient of variation of the intra-particle layer thickness distribution of a uniformly coated single particle can be calculated based on the number of droplets deposited on a particle N_{drop}, the number of positions N_{pos}, and number of positions wetted when the particle is exposed to the spray N'_{pos}:

$$C_{V,intra} = \frac{\sigma_{s,intra}}{\bar{s}_{intra}} = \sqrt{\frac{1}{N_{drop}}\left(\frac{N_{pos}}{N'_{pos}} + \left(N_{drop} - 1\right)\right) - 1}. \tag{4.2}$$

Due to the design of the presented Monte Carlo model, N'_{pos} equals unity. Equation (4.2) was derived,

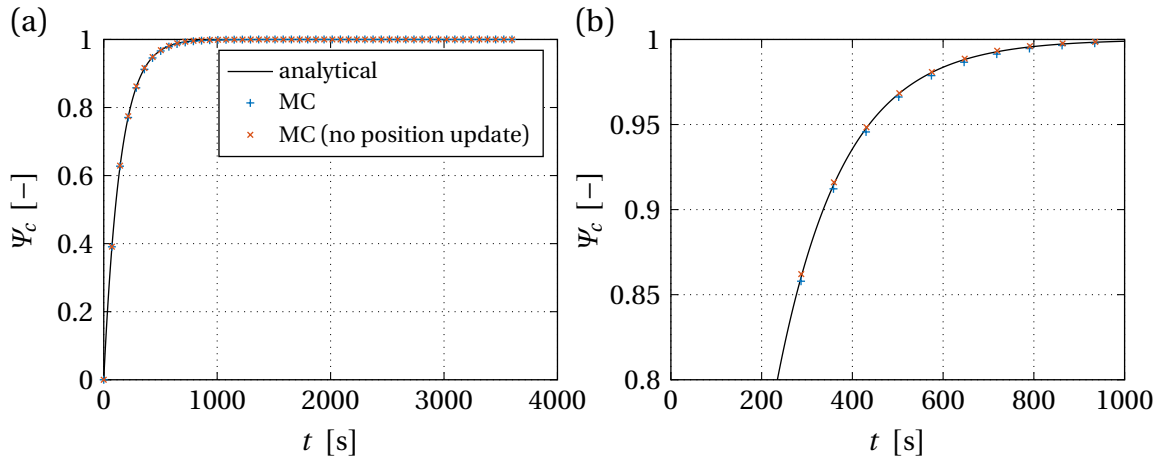

Figure 4.4: Transient behavior of the coated surface fraction obtained from an analytical model (Equation (4.1)) and two Monte Carlo simulations (with and without position update) during the complete coating process (a) and during the first 1000 s (enlarged) (b).

assuming a constant particle surface area and neglecting the radius of curvature of the core particles when calculating the height of solidified droplets. Figure 4.5 shows the transient behavior of the coefficient of variation obtained from Equation (4.2) and two Monte Carlo simulations with parameters corresponding to the reference case. The first simulation (labeled MC) is performed with the algorithm described above, whereas the second simulation includes the assumptions of the analytical model: constant surface area of the particles (no position update), and neglecting the radius of curvature when calculating the height of a solidified droplet (cf. Equation (3.36)). In the simulation, $C_{V,intra}$ is calculated for each single particle from the corresponding layer thickness distribution and then averaged over the population. Similarly, the analytical model is applied to each particle from the Monte Carlo simulation individually and the result is then averaged over the population as well. The number of droplets deposited on each particle required in Equation (4.2) is obtained from the Monte Carlo simulation. Figure 4.5 shows that results obtained from the analytical model and the Monte Carlo simulation including the assumptions agree well. The intra-particle coefficient of variation from the first Monte Carlo simulation (without assumptions) agrees well with the analytical model in the beginning of the coating process when the layer thickness is small. However, the difference increases as the process continues and the coefficient of variation is slightly smaller than the values predicted by the analytical model. These deviations are due to the simplifications made in deriving the analytical model.

Kalbag and Wassgren [165] presented theoretical work on the coefficient of variation of the inter-particle coating mass distribution $C_{V,inter}$. The coefficient of variation can be calculated based on the total number of droplets deposited on all particles $N_{drop,tot}$ and the number of particles coated per coating trial N_p':

$$C_{V,inter} = \frac{\sigma_{M_c}}{\overline{M}_c} = \sqrt{\frac{1}{N_{drop,tot}} \left(\frac{N_{p,MC}}{N_p'} - 1 \right)}. \tag{4.3}$$

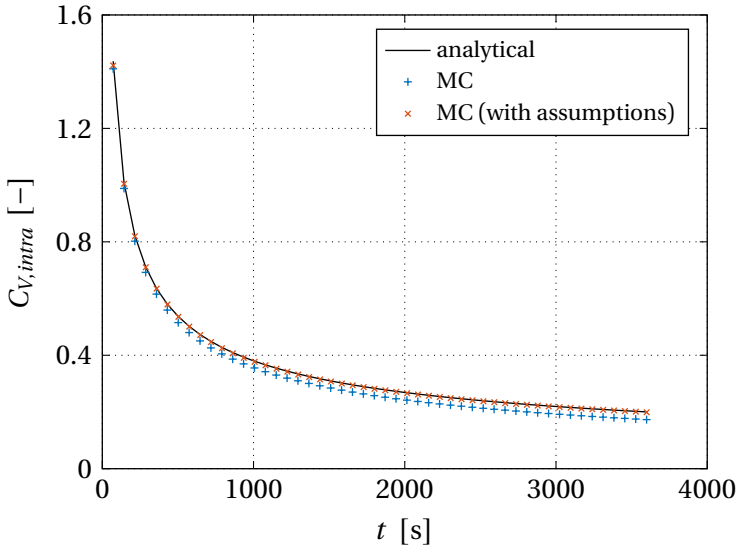

Figure 4.5: Transient behavior of the coefficient of variation of the intra-particle layer thickness distribution obtained from an analytical model (Equation (4.2)) and two Monte Carlo simulations (with and without assumptions of the analytical model).

In the context of the presented Monte Carlo model, a coating trial corresponds to the deposition of a single droplet and the number of particles coated per trial equals unity. The total number of droplets deposited on all particles $N_{drop,tot}$ is directly taken from the Monte Carlo simulation. Figure 4.6a shows the transient behavior of the inter-particle coefficient of variation calculated from Equation (4.3) and from the coating mass distributions obtained from two Monte Carlo simulations. The first simulation (labeled MC) corresponds to the reference case, in which droplets are deposited according to the particle surface area. The second simulation was performed with the same simulation parameters, but with $\Lambda_0 = 1$ in the droplet deposition algorithm described in Section 3.2.1 (i.e., each particle has the same probability to receive droplets). Figure 4.6a shows that the values of $C_{V,inter}$ obtained from the first Monte Carlo simulation are larger than the values calculated with Equation (4.3). In the derivation of the model shown in Equation (4.3), no influence of particle properties on droplet deposition was taken into account. This means each particle has the same probability to be hit by a droplet, which corresponds to $\Lambda_0 = 1$. Consequently, the transient behavior of the inter-particle coefficient of variation obtained in the second simulation matches with the analytical model. The corresponding coating mass distributions are shown in Figure 4.6b. Since in case of $\Lambda_0 = 1$ each particle has the same probability to receive droplets, the coating mass per particle is almost identical (cf. Figure 3.13a) and the coating mass distribution is very narrow. Therefore, the values of $C_{V,inter}$ are small. As mentioned above, the simulation of the reference case was performed with $\Lambda_2 = 1$, which leads to a very narrow distribution of the mean layer thickness in the population (cf. Figure 4.3a). At the same time, this leads to a significant variation of the coating mass in the population (cf. Figure 3.13c) as shown in Figure 4.6b and the corresponding values of $C_{V,inter}$ are larger.

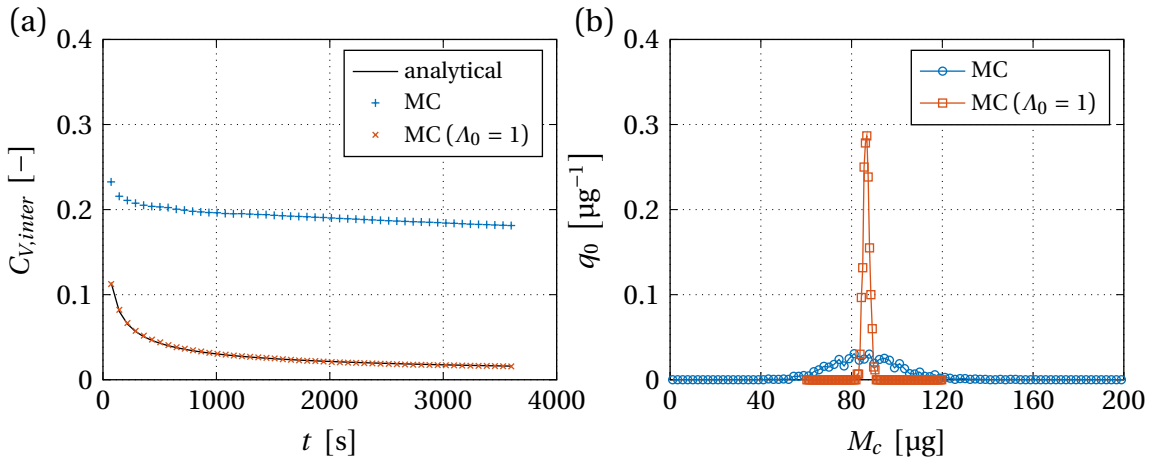

Figure 4.6: Transient behavior of the coefficient of variation of the inter-particle coating mass distribution obtained from an analytical model (Equation (4.3)) and two Monte Carlo simulations (with and without assumptions of the analytical model) (a) and the coating mass distribution at the end of the simulation obtained in the Monte Carlo simulations (b).

4.2.2 Influence of droplet deposition

The influence of the droplet deposition mechanism on selected particle properties is investigated. The simulation parameters correspond to the reference case and the selection property in the droplet deposition algorithm is varied similar to Figure 3.13 in Section 3.2.1: four simulations are performed in which Λ_0 to Λ_3 in Equation (3.17) are sequentially set to unity. The results are shown in Figure 4.7.

Figure 4.7a shows intra-particle layer thickness distributions for each simulation. In contrast to Figure 4.3a, only the layer thickness distribution of the particle with the average mean layer thickness is shown here. The standard deviations of these distributions are similar, while the mean layer thicknesses are slightly decreasing from $\Lambda_0 = 1$ to $\Lambda_3 = 1$. This effect arises since the radius of curvature is taken into account when calculating the layer thickness of a solidified droplet, see Section 3.2.4. First, small particles receive more droplets in case of $\Lambda_0 = 1$ compared to the other cases and second, the calculated layer thickness increases for smaller particles. As a result, the layer thickness distributions are shifted towards smaller thicknesses (from $\Lambda_0 = 1$ to $\Lambda_3 = 1$). However, this influence is relatively small. The inter-particle layer thickness distributions show more distinct differences when varying the selection property in the droplet deposition algorithm, see Figure 4.7b. The shape of these distributions indicates that the standard deviation changes. The smallest standard deviation can be found in case of $\Lambda_2 = 1$, which is the standard case in the simulations presented in this thesis. The largest standard deviation is obtained for $\Lambda_0 = 1$. Consequently, the mean layer thickness is almost the same for each particle in the population in case of $\Lambda_2 = 1$, while in the other cases the mean layer thickness varies to a greater extent within the population. This behavior can also be observed in the particle size distributions shown in Figure 4.7c. Since the mean layer thickness is almost identical for each particle in case of $\Lambda_2 = 1$, the shape of the particle size distribution is preserved during the coating process. For $\Lambda_0 = 1$ and $\Lambda_1 = 1$, the shape of the particle size distributions is not preserved as they become narrower during the coating process. In these cases,

small particles receive more droplets and large particles receive less droplets, compared to the case of $\Lambda_2 = 1$ as shown in Figure 3.13. As a result, smaller particles grow faster and the shape of the particle size distribution changes. If $\Lambda_3 = 1$, the particle size distribution becomes broader. Larger particles are preferred by the droplet deposition algorithm compared to the case of $\Lambda_2 = 1$, leading to faster growth of these particles and a changing shape of the distribution. The mean particle diameter is shown in Figure 4.7d. In the beginning of the simulation the values are very similar, while during the process a small, but growing difference between the values can be observed. The largest mean particle diameter at the end of the process can be found in case of $\Lambda_0 = 1$ and the smallest one for $\Lambda_3 = 1$. This directly follows from the effect of the particle size on the calculated layer thickness shown in Figure 4.7a. Figure 4.7e shows the standard deviation of the particle size distribution confirming the above discussed effects: the standard deviation stays constant for $\Lambda_2 = 1$, decreases for $\Lambda_0 = 1$ and $\Lambda_1 = 1$, and increases if $\Lambda_3 = 1$.

4.2.3 Influence of process and material parameters

The influence of process and material parameters (inlet gas temperature, spraying rate, coating layer porosity, solid mass fraction of the sprayed liquid, droplet size, and contact angle) on particle properties is presented. The used simulation parameters are given in Table 4.1. The selected particle properties are two different intra-particle layer thickness distributions as well as the distribution of the coating time. The first layer thickness distribution belongs to the particle with the average mean layer thickness at the end of the coating process. The second distribution indicates the variation of the layer thickness on single particles at the time of reaching full coverage, which is of interest when a thin, complete layer is desired. This property is obtained by storing the layer thickness distribution for each particle once its coated surface fraction reaches unity. Since this distribution is available for each particle in the simulation, only one of them is shown in this simulation study. Similar to the first layer thickness distribution, the distribution which belongs to the particle with the average mean layer thickness (at the time of reaching full coverage) is selected. The influence of process and material parameters on the selected properties is discussed using further parameters: the number flow rate of droplets (cf. Equation (3.15)), volume of a dry droplet (cf. Equation (3.41)), number of positions (cf. Equation (3.14)), layer thickness generated by a dry droplet (cf. Equation (3.39)), and the drying time (cf. Equation (3.24)).

It was pointed out in Section 2.2.4 that the porosity of coating layers may depend on drying conditions, influenced by inlet gas temperature and the spraying rate. The influence of these parameters on the coating layer porosity is not considered in the presented simulation study. Instead, the influence of each parameter is investigated separately. The results are shown in Figure 4.8 to Figure 4.13 and summarized in Table 4.2.

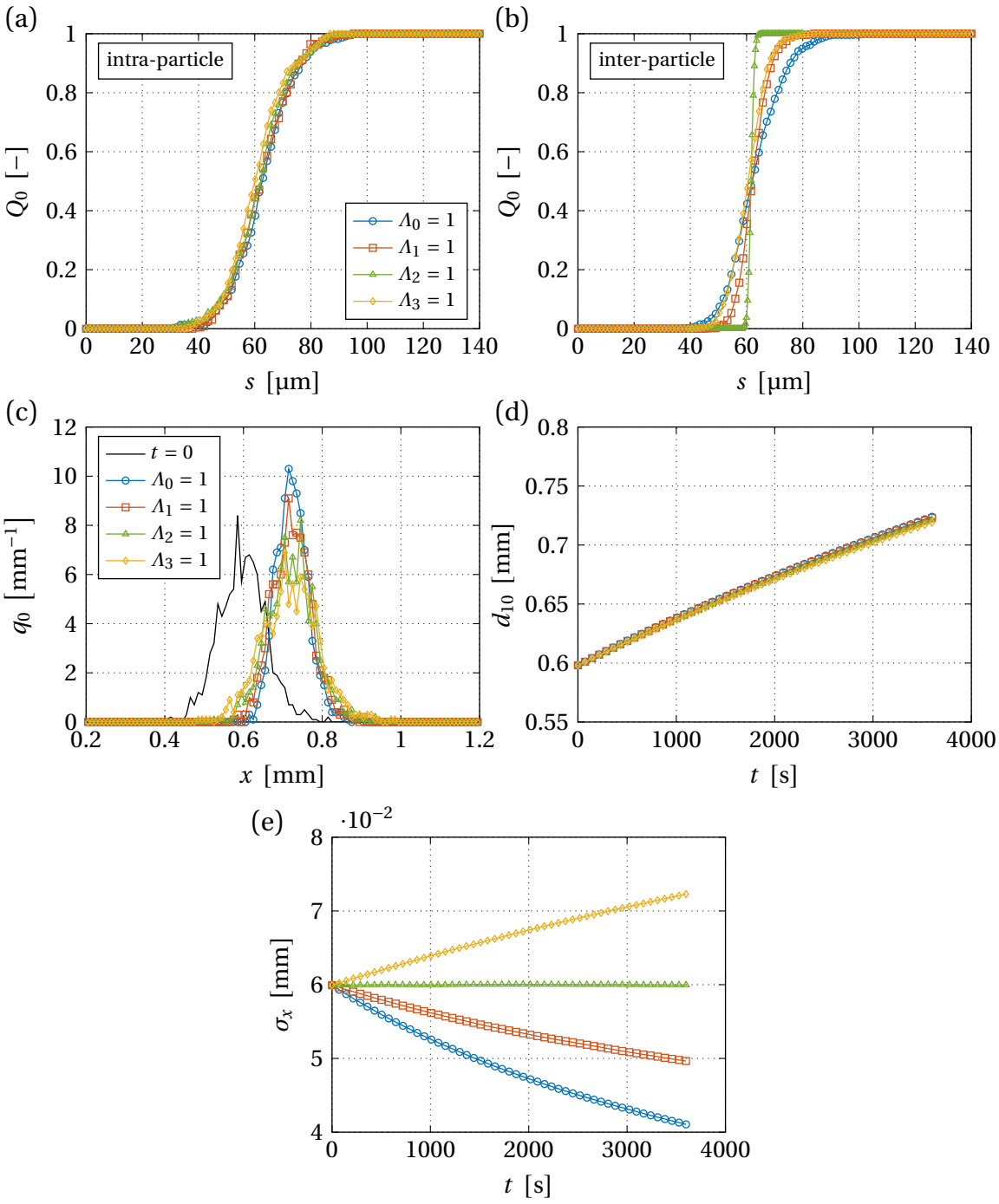

Figure 4.7: Influence of the droplet deposition mechanism on the intra-particle layer thickness distribution (particle with average mean layer thickness) (a), the inter-particle layer thickness distribution (b), the particle size distribution (c), the transient behavior of the mean particle diameter (d), and the standard deviation of the particle size distribution (e).

Influence of inlet gas temperature

An increasing inlet gas temperature does not influence the number flow rate of droplets, dry droplet volume, number of positions, and the layer thickness generated by a single dry droplet, while only the drying time of droplets is decreased. This eventually leads to more dry droplets, which can contribute to the solid layer. However, no significant influence on either intra-particle layer thickness distribution can be seen in Figure 4.8a (at the end of the coating process) or in Figure 4.8b (at the time of reaching full coverage). Correspondingly, the mean values and standard deviations of both distributions shown in Figure 4.8c are constant. No influence of the inlet gas temperature on the distribution of the coating time, see Figure 4.8d, can be observed either.

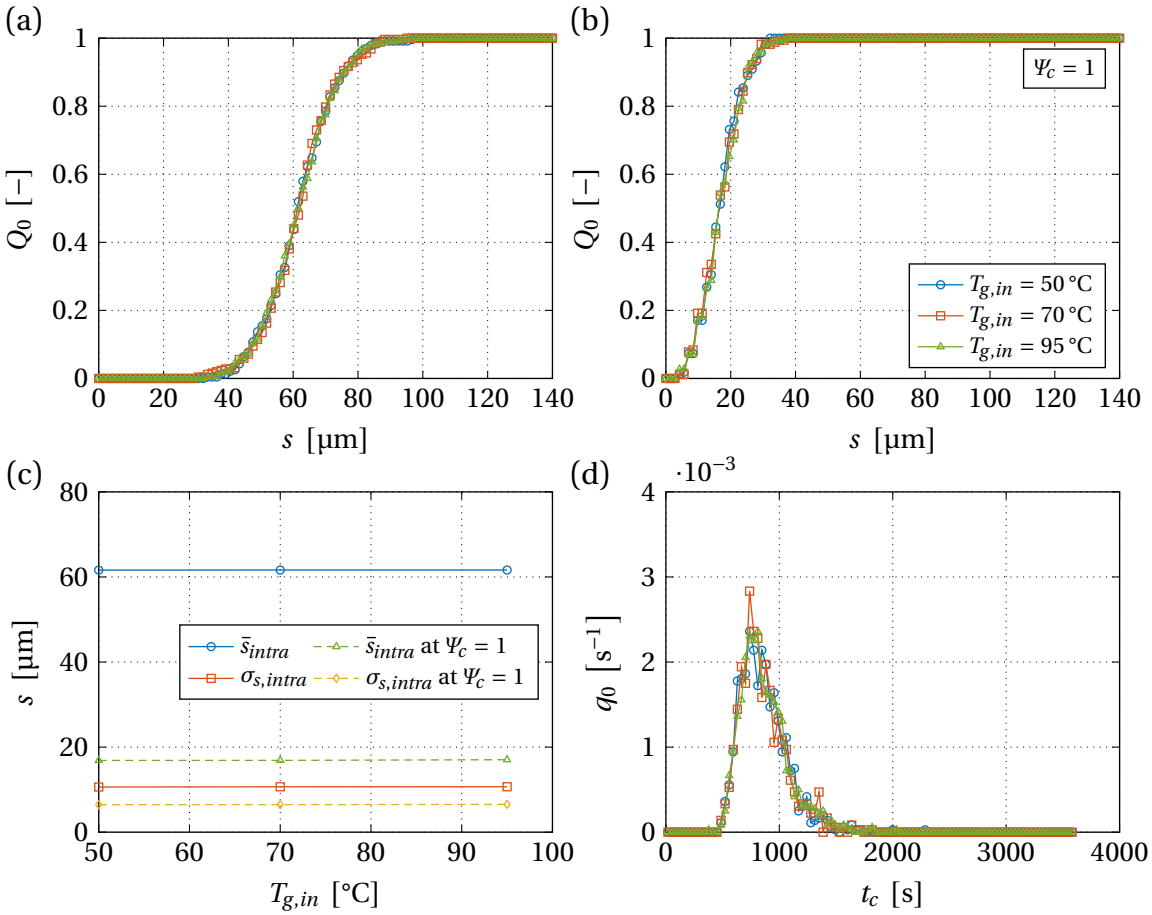

Figure 4.8: Influence of the inlet gas temperature on the intra-particle layer thickness distribution at the end of the coating process (a), and at the time of reaching full coverage (b), the mean values and standard deviations of both layer thickness distributions (c), and the coating time distribution (d).

Influence of spraying rate

An increasing spraying rate leads to a larger number flow rate of droplets, while the dry droplet volume, number of positions, and the layer thickness of a dry droplet are not changed. The drying time of droplets is increased due to a larger moisture content of the gas. Figure 4.9a to Figure 4.9c show that the spraying rate does not influence the intra-particle layer thickness distribution at the end of the coating process and at the time of reaching full coverage. Note that the process times in the simulation are adjusted to achieve the same sprayed solid mass in each simulation, which leads to constant layer thickness distributions. Figure 4.9d indicates that an increasing spraying rate strongly reduces the coating time due to the increased number flow rate of droplets.

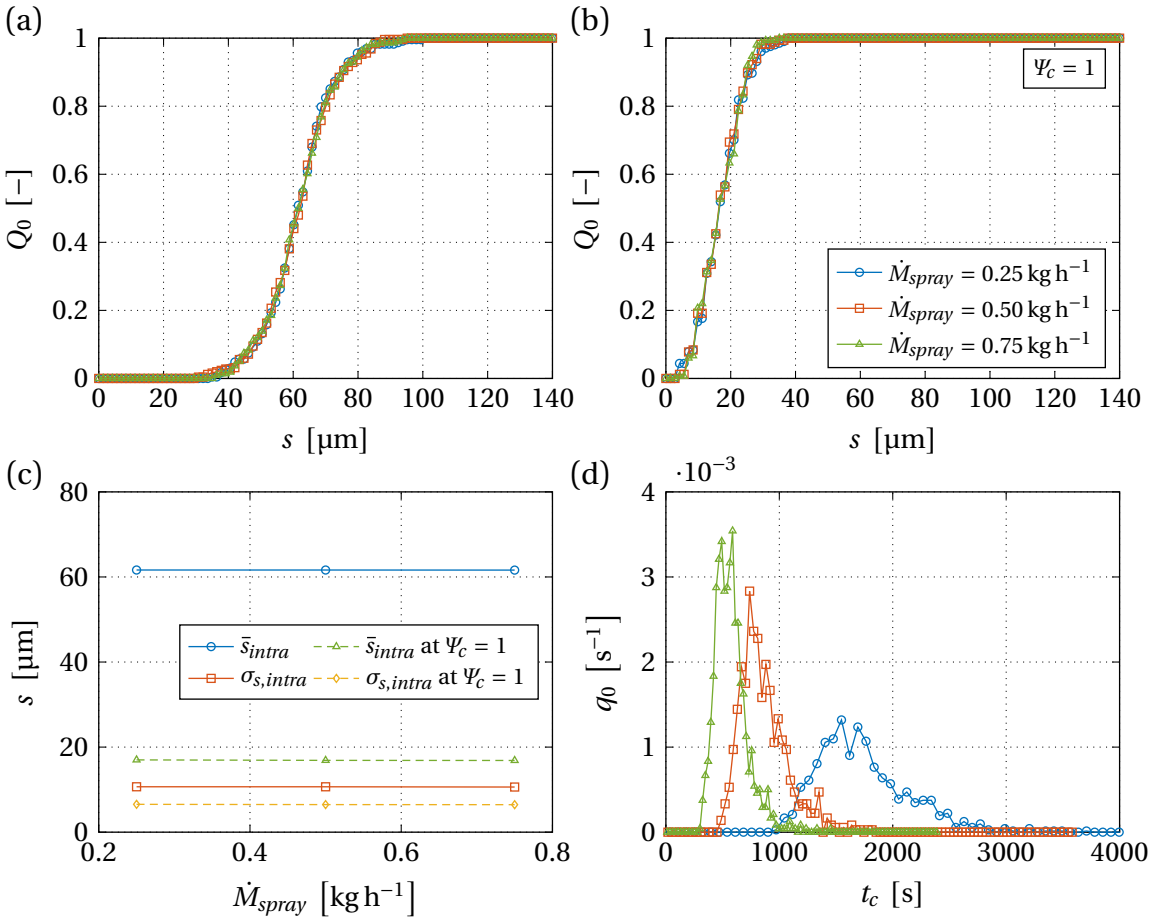

Figure 4.9: Influence of the spraying rate on the intra-particle layer thickness distribution at the end of the coating process (a), and at the time of reaching full coverage (b), the mean values and standard deviations of both layer thickness distributions (c), and the coating time distribution (d).

Influence of coating layer porosity

A larger coating layer porosity does not change the number flow rate of droplets, number of positions, or the drying time, but increases the solid volume of a dry droplet, which leads to an increased layer thickness generated by a single dry droplet. As a result, the intra-particle layer thickness distributions at the end of the coating process and at the time of reaching full coverage are shifted towards larger values, see Figure 4.10a and Figure 4.10b. Simultaneously, an increased layer thickness generated by a single droplet increases the standard deviation of both distributions, see Figure 4.10c. Figure 4.10d shows that the coating time distribution is not influenced by the coating layer porosity.

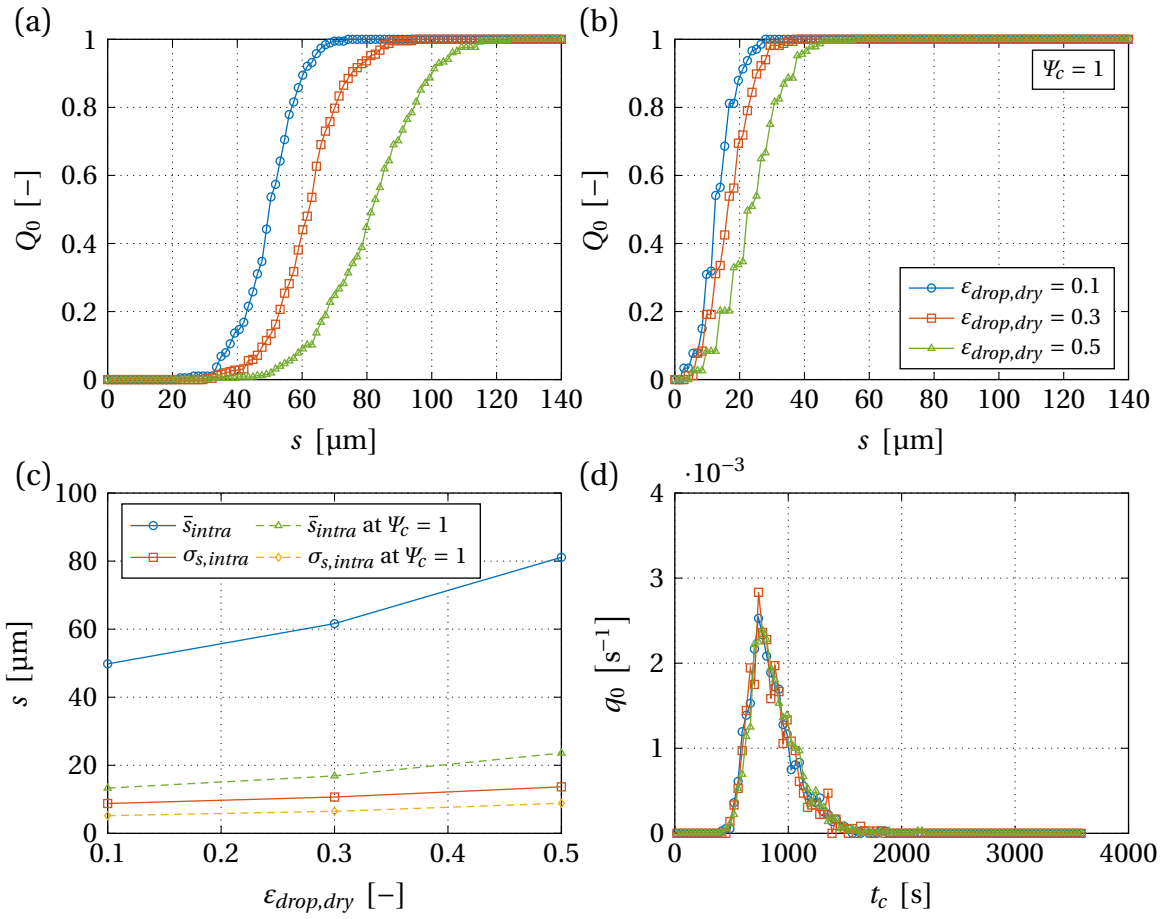

Figure 4.10: Influence of the coating layer porosity on the intra-particle layer thickness distribution at the end of the coating process (a), and at the time of reaching full coverage (b), the mean values and standard deviations of both layer thickness distributions (c), and the coating time distribution (d).

Influence of solid mass fraction

An increased solid mass fraction leads to a smaller number flow rate of droplets since the droplet density is higher (cf. Equation (A.17)), while the spraying rate stays constant. The volume and layer thickness of a dry droplet increase and the drying time is smaller since the droplets contain less water. Figure 4.11a shows the influence of an increased solid mass fraction on the intra-particle layer thickness distribution at the end of the coating process. The mean layer thickness stays constant, while the standard deviation increases, see also Figure 4.11c. Due to the changing number flow rate of the droplets, the process time in the simulation is adjusted resulting in the same sprayed solid mass and a constant mean layer thickness. The standard deviation increases due to the larger layer thickness of a dry droplet. Figure 4.11b shows the intra-particle layer thickness distribution at the time of reaching full coverage. In this case, the mean and standard deviation increase when the solid mass fraction is higher, which is due to the larger layer thickness of a dry droplet. The reduced number flow rate of droplets leads to slightly larger coating times, see Figure 4.11d. However, this influence is small in the investigated range.

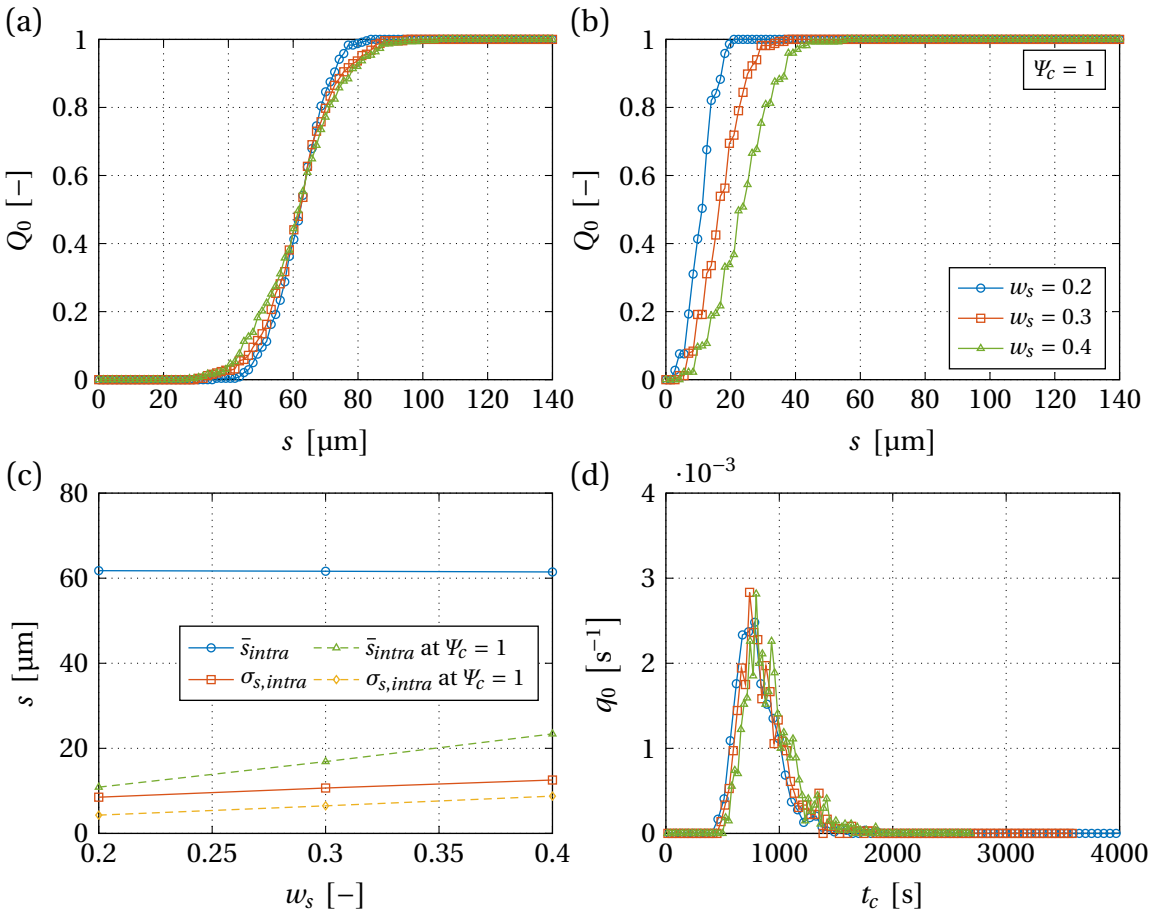

Figure 4.11: Influence of the solid mass fraction on the intra-particle layer thickness distribution at the end of the coating process (a), and at the time of reaching full coverage (b), the mean values and standard deviations of both layer thickness distributions (c), and the coating time distribution (d).

Influence of droplet size

An increasing droplet size leads to a smaller number flow rate of droplets and an increased volume and layer thickness of dry droplets. The number of positions decreases due to a larger contact area and the drying time increases due to the larger droplet volume. The influence of the droplet size on the intra-particle layer thickness distribution at the end of the coating process is shown in Figure 4.12a. The mean layer thickness stays constant since the same amount of solid material is sprayed (larger dry droplet volume, but smaller number flow rate), while the standard deviation increases due to the larger layer thickness generated by dry droplets, see also Figure 4.12c. Figure 4.12b shows the intra-particle layer thickness distribution at the time of reaching full coverage. Due to the larger layer thickness of dry droplets, the mean and standard deviation are both increased. The coating time is influenced by two factors: the reduced number of positions leads to shorter coating times, while the smaller number flow rate would increase it. Eventually, the influence of the number flow rate dominates since $\dot{N}_{drop} \sim d_{drop}^3$ and $A_{contact} \sim d_{drop}^2$ and the coating time is increased when larger droplets are sprayed, see Figure 4.12d.

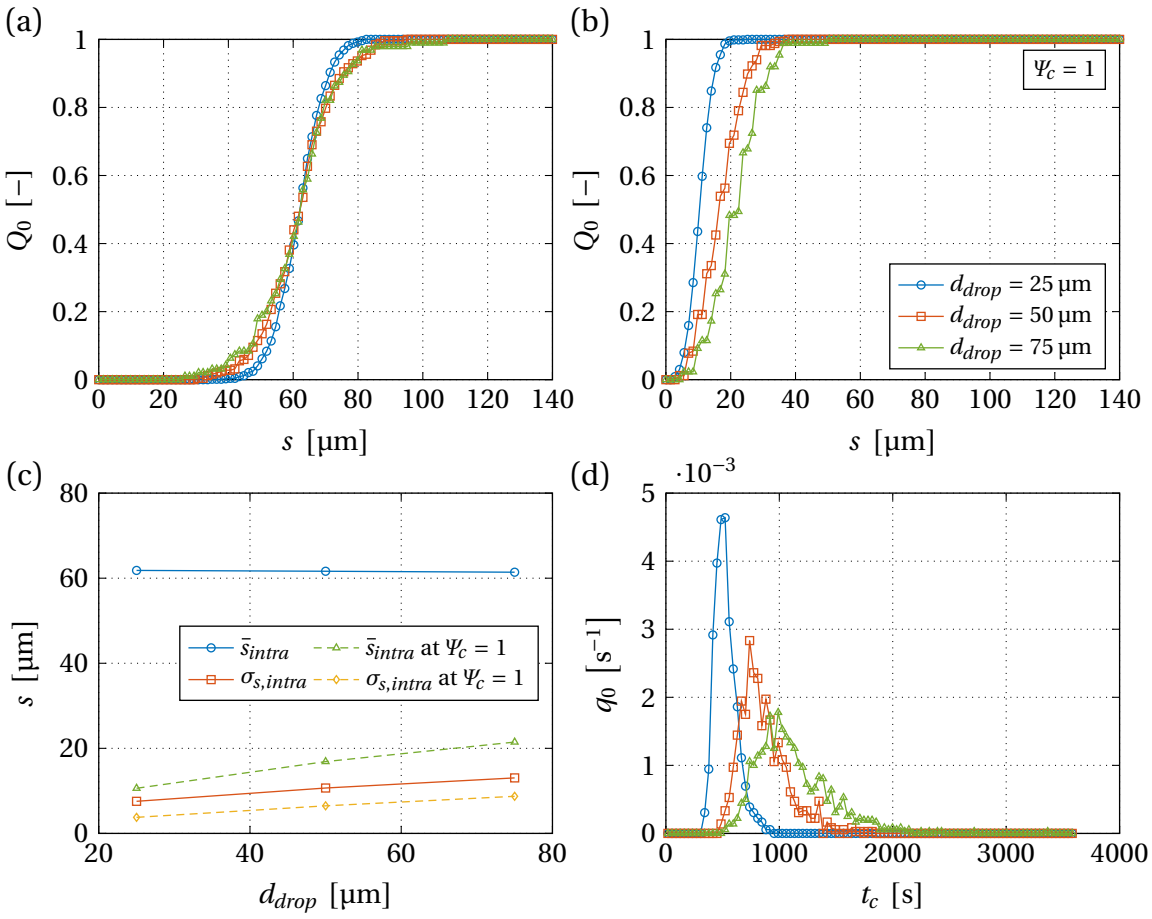

Figure 4.12: Influence of the droplet size on the intra-particle layer thickness distribution at the end of the coating process (a), and at the time of reaching full coverage (b), the mean values and standard deviations of both layer thickness distributions (c), and the coating time distribution (d).

Influence of contact angle

A larger contact angle does not influence the number flow rate of droplets and the dry droplet volume, but leads to an increasing number of positions due to a smaller footprint of deposited droplets. As a result, a larger layer thickness of a single dry droplet is predicted by the model, see Equation (3.40). The drying time is increased since the curved surface area of the droplet is smaller. Figure 4.13a shows the influence of the contact angle on the intra-particle layer thickness distribution at the end of the coating process. When the contact angle increases, the mean value stays constant. Although the layer thickness of a single droplet is larger, less droplets are stacked over each other due to a higher number of positions and the mean layer thickness stays constant. The standard deviation increases due to a larger layer thickness of a single droplet. Figure 4.13b shows that an increasing contact angle increases both the mean value and the standard deviation of the intra-particle layer thickness distribution at the time of reaching full coverage, which is the result of the increased layer thickness of a single droplet. The coating time increases since the number of positions is larger while the number flow rate of droplets is constant, see Figure 4.13d.

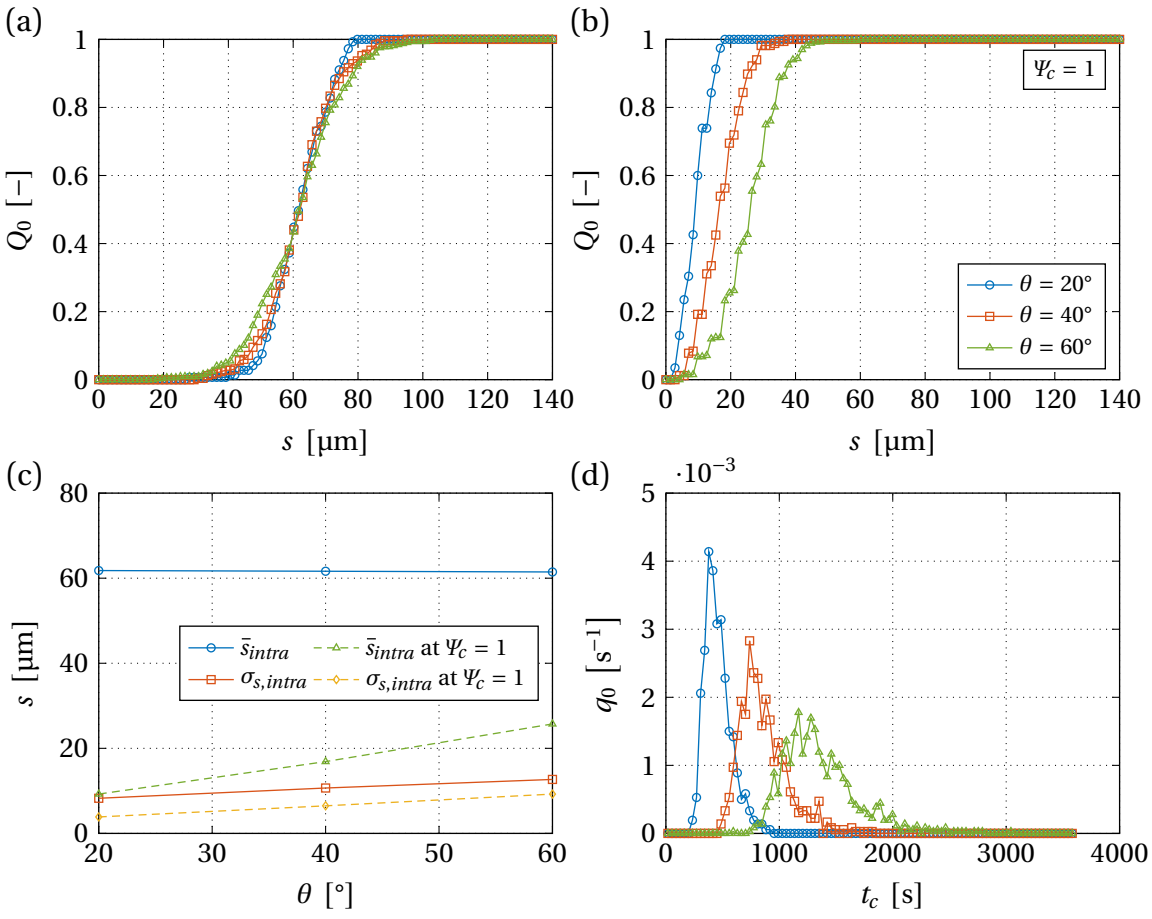

Figure 4.13: Influence of the contact angle on the intra-particle layer thickness distribution at the end of the coating process (a), and at the time of reaching full coverage (b), the mean values and standard deviations of both layer thickness distributions (c), and the coating time distribution (d).

Table 4.2: Influence of process conditions and material parameters on the single particle layer thickness distribution (at the end of the coating process and when reaching full coverage) as well as the mean coating time.

Parameter	$T_{g,in} \uparrow$	$\dot{M}_{spray} \uparrow$	$\varepsilon_{drop,dry} \uparrow$	$w_s \uparrow$	$d_{drop} \uparrow$	$\theta \uparrow$
$\dot{N}_{drop}$	–	↑	–	↓	↓	–
$V_{drop,dry}$	–	–	↑	↑	↑	–
N_{pos}	–	–	–	–	↓	↑
$s_{drop,dry}$	–	–	↑	↑	↑	↑
Δt_{dry}	↓	↑	–	↓	↑	↑
$\bar{s}_{intra}$	–	–	↑	–	–	–
$\sigma_{s,intra}$	–	–	↑	↑	↑	↑
$\bar{s}_{intra}$ at $\Psi_c = 1$	–	–	↑	↑	↑	↑
$\sigma_{s,intra}$ at $\Psi_c = 1$	–	–	↑	↑	↑	↑
$\bar{t}_c$	–	↓	–	↑	↑	↑

Table 4.2 summarizes the influence of the process conditions and material parameters on both layer thickness distributions and the coating time. The mean value of the intra-particle layer thickness distribution at the end of the coating process only increases when the porosity of a dry droplet becomes larger due to an increased layer thickness of dry droplets. Although this value is also larger in case of an increased solid mass fraction, droplet size, and contact angle, the mean layer thickness stays constant in these cases as explained above. The standard deviation of the intra-particle layer thickness distribution at the end of the coating process is always increased when the layer thickness of dry droplets is larger. The same observation can be made in case of the mean and standard deviation of the intra-particle layer thickness distribution at the time of reaching full coverage. The coating time is mainly governed by the number flow rate of droplets in case of varying spraying rate, solid mass fraction, or droplet size. However, the number of positions (influenced by the footprint of deposited droplets) also has an influence when the contact angle is varied.

4.3 Comparison to experimental data

4.3.1 Experimental setup

In this section, several lab-scale fluidized bed coating experiments are used to validate the Monte Carlo model for coating and layering granulation. In total six experiments with varying material properties and process parameters are used. Experiment 1 and 2 have been published by Rieck et al. [57] and the remaining experiments are taken from Sondej et al. [166]. The details of the experiments are described below, before presenting the results.

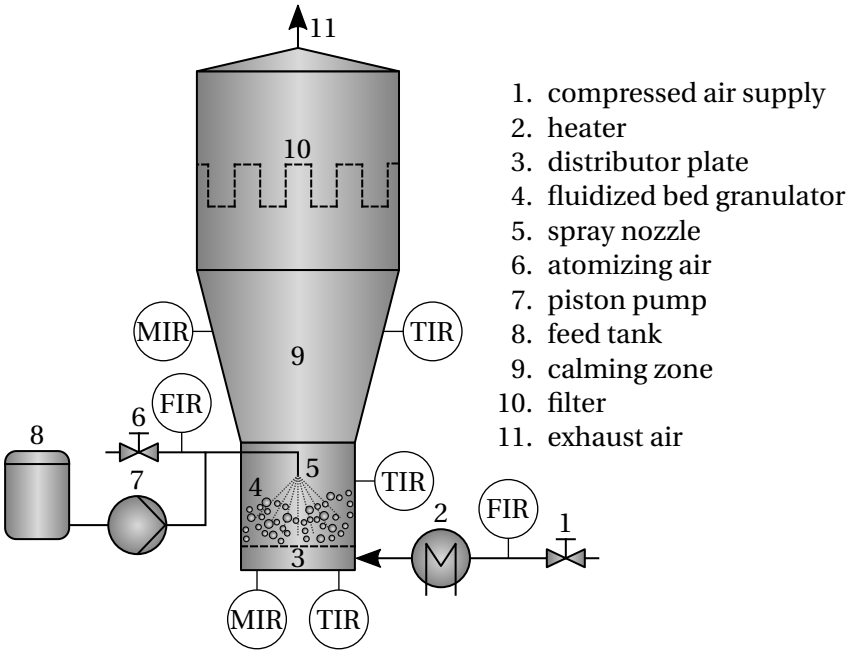

Figure 4.14: Schematic representation of the lab-scale fluidized bed plant used in the experiments (adapted from Rieck et al. [146]).

Materials

The particles used in the presented coating experiments vary in terms of material and particle size distribution. Different non-porous glass beads (Sigmund Lindner GmbH, Germany) with mean diameters of 0.27 mm, 0.53 mm, and 0.64 mm and porous γ-Al_2O_3particles (Sasol Germany GmbH, Germany) with mean diameters of 0.64 mm and 1.8 mm were used. The sprayed materials were aqueous solutions of sodium benzoate (NaB; solid mass fraction ranging between 0.29 and 0.3), sodium benzoate (95 % of added solid mass) and additional hydroxypropyl methylcellulose (HPMC; 5 % of added solid mass) with a total solid mass fraction of 0.3, and shellac dissolved in an aqueous ammonia solution (mass fraction of ammonia equal to 0.02) with a solid mass fraction of 0.15.

Plant description

The experiments were performed in a cylindrical lab-scale fluidized bed (Glatt GmbH, Germany, type: GPCG 1.1, modified) with an inner diameter of the fluidized bed chamber of 0.15 m. A two-fluid nozzle (Düsen Schlick GmbH, type: 970/0 S4) was used in top-spray configuration. The orifice diameter of the liquid tube of the nozzle was 0.8 mm. The distributor plate was made of sintered metal and had a mean pore size of 100 µm. The fluidization gas was air taken from the local compressed air network and heated to the desired temperature by an electrical heater. After passing the fluidized bed chamber, the air is filtered by a textile filter (mean pore size of 7 µm) and blown out. The plant is equipped with various instruments to measure the moisture content of the gas (MIR), temperatures (TIR), and mass flow rates (MIR). An overview is given in Figure 4.14.

Experimental plan and conduction of experiments

The initial bed mass was filled into the fluidized bed chamber, the fluidization was started, and the plant was heated up to the desired temperature. Before starting the coating experiment, a sample of the initial particles was taken. Then, the liquid was sprayed for the desired duration. The atomization air pressure was 1.7 bar in experiments 1 and 2, and 2 bar in the remaining experiments. At the end of each experiment, a sample of the coated particles was taken.

The samples were analyzed offline using different measurement devices. The particle size distribution was determined using a Camsizer (Retsch Technology, Germany), which is a photo-optical measurement system taking images of freely falling particles. Using image processing, the projected area of each particle can be evaluated and converted to diameters of equivalent circles representing the particle diameter. The particle size distribution is then obtained by computing histograms. Additionally, randomly picked single particles were further analyzed using X-ray micro-tomography (ProCon X-Ray GmbH, Germany). The particles were put on a sample holder in front of an X-ray source. The intensity of the X-rays after passing the sample was measured by a detector. Due to differences in X-ray absorption of the core particle, the coating material, and air (in the pores and surrounding the particle), a two-dimensional intensity profile of the X-rays can be obtained. By rotating the sample 360°, a three-dimensional volume image of the scanned particle can be reconstructed with MAVI software (Fraunhofer Institute for Technical and Industrial Mathematics, Germany). Using image processing, the coating layer porosity and the intra-particle layer thickness distribution of the analyzed coated particle can be obtained. Further details regarding the measurement and image analysis can be found in literature, see Sondej et al. [166, 167].

4.3.2 Simulation results

A Monte Carlo simulation was performed for each experiment. The layer porosities measured using X-ray micro-tomography are used in the simulations for the porosity of a dry droplet in Equation (3.41). In each simulation, a set of 1000 particles was created using the measured initial particle size distribution, as explained in Appendix C. In case of the aqueous sodium benzoate solution (experiments 1 to 3), density, viscosity, and surface tension are known (cf. Appendix A) and the Sauter diameter of the sprayed droplets is estimated using an empirical correlation for externally mixing two-fluid nozzles given by Lefebvre and McDonell [168]. The resulting droplet sizes are in the range of 60 µm for experiments 1 and 2 and 35 µm for experiment 3. The necessary parameters are not available for the other materials and, therefore, a droplet size of 35 µm is assumed in experiments 4 to 6. The contact angles were estimated based on photo-optical measurements performed by Terrazas-Velarde [15], who obtained contact angles of aqueous HPMC droplets deposited on glass and γ-Al_2O_3particles. A negligible influence of the solid mass fraction on the contact angle was found. Based on this observation and since the solutions used in the experiments are water-based, the value of the contact angle is set to 40° when glass beads are used and 60° for γ-Al_2O_3particles. The remaining parameters

Table 4.3: Parameters used in the particle coating experiments and the corresponding simulations.

Parameter	Value Exp. 1	Value Exp. 2	Value Exp. 3	Value Exp. 4	Value Exp. 5	Value Exp. 6	Unit
Particle material	glass	glass	γ-Al_2O_3	γ-Al_2O_3	glass	glass	
Sprayed solid material	NaB	NaB	NaB	shellac	shellac	NaB, HPMC	
Sprayed liquid material	water	water	water	aq. NH_3	aq. NH_3	water	
Bed diameter d_{bed}	0.15	0.15	0.15	0.15	0.15	0.15	m
Bed mass M_{bed}	1	1	0.4	0.4	0.4	0.5	kg
Mean particle diameter d_{10}	0.53	0.53	1.80	0.67	0.64	0.27	mm
Standard deviation σ_x	0.10	0.10	0.04	0.04	0.06	0.04	mm
Particle density ϱ_p	2500	2500	1040	1040	2500	2500	$kg\,m^{-3}$
Solid density of coating material ϱ_s	1440	1440	1440	1050	1050	1433	$kg\,m^{-3}$
Spraying rate $\dot{M}_{spray}$	1.28	0.51	0.12	0.37	0.36	0.27	$kg\,h^{-1}$
Droplet diameter d_{drop}	60	60	35	35	35	35	µm
Contact angle θ	40	40	60	60	40	40	°
Solid mass fraction of the solution w_s	0.3	0.3	0.29	0.15	0.15	0.3	–
Porosity of a dry droplet $\varepsilon_{drop,dry}$	0.5	0.46	0.3	0	0	0.1	–
Inlet temperature of the fluidization gas $T_{g,in}$	95	95	75	50	60	60	°C
Inlet moisture content of the fluidization gas Y_{in}	1	1	1	1	1	1	$g\,kg^{-1}$
Mass flow rate of the fluidization gas $\dot{M}_g$	120	120	120	120	120	110	$kg\,h^{-1}$
Process time t	2820	7020	3600	7200	3600	3600	s
Number of particles $N_{p,MC}$	1000	1000	1000	1000	1000	1000	–

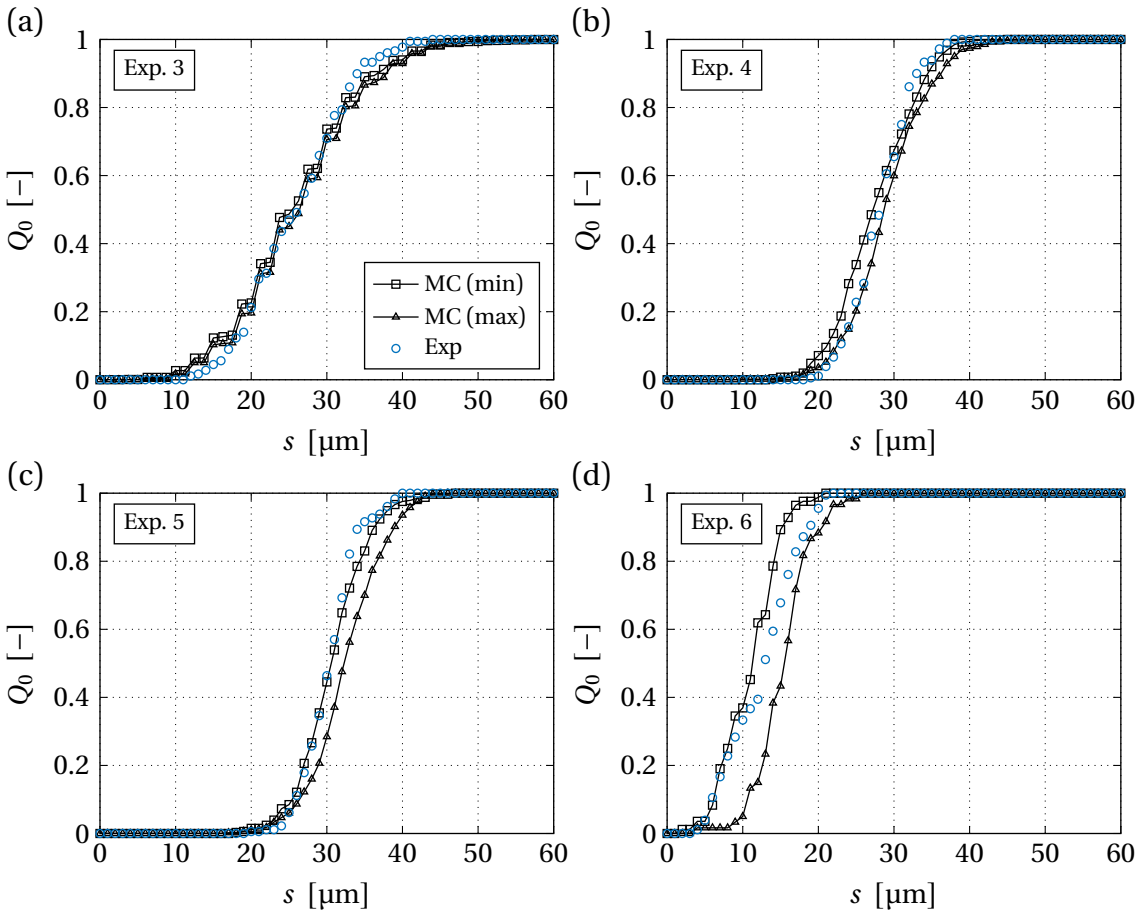

Figure 4.15: Comparison of intra-particle layer thickness distributions obtained from experiments and the Monte Carlo simulation for experiment 3 (a), experiment 4 (b), experiment 5 (c), and experiment 6 (d).

follow directly from the experiments. Table 4.3 gives an overview about the used materials and simulation parameters. Below, particle size distributions and intra-particle layer thickness distributions obtained from experiments and the simulations are compared.

Intra-particle layer thickness distributions were measured for experiments 3 to 6 by randomly picking a single particle from each sample. Figure 4.15 shows the comparison of the distributions from the simulation and the experiments. Since the measured layer thickness distribution corresponds to a randomly picked single particle, the results are compared to two intra-particle layer thickness distributions, which belong to the particles with the smallest (denoted by MC (min)) and largest (denoted by MC (max)) mean layer thickness in the simulation. Then, the measured layer thickness distribution should lie in between the two distributions obtained in the simulation. Figure 4.15 shows that the simulated and measured data agree well for all cases. Table 4.4 shows the mean and standard deviations calculated from the shown intra-particle layer thickness distributions. The values predicted by the simulation are close to the results of the measurement.

Table 4.4 additionally shows the mean and standard deviation of the inter-particle layer thickness distributions obtained in the simulation. As one would expect, these mean values lie between the

Table 4.4: Mean and standard deviation of intra-particle and inter-particle layer thickness distributions obtained in experiments and simulations.

Parameter	Value Exp. 3	Value Exp. 4	Value Exp. 5	Value Exp. 6	Unit
$\bar{s}_{intra,exp}$	26.16	28.09	30.31	12.47	µm
$\sigma_{s,intra,exp}$	6.47	3.94	3.56	4.64	µm
$\bar{s}_{intra,min}$	25.60	27.54	30.67	10.92	µm
$\bar{s}_{intra,max}$	26.40	29.06	32.48	15.33	µm
$\sigma_{s,intra,min}$	8.35	5.17	4.51	3.73	µm
$\sigma_{s,intra,max}$	8.34	5.28	4.86	3.82	µm
$\bar{s}_{inter}$	26.01	28.32	31.52	13.53	µm
$\sigma_{s,inter}$	0.13	0.23	0.27	0.57	µm

mean values of the intra-particle layer thickness distributions $\bar{s}_{intra,min}$ and $\bar{s}_{intra,max}$. However, as already indicated in Figure 4.3a, the corresponding standard deviations are much smaller than those of the intra-particle layer thickness distributions, which is due to the assumptions in the droplet deposition algorithm. Experimental values were not measured in the considered trials, but further results given by Sondej et al. [167] indicate that the standard deviation of inter-particle layer thickness distributions should be larger than the values obtained in the discussed simulations.

Particle size distributions after the coating process were measured for experiments 1, 2, 4, and 6. Figure 4.16 shows the comparison of the simulated and measured particle size distributions before ($t = 0$) and after the coating process. In all cases the simulated and measured data agree well.

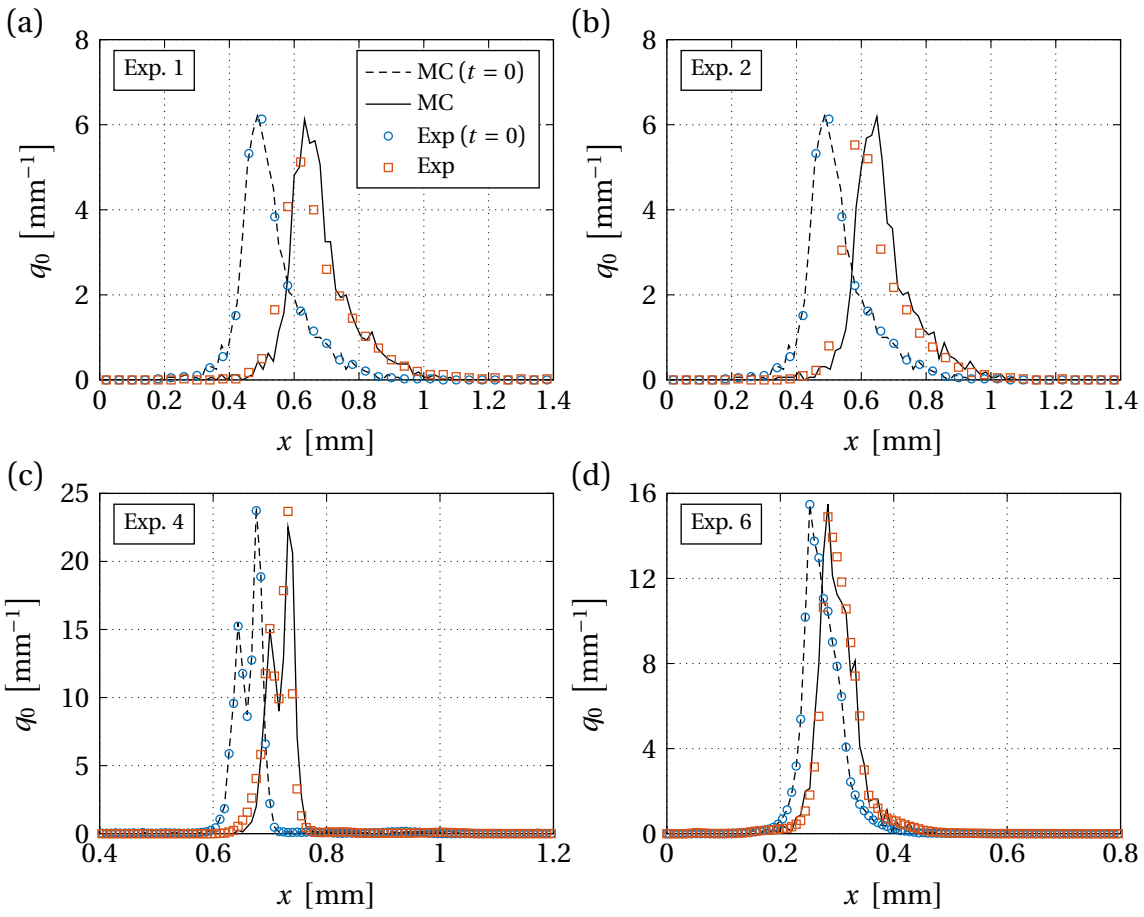

Figure 4.16: Comparison of the particle size distributions before and after the coating process obtained from experiments and the Monte Carlo simulation for experiment 1 (a), experiment 2 (b), experiment 4 (c), and experiment 6 (d).

Chapter 5

Monte Carlo model for binder-less agglomeration due to glass transition

This chapter is an extended version of Rieck et al. [146]. First, the structure of the Monte Carlo model for binder-less agglomeration is presented. A simulation study is used to describe the influence of the droplet deposition mechanism as well as process and material parameters on the agglomeration behavior. Additionally, a comprehensive experimental study is described in detail before simulation results are compared to experimental data.

5.1 Structure of the algorithm

A schematic representation of the micro-processes and events used to model binder-less agglomeration is given in Figure 5.1. Modeling of binder-less agglomeration requires two micro-scale events: deposition of droplets on the particle surface and binary collisions between particles. The deposited droplets wet the particles and are imbibed. Depending on the process conditions, the droplets may cause glass transition of the material, leading to sticky, viscous spots on the particle surface. If particles collide at these spots, agglomerates may be formed. Collisions at dry spots will always result in rebound of the collision partners due to the conditions in this thesis (inlet gas temperature is always lower than the glass transition temperature of the dry solid). The effect of glass transition can be reversed by drying of the wet spots. Re-wetting of these positions is possible, which may again lead to viscous spots. Breakage of viscous and solid bridges is included as well.

Figure 5.2 illustrates the structure of the Monte Carlo algorithm for binder-less agglomeration. Firstly, the particle system is scaled down. Then, the event occurring in a specific time step is chosen according to Equation (3.4). If the chosen event is droplet deposition, one wet droplet is added to a randomly selected particle. If the event collision is chosen, two particles are randomly selected to collide with each other. In this case, the agglomeration criteria described in Section 3.2.5 are checked. If the selected particles agglomerate, they are attached to each other and form a larger compound. Otherwise, rebound occurs, which may result in breakage. If breakage occurs, one randomly selected bridge (wet or dry) of the first collision partner breaks, forming two smaller particles as described in Section 3.2.6. If breakage does not occur, nothing happens to the colliding particles. After successful

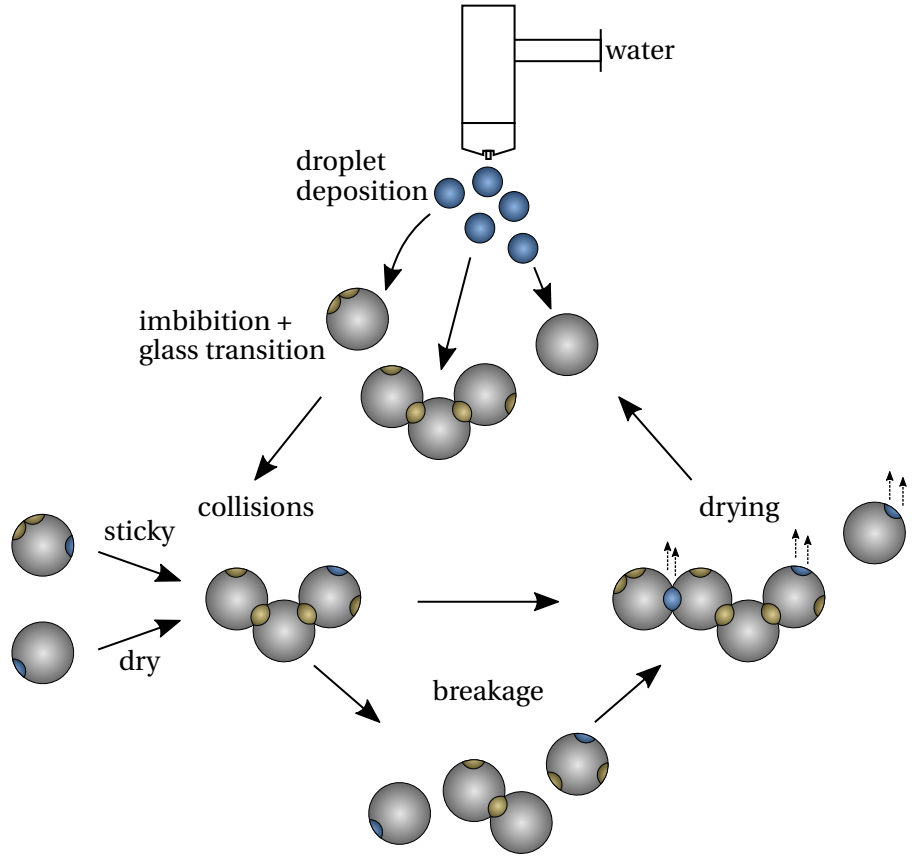

Figure 5.1: Network of the micro-processes and events used to model binder-less agglomeration.

agglomeration or breakage, the particle sizes and the scaling factor are updated in order to re-scale the particle system in the following time step as described in Section 3.1.2. The simulation continues until the process time reaches a pre-defined value. Similar to the Monte Carlo algorithm for coating and layering described in Chapter 4, the variables are saved in total at 50 uniformly distributed points in time during the simulation. In contrast to the Monte Carlo algorithm for coating and layering, the droplet drying algorithm is not used in each time step to update the droplet states. Instead, a time-saving approach is applied as described below.

Calculating droplet drying and updating the droplet state in each time step is computationally expensive and has a large influence on the total computation time. This is necessary in the Monte Carlo algorithm for coating and layering granulation, described in the previous chapter, to obtain the correct time a particle reaches full coverage. However, in case of the Monte Carlo algorithm for binder-less agglomeration, computational time can be saved when the states of all droplets are only updated in the 50 time steps, in which the variables are stored. However, the droplet state is still important for the droplet deposition event (to ensure that the new droplet is deposited on a dry position) and for the collision event (to evaluate the agglomeration criteria) in all other time steps. Consequently, the state of either one droplet (droplet deposition) or two droplets (collision) still needs to be checked in a time step using Equation (3.23). This approach leads to a significant reduction of the computation time compared to checking all droplet states in each time step.

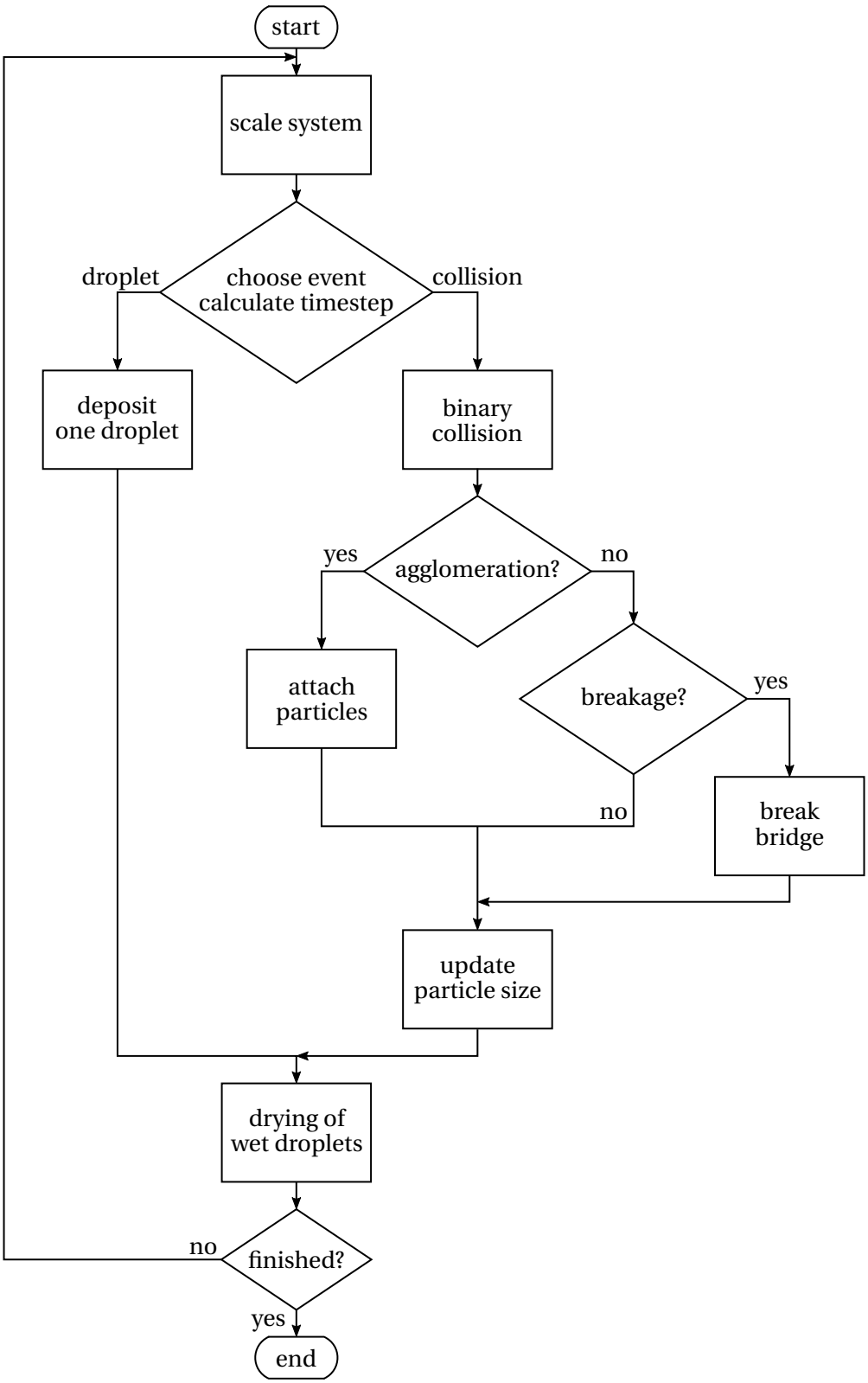

Figure 5.2: Flow chart of the Monte Carlo algorithm for binder-less agglomeration.

5.2 Simulation study

A simulation study is performed to describe the influence of the droplet deposition mechanism as well as process and material parameters on the macroscopic agglomeration behavior in the model. The presented simulation study is based on a comprehensive experimental study on binder-less agglomeration of partly amorphous maltodextrin particles published by Rieck et al. [146], which is described in Section 5.3. Before presenting simulation results, sources and estimation methods for material parameters are given.

The particles used in the experiments are made of maltodextrin, which is a carbohydrate mixture produced by starch hydrolysis. Three different maltodextrins (Glucidex IT, Roquette, France) are used, which can by distinguished by their DE value (dextrose equivalent): DE 6, DE 12, and DE 47 (also denoted by dried glucose syrup). As indicated in Section 3.2.5, application of the Gordon-Taylor equation requires values of the constant k and the glass transition temperature of the dry solid $T_{gt,s}$, which are both material dependent. Values for these parameters are given in literature [43] for DE 5 and DE 10. As the DE of the used materials vary between 5 to 8 (for DE 6) and 11 to 14 (for DE 12), the values given for DE 5 and DE 10 are used. Since no values could be found for DE 47, the value for k was extrapolated linearly from data presented by Roos and Karel [159]. The glass transition temperature of the dry solid was estimated using Equation (3.49) and Equation (3.48), see Section 3.2.5. The resulting values of k and $T_{gt,s}$ are summarized in Table 5.1.

The porosity of the maltodextrin particles was estimated based on the bulk density provided by the manufacturer, which is around 500 kg m^{-3} and the density of the material without pores (approx. 1500 kg m^{-3}), which was measured using a gas pycnometer (Grabner Instruments, Austria, type: Minidens TCO). Assuming a random packing of spheres having a bed porosity of 0.4, the mean porosity of the maltodextrin particles can be estimated. Based on the described values and assumptions, the mean porosity is 0.4 and the corresponding density is 900 kg m^{-3}. In the presented simulation study, the initial particle size distributions are approximated by normal distributions with a mean diameter of 140 µm (corresponds to a Sauter mean diameter of 160 µm) and a standard deviation of 40 µm, which follow from measurement results presented in Section 5.3. A set of 1000 normally distributed particle diameters was then created in each simulation as shown in Appendix C. The collision frequency is calculated as described in Section 3.2.2 and equals 12.6 s^{-1}. For simplification,

Table 5.1: Material parameters used in the Gordon-Taylor equation for maltodextrin DE 6, DE 12, and DE 47.

Material	$T_{gt,s}$ [°C]	k [–]
DE 6	188	7.7
DE 12	160	7.0
DE 47	111	5.3

Table 5.2: Simulation parameters used in the Monte Carlo simulations for binder-less agglomeration (simulation study).

Parameter	Value	Unit
Particle material	DE 6, DE 12, DE 47	
Sprayed liquid material	water	
Bed diameter d_{bed}	0.15	m
Bed mass M_{bed}	0.45	kg
Mean particle diameter d_{10}	140	µm
Standard deviation σ_x	40	µm
Primary particle density ϱ_{pp}	900	$\mathrm{kg\,m^{-3}}$
Solid density ϱ_s	1500	$\mathrm{kg\,m^{-3}}$
Primary particle porosity ε_{pp}	0.4	–
Agglomerate porosity ε_{agg}	0.5	–
Collision frequency f_{coll}	12.6	$\mathrm{s^{-1}}$
Particle velocity (mean) $\overline{u}_p$	0.018	$\mathrm{m\,s^{-1}}$
Collision velocity (mean) $\overline{u}_{coll}$	0.29	$\mathrm{m\,s^{-1}}$
Collision velocity (standard deviation) $\sigma_{u_{coll}}$	0.15	$\mathrm{m\,s^{-1}}$
Breakage probability P_{break}	0.002	–
Coefficient of restitution e'	0.5	–
Height of asperities h_a	5	µm
Spraying rate $\dot{M}_{spray}$	0.3, 0.4, 0.5	$\mathrm{kg\,h^{-1}}$
Droplet diameter d_{drop}	30	µm
Contact angle θ	40	°
Inlet temperature of the fluidization gas $T_{g,in}$	60, 80, 95	°C
Inlet moisture content of the fluidization gas Y_{in}	1	$\mathrm{g\,kg^{-1}}$
Mass flow rate of the fluidization gas $\dot{M}_g$	39	$\mathrm{kg\,h^{-1}}$
Process time t	250	s
Number of particles in the simulation $N_{p,MC}$	1000	–

the value is calculated once at the beginning of the simulation and held constant. The calculated mean particle velocity is 0.018 m s^{-1}. The resulting distribution of the collision velocity follows from the method described in Section 3.2.5 and is characterized by a mean value of 0.29 m s^{-1} and a standard deviation of 0.15 m s^{-1}. The restitution coefficient e' is set to 0.5 based on PTV measurements presented by Jiang et al. [169] and the height of asperities at the bottom of wet spots is estimated to be 5 µm. The Sauter mean diameter of the sprayed water droplets was estimated based on an empirical correlation for externally mixing two-fluid nozzles reported by Lefebvre and McDonell [168] and is 30 µm. The contact angle is assumed to be 40°. Further operating parameters are based on the experimental study, which is described in detail in Section 5.3.1. The parameters used in this simulation study are summarized in Table 5.2.

5.2.1 Influence of droplet deposition

The influence of the droplet deposition mechanism on the agglomeration behavior is investigated in a similar way as shown in Section 4.2.2. In total four simulations are performed, in which Λ_0 to Λ_3 in Equation (3.17) are sequentially set to unity. The simulation parameters correspond to those in Table 5.2 for maltodextrin DE 12 with $T_{g,in} = 60$ °C and $\dot{M}_{spray} = 0.4$ kg h^{-1}. The results are shown in Figure 5.3.

Figure 5.3a shows the initial particle size distribution as well as the particle size distributions after 250 s of spraying for each simulation. Figure 5.3b shows the transient behavior of the corresponding Sauter mean diameter. A significant influence of the selection property in the droplet deposition algorithm on the agglomeration kinetics can be observed. In case of $\Lambda_0 = 1$ (i.e., particles are selected based on their number when receiving droplets), the agglomeration rate is higher than in all other cases, leading to the largest agglomerates. When the particles are selected based on their volume ($\Lambda_3 = 1$), the smallest agglomeration rate and Sauter mean diameter are obtained.

If the particle selection for droplet deposition is based on the particle number, all particles have the same probability to be selected. However, if the selection property is either size, surface area, or volume, the relative amount of droplets received by small particles is reduced, while it increases for larger particles, see Figure 3.13 in Section 3.2.1. As a result, the wet surface area is increased for small particles in case of $\Lambda_0 = 1$ and for large particles in case of $\Lambda_3 = 1$. However, since small particles have less positions due to their small surface area, the resulting wet surface fraction is higher in comparison with large particles, leading to an increased probability of a wet position being randomly chosen in a collision event. At the same time, the selection of collision partners is performed based on the number of the individual particles (i.e., the selection probability is identical for each particle). Therefore, small particles can agglomerate more frequently in case of $\Lambda_0 = 1$. This increases the agglomeration rate, leads to larger agglomerates, and consequently to a small amount of single primary particles in the particle size distribution, see Figure 5.3a.

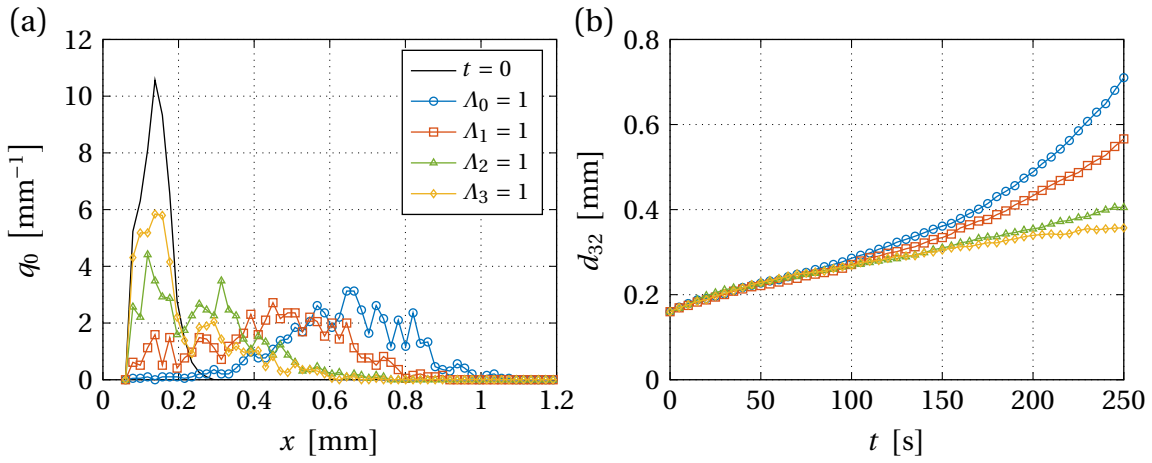

Figure 5.3: Influence of the droplet deposition mechanism on the particle size distribution (a) and the transient behavior of the Sauter mean diameter (b).

5.2.2 Influence of process parameters

The influence of process parameters (inlet gas temperature and spraying rate) and a material parameter (DE value of maltodextrin) on the three agglomeration criteria considered in the model is presented. Therefore, further parameters are considered: drying time (cf. Equation (3.35)), glass transition temperature (cf. Equation (3.47)), temperature of the solid (cf. Equation (3.52)), and viscosity (cf. Equation (3.50)). The agglomeration behavior is quite complex, as changes in these parameters lead to opposing trends on the microscopic level. These trends are discussed below, while the governing trend on the macro-scale is discussed later using the simulation and experimental results. The used simulation parameters are summarized in Table 5.2. To show the influence of the above mentioned parameters on agglomeration, the following simulations are performed:

- simulations with $T_{g,in} = 60\,°C$ and $T_{g,in} = 95\,°C$ (DE 12, $\dot{M}_{spray} = 0.4\,kg\,h^{-1}$),
- simulations with $\dot{M}_{spray} = 0.3\,kg\,h^{-1}$ and $\dot{M}_{spray} = 0.5\,kg\,h^{-1}$ (DE 12, $T_{g,in} = 80\,°C$), and
- simulations with DE 6 and DE 47 ($T_{g,in} = 80\,°C$, $\dot{M}_{spray} = 0.4\,kg\,h^{-1}$).

The results are shown in Figure 5.4 to Figure 5.6 and summarized in Table 5.3.

Figure 5.4 shows the influence of the inlet gas temperature on the agglomeration behavior. Figure 5.4a shows the mean number of wet droplets (scaled up to the real particle system) during the process and Figure 5.4b to Figure 5.4d depict the transient behavior of the water mass fraction w_w, the glass transition temperature T_{gt}, and the viscosity of the wet spots η during the drying time of a droplet. An increase in temperature leads to a shorter drying time and therefore to a smaller number of wet droplets. This directly influences the first agglomeration criterion negatively and leads to less successful collisions. Additionally, the water mass fraction is reduced faster in case of a high inlet gas temperature leading to a faster increase of the glass transition temperature of the wet spot. That is why in case of a high inlet gas temperature it is more likely that the calculated glass transition temperature during a collision is higher, which generally inhibits the second agglomeration criterion from being

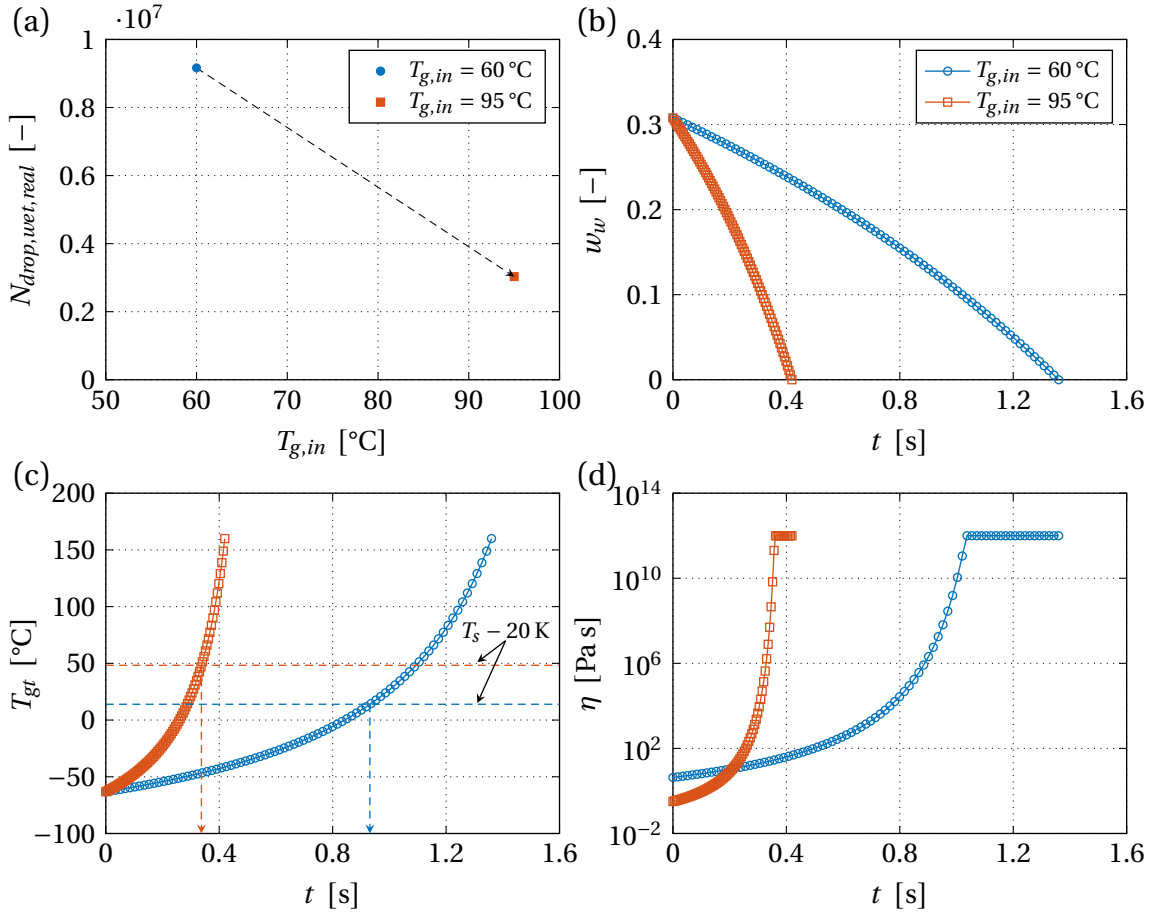

Figure 5.4: Influence of the inlet gas temperature on parameters of the agglomeration citeria: number of wet droplets (a), water mass fraction (b), glass transition temperature (c), and viscosity (d).

fulfilled and impedes agglomeration. At the same time, the temperature of the particles T_s is also higher if the inlet gas temperature is increased, promoting agglomeration. The combination of both effects is shown in Figure 5.4c. According to the second agglomeration criterion, the glass transition temperature must be smaller than the temperature of the solid material reduced by 20 K (indicated by the dashed lines in Figure 5.4c) to ensure stickiness of the material. The intersection of the curves for T_{gt} and $T_s - 20$ K yields the time interval, in which the second agglomeration criterion is fulfilled. This time interval is reduced in case of a high temperature, which means that the negative influence on the second criterion (higher glass transition temperature) prevails, leading to less agglomeration events. The third agglomeration criterion (Stokes criterion) is influenced by the viscosity of the material. Figure 5.4d shows that the viscosity is lower at the beginning of the drying process in case of a high inlet gas temperature due to a higher particle temperature. At the same time, drying is faster in this case and therefore the viscosity increases faster. Depending on the time of the collision, the viscosity may be smaller or larger in case of a higher inlet gas temperature and agglomeration may be impeded or promoted.

Figure 5.5 shows the influence of the spraying rate on the agglomeration behavior. A higher spraying

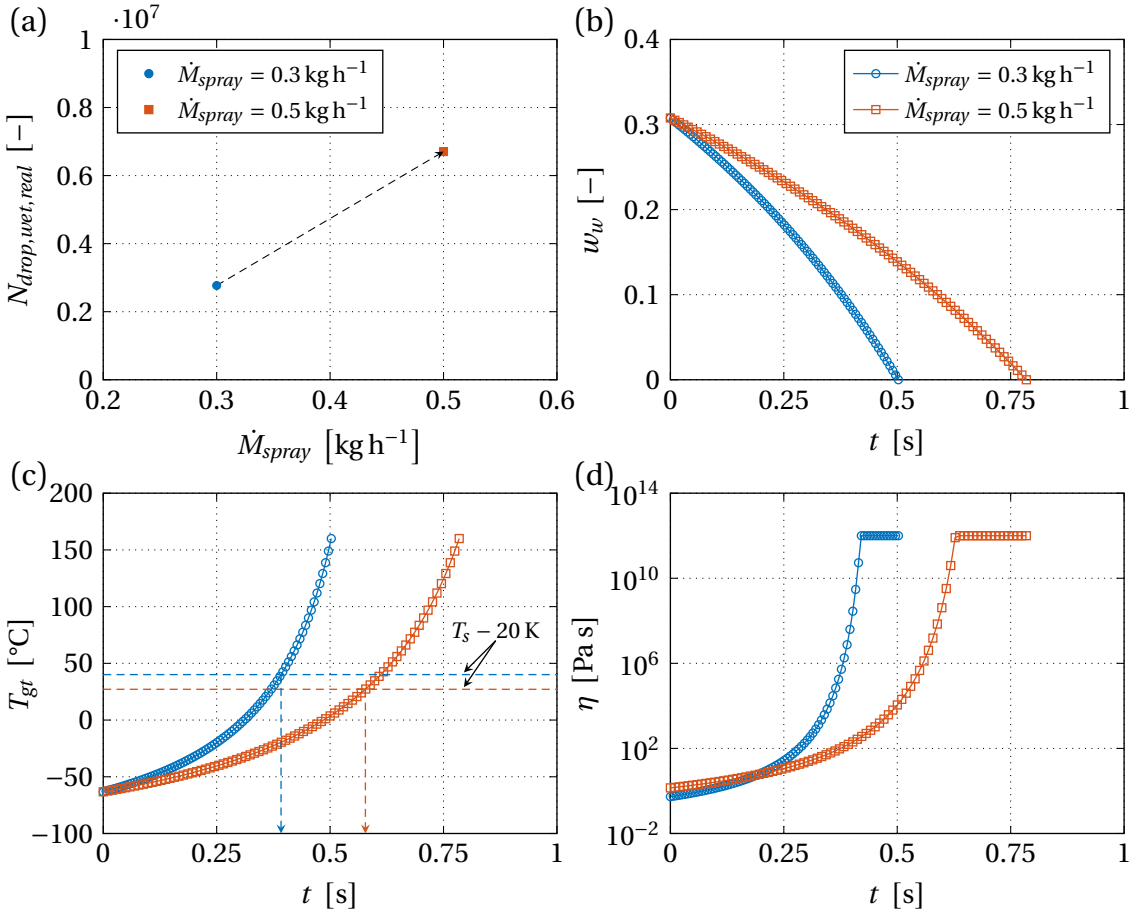

Figure 5.5: Influence of the spraying rate on parameters of the agglomeration citeria: number of wet droplets (a), water mass fraction (b), glass transition temperature (c), and viscosity (d).

rate leads to an increased number of wet droplets (see Figure 5.5a) due to a higher number flow rate of droplets (see Equation (3.15)) and an increased drying time. This directly influences the first agglomeration criterion, leading to more agglomeration events. As drying is slower in case of a higher spraying rate, the reduction of the water mass fraction is slower (see Figure 5.5b) and correspondingly the glass transition temperature increases slower during the drying process. This leads to lower values for T_{gt} during collisions and therefore positively influences the second agglomeration criterion. However, the temperature of the solid material is lower, which inhibits the fulfillment of the second agglomeration criterion. Considering both effects simultaneously in Figure 5.5c, it can be seen that the time interval in which the second agglomeration criterion is fulfilled increases with an increasing spraying rate, which ultimately promotes agglomeration as the positive influence (lower glass transition temperature) prevails. Figure 5.5d shows that the viscosity at the beginning of the drying process is larger in case of a high spraying rate, but increases slower during drying. Similar to the case shown in Figure 5.4d, a higher spraying rate may lead to higher or smaller viscosities during collisions. Depending on the time of the collision, agglomeration may be promoted or inhibited according to the third agglomeration criterion.

Figure 5.6 shows the influence of the DE value of the maltodextrin on the agglomeration behavior.

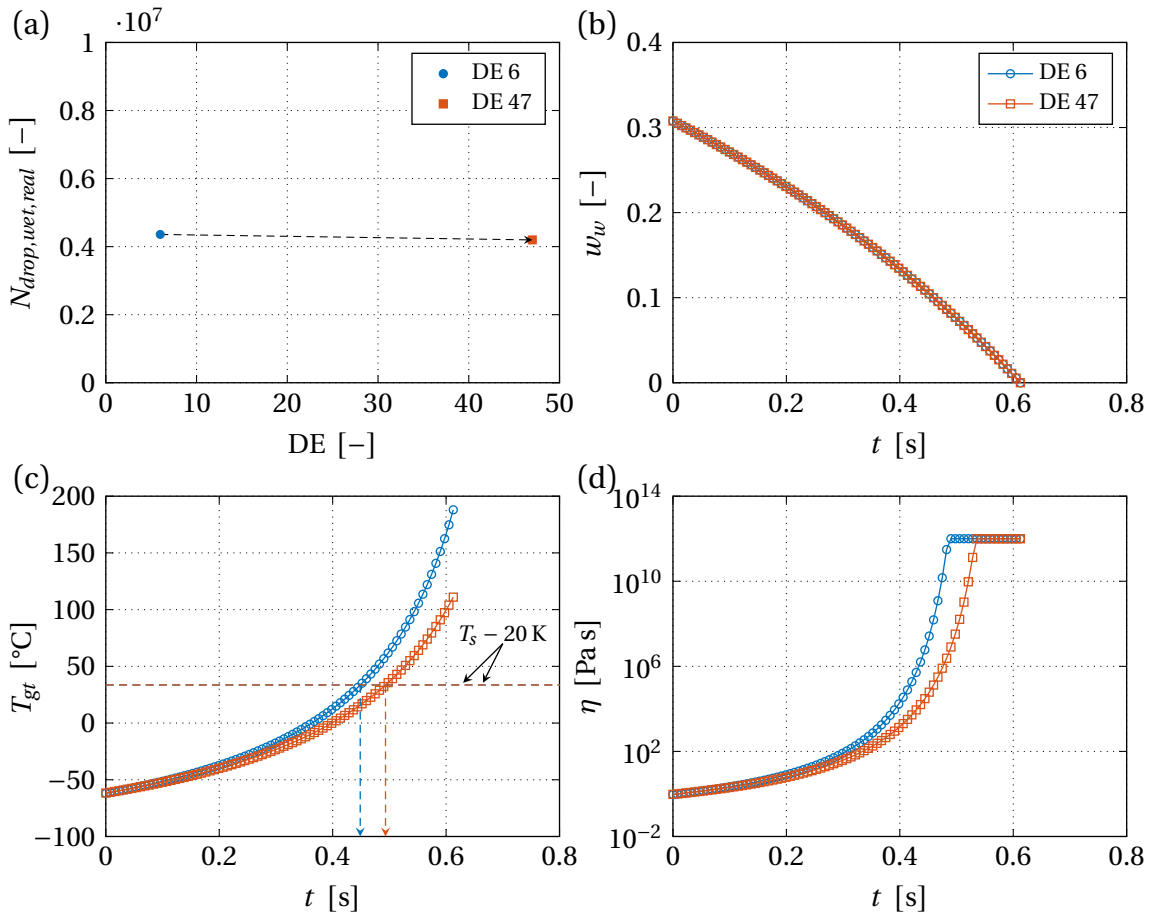

Figure 5.6: Influence of the DE value on parameters of the agglomeration citeria: number of wet droplets (a), water mass fraction (b), glass transition temperature (c), and viscosity (d).

As stated in Section 3.2.3, the drying model assumes gas-side controlled drying, neglecting material influence such as hygroscopicity. Therefore, the drying time is not influenced when varying the DE value and the number of wet positions does not change. The small difference in Figure 5.6a results from the stochastic nature of the model. Note that the simulation for DE 47 was performed with the same initial particle size distribution as the simulation for DE 6 in this case, since the larger particle size (cf. Table 5.2) would otherwise lead to a slightly larger drying time due to a smaller mass transfer coefficient for DE 47, interfering with the impact of the DE value. Since the drying time is identical, the first agglomeration criterion is not influenced. The reduction of the water mass fraction is not changed as well, see Figure 5.6b. However, a higher DE value leads to smaller glass transition temperatures, promoting agglomeration. As the temperature of the solid material is not changed, the time interval in which the second agglomeration criterion is fulfilled is larger when the DE value is increased. Consequently, the combination of both effects results in more successful collisions according to the second agglomeration criterion in case of a higher DE value, see Figure 5.6c. Figure 5.6d shows that the viscosity of a wet spot will be lower if the DE value increases. Therefore, the third agglomeration criterion predicts less agglomeration events in this case.

Table 5.3: Influence of inlet gas temperature, spraying rate, and DE value on the parameters of the agglomeration criteria of the presented model.

Parameter	$T_{g,in} \uparrow$	$\dot{M}_{spray} \uparrow$	DE $\uparrow$
Δt_{dry}	$\downarrow$	$\uparrow$	–
T_{gt}	$\uparrow$	$\downarrow$	$\downarrow$
T_s	$\uparrow$	$\downarrow$	–
η	$\uparrow\downarrow$	$\uparrow\downarrow$	$\downarrow$
1. criterion	$\downarrow$	$\uparrow$	–
2. criterion	$\downarrow$	$\uparrow$	$\uparrow$
3. criterion	$\uparrow\downarrow$	$\uparrow\downarrow$	$\downarrow$

5.3 Comparison to experimental data

In this section, the Monte Carlo simulation results are compared to experimental data. Before presenting the results, details about the experimental study are presented.

5.3.1 Experimental setup

Materials

The primary particles used in the agglomeration experiments are made of three different types of maltodextrin: DE 6, DE 12, and DE 47 (Glucidex IT, Roquette, France). The used maltodextrin is probably only partly amorphous, the rest being crystalline. According to Takeiti et al. [170], who measured the crystallinity index of different maltodextrins, it can be estimated that approximately 30 % of the material is amorphous. The primary particles have been sieved before the experiments to ensure a constant initial particle size throughout the experimental study. In each case, the fraction between the 100 µm and 200 µm meshes were used. Tap water was sprayed during the experiments to induce agglomeration.

Plant description

The agglomeration experiments were performed in the same lab-scale fluidized bed plant as the coating experiments described in Chapter 4. Details of the plant can be found in Section 4.3.1.

Experimental plan and conduction of experiments

As shown in Table 5.4, the experimental study consists of 27 experiments, in which inlet gas temperature, spraying rate, and the DE value of the material were varied. The remaining process parameters

Table 5.4: Parameters used in the binder-less agglomeration experiments and the corresponding simulations.

Exp.	Material	$\dot{M}_{spray}$ $[\mathrm{kg\,h^{-1}}]$	$T_{g,in}$ [°C]	$d_{10,0}$ [µm]	$d_{32,0}$ [µm]	$\sigma_{x,0}$ [µm]	f_{coll} $[\mathrm{s^{-1}}]$	$\overline{u}_p$ $[\mathrm{m\,s^{-1}}]$	$\overline{u}_{coll}$ $[\mathrm{m\,s^{-1}}]$	$\sigma_{u_{coll}}$ $[\mathrm{m\,s^{-1}}]$
1	DE 6	0.30	60	133	157	41	13.2	0.018	0.29	0.15
2	DE 6	0.29	80	127	158	42	11.5	0.016	0.26	0.14
3	DE 6	0.30	95	135	166	46	11.4	0.017	0.27	0.15
4	DE 6	0.39	60	132	158	41	13.1	0.018	0.29	0.15
5	DE 6	0.43	80	128	154	40	11.6	0.016	0.26	0.14
6	DE 6	0.38	95	132	156	39	11.2	0.016	0.26	0.14
7	DE 6	0.56	60	132	158	40	13.1	0.018	0.29	0.15
8	DE 6	0.53	80	134	161	43	12.1	0.017	0.27	0.15
9	DE 6	0.53	95	126	152	41	10.7	0.016	0.26	0.14
10	DE 12	0.30	60	133	162	44	13.2	0.018	0.29	0.15
11	DE 12	0.28	80	145	173	45	13.0	0.018	0.29	0.15
12	DE 12	0.30	95	143	179	49	12.0	0.018	0.29	0.15
13	DE 12	0.40	60	134	160	40	13.3	0.018	0.29	0.15
14	DE 12	0.40	80	135	161	42	12.2	0.017	0.27	0.15
15	DE 12	0.40	95	134	168	46	11.4	0.017	0.27	0.15
16	DE 12	0.56	60	133	161	43	13.2	0.018	0.29	0.15
17	DE 12	0.48	80	142	170	44	12.8	0.018	0.29	0.15
18	DE 12	0.49	95	132	161	43	11.2	0.016	0.26	0.14
19	DE 47	0.30	60	148	195	54	14.6	0.020	0.32	0.17
20	DE 47	0.30	80	152	195	51	13.5	0.019	0.30	0.16
21	DE 47	0.30	95	139	172	46	11.7	0.017	0.27	0.15
22	DE 47	0.42	60	136	171	47	13.5	0.018	0.29	0.15
23	DE 47	0.40	80	143	177	46	12.9	0.018	0.29	0.15
24	DE 47	0.43	95	149	201	56	12.5	0.018	0.29	0.15
25	DE 47	0.51	60	146	176	45	14.3	0.019	0.30	0.16
26	DE 47	0.52	80	151	198	54	13.5	0.019	0.30	0.16
27	DE 47	0.54	95	162	223	64	13.4	0.020	0.32	0.17

were constant: initial bed mass, 0.45 kg; mass flow rate of the fluidization gas, 39 kg h^{-1}; atomization air pressure, 2.3 bar.

The initial bed mass was filled into the fluidized bed chamber, fluidization was started, and the plant was heated up to the desired temperature. The agglomeration experiment was initiated by starting the spray. The experiments were performed until de-fluidization was visually observed, except in experiment 3, 12, and 15, in which de-fluidization did not occur due to an equilibrium between agglomeration and breakage. During each experiment, samples with a mass between 4 g to 7 g were taken in time intervals corresponding to a sprayed water mass of 25 g (including a sample before starting the spray). In case of fast agglomeration experiments, samples were also taken after spraying 12.5 g and 37.5 g of water.

The samples were analyzed offline using a Camsizer (Retsch Technology, Germany), yielding the particle size distribution of each sample. Additionally, the moisture content of each sample was determined thermogravimetrically with a drying oven. The initial mass fractions $w_{w,0}$ varied between 0.02 and 0.05.

Drying of wetted maltodextrin surfaces

In addition to the agglomeration experiments described above, the drying behavior of wetted maltodextrin surfaces was investigated. Therefore, particles from all used maltodextrin grades were pressed into tablets with a hydraulic press using a pressure of 1.3 MPa. The dry mass of the tablets ranged from 226 mg to 268 mg, see Table 5.5. The drying behavior was investigated using a magnetic suspension balance (Rubotherm, Germany). The accuracy of the measurement is 1 µm. Peglow et al. [171] give a detailed description of the magnetic suspension balance. Each tablet was placed into the sample holder of the magnetic suspension balance and dried with pure nitrogen until the measured mass reached a constant value. This procedure took up to five days. Then, a water droplet with a mass ranging between 4.69 mg and 5.3 mg, see Table 5.5, was placed onto the tablet with a pipette. These masses correspond to a spherical droplet diameter of approximately 2 mm. It was observed that the droplet was instantly imbibed into the porous structure of the tablet. After deposition of the droplet, the decrease of the tablet mass due to drying of the droplet was recorded. The mass flow rate of the used nitrogen was 23.3 g h^{-1} in all experiments.

Table 5.5: Masses of the dry tablets and droplets in the drying experiments.

Material	$M_{tab,dry}$ [mg]	M_{drop} [mg]
DE 6	239.60	4.69
DE 12	225.98	5.19
DE 47	268.16	5.30

5.3.2 Simulation results

A simulation for each experiment shown in Table 5.4 was performed with the corresponding inlet gas temperature, spraying rate, and DE value. In each simulation, a set of 1000 particles was created using the measured initial particle size distribution as shown in Appendix C. The mean particle diameter, Sauter mean diameter, and standard deviation of the measured initial particle size distributions are given in Table 5.4 as well. Due to the observed variation of these parameters, collision frequency and mean particle velocity were calculated according to Section 3.2.2 in each simulation individually. The results are shown in Table 5.4 along with the mean and standard deviation of the corresponding distribution of the collision velocity. The remaining simulation parameters are identical to the ones shown in Table 5.2. In order to avoid presenting the results of all experiments and simulations, the focus lies on presenting the results of selected parameter combinations to illustrate the governing influence of the inlet gas temperature, the spraying rate, and the DE value on the agglomeration process. Therefore, the transient behavior of the Sauter mean diameter d_{32} (normalized to its initial value $d_{32,0}$) of both the experimental and simulation results of the following experiments are shown:

- 4-6; 13-15; and 22-24 (influence of inlet gas temperature and DE value),
- 2, 5, 8; 11, 14, 17; and 20, 23, 26 (influence of spraying rate).

The omitted simulation and experimental data show the same trends as the presented data. The results are shown in Figure 5.7 to Figure 5.9.

In Figure 5.7 the results from the experiments and the simulations for maltodextrin DE 6 are shown. The influence of temperature is shown in Figure 5.7a. A low temperature leads to faster agglomeration, while a high temperature consequently leads to slower agglomeration. This trend can be observed for both the experimental and the simulation data and is in accordance to the results of the above presented simulation study. Ultimately, the negative influence of a high temperature on agglomeration on the first two criteria and partly on the third criterion seems to be dominant. Figure 5.7b shows the influence of the spraying rate. A high spraying rate leads to faster agglomeration, while a lower spraying rate results in a slower agglomeration process. This trend can be observed in both the experimental and simulation results and agrees with the simulation study as well. The positive influence of a high spraying rate on the first two criteria and partly on the third criterion prevails. The simulation overestimates the agglomeration rate in the case of fast agglomeration in Figure 5.7a (combination of 60 °C and 0.4 kg h^{-1}) and agrees well for fast agglomeration in Figure 5.7b (combination of 80 °C and 0.5 kg h^{-1}). In all other cases shown in Figure 5.7, the net rate of agglomeration is underestimated. In case of the highest inlet gas temperature and the lowest spraying rate, an equilibrium between agglomeration and breakage is predicted by the simulation, while the experiment indicates net growth in these cases. Furthermore, the experimental data shows only minor differences between low and medium temperature in Figure 5.7a (60 °C and 80 °C) as well as high and medium spraying rate in Figure 5.7b (0.5 kg h^{-1} and 0.4 kg h^{-1}) in contrast to the simulation results.

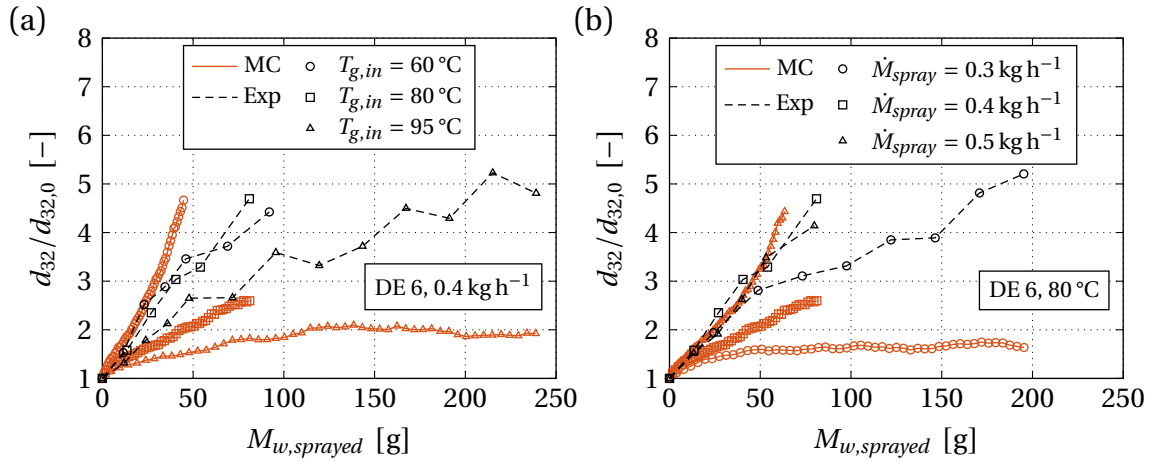

Figure 5.7: Transient behavior of the Sauter mean diameter for different temperatures at a spraying rate of 0.4 kg h^{-1} (a) and different spraying rates at a temperature of 80 °C (b) for maltodextrin DE 6 particles. The results from the simulation and the experiments are represented by the solid lines and the dashed lines, respectively. Different temperatures and spraying rates are distinguished by the symbols.

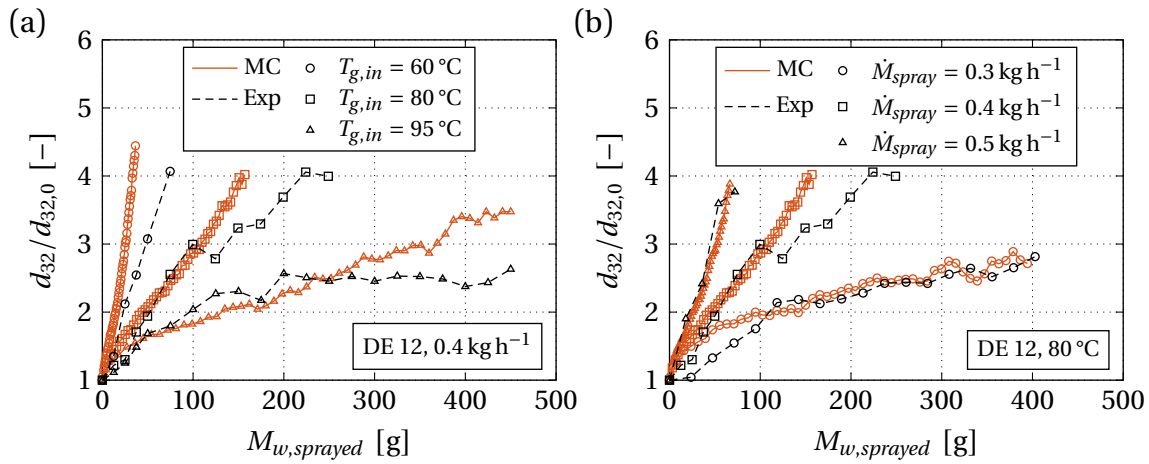

Figure 5.8: Transient behavior of the Sauter mean diameter for different temperatures at a spraying rate of 0.4 kg h^{-1} (a) and different spraying rates at a temperature of 80 °C (b) for maltodextrin DE 12 particles. The results from the simulation and the experiments are represented by the solid lines and the dashed lines, respectively. Different temperatures and spraying rates are distinguished by the symbols.

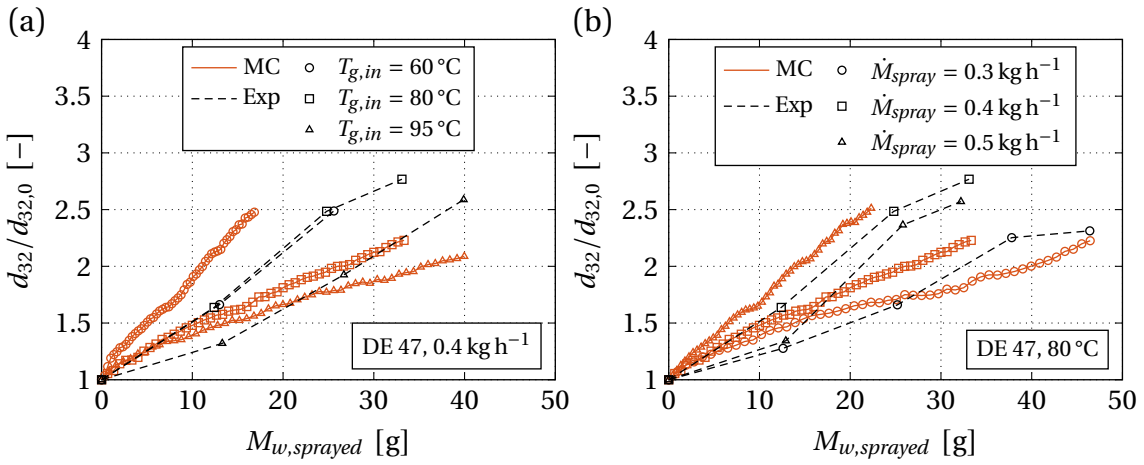

Figure 5.9: Transient behavior of the Sauter mean diameter for different temperatures at a spraying rate of 0.4 kg h^{-1} (a) and different spraying rates at a temperature of 80 °C (b) for maltodextrin DE 47 particles. The results from the simulation and the experiments are represented by the solid lines and the dashed lines, respectively. Different temperatures and spraying rates are distinguished by the symbols.

Figure 5.8 shows the results from the experiments and the simulations for maltodextrin DE 12. The influence of the inlet gas temperature and the spraying rate is the same as for DE 6 particles. The simulation results agree well with the experiment for all varied parameters. Note that experiment 17 (combination of 80 °C and 0.5 kg h^{-1}), which is shown in Figure 5.8b, was used to fit the fraction of unsuccessful collisions leading to breakage P_{break} as described in Section 3.2.6.

Figure 5.9 shows the results from the experiments and the simulations for maltodextrin DE 47. The general trends discussed above are the same as for DE 6 and DE 12 particles. Similar to the experiments with DE 6, the experimental data shows almost no difference between inlet gas temperatures of 60 °C and 80 °C (Figure 5.9a) and spraying rates of 0.4 kg h^{-1} and 0.5 kg h^{-1} (Figure 5.9b). The model overestimates agglomeration in case of fast agglomeration (combination of 60 °C and 0.4 kg h^{-1} in Figure 5.9a; combination of 80 °C and 0.5 kg h^{-1} in Figure 5.9b) and underestimates agglomeration for the rest of the parameter combinations except for slow agglomeration (combination of 80 °C and 0.3 kg h^{-1}) in Figure 5.9b.

In Figure 5.10, the influence of the DE value on the agglomeration behavior is shown for all investigated inlet gas temperatures at a spraying rate of 0.4 kg h^{-1}. The simulation results are given on the left-hand side (Figure 5.10a, Figure 5.10c, and Figure 5.10e). It can be observed that the agglomeration rate increases with increasing DE value in the simulation: DE 47 particles show the highest agglomeration rate, while DE 6 particles agglomerate with the smallest rate. Comparing to Figure 5.6 and Table 5.3, the positive influence of an increasing DE value on the second agglomeration criterion outweighs the negative influence on the third criterion. An exception can be observed in Figure 5.10c, where DE 6 and DE 12 agglomerate with very similar rates in the simulation, resulting from the slightly higher spraying rate in case of DE 6 compared to DE 12 (see Table 5.4). The experimental results are given in Figure 5.10b, Figure 5.10d, and Figure 5.10f. They show that DE 6 and DE 47 particles

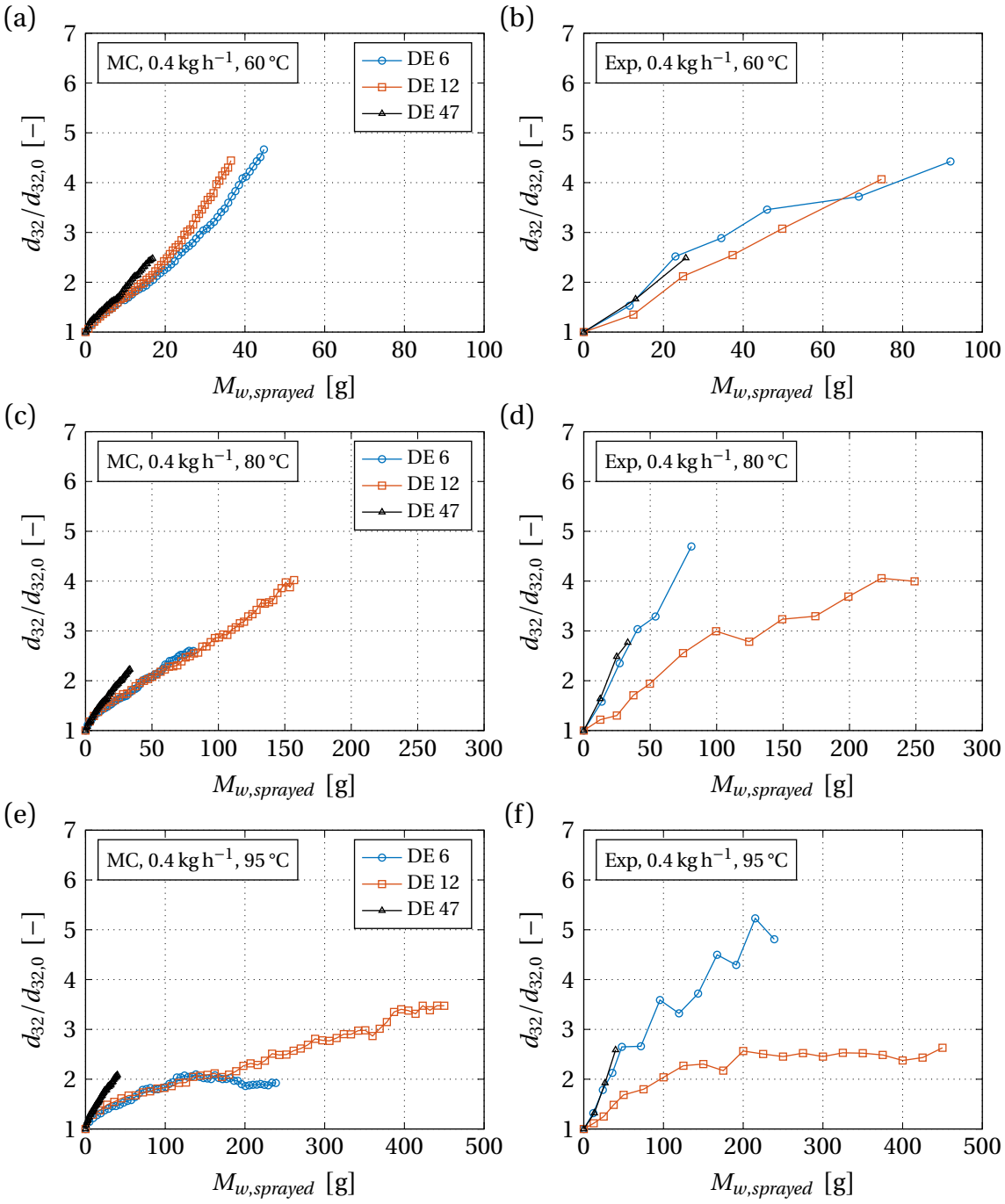

Figure 5.10: Transient behavior of the Sauter mean diameter for all used materials at a spraying rate of 0.4 kg h^{-1} and a temperature of 60 °C in the simulation (a) and the experiment (b), 80 °C in the simulation (c) and the experiment (d), and 95 °C in the simulation (e) and the experiment (f).

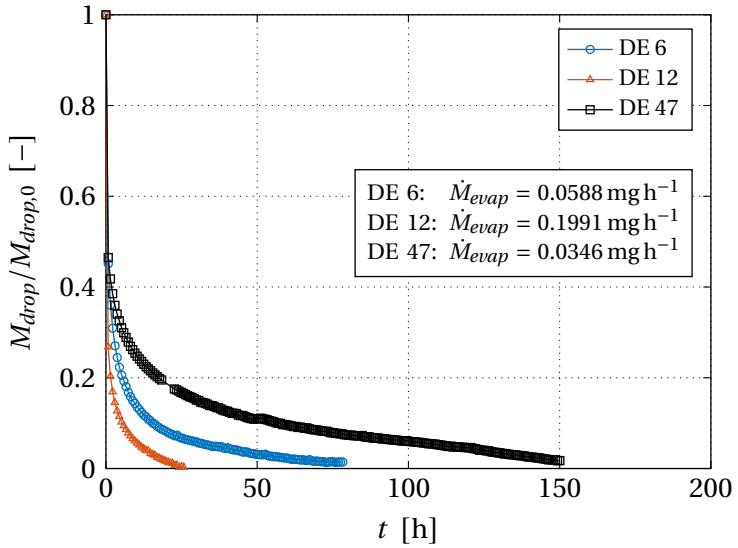

Figure 5.11: Transient behavior of the normalized mass during drying of water droplets deposited on maltodextrin tablets with different DE values in a magnetic suspension balance.

agglomerate with similar rates, which are higher than the agglomeration rate of DE 12 particles. The trend predicted by the model is in this case not in agreement with the experimentally observed trend. Below, the results of the tablet drying experiments are used to explain these differences.

As described in Section 5.3.1, the drying behavior of wetted maltodextrin surfaces was investigated. Figure 5.11 shows the results of these experiments, in which the decrease of the droplet mass (normalized to its initial value at the time of deposition, see Table 5.5) due to drying is shown for all used materials. The results show that the drying behavior is greatly influenced by the DE value of the material. The drying time of the deposited droplets is equal to 26 h in case of the DE 12 tablet, 79 h in case of the DE 6 tablet and 150 h for the DE 47 tablet. The corresponding mean evaporation rates are shown in Figure 5.11. The unexpected drying behavior in case of the DE 12 tablet may be used to explain the experimentally observed agglomeration behavior shown in Figure 5.10b. Since the water droplets seem to dry significantly faster in case of maltodextrin DE 12, the probability of a wet collision is reduced, leading to a slower agglomeration rate. It should though be noted that despite using the same pressure and particle size distribution in the production of the tablets, the behavior of DE 12 might be due to a different pore system of the tablet. Nevertheless, these results indicate that the DE value or associated material properties influence the drying behavior.

Chapter 6

Macroscopic modeling of the dominant size enlargement mechanism

This chapter is an extended version of Rieck et al. [172] and deals with estimation of the dominant size enlargement mechanism in a spray fluidized bed process. The underlying model is described in detail, before presenting results of a simulation study indicating the influence of the inlet gas temperature, viscosity, droplet size, and contact angle on the dominant size enlargement mechanism. Furthermore, a classification of the dominant mechanism based on the probability of successful collisions is proposed, which follows from experimental data and simulation results and allows for regime maps to be created.

6.1 Model description

In the following sections, a model for estimating the dominant size enlargement mechanism from the point of view of layering is presented. The dominant size enlargement mechanism is classified based on the probability of successful collisions, which is calculated from the probability of wet collisions and the probability of successful wet collisions (in terms of dissipation of kinetic energy), respectively. The probability of wet collisions follows from a new dynamic model for the wet surface fraction and a heat and mass transfer model for spray fluidized beds. Additionally, a method for calculating the probability of successful wet collisions based on the Stokes criterion is presented.

6.1.1 Estimating the probability of successful collisions

As shown in the modeling approach presented by Hussain et al. [108], the aggregation kernel depends on the probability of a wet collision $P_{coll,wet}$ (at least one droplet must be involved in the collision) and the probability that such a wet collision is successful in terms of kinetic energy dissipation $P_{coll,wet,suc}$, leading to agglomeration. The product of these parameters yields the probability of successful

collisions $P_{coll,suc}$, which is used in the present work to estimate the dominant size enlargement mechanism:

$$P_{coll,suc} = P_{coll,wet} \cdot P_{coll,wet,suc}. \tag{6.1}$$

Depending on this parameter, the dominant size enlargement mechanism will then be:

$$\text{dominant mechanism} = \begin{cases} \text{layering} & P_{coll,suc} \to 0, \\ \text{agglomeration} & P_{coll,suc} \to 1. \end{cases} \tag{6.2}$$

For layering to be dominant, the probability of successful collisions must approach zero, which can be due to a low probability of wet collisions ($P_{coll,wet} \to 0$), a low probability of successful wet collisions ($P_{coll,wet,suc} \to 0$), or both. If the probability of successful collisions is sufficiently large (ideally if $P_{coll,wet} \to 1$), agglomeration will be dominant. This condition will certainly be fulfilled if both the probability of wet collisions and the probability of successful wet collisions approach unity ($P_{coll,wet} \to 1$ and $P_{coll,wet,suc} \to 1$). Note that this approach neglects the influence of liquid and solid bridge breakage. Consequently, a major model assumption is that breakage does not dominate the process and therefore the probability of successful collisions calculated using Equation (6.1) can be used as a suitable parameter to estimate the dominant size enlargement mechanism. Below, the calculation of the considered probabilities is presented.

Probability of wet collisions

The probability of wet collisions depends on the wet surface fraction Ψ_{wet}. Following Rajniak et al. [173], it is assumed that all particles are wet and have the same wet surface fraction. Since only binary collisions are considered, either one or two droplets can be involved in a collision. The probability of wet collisions is then comprised of the probabilities of both individual events (exactly one droplet and exactly two droplets take part in a collision):

$$P_{coll,wet} = 2\Psi_{wet}(1 - \Psi_{wet}) + \Psi_{wet}^2 = 2\Psi_{wet} - \Psi_{wet}^2. \tag{6.3}$$

Probability of successful wet collisions

The probability of successful wet collisions is calculated based on the Stokes criterion in this approach. As described in Section 2.2.1, spherical, non-deformable particles, which are always larger in diameter than the sprayed droplets, are considered. Using these assumptions and the Stokes criterion for particles with rough surfaces given in Section 2.2.5, a critical particle size x_{crit} can be obtained:

$$x_{crit} = \frac{9}{4}\frac{\eta}{\varrho_p u_{coll}}\left(1 + \frac{1}{e'}\right)\ln\left(\frac{h_l}{h_a}\right). \tag{6.4}$$

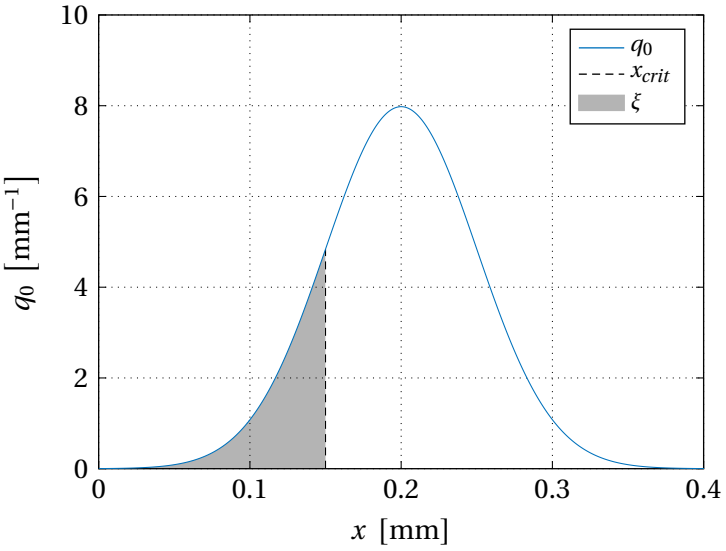

Figure 6.1: Plot of a particle size distribution (mean value and standard deviation equal to 0.2 mm and 0.05 mm, respectively) with x_{crit} equal to 0.15 mm and the corresponding fraction of particles with a fulfilled Stokes criterion.

Here, the liquid film height h_l is set to the height of the individual deposited droplets calculated according to Equation (3.10). Since the Stokes criterion is fulfilled, particles which are smaller than or equal to x_{crit} have the possibility to agglomerate upon a wet collision. The critical particle size is then used to calculate the fraction of particles with a fulfilled Stokes criterion from the number-based, normalized particle size distribution q_0:

$$\xi = \int_0^{x_{crit}} q_0 \, \mathrm{d}x \tag{6.5}$$

Figure 6.1 shows a normalized particle size distribution (normal distribution with a mean diameter of 0.2 mm and a standard deviation of 0.05 mm) and the fraction of particles with a fulfilled Stokes criterion for $x_{crit} = 0.15$ mm. In this example, ξ is equal to 0.16. The probability of successful wet collisions can then be calculated based on ξ as presented below.

Since the Stokes criterion presented by Ennis et al. [69] is derived for spherical particles with equal sizes, the size of the colliding particles should be smaller than x_{crit} in order for agglomeration to occur. As described in Chapter 2, the criterion can be extended to spherical particles of unequal size when the harmonic mean of the particle sizes is used. Correspondingly, a wet collision results in agglomeration when the harmonic mean is smaller than or equal to x_{crit}:

$$\frac{2x_1x_2}{x_1 + x_2} \leq x_{crit}. \tag{6.6}$$

Note that in this case many size combinations resulting in a successful collision are possible. For example, one of the two particles may be larger than x_{crit}, as long as the resulting harmonic mean is still smaller. Re-arranging Equation (6.6) yields x_2 as a function of x_1. Since this function has a pole

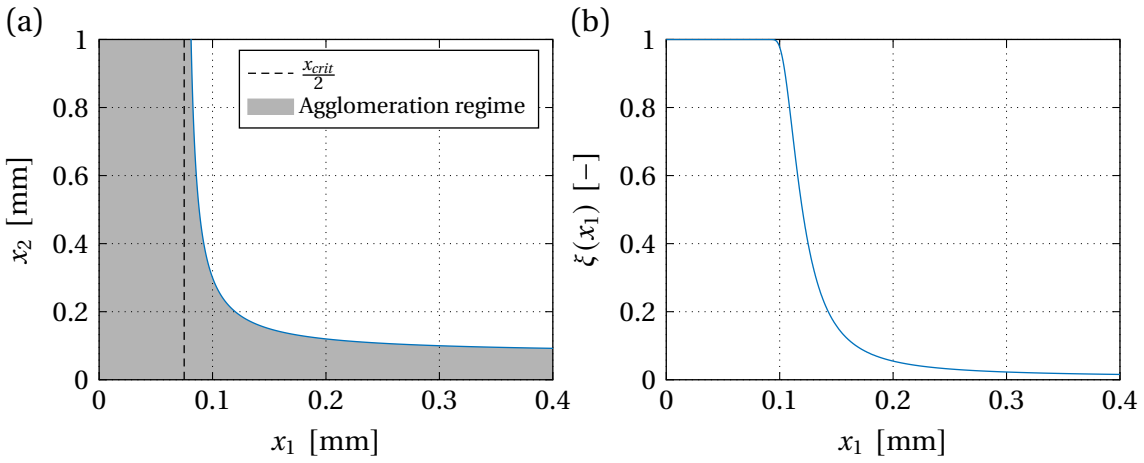

Figure 6.2: Plot of the particle size x_2 (a) and the corresponding fraction of particles with a fulfilled Stokes criterion ξ (b) as a function of x_1 for the corresponding example.

at $\frac{x_{crit}}{2}$, two cases are obtained:

$$x_2 \geq \frac{x_1 x_{crit}}{2x_1 - x_{crit}} \quad \text{for} \quad x_1 < \frac{x_{crit}}{2}, \tag{6.7a}$$

$$x_2 \leq \frac{x_1 x_{crit}}{2x_1 - x_{crit}} \quad \text{for} \quad x_1 > \frac{x_{crit}}{2}. \tag{6.7b}$$

Evaluating Equation (6.7) for the limit cases yields:

$$0 < x_1 < \frac{x_{crit}}{2}: \quad \lim_{x_1 \to 0^+} \frac{x_1 x_{crit}}{2x_1 - x_{crit}} = 0 \quad \text{and} \quad \lim_{x_1 \to \frac{x_{crit}}{2}^-} \frac{x_1 x_{crit}}{2x_1 - x_{crit}} = -\infty, \tag{6.8a}$$

$$\frac{x_{crit}}{2} < x_1 < \infty: \quad \lim_{x_1 \to \frac{x_{crit}}{2}^+} \frac{x_1 x_{crit}}{2x_1 - x_{crit}} = \infty \quad \text{and} \quad \lim_{x_1 \to \infty} \frac{x_1 x_{crit}}{2x_1 - x_{crit}} = \frac{x_{crit}}{2}. \tag{6.8b}$$

Both cases are shown in Figure 6.2a for the same example as in Figure 6.1. For $x_1 < \frac{x_{crit}}{2}$, x_2 must be larger than the value calculated with Equation (6.7a). Since this value lies between 0 and $-\infty$ and only positive values for x_2 are reasonable, the Stokes criterion is fulfilled for any value of x_2 when $x_1 < \frac{x_{crit}}{2}$, leading to agglomeration. For $x_1 > \frac{x_{crit}}{2}$, x_2 must be smaller than the value calculated with Equation (6.7b), which starts at ∞ and decreases asymptotically to $\frac{x_{crit}}{2}$. In this case, the particle size distribution plays a role in whether agglomeration occurs. The values of x_2 for which Equation (6.7) is fulfilled are represented by the gray area in Figure 6.2a for this example.

The fraction of particles with a fulfilled Stokes criterion can be calculated similarly to Equation (6.5). However, in this case ξ depends on x_1. The limit cases show that ξ equals unity for $x_1 < \frac{x_{crit}}{2}$. For $x_1 > \frac{x_{crit}}{2}$, it can be calculated in a similar way as shown above, leading to:

$$\xi(x_1) = \begin{cases} 1 & x_1 < \dfrac{x_{crit}}{2}, \\ \displaystyle\int_0^{x_2} q_0 \, \mathrm{d}x & x_1 > \dfrac{x_{crit}}{2}. \end{cases} \tag{6.9}$$

For the current example, ξ is shown in Figure 6.2b as a function of x_1. For small values of x_1, ξ is equal to unity and decreases to zero for increasing values of x_1.

The probability of successful wet collisions then follows from ξ and the probability distribution of the particle size, which is given by the normalized particle size distribution q_0:

$$P_{coll,wet,suc}(x, x_1) = \int_0^\infty \xi(x_1)\, q_0(x)\, \mathrm{d}x. \tag{6.10}$$

Theoretical validation

The proposed model to calculate the probability of successful wet collisions can be validated theoretically by comparison to results obtained with a Monte Carlo model. In this model, a set of particles with different diameters is created according to a given particle size distribution using the algorithm described in Appendix C. In this example, the particle size distribution shown in Figure 6.1 is used to create a set of 10^8 particles. Binary collisions between these particles are mimicked by randomly choosing two collision partners (according to their number). In each collision, both diameters are checked. A collision is then labeled "successful" when the harmonic mean diameter is smaller than a given critical value. In this example, 10^7 collisions are performed and the fraction of successful wet collisions is calculated. Note that it is implicitly assumed in this example that each collision is "wet" for simplification. Furthermore, besides checking whether a collision is successful, nothing else happens in this Monte Carlo model. Actual agglomeration, as in Chapter 5, is not considered since the purpose of this model is to validate Equation (6.10).

The Monte Carlo simulation was performed for different values of the critical particle size ranging between 0.15 mm and 0.4 mm. The results are then compared with the analytical model (Equation (6.10)) in Figure 6.3. An increasing x_{crit} leads to larger values of the probability of successful wet collisions since the fraction of particles with a fulfilled Stokes criterion is increased. The results obtained from Equation (6.10) and the Monte Carlo model agree well for all investigated values of the critical particle size.

In order to calculate the probability of successful collisions, a process model providing the necessary parameters is required. The probability of wet collisions (see Equation (6.3)) depends on the wet surface fraction, which is calculated using a novel approach within a spray fluidized bed drying model. Looking at the processes from the point of view of layering, a population balance model for layering growth is used to obtain the transient behavior of the particle size distribution, which is necessary to calculate the probability of successful wet collisions according to Equation (6.10). The process model is presented in the following sections.

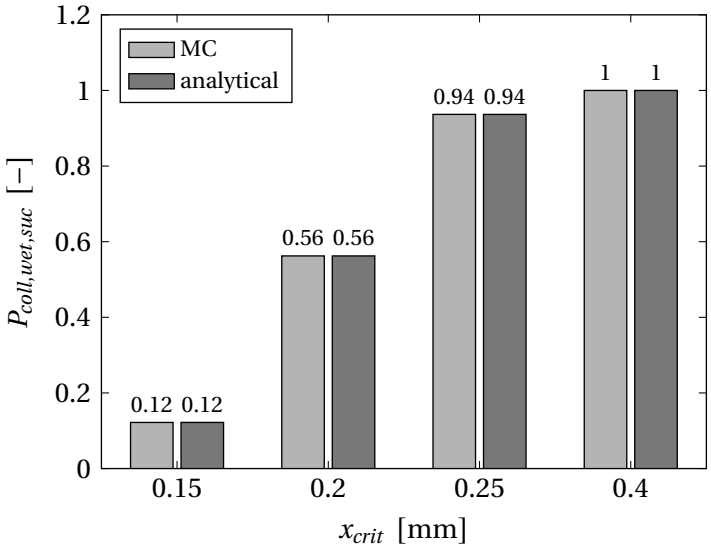

Figure 6.3: Comparison of the probability of successful wet collisions obtained with the proposed analytical model and a Monte Carlo model.

6.1.2 Heat and mass transfer model

The heat and mass transfer model for spray fluidized beds presented in this work is based on several assumptions for simplification (a complete list is given in Section 6.1.5). In this model three phases (liquid film, particle, and gas phase) are considered. The main assumptions for deriving the heat and mass transfer model are:

- no distinction between suspension and bubble phase,
- perfectly mixed solid and film phase, and
- plug flow of the gas phase.

The heat and mass flow rates considered in the model are shown in Figure 6.4. Heat can be exchanged between the gas and particle phase (index “gp”), between the particle and liquid phase (index “pl”), and between the gas and liquid phase (index “gl”), respectively. Mass and enthalpy transfer between the liquid and the gas phase due to evaporation is taken into account.

Below, the approach used to model the wet surface fraction is presented. Furthermore, the mass and enthalpy balances along with the corresponding kinetics are described.

Wet surface fraction

The wet surface fraction Ψ_{wet} is defined as the ratio between the wet surface area A_{pl} (interface between particle and liquid) and the total particle surface area $A_{p,tot}$. This parameter can lie between zero (the particles are completely dry) and unity (the whole surface area of the particles is covered by liquid). If $\Psi_{wet} \rightarrow 1$, the surface area of the particles is completely wetted and the evaporation rate is

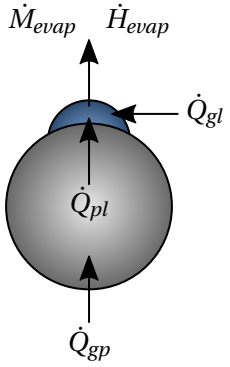

Figure 6.4: Schematic representation of the considered mass, enthalpy, and heat flow rates in the presented model.

equal to its maximum. Correspondingly, the evaporation rate lies between zero and the maximum for $0 \leq \Psi_{wet} \leq 1$. Changes in the wet surface area can be attributed to changing wet surface fraction due to drying and changing total particle surface area due to size enlargement:

$$\frac{\mathrm{d}A_{pl}}{\mathrm{d}t} = \frac{\mathrm{d}}{\mathrm{d}t}\left(\Psi_{wet}A_{p,tot}\right) = \Psi_{wet}\frac{\mathrm{d}A_{p,tot}}{\mathrm{d}t} + A_{p,tot}\frac{\mathrm{d}\Psi_{wet}}{\mathrm{d}t}. \tag{6.11}$$

The change of total surface area can be calculated from the transient behavior of the second moment of the particle size distribution n:

$$\Psi_{wet}\frac{\mathrm{d}A_{p,tot}}{\mathrm{d}t} = \Psi_{wet}\pi\int_0^\infty x^2\frac{\partial n}{\partial t}\mathrm{d}x. \tag{6.12}$$

In contrast to Heinrich and Mörl [141], who assume a coherent film, the liquid phase is here described by a number of individual droplets deposited on the particle surface. Similar to the presented Monte Carlo models, the droplets are assumed to be monodisperse, each covering a certain surface area of the particle. Coalescence or overlapping of droplets are not taken into account. Using these assumptions, the wet surface area can be described based on the contact area between a deposited droplet and the particle $A_{contact}$ (footprint), the droplet mass M_{drop}, and the liquid mass M_l:

$$\frac{\mathrm{d}A_{pl}}{\mathrm{d}t} = \frac{A_{contact}}{M_{drop}}\frac{\mathrm{d}M_l}{\mathrm{d}t}. \tag{6.13}$$

The transient behavior of the wet surface fraction can then be written as follows, assuming that it does not exceed unity:

$$\frac{\mathrm{d}\Psi_{wet}}{\mathrm{d}t} = \begin{cases} \dfrac{1}{A_{p,tot}}\left[\dfrac{A_{contact}}{M_{drop}}\dfrac{\mathrm{d}M_l}{\mathrm{d}t} - \Psi_{wet}\pi\displaystyle\int_0^\infty x^2\frac{\partial n}{\partial t}\mathrm{d}x\right] & \Psi_{wet} < 1, \\ 0 & \text{otherwise.} \end{cases} \tag{6.14}$$

The geometry of a deposited droplet is assumed to be a spherical cap, described by the model proposed by Meric and Erbil [151]. The contact area between the droplet and the particle required in Equation (6.14) is calculated using Equation (3.12). Since this parameter depends on the droplet size (volume) and the contact angle, the influence of the wetting parameters on the wet surface fraction and therefore the dominant size enlargement mechanism can be taken into account. In this study, shrinkage and an increasing viscosity of deposited droplets during drying is not considered. The droplet properties are calculated using the initial droplet volume, which follows from the droplet diameter. Extensions in this direction can be made without conceptional difficulties.

Mass and enthalpy balances

The water mass and enthalpy balances for the gas phase are given in Equation (6.15) and Equation (6.16), respectively. Since the gas phase is modeled assuming plug flow, the water mass and enthalpy depend on the spatial location in the fluidized bed, represented by a normalized height coordinate ζ. Both the water mass and enthalpy are transported along ζ with flow rates equal to $\dot{M}_{w,g}$ and $\dot{H}_g$, respectively. Furthermore, the water mass changes due to the mass flow rate of evaporation $\dot{M}_{evap}$ and the enthalpy changes due to the enthalpy flow rate of evaporation $\dot{H}_{evap}$, the heat flow rates between the gas and particle phase $\dot{Q}_{gp}$, and the gas and liquid phase $\dot{Q}_{gl}$:

$$\frac{\partial M_{w,g}}{\partial t} = -\frac{\partial \dot{M}_{w,g}}{\partial \zeta} + \dot{M}_{evap}, \tag{6.15}$$

$$\frac{\partial H_g}{\partial t} = -\frac{\partial \dot{H}_g}{\partial \zeta} + \dot{H}_{evap} - \dot{Q}_{gp} - \dot{Q}_{gl}. \tag{6.16}$$

In the presented model, the sprayed material is instantly distributed between the film phase and the particle phase. This means that the liquid part of the sprayed material is added to the film phase and the solid part is added to the particle phase. In this way, the kinetics of the underlying process (e.g., crystallization or precipitation) is not explicitly modeled. Then, the mass of the liquid film phase M_l depends on the liquid part of the spraying rate and the mass flow rate of evaporation. The liquid film enthalpy H_l changes due to evaporation and the heat flow rates between the liquid phase and the gas and particle phase, respectively. Since the liquid phase is assumed to be perfectly mixed, no dependency on the spatial location in the fluidized bed needs to be considered:

$$\frac{\mathrm{d}M_l}{\mathrm{d}t} = \dot{M}_{spray,l} - \overline{\dot{M}}_{evap}, \tag{6.17}$$

$$\frac{\mathrm{d}H_l}{\mathrm{d}t} = -\overline{\dot{H}}_{evap} + \overline{\dot{Q}}_{gl} + \dot{Q}_{pl}. \tag{6.18}$$

The mass of the particle phase M_p can be calculated from the third moment of the particle size distribution. The enthalpy H_p depends on the heat flow rates between the particle phase and the gas and liquid phase, respectively. The mass and enthalpy of the particle phase are independent of the

spatial location as well:

$$M_p = \frac{\pi}{6}\varrho_p \mu_3 = \frac{\pi}{6}\varrho_p \int_0^\infty x^3 n \, \mathrm{d}x, \tag{6.19}$$

$$\frac{\mathrm{d}H_p}{\mathrm{d}t} = \overline{\dot{Q}}_{gp} - \dot{Q}_{pl}. \tag{6.20}$$

Since the mass flow rate of evaporation, the corresponding enthalpy flow rate and the heat flow rates between the gas phase and the liquid phase, and between the gas phase and the particle phase depend on the spatial location ζ, their average values are used in the above shown mass and enthalpy balances for the film and particle phase. The averaged values are calculated as follows:

$$\overline{\dot{M}}_{evap} = \int \dot{M}_{evap} \, \mathrm{d}\zeta, \tag{6.21}$$

$$\overline{\dot{H}}_{evap} = \int \dot{H}_{evap} \, \mathrm{d}\zeta, \tag{6.22}$$

$$\overline{\dot{Q}}_{gl} = \int \dot{Q}_{gl} \, \mathrm{d}\zeta, \tag{6.23}$$

$$\overline{\dot{Q}}_{gp} = \int \dot{Q}_{gp} \, \mathrm{d}\zeta. \tag{6.24}$$

Kinetics

The mass flow rate of evaporation is calculated using the following equation:

$$\dot{M}_{evap} = \beta \varrho_g A_{gl} (Y_{sat}(T_l) - Y) \quad \text{with} \quad A_{gl} = \Psi_{wet} \frac{A_{drop}}{A_{contact}} A_{p,tot}. \tag{6.25}$$

In this equation, β is the mass transfer coefficient calculated according to Groenewold and Tsotsas [143] as shown in Appendix B, ϱ_g is the density of the fluidization gas, A_{gl} is the gas liquid interface (curved droplet surface area), $Y_{sat}(T_l)$ is the saturation moisture content of the fluidization gas at liquid film temperature T_l calculated using Equation (A.11), and Y is the moisture content of the bulk gas. The gas liquid interface is calculated using the wet surface fraction, the total particle surface area and the ratio of the curved droplet surface area and the contact area. In contrast to Heinrich and Mörl [141], the curved droplet surface area and the contact area are not identical in the present approach due to the used droplet geometry model. As a result, the ratio of A_{drop} and $A_{contact}$ must be taken into account when calculating the area of the interface between gas and liquid. Equation (6.25) shows that the wet surface fraction directly influences the mass flow rate of evaporation. The resulting drying rate reaches its maximum if $\Psi_{wet} \to 1$ and goes to zero if $\Psi_{wet} \to 0$, resembling the behavior of particles which first dry from their surface and then from their interior. The curved surface area of the droplet A_{drop} is calculated using Equation (3.9).

The moisture content of the bulk gas is calculated from the water mass in the gas phase and the mass

of dry gas in the fluidized bed:

$$Y = \frac{M_{w,g}}{M_{g,dry}} \quad \text{with} \quad M_{g,dry} = \varepsilon_{bed} \frac{\pi}{4} d_{bed}^2 \varrho_g h_{bed}. \tag{6.26}$$

The calculation of the porosity and the height of the bed is performed as shown in Appendix B. The bed diameter d_{bed} is given by the diameter of the fluidized bed chamber. Similar to Equation (6.26), the moisture content of the particles is calculated using the liquid film mass and the dry bed mass given by the mass of the particles:

$$X = \frac{M_l}{M_p}. \tag{6.27}$$

The enthalpy flow rate used in the differential equations shown above is calculated as follows:

$$\dot{H}_{evap} = \dot{M}_{evap}\left(c_v T_l + \Delta h_{evap}\right). \tag{6.28}$$

The heat flow rates between the respective phases are calculated using the following equations:

$$\dot{Q}_{gl} = \alpha_{gl} A_{gl}\left(T_g - T_l\right), \tag{6.29}$$

$$\dot{Q}_{pl} = \alpha_{pl} A_{pl}\left(T_p - T_l\right) \quad \text{with} \quad A_{pl} = \Psi_{wet} A_{p,tot}, \tag{6.30}$$

$$\dot{Q}_{gp} = \alpha_{gp} A_{gp}\left(T_g - T_p\right) \quad \text{with} \quad A_{gp} = (1 - \Psi_{wet}) A_{p,tot}. \tag{6.31}$$

In these equations, α is the heat transfer coefficient between the respective phases. The heat transfer coefficient for the gas-particle heat transfer α_{gp} is calculated according to Groenewold and Tsotsas [143] as shown in Appendix B. Following Heinrich and Mörl [141], the gas-liquid heat transfer coefficient α_{gl} is assumed to be equal to α_{gp}. Heat transfer between particle and liquid is assumed to be purely conductive, neglecting any convection. For this special case (spherical particle in contact with a fluid), α_{pl} can be calculated using a Nusselt number equal to two. The interfaces between the particle and liquid phase A_{pl} and the gas and particle phase A_{gp} represent the wet surface area and the dry surface area, respectively. They are calculated as shown in Equation (6.30) and Equation (6.31).

The following equations are used to relate the temperature of each phase with the corresponding enthalpy:

$$H_g = M_{g,dry}\left(c_g T_g + Y\left(c_v T_g + \Delta h_{evap}\right)\right), \tag{6.32}$$

$$H_p = M_p c_p T_p, \tag{6.33}$$

$$H_l = M_l c_l T_l. \tag{6.34}$$

In these equations, c_g, c_v, c_p, and c_l are the specific heat capacities of the gas phase (air), vapor, particle phase, and the liquid phase (water), respectively. The calculation of the specific heat capacities of air, vapor, and water is shown in Appendix A. The specific heat capacity of the particles is given in the corresponding tables along with further simulation parameters.

6.1.3 Growth model

The transient behavior of the particle size distribution is modeled with a population balance for layering growth for a single compartment, see Section 2.3.2:

$$\frac{\partial n(t,x)}{\partial t} = -\frac{\partial (Gn)}{\partial x}. \tag{6.35}$$

Growth kinetics G is calculated using Equation (2.28) and Equation (2.29) with $\Lambda_2 = 1$ (sprayed liquid material distribution is related to the total particle surface area). Note that only the solid part of the sprayed material is subjected to the growth kinetics G as described above.

Layering growth leads to a changing particle density. Since a batch process is considered here, the particle density can be calculated using the third moment μ_3, solid density ϱ_s, solid layer porosity ε_{layer}, and the initial values of the particle density $\varrho_{p,0}$ and the third moment $\mu_{3,0}$, respectively:

$$\varrho_p(t) = \varrho_{p,0}\frac{\mu_{3,0}}{\mu_3(t)} + \varrho_s\left(1-\varepsilon_{layer}\right)\frac{\mu_3(t)-\mu_{3,0}}{\mu_3(t)}. \tag{6.36}$$

6.1.4 Solution of the model equations

The system of differential equations is solved numerically in MATLAB using the solver ode15s. The partial differential equations (Equations (6.15), (6.16), and (6.35)) are discretized using a finite volume scheme to transform them into ordinary differential equations. Additionally, a flux-limiter function given by Koren [174] is used in case of Equation (6.35) to reduce numerical diffusion. The derivation of the used discretized equations is given in detail in Appendix D.

6.1.5 Summary of model assumptions

The assumptions used in the above described model are summarized below:

- no distinction between suspension and bubble phase,
- perfectly mixed solid and film phase,
- plug flow of gas phase,
- no dominant influence of breakage,
- spherical, non-deformable particles,
- normal, binary collisions,
- all particles are wet with identical wet surface fraction,
- sprayed droplets are monodisperse and spherical,
- droplets attain spherical cap geometry instantly after deposition,

- no overlapping or coalescence of deposited droplets,
- shrinkage and increasing viscosity of drying droplets is not considered,
- sprayed material is instantly distributed among the film phase and particle phase,
- heat transfer coefficient between gas and liquid phase is equal to heat transfer coefficient between gas and particle phase,
- heat transfer between particle and liquid phase is purely conductive (Nusselt number equal to two).

6.2 Simulation study

6.2.1 Influence of process and wetting parameters

A simulation study was performed to investigate the influence of inlet gas temperature, viscosity, and wetting parameters (droplet size and contact angle) on the probability of successful collisions representing the dominant size enlargement mechanism. The simulation parameters and the initial and boundary conditions used to solve the system of differential equations are given in Table 6.1 and Table 6.2, respectively. The simulation parameters correspond to a lab-scale spray fluidized bed coating process in which glass beads are coated with a sodium benzoate solution. The specific heat capacity of glass particles is taken from Kuchling [175]. Terrazas-Velarde et al. [123] suggest a coefficient of restitution for glass particles of 0.8 based on literature values ranging between 0.7 and 0.9. The height of surface asperities (surface roughness) is assumed to be small, in the range of 1 µm, following Dernedde [132]. The collision velocity is calculated according to the method described in Section 3.2.5. In this case, only the mean value $\overline{u}_{coll}$ of the collision velocity distribution is used. Note that this value is kept constant (i.e., it is not adjusted according to changing particle properties during the simulation). The viscosity of the sodium benzoate solution is calculated using an empirical correlation based on measurements using a Höppler viscometer, see Equation (A.19). This equation allows to calculate the viscosity of a sodium benzoate solution with a solid mass fraction of 0.3 based on its temperature. In the simulation, the viscosity is calculated at liquid film temperature T_l. In order to study the influence of liquid viscosity, two cases are considered. In the simulations denoted by “low viscosity”, the viscosity is calculated with Equation (A.19). In case of simulations denoted by “high viscosity”, the same equation is used, but the obtained value is multiplied with a factor equal to 3, mimicking an increased viscosity due to the addition of thickener. The resulting liquid viscosities at 20 °C are 4.18 Pa s (“low viscosity”) and 12.54 Pa s (“high viscosity”). Depending on the material, even higher viscosities are possible as shown by Dewettinck et al. [59], who used different gums as coating material. The simulation results are presented below in Figure 6.5 to Figure 6.9 and summarized in Table 6.3.

Figure 6.5 shows the transient behavior of the particle size distribution and the influence of inlet gas temperature on the wet surface fraction, viscosity, and the critical particle size during 1 h of process

Table 6.1: Simulation parameters (parameters for the reference case are printed in bold).

Parameter	Value	Unit
Particle material	glass	
Sprayed solid material	NaB	
Sprayed liquid material	water	
Bed diameter d_{bed}	0.15	m
Bed mass M_{bed}	0.5	kg
Mass flow rate of the fluidization gas $\dot{M}_g$	40	$\mathrm{kg\,h^{-1}}$
Particle density ϱ_p	2500	$\mathrm{kg\,m^{-3}}$
Specific heat capacity particles c_p	729	$\mathrm{J\,kg^{-1}\,K^{-1}}$
Spraying rate $\dot{M}_{spray}$	0.7	$\mathrm{kg\,h^{-1}}$
Solid mass fraction w_s	0.3	–
Droplet diameter d_{drop}	25, **50**, 100	µm
Contact angle θ	20, **40**, 60	°
Solid density ϱ_s	1440	$\mathrm{kg\,m^{-3}}$
Solid layer porosity ε_{layer}	0.3	–
Collision velocity (mean) $\overline{u}_{coll}$	0.42	$\mathrm{m\,s^{-1}}$
Coefficient of restitution e'	0.8	–
Height of surface asperities h_a	1	µm
Process time t	3600	s

Table 6.2: Initial and boundary conditions (parameters for the reference case are printed in bold).

Parameter	Value	Unit
$B_0(t)$	0	$\mathrm{s^{-1}}$
$n(t=0,x)$	$n_0 = f(d_{10,0}, \sigma_{x,0})$	$\mathrm{mm^{-1}}$
$d_{10,0}$	0.2	mm
$\sigma_{x,0}$	0.05	mm
$\Psi_{wet}(t=0)$	0	–
$Y_{in} = Y(t, \zeta = 0) = Y(t = 0, \zeta)$	1	$\mathrm{g\,kg^{-1}}$
$T_{g,in} = T_g(t, \zeta = 0) = T_g(t = 0, \zeta)$	50, **70**, 95	°C
$X(t=0)$	0	$\mathrm{g\,kg^{-1}}$
$T_l(t=0)$	20	°C
$M_p(t=0)$	0.5	kg
$T_p(t=0)$	50, **70**, 95	°C

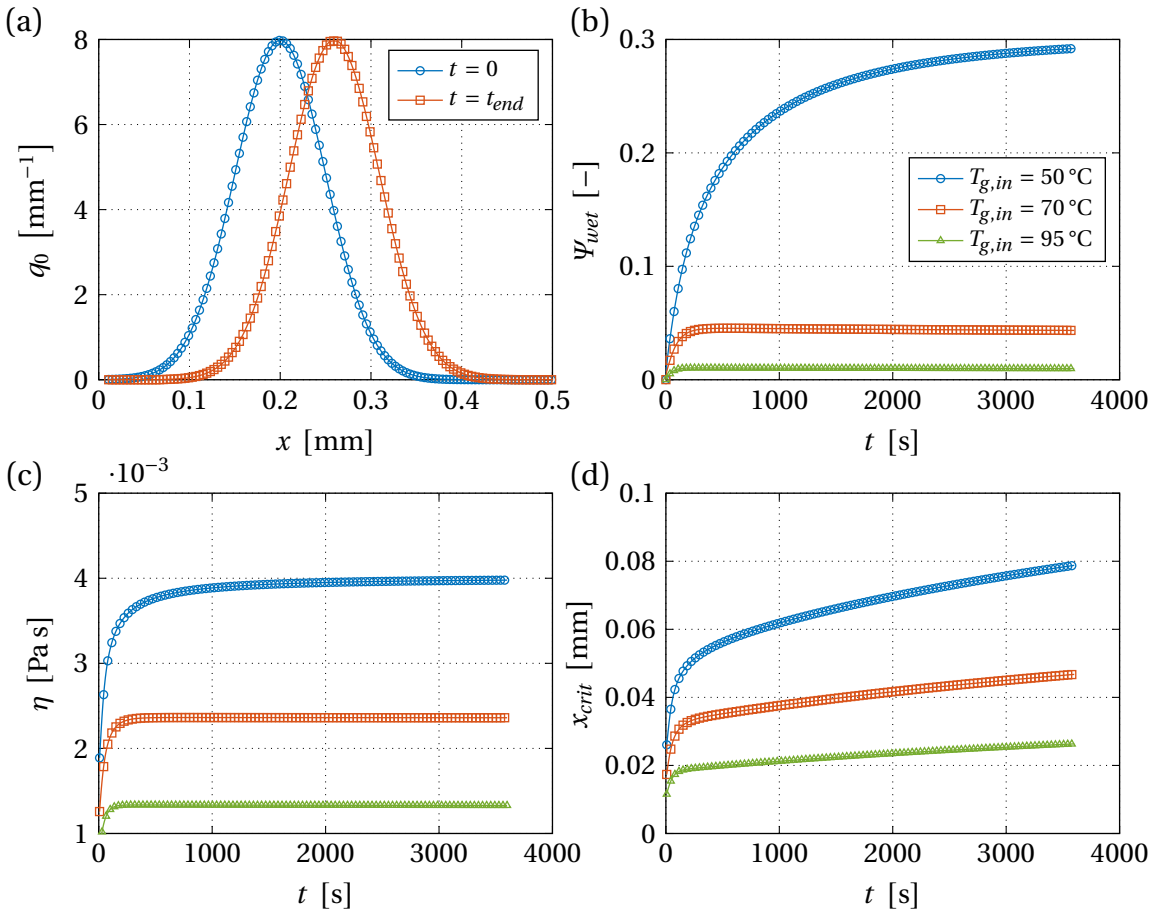

Figure 6.5: Plot of the particle size distribution (before and after layering growth) (a), and influence of the inlet gas temperature on the wet surface fraction (b), liquid viscosity (c), and the critical particle size (d).

time. Figure 6.5a shows that the particle size distribution is shifted towards larger sizes (mean value increased from 0.2 mm to 0.26 mm), while its shape is preserved. The wet surface fraction is shown in Figure 6.5b. An increasing inlet gas temperature leads to smaller values of the wet surface fraction ranging between 0.29 (50 °C) and 0.01 (95 °C) since the evaporation rate is higher. As a result, less liquid material is present on the particle surface. The viscosity of the solution decreases as well since the liquid film temperature is increased, see Figure 6.5c. Figure 6.5d shows the critical particle size, which decreases when temperature is higher due to lower viscosity. Therefore, agglomeration is less likely to occur for high inlet gas temperatures since the wet surface fraction and the critical particle size are decreased, lowering both the probability of wet collisions and the probability of successful wet collisions, respectively.

The influence of temperature and viscosity on the considered probabilities is shown in Figure 6.6 and Table 6.3. Figure 6.6a shows the probability of wet collisions for different inlet gas temperatures, following the behavior of the wet surface fraction from Figure 6.5b. The values range between 0.5 (50 °C) and 0.02 (95 °C). Figure 6.6b and Figure 6.6c show the influence of inlet gas temperature on the probability of successful wet collisions for low and high viscosity. In both cases, the values are

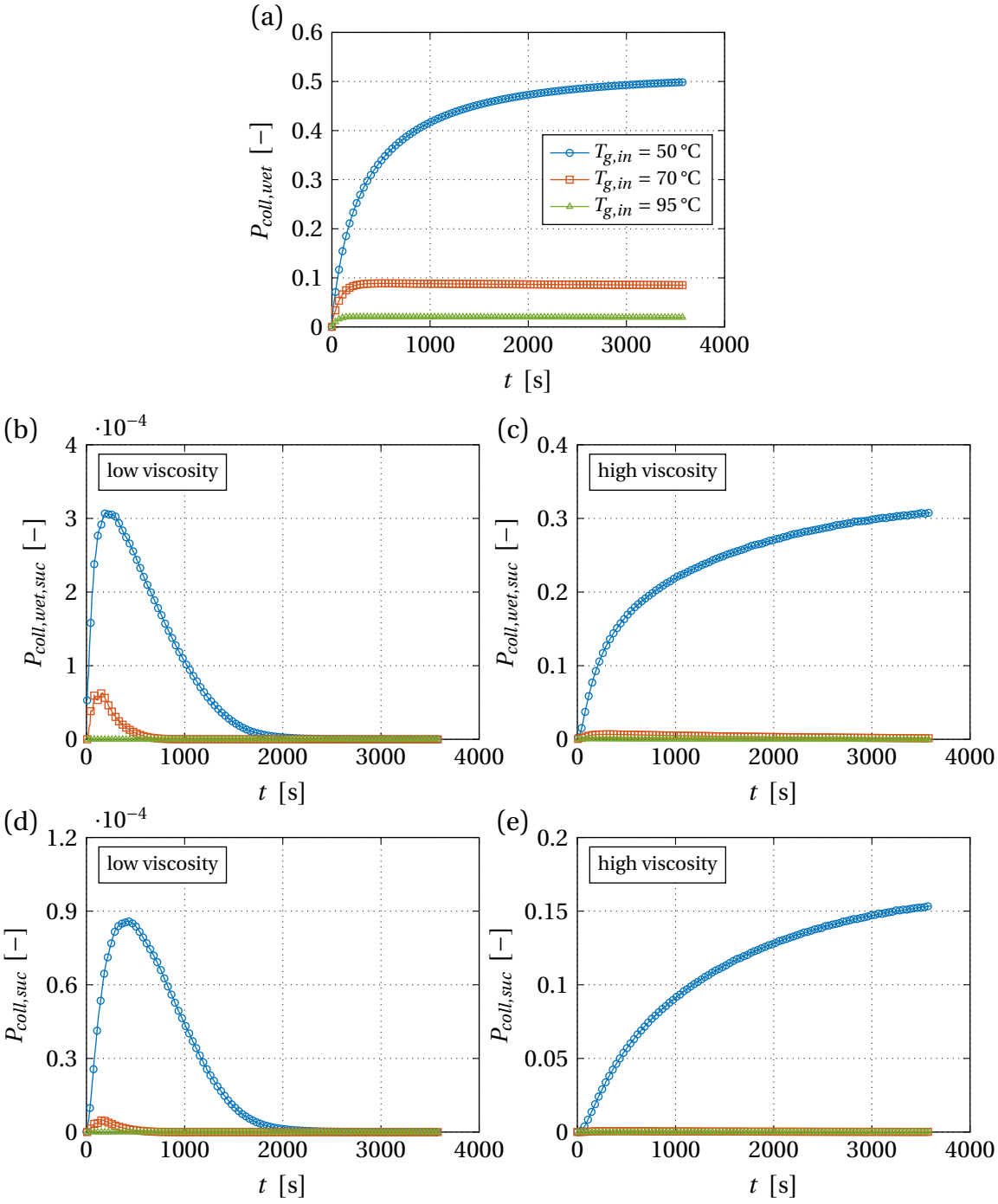

Figure 6.6: Influence of the inlet gas temperature on the probability of wet collisions (a), the probability of successful wet collisions for low viscosity (b) and high viscosity (c), and the probability of successful collisions for low viscosity (d) and high viscosity (e).

smaller when the temperature is increased due to smaller values of x_{crit}, see Figure 6.5d. In case of low viscosity, the resulting values are very small, indicating that wet collisions are rarely successful. If the viscosity is increased, the probability of successful wet collisions is significantly increased, resulting in values ranging between 0.3 (50 °C) and 0.0005 (95 °C). The resulting probability of successful collisions is shown in Figure 6.6d and Figure 6.6e. In both cases, an increased inlet gas temperature leads to smaller values. In case of low viscosity, agglomeration is unlikely since the probability of successful collisions is smaller than 0.001 for all considered temperatures. However in case of high viscosity, significant agglomeration may occur in case of (50 °C) since up to 15 % of all collisions are successful. For higher temperatures, the values are smaller than 0.001 and agglomeration is unlikely.

Figure 6.7 and Table 6.3 show the influence of wetting parameters (droplet size and contact angle) on the wet surface fraction and the probability of wet collisions at low and high inlet gas temperatures. According to Figure 6.7a, the wet surface fraction is increased when droplet size and contact angle are decreased. Smaller droplets lead to a decreased contact area $A_{contact}$ and droplet mass M_{drop}. Since $A_{contact} \sim d_{drop}^2$ and $M_{drop} \sim d_{drop}^3$, the wet surface fraction increases, see Equation (6.14). At the same time, a higher wet surface fraction increases the evaporation rate, while the ratio between the curved surface area and the contact area is constant (cf. Equation (6.25)). As a result, the liquid mass is reduced, which would in turn decrease the wet surface fraction. Eventually, the first effect prevails and the wet surface fraction is increased in case of smaller droplets. A smaller contact angle leads to a larger contact area, but does not influence the droplet mass, leading to an increased wet surface fraction. As a result, the evaporation rate is higher as well. However, in this case the ratio between the curved surface area and the contact area is reduced, which would lead to a smaller evaporation rate. Under the given conditions, the first effect prevails and the evaporation rate is increased. Similar to the above discussed influence of the droplet size, this would decrease the wet surface fraction since the liquid mass is reduced as well. Eventually, the influence of the contact angle on the wet surface fraction through Equation (6.14) is predominant and the wet surface fraction increases when the contact angle is smaller. Figure 6.7b shows the influence of wetting parameters on the wet surface fraction for a high inlet gas temperature. In this case, the evaporation rate is higher compared to Figure 6.7a. When the droplet size is decreased, the influence of droplet geometry, which would increase the wet surface fraction, is balanced by the influence of drying, which would decrease the wet surface fraction, leading to a constant wet surface fraction. However, when the contact angle is reduced, the influences of droplet geometry and drying do not balance each other. In this case, the ratio between the curved surface area and the contact area also decreases as discussed above. The resulting evaporation rate is decreased, leading to a positive influence on the wet surface fraction. Therefore, the contact angle still has an influence on the wet surface fraction at high temperatures, although it is small under the given conditions. Figure 6.7c and Figure 6.7d show that the behavior of the probability of successful wet collisions follows the trend of the wet surface fraction.

Figure 6.8 and Table 6.3 show the influence of the wetting parameters on the probability of successful wet collisions at low and high inlet gas temperatures for low and high liquid viscosity. The probability of successful wet collisions is smaller when the droplet size and the contact angle are decreased since

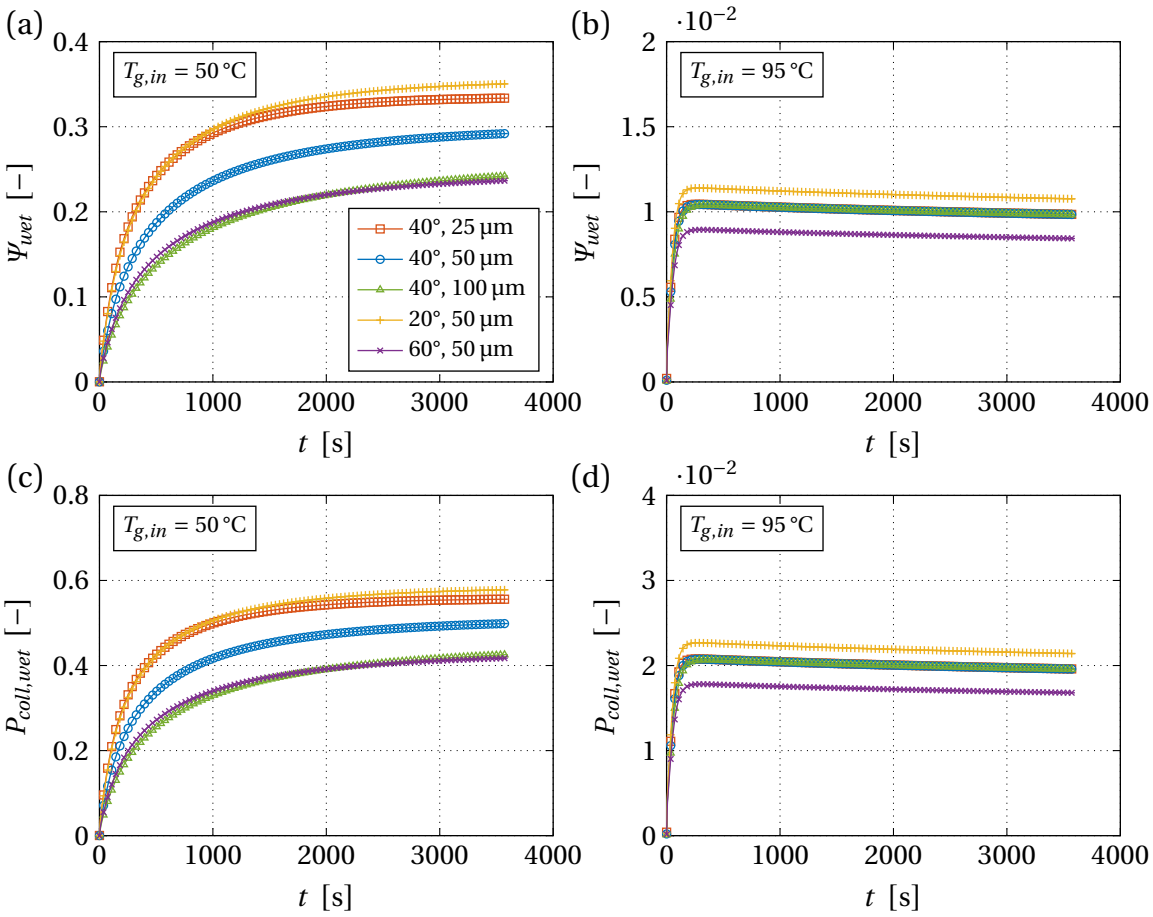

Figure 6.7: Influence of droplet size and contact angle on the wet surface fraction at an inlet gas temperature of 50 °C (a) and 95 °C (b) and the probability of wet collisions at an inlet gas temperature of 50 °C (c) and 95 °C (d).

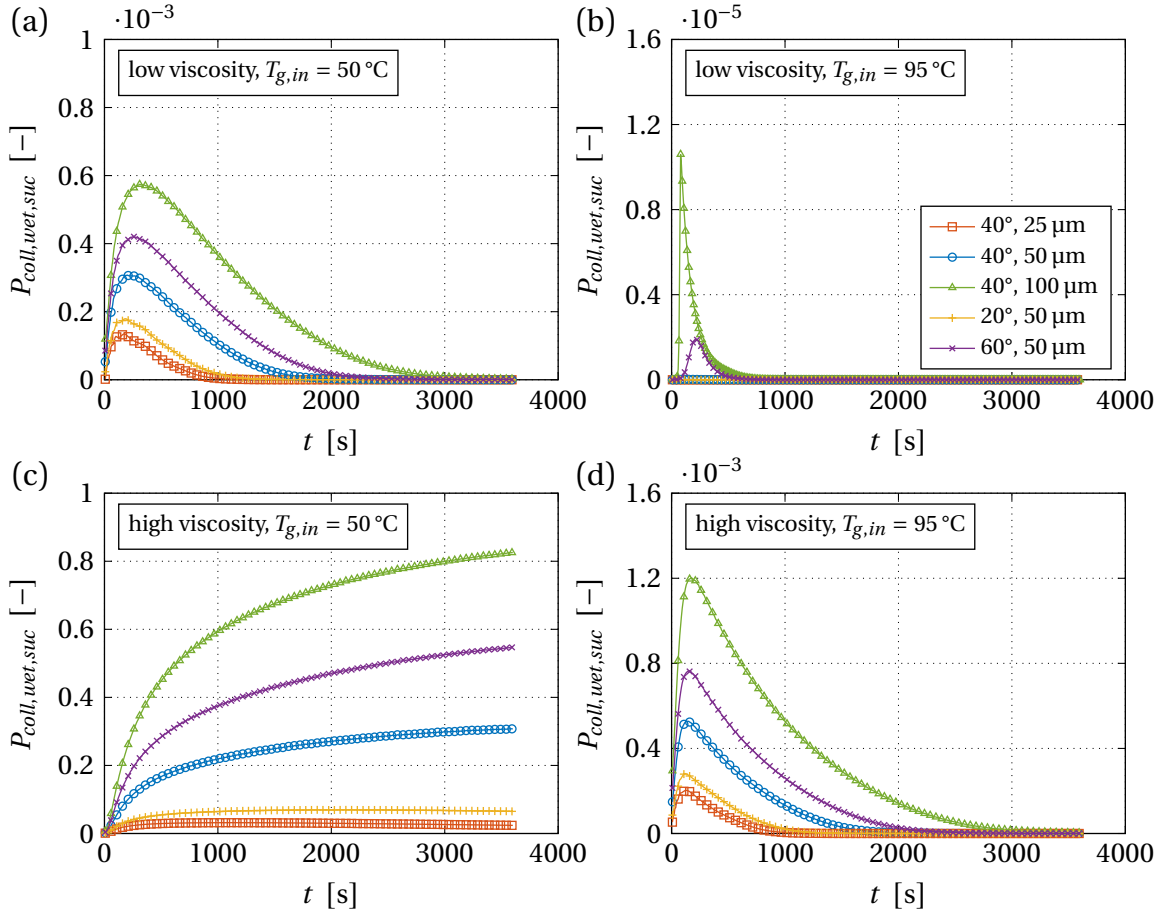

Figure 6.8: Influence of droplet size and contact angle on the probability of successful wet collisions for low viscosity at an inlet gas temperature of 50 °C (a) and 95 °C (b) and for high viscosity at an inlet gas temperature of 50 °C (c) and 95 °C (d).

in both cases the resulting droplet height is smaller (see Equation (3.10)), decreasing the critical particle size. In case of low viscosity, the probability of successful wet collisions is small, while in case of high viscosity the values are significantly increased. As discussed above, the probability of successful wet collisions is higher when lower inlet gas temperatures are used due to higher liquid viscosity at low temperatures.

The influence of droplet size, contact angle, viscosity, and inlet gas temperature on the probability of successful collisions is shown in Figure 6.9 and Table 6.3. Although in case of 50 °C the probability of wet collisions is relatively high, ranging between 0.4 and 0.6, the probability of successful collisions is small when a low viscosity is used due to a low probability of successful wet collisions. At 95 °C, the probability of successful collisions is even smaller since both the probability of wet collisions and the probability of successful wet collisions are low. For high liquid viscosity, the probability of successful collisions is significantly increased due to a larger probability of successful wet collisions. Significant agglomeration is to be expected in case of high viscosity and 50 °C since $P_{coll,suc}$ exceeds 0.001 in all simulations shown in Figure 6.9c, especially for large droplet sizes and contact angles since up to 35 % of all collisions are successful. Layering will be the dominant mechanism for all

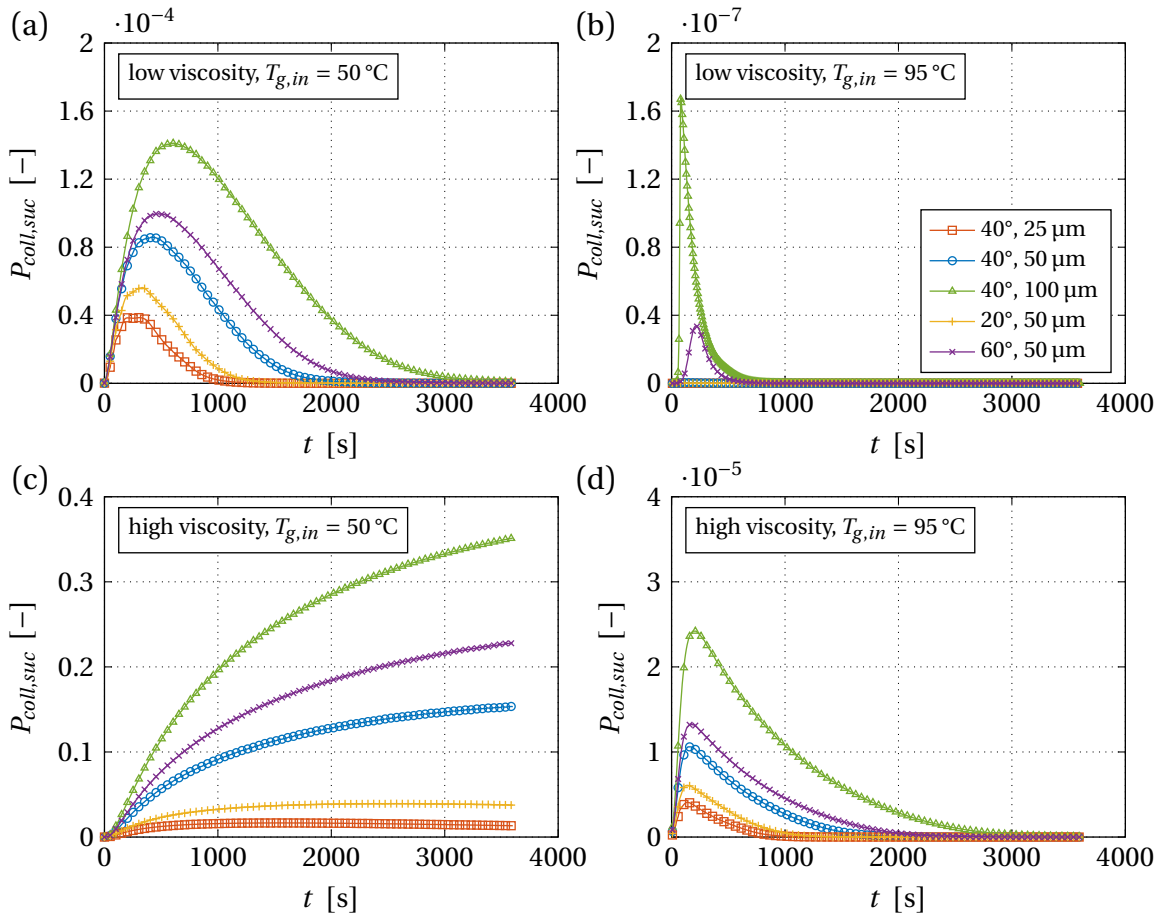

Figure 6.9: Influence of droplet size and contact angle on the probability of successful collisions for low viscosity at an inlet gas temperature of 50 °C (a) and 95 °C (b) and for high viscosity at an inlet gas temperature of 50 °C (c) and 95 °C (d).

Table 6.3: Summarized influence of the inlet gas temperature, droplet size, contact angle and liquid viscosity on the probability of wet collisions, probability of successful wet collisions and the probability of successful collisions.

Parameter	$T_{g,in}\uparrow$	$d_{drop}\uparrow$	$\theta\uparrow$	$\eta\uparrow$
$P_{coll,wet}$	↓	↓	↓	–
$P_{coll,wet,suc}$	↓	↑	↑	↑
$P_{coll,suc}$	↓	↑	↑	↑

other simulations shown in Figure 6.9 since $P_{coll,suc}$ is smaller than 0.001 in these cases.

The above shown simulation results show that the probability of successful collisions is influenced by inlet gas temperature, liquid viscosity, droplet size and contact angle. In order to link the probability of successful collisions with the dominant size enlargement mechanism, a classification based on simulations and experimental data is presented.

6.2.2 Regime maps

In total 63 simulations based on experimental investigations of spray fluidized bed processes available in the literature were performed to classify the dominant size enlargement mechanism based on the probability of successful collisions. In these experiments, either layering or agglomeration is dominant, which is in each case determined by the authors of the respective study (e.g., by SEM images, measured particle size distributions, or the fraction of agglomerated particles). Since in the simulation the dominant size enlargement mechanism is unknown, particle growth due to layering or agglomeration is not considered (i.e., the particle size distribution and density are kept constant). The simulations were performed with the corresponding parameters until the considered probabilities reach a steady state. These steady state values represent the conditions in each simulation and are linked to the dominant size enlargement mechanism determined by the authors of the study. Comments on the selection of the simulation parameters of each study are given below before presenting the results.

In this work, three studies focusing on spray fluidized bed agglomeration performed by Terrazas-Velarde [15], Hampel [176], and Jiménez et al. [177] and three studies performed by Rieck et al. [57] and Saleh et al. [178, 179] dealing with spray fluidized bed coating are considered. The corresponding simulation parameters are given in Table 6.4. Terrazas-Velarde [15] and Hampel [176] used porous γ-Al_2O_3particles and non-porous glass beads, which were agglomerated using aqueous HPMC solution. Glass beads were also used by Jiménez et al. [177], along with aqueous acacia gum as binder. Jiménez et al. [177] used a conical fluidized bed with a diameter of 140 mm at the bottom and 225 mm at the top. Based on these values, a mean diameter of the fluidized bed chamber is calculated since the presented model has been derived for cylindrical fluidized beds. Jiménez et al. [177] report a relatively high bed porosity of 0.95, which is obtained in the simulation as well despite using a mean diameter of the fluidized bed chamber. Rieck et al. [57] coated γ-Al_2O_3particles and glass beads with aqueous sodium benzoate solution. Saleh et al. [178, 179] focus on coating of sand particles by spraying aqueous sodium chloride solution. In these studies, the mass flow rate of the fluidization gas was not directly stated and had to be calculated based on the given bed diameter and excess gas velocity. Additionally, the authors report the bed temperature instead of the inlet gas temperature, which was adjusted in the simulation to match the given bed temperature. The inlet gas moisture content was estimated based on the generation of the gas flow. In case of Terrazas-Velarde [15], Rieck et al. [57], Hampel [176], and Saleh et al. [178, 179] pressurized air was used and a correspondingly small moisture content of 1 g kg^{-1} has been assumed. According to Jiménez [180], ambient air was used

for fluidization. In these simulations, a moisture content equal to 9 g kg^{-1} based on a temperature of 20 °C and a relative humidity of 0.6 was used.

In each study, most of the necessary material properties were given along with the process parameters. However, certain parameters were missing and had to be either assumed or taken from other sources. References and estimation methods regarding the material parameters are summarized below.

- The particle densities were in each case given by the authors in the respective study.
- The coefficient of restitution of glass beads and γ-Al_2O_3particles are given by Terrazas-Velarde [15] and the corresponding value for sand particles is taken from Derakhshani et al. [181].
- Contact angles between aqueous HPMC and glass beads or γ-Al_2O_3particles are given by Terrazas-Velarde [15] based on photo-optical measurements. Values for the other systems (acacia gum-glass, sodium benzoate-glass, sodium benzoate-γ-Al_2O_3, sodium chloride-sand) were not available in literature. As discussed in Section 4.3.2, the influence of the solid mass fraction on the contact angle was found to be negligible by Terrazas-Velarde [15]. Based on this observation and since all liquids used in the considered experimental studies are water-based, the contact angle for the systems acacia gum-glass, sodium benzoate-glass, and sodium chloride-sand is estimated to be 40° and 60° in case of sodium benzoate-γ-Al_2O_3.
- The droplet sizes were given by the original authors in case of Terrazas-Velarde [15], Hampel [176], and Saleh et al. [178, 179]. Jiménez et al. [177] report some values, but do not present detailed information. For a reference experiment 35 µm are stated, which is used in each of the corresponding simulations. In case of Rieck et al. [57], the droplet size was not given, but it was subsequently calculated using an empirical correlation for externally mixing two-fluid nozzles reported by Lefebvre and McDonell [168]. The viscosity and surface tension used in this calculation are given in Appendix A. The corresponding droplet diameters are in the range of 60 µm, which is the value used in the simulations.
- The height of surface asperities for glass and γ-Al_2O_3particles is taken from Dernedde [132]. No values were available for sand particles. It is assumed that the surface structure of sand and glass particles is similar and thus the same value is used.
- The specific heat capacity of the particles is taken from literature: Kuchling [175] (glass and sand), and Burgschweiger et al. [140] (γ-Al_2O_3).
- The viscosity of aqueous HPMC is taken from Dernedde [132] and the viscosity of aqueous sodium chloride follows from Zhang and Han [182]. The viscosity of the acacia gum solution is given by Jiménez et al. [177]. Since the temperature dependency of the above mentioned viscosities is unknown, constant values were used. In case of Rieck et al. [57], the above mentioned correlation based on measured viscosities was used, see Equation (A.19).
- The density of the sprayed solid was given by Terrazas-Velarde [15], Rieck et al. [57], and Hampel [176] in case of HPMC and sodium benzoate, respectively. The values for acacia gum and sodium chloride are taken from safety data sheets [183, 184].

Table 6.4: Simulation parameters for each experimental study used to derive the classification of the dominant size enlargement mechanism.

Parameter	Hampel [176]	Terrazas-Velarde [15]	Jiménez et al. [177]	Rieck et al. [57]	Saleh et al. [178]	Saleh et al. [179]	Unit
Particle material	γ-Al_2O_3(A) glass (G)	γ-Al_2O_3(A) glass (G)	glass	γ-Al_2O_3(A) glass (G)	sand	sand	
Sprayed solid material	HPMC	HPMC	acacia gum	NaB	NaCl	NaCl	
Sprayed liquid material	water	water	water	water	water	water	
Dominant mechanism	agglomeration	agglomeration	agglomeration	layering	layering	layering	
Bed diameter d_{bed}	0.15	0.15	0.184	0.15	0.1	0.1	m
Bed mass M_{bed}	0.5 (A) 0.85 (G)	0.3 (A) 0.5 (G)	0.25–0.75	0.5 (A) 1 (G)	1.25–2.53	2	kg
Spraying rate $\dot{M}_{spray}$	0.2–0.3	0.1–0.5	0.172–0.502	0.5–1.28	0.274–0.598	0.46	$kg\,h^{-1}$
Mass flow rate of the fluidization gas $\dot{M}_g$	20–30	58 (A) 70–110 (G)	160	75 (A) 120 (G)	11	10–17.5	$kg\,h^{-1}$
Inlet gas temperature $T_{g,in}$	50–100	30–80	60–80	50–95	185–255	100–145	°C
Inlet gas moisture content Y_{in}	1	1	9	1	1	1	$g\,kg^{-1}$
Particle density ϱ_p	1040 (A) 2500 (G)	1400 (A) 2500 (G)	2450	1280 (A) 2500 (G)	2630	2630	$kg\,m^{-3}$
Solid density ϱ_s	1390	1390	1400	1440	2170	2170	$kg\,m^{-3}$
Coefficient of restitution e'	0.6 (A) 0.8 (G)	0.6 (A) 0.8 (G)	0.8	0.6 (A) 0.8 (G)	0.9	0.9	–

Table 6.4: (continued).

Parameter	Hampel [176]	Terrazas-Velarde [15]	Jiménez et al. [177]	Rieck et al. [57]	Saleh et al. [178]	Saleh et al. [179]	Unit
Height of asperities h_a	5 (A) 1 (G)	5 (A) 1 (G)	1	5 (A) 1 (G)	1	1	µm
Droplet diameter d_{drop}	40	80	35	60	15–60	20	µm
Contact angle θ	60 (A) 40 (G)	60 (A) 40 (G)	40	60 (A) 40 (G)	40	40	°
Collision velocity (mean) $\overline{u}_{coll}$	0.16–0.24 (A) 0.13–0.19 (G)	1.17 (A) 1.53–2.26 (G)	0.88	2.16 (A) 2.82 (G)	0.23	0.28–1.20	$m\,s^{-1}$
Solution viscosity η	5.98 (w_s = 0.02) 21.44 (w_s = 0.04) 61.86 (w_s = 0.06)	21.44 (w_s = 0.04) 147.11 (w_s = 0.08) 383.90 (w_s = 0.10)	43 (w_s = 0.20) 200 (w_s = 0.30)	4.18 (20 °C) (Equation (A.19))	1.05 (w_s = 0.10) 1.26 (w_s = 0.20) 1.40 (w_s = 0.25)	1.26	mPa s
Solid mass fraction w_s	0.02–0.06	0.04–0.10	0.20–0.30	0.30	0.10–0.25	0.20	–
Specific heat capacity particles c_p	944 (A) 729 (G)	944 (A) 729 (G)	729	944 (A) 729 (G)	840	840	$J\,kg^{-1}\,K^{-1}$
Mean particle diameter d_{10}	150 (A) 120 (G)	360 (A) 400 (G)	160	610 (A) 530 (G)	229	267–639	µm
Number of simulations	22	14	8	8	8	3	–

- The measured particle size distributions were available in case of Rieck et al. [57], Hampel [176], and Saleh et al. [178] in the form of either files or tables. In case of Terrazas-Velarde [15], plots of the measured particle size distributions of the glass beads and γ-Al_2O_3particles were given. Normal distributions were then created in the simulation to visually fit the plots of the distributions. In case of Jiménez et al. [177] and Saleh et al. [179], no plots or data were available other than the mean diameter. In these cases, a normal distribution was used as well, where the standard deviation was set to 10 % of the mean diameter.
- The collision velocity is calculated according to the method proposed by Dernedde [132], which is described in Section 3.2.5.

The results are shown in Figure 6.10. The coordinate axes represent the probability of wet collisions and the probability of successful wet collisions, respectively. Contour lines indicate the level of the probability of successful collisions. For each simulation, the steady-state values of the probability of wet collisions and the probability of successful wet collisions are calculated as described above. Based on these values, one data point can be drawn into the plot per simulation. Figure 6.10 shows that the simulations corresponding to experiments in which layering was dominant are located on the left side of the plot, where the probability of successful wet collisions is low. In fact, the probability of successful wet collisions is 0 in these simulations, while the steady-state probability of wet collisions ranges between 0.00016 and 0.3. The simulations corresponding to experiments in which agglomeration was dominant are placed on the right side of the plot at high values of the probability of wet collisions. These values range between 0.92 (one point) and 1, while the probability of wet collisions varies between 0.0014 and 0.42. Exceptions are three data points, which belong to agglomeration experiments performed by Terrazas-Velarde [15]. These are placed on the left side of the plot since the predicted probability of successful wet collisions is 0. In the corresponding experiments, the smallest amount of HPMC was used ($w_s = 0.04$) leading to a relatively low liquid viscosity. Terrazas-Velarde [15] reports that during these experiments an initial non-growth period was observed. This means that, initially, the Stokes criterion is not fulfilled. Size enlargement by agglomeration is therefore not possible under these conditions, which is also found in the simulations shown in Figure 6.10. However, as the droplets dry in the experiment they increase in viscosity (up to the range of 10 Pa s), which eventually enables size enlargement by agglomeration. Since this mechanism is not included in the presented model and the probability of successful wet collisions is calculated with initial droplet properties (height and viscosity), the presented model cannot predict the dominant size enlargement mechanism for these experiments. Nevertheless, Figure 6.10 indicates that the border between layering and agglomeration can be characterized by $P_{coll,suc} = 0.001$. This means that for agglomeration to become dominant, the probability of successful collisions does not need to be high (i.e., close to unity). Instead, exceeding a rather small value of 0.001 is enough to shift the dominant size enlargement mechanism towards agglomeration. Consequently, layering will be dominant when the probability of successful collisions is lower than 0.001. Based on this classification, the agglomeration regime and the layering regime are represented by the gray and white areas in Figure 6.10, respectively.

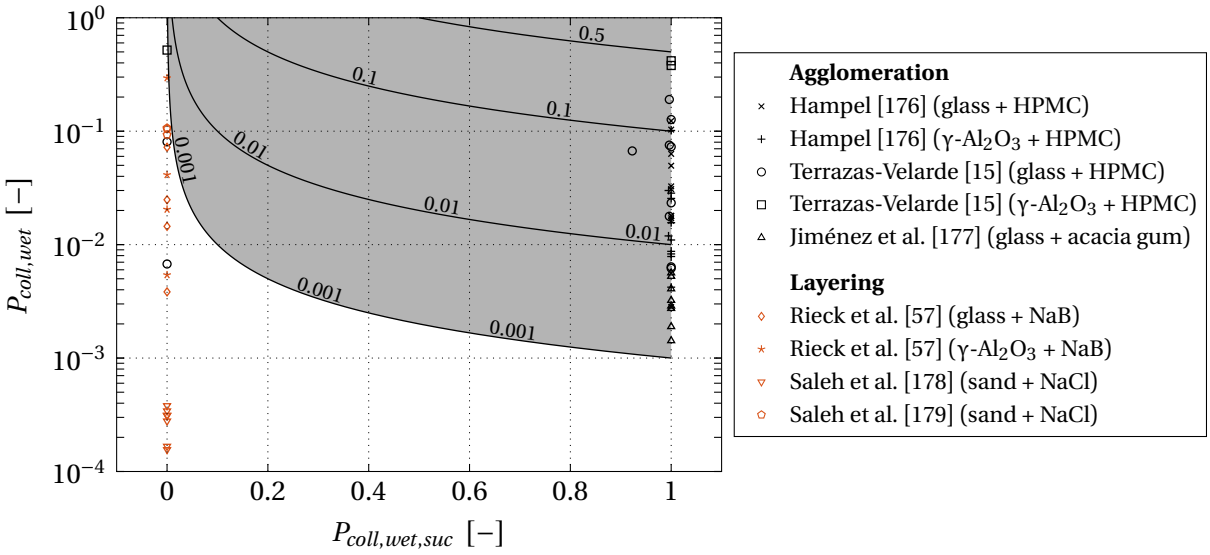

Figure 6.10: Regime map consisting of contour lines illustrating different levels of the probability of successful collisions and data points representing simulation results corresponding to experimental investigations available in the literature.

Since the collision velocity is usually a distributed parameter in spray fluidized bed processes, the influence of this parameter is further investigated. Therefore, the simulations shown in Figure 6.10 were repeated twice with a small collision velocity (reduced by 50 % compared to the original value) and a high collision velocity (increased by 50 % compared to the original value). The results are shown in Figure 6.11 (small collision velocity) and Figure 6.12 (high collision velocity). In case of a small collision velocity, data points corresponding to experiments with dominant agglomeration are shifted to the right side of the plot since the probability of successful wet collisions is increased. Two data points from the experiments performed by Terrazas-Velarde [15] are affected and shifted to the right. The probability of successful wet collisions is increased from 0.92 to unity, and from 0 to 0.18. The latter was previously plotted in the layering regime and is now in the agglomeration regime. Two data points from the same study are still predicted to be in the layering regime by the simulation. Other data points are not affected since their values of the probability of successful wet collisions were already unity (cf. Figure 6.10). The data points corresponding to experiments with dominant layering are not changed. In case of a high collision velocity, data points corresponding to experiments with dominant agglomeration are shifted to the left side of the plot since the probability of successful wet collisions is decreased. The values of the probability of successful wet collisions now range between 0.29 and 1. In comparison to Figure 6.10, more data points (previously three, now seven) from the study of Terrazas-Velarde [15] are placed on the left side of the plot since the probability of successful wet collisions is 0, although agglomeration is dominant in the experiments. In these four cases, the solid mass fraction of HPMC is equal to 0.08. Similar as described above, the missing mechanism of increasing viscosity during drying causes the prediction of the wrong size enlargement mechanism. The data points corresponding to experiments with dominant layering are not affected. The above shown figures indicate that the collision velocity may significantly influence

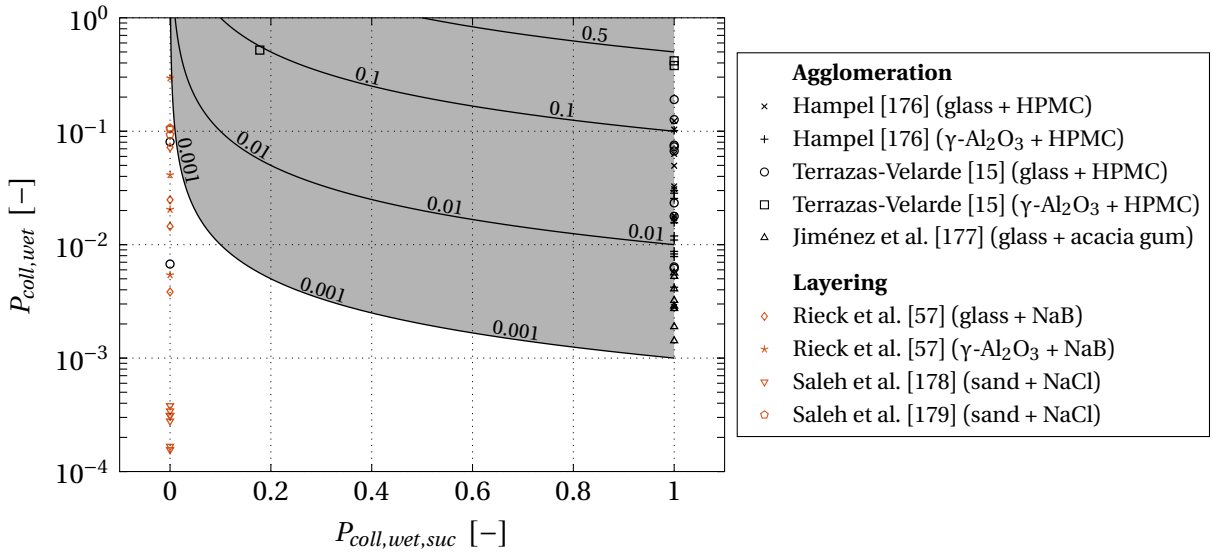

Figure 6.11: Regime map illustrating simulation results obtained with a small collision velocity.

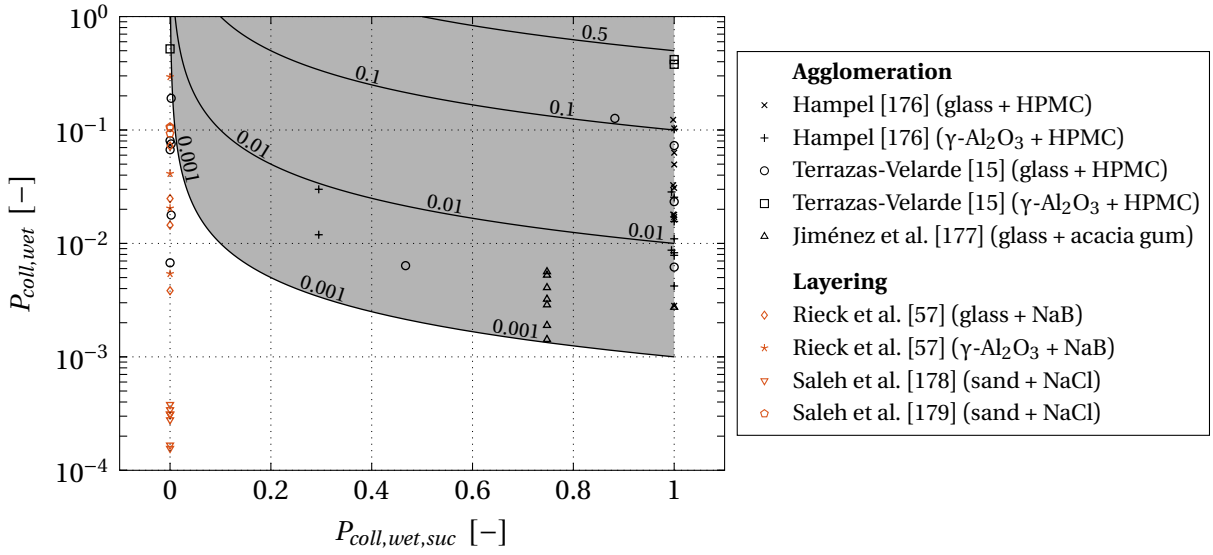

Figure 6.12: Regime map illustrating simulation results obtained with a high collision velocity.

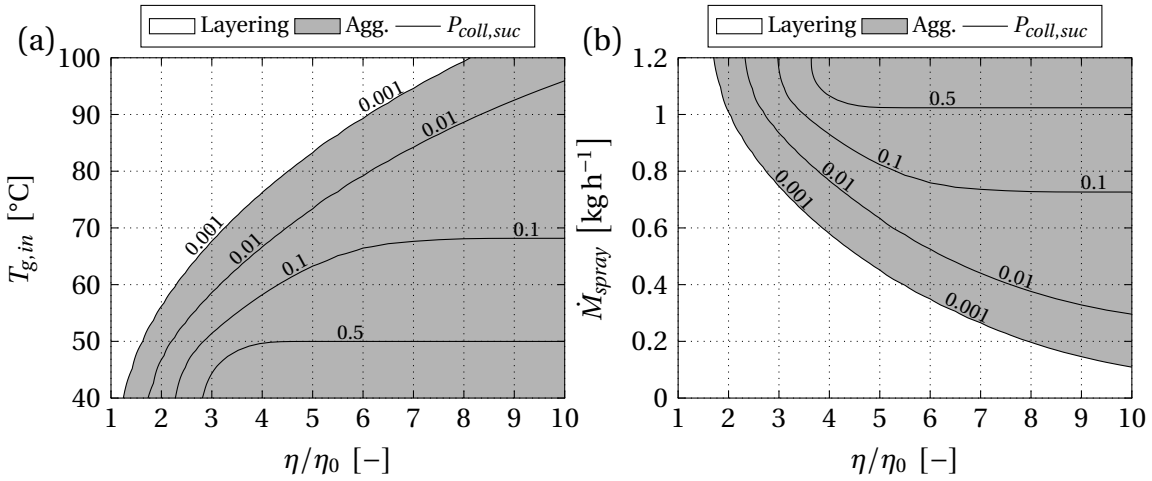

Figure 6.13: Regime maps obtained for the simulation parameters given in Table 6.1 and Table 6.2 for a changing inlet gas temperature (a) and spraying rate (b).

the probability of successful wet collisions. However, they also show that the border of the size enlargement mechanisms may still be described by a probability of successful collisions equal to 0.001, although the collision velocity was varied in this relatively wide range.

The presented classification based on the probability of successful collisions allows for creating specific regime maps, which show the influence of actual process parameters rather than probabilities on the dominant size enlargement mechanism. Figure 6.13 shows two regime maps, each based on 3000 simulations, which were created using the same parameters as in the previously shown simulation study, see Table 6.1 and Table 6.2. The parameters of the reference case (printed in bold) were used here. The regime map in Figure 6.13a shows the influence of inlet gas temperature on the dominant size enlargement mechanism. The inlet gas temperature was varied between 40 °C and 100 °C. The viscosity was calculated with Equation (A.19) as in the simulation study presented in Section 6.2.1, but the constant factor was varied between 1 and 10. Figure 6.13b shows the regime map for a spraying rate varying between 0 kg h^{-1} and 1.2 kg h^{-1}. The contour lines represent different levels of the probability of successful collisions and the gray and white areas illustrate the agglomeration and layering regime based on the above presented classification. Figure 6.13 shows that layering is dominant for high temperatures and low viscosity as well as low spraying rates and low viscosity.

The influence of droplet size and contact angle can also be shown using regime maps. Figure 6.14 shows the border between the size enlargement mechanisms (defined by $P_{coll,suc} = 0.001$) for different droplet sizes and contact angles. The other simulation parameters correspond to those in Table 6.1 and Table 6.2. The border between layering and agglomeration is shown in Figure 6.14a for droplet sizes equal to 25 µm and 100 µm and in Figure 6.14b for contact angles equal to 20° and 60°. These plots illustrate that both large droplets and large contact angles increase the size of the area representing dominant agglomeration.

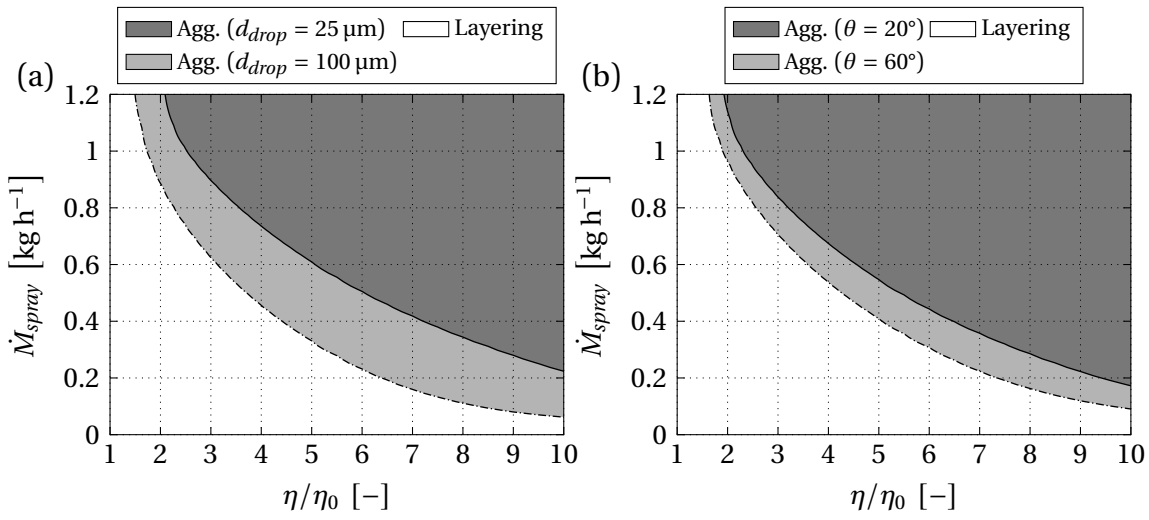

Figure 6.14: Influence of droplet size (a) and contact angle (b) on the size of the agglomeration and layering regime.

Chapter 7

Conclusions and outlook

A Monte Carlo model for coating and layering granulation was derived by modeling droplet deposition, deposited droplet drying, and calculating the layer thickness generated by dry droplets as described in Chapter 3. Chapter 4 shows that the presented model is able to predict the transient behavior of several important product properties such as the intra-particle layer thickness distribution (for each particle considered in the simulation), inter-particle layer thickness distribution, particle size distribution, coating mass distribution, coating time distribution and the coated surface fraction. The transient behavior of the coated surface fraction was compared to an analytical model, showing good agreement. Furthermore, the transient behavior of the coefficient of variation of both the intra-particle layer thickness distribution and the coating mass distribution were compared to analytical models available in literature [157, 165], which showed good agreement as well. A simulation study was performed to investigate the influence of droplet deposition on the intra-particle and inter-particle layer thickness distribution and the particle size distribution. It was found that the influence on the intra-particle layer thickness distribution is small, while properties of the population (inter-particle layer thickness distribution and particle size distribution) are significantly changed by the droplet deposition mechanism. Additionally, a simulation study was performed to investigate the influence of inlet gas temperature, spraying rate, dry droplet porosity, solid mass fraction, droplet size, and contact angle on the intra-particle layer thickness distribution (at the end of the coating process and upon reaching full coverage) and the coating time distribution. The simulations show that the mean of the intra-particle layer thickness distribution is only increased when the dry droplet porosity is increased. Otherwise, this value remains constant since the same solid mass was added to the particle system in each simulation. The corresponding standard deviation is larger when the layer thickness generated by a single dry droplet is increased, which occurs when increasing the dry droplet porosity, solid mass fraction, droplet size and contact angle. For the same reason, both mean and standard deviation of the intra-particle layer thickness distribution (upon reaching full coverage) increase in the same cases. The coating time is increased when the number flow rate of droplets and the footprint of a single droplet are smaller, which occurs when decreasing the spraying rate and increasing the solid mass fraction, droplet size, and contact angle. It was also shown that the drying time of droplets does not significantly influence the product properties in the investigated range. Further simulations were performed with parameters corresponding to experimental studies of spray

fluidized bed coating. The simulation results were compared to experimental data on intra-particle layer thickness distributions and particle size distributions, showing good agreement.

In comparison to macroscopic approaches, which use population balances to calculate the transient behavior of property distributions, the presented Monte Carlo model for coating and layering granulation is able to predict a variety of property distributions at once, which has not been available in literature before. The simulation results were validated both theoretically and experimentally. The presented model can therefore be used to predict intra-particle and inter-particle properties, which may be useful for process design. However, an application for process optimization and control is still limited due to higher computational cost in comparison to macroscopic models. Although validation yielded good agreement in the investigated cases, the model may be extended by removing restrictions generated by model assumptions.

Future research should focus on extending the model regarding compartments and calculating the porosity of dry droplets. It has been shown that without considering compartments the variation of the inter-particle mean layer thickness is very small in combination with droplet deposition related to the particle surface area. By introducing compartments (e.g., spray and drying zones), a larger variation of the inter-particle layer thickness distributions is to be expected, which may be more realistic. Additionally, the proposed model is not able to predict the porosity of the formed solid layer. Instead, this value has to be measured, e.g., by X-ray micro-tomography. The porosity of dry droplets is then assumed to be equal to the measured layer porosity. A more advanced model for deposited droplet drying including the structure formation is necessary. Several assumptions regarding the multiphase flow can be eliminated by coupling the Monte Carlo model with a CFD-DEM approach as shown by Jiang et al. [185].

A Monte Carlo model for binder-less agglomeration of amorphous particles due to glass transition was derived by modeling droplet deposition, glass transition, binary collisions, breakage, and droplet drying as described in Chapter 3. Based on these micro-scale events and processes and three agglomeration criteria, the model presented in Chapter 5 is able to calculate the transient behavior of the particle size distribution during an agglomeration process. Using the example of maltodextrin particles, a simulation study investigating the influence of droplet deposition on the particle size distribution was performed. It was shown that the droplet deposition mechanism strongly influences the particle size distribution. In a further simulation study, the influence of inlet gas temperature, spraying rate, and the DE value of maltodextrin particles on the agglomeration criteria was presented in detail. Opposing trends on the microscopic level have been identified. The governing trend on the macro-scale was then discussed using experimental data and corresponding simulations. In the investigated range, the first two agglomeration criteria (at least one wet droplet must be present at the contact point and the solid temperature must exceed the sticky point temperature) seem to dominate the macroscopic behavior. It was found that agglomeration is faster and therefore leads to larger agglomerates when the inlet gas temperature is lower and the spraying rate as well as the DE value are higher. A comparison between experimental data and corresponding simulations shows that the agglomeration behavior is correctly described by the model for varying inlet gas temperatures and

spraying rates. However, the model predicts faster agglomeration kinetics for increasing DE values, which is not fully supported by the experiments.

The presented model is the first one to account for binder-less agglomeration due to glass transition. Despite of several assumptions, the model is able to correctly describe the influence of process parameters on the macroscopic agglomeration behavior. The influence of the DE value could not be fully described by the presented version of the model, which is considered to be a result of the assumptions in the drying model (gas-side controlled drying). Nevertheless, if the necessary model parameters are available, the model may be used for process design. However, an application in optimization or process control is unlikely due to the computation times. Instead, an extended macroscopic model similar to the one presented by Hussain et al. [108] for binder-less agglomeration could be derived, which may then be applied to optimization or process control. Beyond that, the Monte Carlo method was extended in terms of taking an initial particle size distribution into account. Therefore, an algorithm was developed, which is able to create particle diameters according to an arbitrary measured size distribution. The concept of positions and the scaling procedure for mass conservation were modified accordingly.

Future work should focus on eliminating assumptions made in deriving the presented model. As indicated by the drying experiments of maltodextrin surfaces in the magnetic suspension balance, the material grade may have an influence on drying. Therefore, it could be interesting to investigate wetting and drying behavior of amorphous single particles (instead of tablets) experimentally. In this way, the drying model could be improved, enhancing the predictive ability of the model. Beyond that, the description of the collision frequency should be improved. Although models available in literature may be used to calculate the collision frequency, it was necessary to reduce the calculated value by a constant factor in the presented model similar to previously developed Monte Carlo models. This parameter significantly influences agglomeration kinetics and particle properties in the simulation and could be described more accurately using CFD-DEM approaches. Assumptions regarding the agglomerate structure such as spherical particles, constant agglomerate porosity, and maximum coordination number should also be eliminated. This topic is currently under investigation by Singh and Tsotsas [186], who are able to predict the morphology of agglomerates in addition to the kinetics.

A macroscopic model for estimating the dominant size enlargement mechanism for spray fluidized bed processes from the point of view of layering is presented in Chapter 6. The dominant size enlargement mechanism is linked to the probability of successful collisions, which can be calculated using the probability of wet collisions and the probability of successful wet collisions (in terms of dissipation of kinetic energy). The probability of wet collisions is calculated from the wet surface fraction, which follows from a new dynamic model and a heat and mass transfer model for spray fluidized beds. The probability of successful wet collisions is then calculated from the Stokes criterion using a new model, which is validated theoretically by a Monte Carlo method. A simulation study is performed, which shows the influence of inlet gas temperature, viscosity, droplet size, and contact angle on the probability of successful collisions. It is shown that the agglomeration tendency decreases when

the inlet gas temperature is high and the viscosity, droplet size, and contact angle are decreased. Further simulations based on experimental work published in literature were performed, which are used to classify the experimentally observed dominant size enlargement mechanism based on the calculated probability of successful collisions. The results indicate that layering will be dominant if this parameter is smaller than 0.001. Consequently, agglomeration will become dominant if this value is exceeded. The obtained classification is then used to create regime maps, which are able to show the border between the size enlargement mechanisms for different parameters.

The presented model combines microscopic and macroscopic parameters in order to estimate the dominant size enlargement mechanism for spray fluidized bed processes. The model includes a new dynamic model for calculating the wet surface fraction, taking the geometry of deposited droplets and drying conditions into account. Further, a new theoretically validated model for calculating the probability of successful wet collisions based on the Stokes criterion is presented. Both models were not available in literature before. An interesting result of the simulation study based on experiments taken from literature is that for agglomeration to become dominant, the probability of successful collisions does not need to be high (i.e., close to unity). Instead, a relatively small value of 0.001 represents the border between the size enlargement mechanisms based on the considered simulations and experiments. The presented model may be used in process design to estimate the dominant size enlargement mechanism. Further applications may be a comprehensive macroscopic process model considering particle size enlargement by simultaneous layering and agglomeration including the effect of drying conditions and wetting parameters on the process kinetics.

Future research should include model extensions regarding changing droplet properties during drying. As it was shown in this work, considering the initial droplet properties alone may lead to prediction of the wrong size enlargement mechanism if droplet properties such as viscosity change significantly during drying. This may be achieved by introducing a population balance model to calculate the residence time distribution of deposited droplets. Then, changes in droplet properties can be linked to the residence time. Although the presented simulations show that the border between the size enlargement mechanisms can be described by a probability of successful collisions equal to 0.001 even when the collision velocity is varied in a relatively wide range, the model should be extended by taking droplet size distributions into account. The predictive ability of the model may be further improved by considering compartments as well as imbibition of liquid droplets into porous particles.

Appendix A

Material properties

A.1 Properties of dry air

Molar mass

$$\widetilde{M}_g = 28.96\,\mathrm{kg\,kmol^{-1}} \tag{A.1}$$

Source: Glück [187]

Density

$$\varrho_g = \frac{P_{tot}\widetilde{M}_g}{\widetilde{R}(T+273.15)} \quad \text{with} \quad \widetilde{R} = 8314.4\,\mathrm{J\,kmol^{-1}\,K^{-1}} \tag{A.2}$$

Specific heat capacity

$$c_g = a_0 + a_1 T + a_2 T^2 + a_3 T^3 \tag{A.3}$$

with

$$a_0 = +1.0065$$
$$a_1 = +5.309\,587 \cdot 10^{-6}$$
$$a_2 = +4.758\,596 \cdot 10^{-7}$$
$$a_3 = -1.136\,145 \cdot 10^{-10}$$

Units: $\left[c_g\right] = \mathrm{kJ\,kg^{-1}}$, $[T] = \mathrm{°C}$
Source: Glück [187]

Thermal conductivity

$$\lambda_g = a_0 + a_1 T + a_2 T^2 + a_3 T^3 \tag{A.4}$$

with

$$a_0 = +2.417\,800 \cdot 10^{-2}$$
$$a_1 = +7.634\,878 \cdot 10^{-5}$$
$$a_2 = -4.663\,859 \cdot 10^{-8}$$
$$a_3 = +4.612\,639 \cdot 10^{-11}$$

Units: $\left[\lambda_g\right] = \mathrm{W\,m^{-1}\,K^{-1}}$, $[T] = \mathrm{°C}$
Source: Glück [187]

Kinematic viscosity

$$\nu_g = a_0 + a_1 T + a_2 T^2 + a_3 T^3 \tag{A.5}$$

with

$$a_0 = +1.351\,980 \cdot 10^{-5}$$
$$a_1 = +8.930\,841 \cdot 10^{-8}$$
$$a_2 = +1.094\,808 \cdot 10^{-10}$$
$$a_3 = -3.659\,345 \cdot 10^{-14}$$

Units: $\left[\nu_g\right] = \mathrm{m^2\,s^{-1}}$, $[T] = \mathrm{°C}$
Source: Glück [187]

Prandtl number

$$\mathrm{Pr} = a_0 + a_1 T + a_2 T^2 + a_3 T^3 \tag{A.6}$$

with

$$a_0 = +7.178\,900 \cdot 10^{-1}$$
$$a_1 = -1.675\,739 \cdot 10^{-4}$$
$$a_2 = +6.514\,142 \cdot 10^{-7}$$
$$a_3 = -6.687\,762 \cdot 10^{-10}$$

Units: $[\mathrm{Pr}] = 1$, $[T] = \mathrm{°C}$
Source: Glück [187]

A.2 Properties of water vapor

Molar mass

$$\widetilde{M}_v = 18.02\,\mathrm{kg\,kmol^{-1}} \tag{A.7}$$

Source: Glück [187]

Specific heat capacity

$$c_v = a_0 + a_1 T + a_2 T^2 + a_3 T^3 \tag{A.8}$$

with

$$a_0 = +1.854\,283$$
$$a_1 = +1.126\,740 \cdot 10^{-3}$$
$$a_2 = -6.939\,165 \cdot 10^{-6}$$
$$a_3 = +1.344\,783 \cdot 10^{-7}$$

Units: $[c_v] = \mathrm{kJ\,kg^{-1}}$, $[T] = °\mathrm{C}$
Source: Glück [187]

Diffusion coefficient in air

$$\delta = \frac{0.00143\,(T + 273.15)^{1.75}\left[\frac{1}{\widetilde{M}_v} + \frac{1}{\widetilde{M}_g}\right]^{\frac{1}{2}}}{\sqrt{2}\,P_{tot}\left[\left(V_{diff,v}\right)^{\frac{1}{3}} + \left(V_{diff,g}\right)^{\frac{1}{3}}\right]^2} \tag{A.9}$$

with

$$V_{diff,v} = 13.1$$
$$V_{diff,g} = 19.7$$

Units: $[\delta] = \mathrm{cm^2\,s^{-1}}$, $[T] = °\mathrm{C}$, $[P_{tot}] = \mathrm{bar}$
Source: Poling et al. [188]

Saturation vapor pressure in air

$$p_{sat} = a_0 \exp\left(a_1 + a_2 T + a_3 T^2 + a_4 T^3 + a_5 T^4\right) \tag{A.10}$$

with

$$a_0 = +611$$
$$a_1 = -1.912\,75 \cdot 10^{-4}$$
$$a_2 = +7.258\,00 \cdot 10^{-2}$$
$$a_3 = -2.939\,00 \cdot 10^{-4}$$
$$a_4 = +9.841\,00 \cdot 10^{-7}$$
$$a_5 = -1.920\,00 \cdot 10^{-9}$$

Units: $[p_{sat}]$ = Pa, $[T]$ = °C
Source: Glück [187]

Moisture content at adiabatic saturation

The saturation moisture content of water vapor in air follows from the saturation vapor pressure, the total pressure, and the ratio of the corresponding molar masses:

$$Y_{sat} = \frac{\widetilde{M}_v}{\widetilde{M}_g} \frac{p_{sat}(T)}{P_{tot} - p_{sat}(T)}. \tag{A.11}$$

The moisture content at adiabatic saturation Y_{as} can be calculated using Equation (A.11) when the saturation vapor pressure calculated at the adiabatic saturation temperature T_{as} is used. The adiabatic saturation temperature and the corresponding moisture content can be calculated iteratively using the following equations:

$$Y_{as} = Y_{sat}(T_{as}), \tag{A.12}$$
$$T_{as} = T_{g,in} - \frac{\Delta h_{evap} + (c_v - c_l)T_{as}}{c_g + Y_{in}c_v}(Y_{as} - Y_{in}). \tag{A.13}$$

A.3 Properties of water

Density

$$\varrho_w = a_0 + a_1 T + a_2 T^2 + a_3 T^3 \tag{A.14}$$

with

$$a_0 = +1.002\,045 \cdot 10^3$$
$$a_1 = -1.029\,905 \cdot 10^{-1}$$
$$a_2 = -3.698\,162 \cdot 10^{-3}$$
$$a_3 = +3.991\,053 \cdot 10^{-6}$$

Units: $[\varrho_w] = \mathrm{kg\,m^{-3}}$, $[T] = °\mathrm{C}$
Source: Glück [187]

Specific heat capacity

$$c_w = a_0 + a_1 T + a_2 T^2 + a_3 T^3 \tag{A.15}$$

with

$$a_0 = +4.177\,375$$
$$a_1 = -2.144\,614 \cdot 10^{-6}$$
$$a_2 = -3.165\,823 \cdot 10^{-7}$$
$$a_3 = +4.134\,309 \cdot 10^{-8}$$

Units: $[c_w] = \mathrm{kJ\,kg^{-1}}$, $[T] = °\mathrm{C}$
Source: Glück [187]

Thermal conductivity

$$\lambda_w = a_0 + a_1 T + a_2 T^2 + a_3 T^3 \tag{A.16}$$

with

$$a_0 = +5.587\,913 \cdot 10^{-1}$$
$$a_1 = +2.268\,458 \cdot 10^{-3}$$
$$a_2 = -1.248\,304 \cdot 10^{-5}$$
$$a_3 = +1.890\,318 \cdot 10^{-8}$$

Units: $[\lambda_w] = \mathrm{W\,m^{-1}\,K^{-1}}$, $[T] = °\mathrm{C}$
Source: Glück [187]

A.4 Properties of aqueous sodium benzoate solution

Density

The density of aqueous sodium benzoate solution is approximated using the following equation:

$$\varrho_l = (1 - w_s)\varrho_w + w_s \varrho_s. \tag{A.17}$$

The solid density of sodium benzoate is $1440\,\mathrm{kg\,m^{-3}}$ [189].

Surface tension

The surface tension of aqueous sodium benzoate solution with a solid mass fraction equal to 0.3 was measured with a Du Noüy tensiometer at a temperature of 20 °C. The obtained surface tension is:

$$\gamma = 60.74\,\mathrm{mN\,m^{-1}}. \tag{A.18}$$

Viscosity

The viscosity of aqueous sodium benzoate solution with a solid mass fraction equal to 0.3 was measured with a Höppler viscometer for different temperatures between 15 °C and 50 °C. This data was used to create an empirical correlation yielding the viscosity of the solution from its temperature. Following Poling et al. [188], an exponential function was used and the correlation shown in Equation (A.19) was obtained. Table A.1 shows the measured and calculated viscosities.

$$\ln \eta = a_0 + \frac{a_1}{T + 273.15} \tag{A.19}$$

with

$$a_0 = -7.31$$
$$a_1 = +2545$$

Units: $[\eta]$ = mPa s, $[T]$ = °C

Table A.1: Measured and calculated viscosity for aqueous sodium benzoate solution ($w_s = 0.3$).

T [°C]	η (measured) [mPa s]	η (Equation (A.19)) [mPa s]
15	4.3621	4.5823
20	4.1848	3.9415
25	3.3516	3.4075
30	3.0233	2.9600
50	1.7374	1.7605

Appendix B

Fluidized bed properties

B.1 Hydrodynamics

The range of existence of a fluidized bed is described by the gas velocity at minimum fluidization u_{mf} and at elutriation u_{elu}. In order to fluidize a particle bed, the gas velocity u_g must lie between these velocities:

$$u_{mf} < u_g < u_{elu}. \tag{B.1}$$

In dimensionless form, the gas velocity can be represented by the Reynolds number defined as:

$$\mathrm{Re} = \frac{u_g d_p}{\nu_g}. \tag{B.2}$$

The Reynolds numbers at minimum fluidization Re_{mf} and elutriation Re_{elu} can be calculated by the following dimensionless correlations given by Martin [190]:

$$\mathrm{Re}_{mf} = 42.9\left(1-\varepsilon_{bed,mf}\right)\left(\sqrt{1+\frac{\varepsilon_{bed,mf}^3}{\left(1-\varepsilon_{bed,mf}\right)^2}\frac{\mathrm{Ar}}{3214}}-1\right), \tag{B.3}$$

$$\mathrm{Re}_{elu} = \sqrt{\frac{4}{3}\mathrm{Ar}}. \tag{B.4}$$

The Archimedes number Ar used in Equation (B.3) and Equation (B.4) is defined as:

$$\mathrm{Ar} = \frac{g d_p^3}{\nu_g^2}\frac{\varrho_p - \varrho_g}{\varrho_g}. \tag{B.5}$$

The change in bed porosity due to expansion of the bed is calculated according to Martin [190]:

$$\varepsilon_{bed}^m = \frac{\mathrm{Re}}{\mathrm{Re}_{elu}} \quad \text{with} \quad m = \frac{\ln\left(\dfrac{\mathrm{Re}_{mf}}{\mathrm{Re}_{elu}}\right)}{\ln \varepsilon_{bed,mf}}. \tag{B.6}$$

The bed porosity at minimum fluidization $\varepsilon_{bed,mf}$ ranges practically between 0.4 and 0.7 [190]. In this work, the value of 0.4 is used.

B.2 Heat- and mass transfer

B.2.1 Correlations from Martin

The drying time in the presented Monte Carlo models (cf. Chapter 3) is calculated with a mass transfer coefficient obtained from correlations given by Martin [190], which are based on the model of Gnielinski [191] for packed beds. According to Martin [190], the Nusselt number of a single particle Nu_p is calculated as follows:

$$\mathrm{Re}_\varepsilon = \frac{\mathrm{Re}}{\varepsilon_{bed}}, \tag{B.7}$$

$$\mathrm{Nu}_{lam} = 0.664\,\mathrm{Re}_\varepsilon^{1/2}\,\mathrm{Pr}^{1/3}, \tag{B.8}$$

$$\mathrm{Nu}_{turb} = \frac{0.037\,\mathrm{Re}_\varepsilon^{0.8}\,\mathrm{Pr}}{1 + 2.443\,\mathrm{Re}_\varepsilon^{-0.1}\left(\mathrm{Pr}^{2/3} - 1\right)}, \tag{B.9}$$

$$\mathrm{Nu}_p = 2 + \sqrt{\mathrm{Nu}_{lam}^2 + \mathrm{Nu}_{turb}^2}. \tag{B.10}$$

The corresponding Sherwood number Sh_p can be calculated using the Lewis number Le:

$$\mathrm{Sh}_p = \mathrm{Nu}_p\,\mathrm{Le}^{1/3}. \tag{B.11}$$

The Lewis number is obtained from the Schmidt number Sc and the Prandtl number Pr:

$$\mathrm{Le} = \frac{\mathrm{Sc}}{\mathrm{Pr}}, \tag{B.12}$$

$$\mathrm{Sc} = \frac{\nu_g}{\delta}, \tag{B.13}$$

$$\mathrm{Pr} = \frac{\nu_g \varrho_g c_g}{\lambda_g}. \tag{B.14}$$

Similar to Dernedde [132] the mass transfer coefficient β then follows from the Sherwood number of a single particle Sh_p:

$$\beta = \frac{\mathrm{Sh}_p\,\delta}{d_p}. \tag{B.15}$$

B.2.2 Correlations from Groenewold and Tsotsas

In Chapter 6 the model presented by Groenewold and Tsotsas [143] is used to calculate the heat and mass transfer coefficients in the fluidized bed. They propose to calculate the Sherwood number

Sh_{bed} using the model given by Gnielinski [191] at minimum fluidization conditions. The Nusselt number of a single particle is obtained from Equation (B.8) to Equation (B.10), but with:

$$\mathrm{Re}_{\varepsilon} = \frac{\mathrm{Re}_{mf}}{\varepsilon_{bed,mf}}. \tag{B.16}$$

The Nusselt number of the bed then follows from the Nusselt number of a single particle:

$$\mathrm{Nu}_{bed} = \left[1 + 1.5\left(1 - \varepsilon_{bed,mf}\right)\right]\mathrm{Nu}_{p}. \tag{B.17}$$

The corresponding Sherwood number of the bed is calculated using the Lewis number:

$$\mathrm{Sh}_{bed} = \mathrm{Nu}_{bed}\,\mathrm{Le}^{1/3}. \tag{B.18}$$

Following Groenewold and Tsotsas [143], the apparent Sherwood number Sh'_{bed} can then be derived from Sh_{bed}:

$$\mathrm{Sh}'_{bed} = \frac{\mathrm{Re}\,\mathrm{Sc}}{A_V h_{bed}} \ln\left(1 + \frac{\mathrm{Sh}_{bed} A_V h_{bed}}{\mathrm{Re}\,\mathrm{Sc}}\right). \tag{B.19}$$

In this equation, A_V is the particle surface area per bed volume and h_{bed} is the height of the fluidized bed, which are calculated using:

$$A_V = \frac{4A_{p,tot}}{\pi d_{bed}^2 h_{bed}}, \tag{B.20}$$

$$h_{bed} = \frac{4M_{bed}}{\rho_p(1 - \varepsilon_{bed})\pi d_{bed}^2}. \tag{B.21}$$

The apparent Nusselt number Nu'_{bed} follows from Equation (B.18) and the corresponding heat and mass transfer coefficients can be calculated as follows:

$$\alpha = \frac{\mathrm{Nu}'_{bed}\lambda_g}{d_p}, \tag{B.22}$$

$$\beta = \frac{\mathrm{Sh}'_{bed}\delta}{d_p}. \tag{B.23}$$

Appendix C

Mathematical derivations

C.1 Calculation of distributed particle diameters based on particle size distributions

In the Monte Carlo models presented by Terrazas-Velarde [15] and Hussain [97], the initial particle bed is assumed to consist of monodisperse particles. The model presented by Dernedde [132] is able to consider a size distribution, which is, however, restricted to a normal distribution. A set of normally distributed particle diameters with a mean diameter d_{10} and a standard deviation of σ_x can be created by drawing random numbers r_n from the standard normal distribution:

$$d_{p,j} = d_{10} + \sigma_x r_{n,j}. \tag{C.1}$$

In the present work, a novel algorithm for Monte Carlo models has been developed, allowing to create a set of particle diameters according to an arbitrary particle size distribution. This method is used to create an initial set of particle diameters in the Monte Carlo simulations based on measured size distributions of the particle material. The set of particle diameters in the simulations with parameters corresponding to experimental conditions shown in Section 4.3.2 and Section 5.3.2 were created with this method.

Assume that a normalized number-based particle size distribution q_0 and the corresponding size classes are available in discrete form (e.g., from measurements). The size classes are represented by their boundary values x_j and x_{j+1} and the corresponding class centers $\bar{x}_j$. First, the absolute number of particles is calculated for each size class, assuming spherical particles:

$$N_{p,j} = n_j \Delta x_j = \frac{6 M_{bed}}{\pi \varrho_p} \frac{q_{0,j}}{\sum\limits_j \bar{x}_j^3 q_{0,j} \Delta x_j}. \tag{C.2}$$

The total number of particles $N_{p,tot}$ then follows from $N_{p,j}$:

$$N_{p,tot} = \sum_j N_{p,j}. \tag{C.3}$$

The values $N_{p,j}$ and $N_{p,tot}$ characterize the size distribution of the real particle system with a normalized size distribution q_0, a total mass of M_{bed}, and a particle density of ϱ_p. In order to obtain the absolute particle number for each size class of the Monte Carlo system, $N_{p,j}$ must be scaled down by the ratio of the number of particles in both systems:

$$N_{p,MC,j} = \mathrm{nint}\left(N_{p,j}\frac{N_{p,MC}}{N_{p,tot}}\right). \tag{C.4}$$

Note that scaling using the ratio of the particle number is sufficient here (cf. Section 3.1.2) since scaling using the particle mass is only needed in the actual Monte Carlo algorithm when sample size regulations are performed. The value of $N_{p,MC,j}$ is rounded to the nearest integer. As a result, the total number of particles in the Monte Carlo system may not exactly match the set value of $N_{p,MC}$. In order to achieve that

$$\sum_j N_{p,MC,j} = N_{p,MC}, \tag{C.5}$$

the values of $N_{p,MC,j}$ must be increased or decreased accordingly. Therefore, the difference in particle number is calculated:

$$\Delta N_p = N_{p,MC} - \sum_j N_{p,MC,j}, \tag{C.6}$$

which may be positive (particles need to be added) or negative (particles need to be removed). Several ways of modifying $N_{p,MC,j}$ to fulfill Equation (C.5) exist. The easiest way would be to change the values of $N_{p,MC,j}$ in a single size class by ΔN_p. However, this method could alter the shape of the resulting size distribution by creating bumps or peaks. Therefore, several values of $N_{p,MC,j}$ should be changed simultaneously. Additionally, to minimize the impact of adding or removing particles in a size class, only the size classes with the largest values of $N_{p,MC,j}$ are modified. Both aspects are taken into account in the following method:

- sort the values of $N_{p,MC,j}$ in descending order and
- modify the first ΔN_p values of the sorted $N_{p,MC,j}$ by adding or subtracting unity.

For example, if $\Delta N_p = 5$, five particles need to be added to $N_{p,MC,j}$, which is achieved by increasing the values of $N_{p,MC,j}$ in the five size classes with the largest numbers by unity. In this way, the condition in Equation (C.5) is fulfilled and the impact on the shape of the particle size distribution is minimized.

The next step is calculating random particle diameters for each size class. The values of the diameters may range between the boundary values x_j and x_{j+1} of each class. Using a uniformly distributed random number r from the open interval $(0, 1)$, a random diameter in size class j is calculated as follows:

$$d_{p,j} = x_j + (x_{j+1} - x_j)r. \tag{C.7}$$

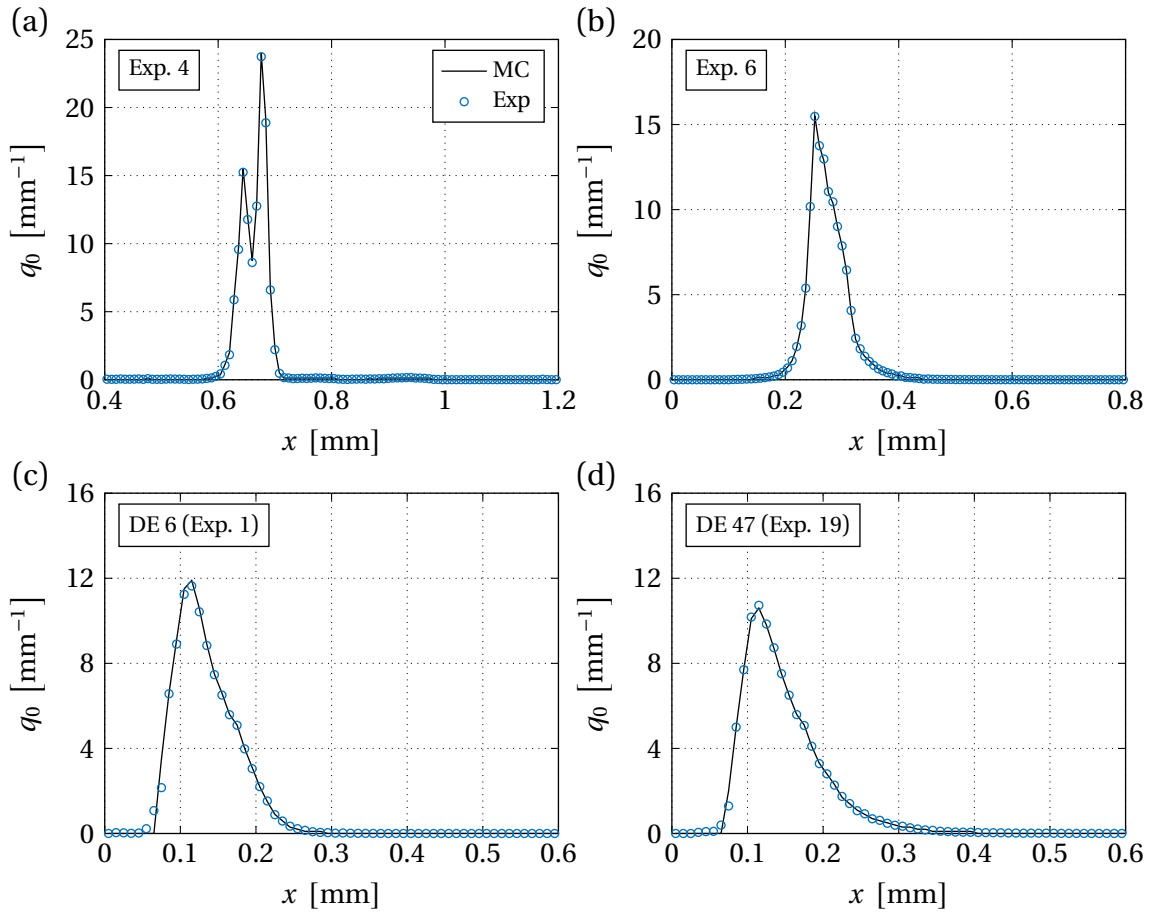

Figure C.1: Comparison between initial particle size distributions obtained by measurements and the proposed algorithm for experiment 4 (Chapter 4) (a), experiment 6 (Chapter 4) (b), experiment 1 (Chapter 5) (c), and experiment 19 (Chapter 5) (d).

Since each size class needs a number of diameters equal to $N_{p,MC,j}$, the procedure is repeated accordingly. The particle size distribution of the created set of particle diameters can then be obtained by computing histograms.

A comparison between particle size distributions obtained by measurements and the above described method is shown in Figure C.1 using the example of experiments 4 and 6 from Chapter 4 and experiments 1 and 19 from Chapter 5. In all cases, the particle size distributions agree well. However, note that in Figure C.1c and Figure C.1d (experiments 1 and 19) small deviations can be observed for particle sizes smaller than 0.1 mm. In these cases, the calculated diameters were smaller than the minimum particle diameter that can be considered in the simulation (see Section 3.1.5) and were replaced with $d_{p,min}$.

C.2 Analytical calculation of the coated surface fraction

In this section, an analytical model for the transient behavior of the coated surface fraction during a layering process is presented, assuming that the particle surface area is constant. The coated surface fraction Ψ_c is defined as the ratio between the coated surface area and the total surface area of a particle:

$$\Psi_c = \frac{A_c}{A_p} = \frac{A_p - A_{p,free}}{A_p}. \tag{C.8}$$

If the particle surface area is constant, the time derivative of Ψ_c reads:

$$\frac{\mathrm{d}\Psi_c}{\mathrm{d}t} = \frac{1}{A_p}\frac{\mathrm{d}A_c}{\mathrm{d}t}. \tag{C.9}$$

The transient behavior of the coated surface area depends on the footprint of a single deposited droplet $A_{contact}$, the number flow rate of droplets $\dot{N}_{drop}$, and the distribution of droplets among the particles. If the droplets are distributed based on the surface area of the particles, following the idea proposed by Mörl et al. [6], a particle receives droplets based on the fraction of its surface area in the bed. Consequently, the transient of A_c is proportional to this fraction:

$$\frac{\mathrm{d}A_c}{\mathrm{d}t} \sim \frac{A_p}{A_{p,tot}}. \tag{C.10}$$

Additionally, droplets may hit spots on the particle surface which are either empty or already covered by a droplet. As a result, the transient of A_c is also proportional to the uncoated surface fraction of a particle:

$$\frac{\mathrm{d}A_c}{\mathrm{d}t} \sim \frac{A_{p,free}}{A_p}. \tag{C.11}$$

Combining these ideas, the time derivative of the coated surface area reads:

$$\frac{\mathrm{d}A_c}{\mathrm{d}t} = A_{contact}\dot{N}_{drop}\frac{A_p}{A_{p,tot}}\frac{A_{p,free}}{A_p} = A_{contact}\dot{N}_{drop}\frac{A_{p,free}}{A_{p,tot}}. \tag{C.12}$$

Combining Equation (C.12), Equation (C.9), and Equation (C.8) yields:

$$\frac{\mathrm{d}\Psi_c}{\mathrm{d}t} = \frac{A_{contact}}{A_{p,tot}}\dot{N}_{drop}(1 - \Psi_c). \tag{C.13}$$

Equation (C.13) can be solved by integration. Since the natural logarithm of zero is undefined, the case $\Psi_c = 1$ has to be excluded. Then, $1 - \Psi_c > 0$ and the following solution is obtained:

$$\int_0^{\Psi_c} \frac{\mathrm{d}\Psi_c}{1-\Psi_c} = \int_0^t \frac{A_{contact}}{A_{p,tot}} \dot{N}_{drop}\, \mathrm{d}t, \tag{C.14}$$

$$-\ln|1-\Psi_c|\Big|_0^{\Psi_c} = \frac{A_{contact}}{A_{p,tot}} \dot{N}_{drop} t\Big|_0^t, \tag{C.15}$$

$$\Psi_c = 1 - \exp\left(-\frac{A_{contact}}{A_{p,tot}} \dot{N}_{drop} t\right). \tag{C.16}$$

Appendix D

Discretization of partial differential equations using a finite volume method

The finite volume method is used in this work to discretize partial differential equations and transform them into ordinary differential equations, which are then solved numerically. In this chapter, the finite volume method is presented in detail using the example of the one-dimensional population balance for layering growth. Since the approach is identical for the partial differential equations describing water mass and enthalpy of the fluidization gas, the resulting discretized equations are given without detailed explanation.

D.1 Population balance

In the finite volume method, the calculation domain is divided into several non-overlapping control volumes, see Patankar [192]. The differential equation is then integrated over each control volume. In order to evaluate the integrals, profiles between the grid points representing the control volume have to be assumed. The resulting equations can then be solved numerically.

The one-dimensional population balance for a batch layering growth process reads:

$$\frac{\partial n(t,x)}{\partial t} = -\frac{\partial (Gn)}{\partial x}. \tag{D.1}$$

The property coordinate x representing the particle size is discretized as shown in Figure D.1. The faces of the control volumes are represented by x_j, while $\bar{x}_j$ are the grid points placed in the center of each control volume. Integration of the left-hand side of Equation (D.1) over control volume j is performed by interchanging differentiation and integration [193]. Additionally, it is assumed that n is constant in this control volume (represented by n_j), leading to:

$$\int_{x_j}^{x_{j+1}} \frac{\partial n}{\partial t} \mathrm{d}x = \frac{\mathrm{d}}{\mathrm{d}t} \int_{x_j}^{x_{j+1}} n \, \mathrm{d}x = \frac{\mathrm{d}n_j}{\mathrm{d}t} \left(x_{j+1} - x_j \right) = \frac{\mathrm{d}n_j}{\mathrm{d}t} \Delta x_j. \tag{D.2}$$

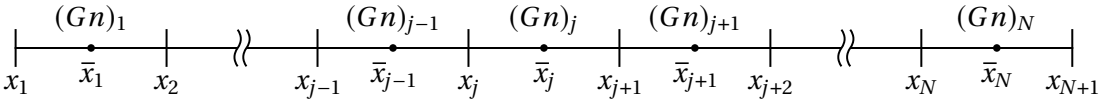

Figure D.1: Discretization of the property coordinate x into N control volumes.

Integrating the right-hand side of Equation (D.1) is performed applying Gauss' theorem [194]:

$$-\int_{x_j}^{x_{j+1}} \frac{\partial(Gn)}{\partial x}\mathrm{d}x = -[Gn]_{x_j}^{x_{j+1}} = -\Big((Gn)|_{x_{j+1}} - (Gn)|_{x_j}\Big). \tag{D.3}$$

Combining the above shown equations, Equation (D.4) is obtained:

$$\frac{\mathrm{d}n_j}{\mathrm{d}t} = -\frac{(Gn)|_{x_{j+1}} - (Gn)|_{x_j}}{\Delta x_j}. \tag{D.4}$$

Further assumptions are necessary to evaluate the fluxes at the faces of the control volumes, which are discussed in the following sections.

D.1.1 First order upwind scheme

The first order upwind scheme can be used to further evaluate Equation (D.4). Using the upwind scheme for $G > 0$, the fluxes $(Gn)|_{x_{j+1}}$ and $(Gn)|_{x_j}$ can be written as [192]:

$$(Gn)|_{x_{j+1}} = (Gn)|_{\bar{x}_j} = (Gn)_j, \tag{D.5}$$

$$(Gn)|_{x_j} = (Gn)|_{\bar{x}_{j-1}} = (Gn)_{j-1}. \tag{D.6}$$

Note that the flux entering the first control volume $(Gn)|_{x_1}$ is defined by the boundary condition and is therefore not evaluated with the above shown equations. Incorporating the boundary condition $B_0(t)$ (birth rate of particles with smallest size), the flux entering the first control volume reads:

$$(Gn)|_{x_1} = B_0(t). \tag{D.7}$$

Then, the discretized form of Equation (D.1) is obtained:

$$\frac{\mathrm{d}n_1}{\mathrm{d}t} = -\frac{(Gn)_1 - B_0(t)}{\Delta x_1}, \tag{D.8}$$

$$\frac{\mathrm{d}n_j}{\mathrm{d}t} = -\frac{(Gn)_j - (Gn)_{j-1}}{\Delta x_j}. \tag{D.9}$$

D.1.2 Flux limiter

According to LeVeque [109], methods such as the first order upwind scheme are known to exhibit significant numerical diffusion. Higher order methods are more accurate, but oscillatory behavior

may be observed. Flux-limiter methods combine both low and high order methods to obtain reduced numerical diffusion without oscillations. In this work, the flux-limiter method proposed by Koren [174] is used, which is described below.

Evaluating the fluxes at the faces of the control volumes in Equation (D.4) using the flux-limiter method yields:

$$(Gn)|_{x_{j+1}} = (Gn)_j + \frac{1}{2}\phi\Big(r'|_{x_{j+1}}\Big)\big((Gn)_j - (Gn)_{j-1}\big), \tag{D.10}$$

$$(Gn)|_{x_j} = (Gn)_{j-1} + \frac{1}{2}\phi\Big(r'|_{x_j}\Big)\big((Gn)_{j-1} - (Gn)_{j-2}\big). \tag{D.11}$$

In these equations, $\phi(r')$ is the limiter function, which depends on the ratio of consecutive solution gradients r' defined as:

$$r'|_{x_{j+1}} = \frac{(Gn)_{j+1} - (Gn)_j + \kappa}{(Gn)_j - (Gn)_{j-1} + \kappa}. \tag{D.12}$$

The parameter κ is introduced to avoid division by zero. In this work, κ is set to 10^{-20}. The limiter function proposed by Koren [174] is defined as:

$$\phi(r') = \max\left(0, \min\left(2r', \min\left(\frac{1}{3} + \frac{2}{3}r', 2\right)\right)\right). \tag{D.13}$$

Similar to the above described first order upwind scheme, the flux entering the first control volume is defined by the boundary condition:

$$(Gn)|_{x_1} = B_0(t). \tag{D.14}$$

Fluxes entering the second and leaving the last control volume need a special treatment as well, since they cannot be evaluated using the equations shown above. These fluxes are evaluated with the first order upwind scheme in this work:

$$(Gn)|_{x_2} = (Gn)_1, \tag{D.15}$$

$$(Gn)|_{x_{N+1}} = (Gn)_N. \tag{D.16}$$

D.2 Mass and enthalpy balances

The mass and enthalpy balances of the fluidization gas are partial differential equations as well. They are discretized using the finite volume method (first order upwind scheme) and then solved

numerically. The resulting discretized equations for control volume j read:

$$\frac{\mathrm{d}M_{w,g,j}}{\mathrm{d}t} = -\frac{\dot{M}_{w,g,j} - \dot{M}_{w,g,j-1}}{\Delta\zeta_j} + \dot{M}_{evap,j}, \tag{D.17}$$

$$\frac{\mathrm{d}H_{g,j}}{\mathrm{d}t} = -\frac{\dot{H}_{g,j} - \dot{H}_{g,j-1}}{\Delta\zeta_j} + \dot{H}_{evap,j} - \dot{Q}_{gp,j} - \dot{Q}_{gl,j}. \tag{D.18}$$

The boundary conditions are incorporated in the discretized equations for the first control volume:

$$\frac{\mathrm{d}M_{w,g,1}}{\mathrm{d}t} = -\frac{\dot{M}_{w,g,1} - \dot{M}_{w,g,in}}{\Delta\zeta_1} + \dot{M}_{evap,1}, \tag{D.19}$$

$$\frac{\mathrm{d}H_{g,1}}{\mathrm{d}t} = -\frac{\dot{H}_{g,1} - \dot{H}_{g,in}}{\Delta\zeta_1} + \dot{H}_{evap,1} - \dot{Q}_{gp,1} - \dot{Q}_{gl,1}. \tag{D.20}$$

The water mass flow rate and the enthalpy flow rate entering the first control volume are calculated using the moisture content and temperature of the inlet gas Y_{in} and $T_{g,in}$:

$$\dot{M}_{w,g,in} = \dot{M}_{g,dry} Y_{in}, \tag{D.21}$$

$$\dot{H}_{g,in} = \dot{M}_{g,dry}\left(c_g T_{g,in} + Y_{in}\left(c_v T_{g,in} + \Delta h_{evap}\right)\right). \tag{D.22}$$

Bibliography

[1] Schulze, D. *Pulver und Schüttgüter: Fließeigenschaften und Handhabung*. 4th ed. Berlin: Springer Vieweg, 2019. DOI: 10.1007/978-3-662-58776-8.

[2] Merkus, H. G. Introduction. In: *Production, Handling and Characterization of Particulate Materials*. Ed. by Merkus, H. G. and Meesters, G. M. Cham: Springer International Publishing, 2016, 1–29.

[3] Stieß, M. *Mechanische Verfahrenstechnik - Partikeltechnologie 1*. 3rd ed. Berlin: Springer-Verlag, 2009. DOI: 10.1007/978/3-540-32552-9.

[4] Kunii, D. and Levenspiel, O. *Fluidization Engineering*. 2nd ed. Boston: Butterworth-Heinemann, 1991.

[5] Wirth, K.-E. Flow patterns and pressure drop in fluidized beds. In: *VDI Heat Atlas*. Ed. by VDI e.V. Berlin: Springer-Verlag, 2010, 1197–1206.

[6] Mörl, L., Heinrich, S., and Peglow, M. Fluidized bed spray granulation. In: *Handbook of Powder Technology: Granulation*. Ed. by Salman, A. D., Hounslow, M. J., and Seville, J. P. K. Vol. 11. Amsterdam: Elsevier Science B.V., 2007, 21–188. DOI: 10.1016/S0167-3785(07)80037-6.

[7] Geldart, D. Types of gas fluidization. *Powder Technology* 7(5) (1973), 285–292. DOI: 10.1016/0032-5910(73)80037-3.

[8] Seville, J. P. K. Fluidisation of cohesive particles. In: *Handbook of Powder Technology: Granulation*. Ed. by Salman, A. D., Hounslow, M. J., and Seville, J. P. K. Vol. 11. Amsterdam: Elsevier Science B.V., 2007, 1041–1069. DOI: 10.1016/S0167-3785(07)80057-1.

[9] Geldart, D. *Gas Fluidization Technology*. Chichester: John Wiley & Sons, 1986.

[10] Jacob, M. Granulation equipment. In: *Handbook of Powder Technology: Granulation*. Ed. by Salman, A. D., Hounslow, M. J., and Seville, J. P. K. Vol. 11. Amsterdam: Elsevier Science B.V., 2007, 417–476. DOI: 10.1016/S0167-3785(07)80044-3.

[11] Wurster, D. E. Particle-coating methods. In: *Pharmaceutical dosage forms: Tablets*. Ed. by Lieberman, H. A., Lachman, L., and Schwartz, J. B. Vol. 3. New York: Dekker, 1990, 161–197.

[12] Tan, H. S., Salman, A. D., and Hounslow, M. J. Kinetics of fluidised bed melt granulation I: The effect of process variables. *Chemical Engineering Science* 61(5) (2006), 1585–1601. DOI: 10.1016/j.ces.2005.09.012.

[13] Guignon, B., Duquenoy, A., and Dumoulin, E. D. Fluid bed encapsulation of particles: Principles and practice. *Drying Technology* 20(2) (2002), 419–447. DOI: 10.1081/DRT-120002550.

[14] Werner, S. R. L., Jones, J. R., Paterson, A. H. J., Archer, R. H., and Pearce, D. L. Air-suspension coating in the food industry: Part II - micro-level process approach. *Powder Technology* 171(1) (2007), 34–45. DOI: 10.1016/j.powtec.2006.08.015.

[15] Terrazas-Velarde, K. *Monte Carlo simulation of fluidized bed spray agglomeration*. Ph.D. Thesis. Otto von Guericke University Magdeburg. Göttingen: Sierke Verlag, 2010.

[16] Tran, T. T. H., Jaskulski, M., Avila-Acevedo, J. G., and Tsotsas, E. Model parameters for single-droplet drying of skim milk and its constituents at moderate and elevated temperatures. *Drying Technology* 35(4) (2017), 444–464. DOI: 10.1080/07373937.2016.1182548.

[17] Walton, D. E. The morphology of spray-dried particles: A qualitative view. *Drying Technology* 18(9) (2000), 1943–1986. DOI: 10.1080/07373930008917822.

[18] Handscomb, C. S., Kraft, M., and Bayly, A. E. A new model for the drying of droplets containing suspended solids. *Chemical Engineering Science* 64(4) (2009), 628–637. DOI: 10.1016/j.ces.2008.04.051.

[19] Abberger, T., Seo, A., and Schæfer, T. The effect of droplet size and powder particle size on the mechanisms of nucleation and growth in fluid bed melt agglomeration. *International Journal of Pharmaceutics* 249(1-2) (2002), 185–197. DOI: 10.1016/S0378-5173(02)00530-6.

[20] Seo, A., Holm, P., and Schæfer, T. Effects of droplet size and type of binder on the agglomerate growth mechanisms by melt agglomeration in a fluidised bed. *European Journal of Pharmaceutical Sciences* 16(3) (2002), 95–105. DOI: 10.1016/S0928-0987(02)00086-6.

[21] Boerefijn, R. and Hounslow, M. J. Studies of fluid bed granulation in an industrial R&D context. *Chemical Engineering Science* 60(14) (2005), 3879–3890. DOI: 10.1016/j.ces.2005.02.021.

[22] Iveson, S. M., Litster, J. D., Hapgood, K. P., and Ennis, B. J. Nucleation, growth and breakage phenomena in agitated wet granulation processes: A review. *Powder Technology* 117(1-2) (2001), 3–39. DOI: 10.1016/S0032-5910(01)00313-8.

[23] Hapgood, K. P., lveson, S. M., Litster, J. D., and Liu, L. X. Granulation rate processes. In: *Handbook of Powder Technology: Granulation*. Ed. by Salman, A. D., Hounslow, M. J., and Seville, J. P. K. Vol. 11. Amsterdam: Elsevier Science B.V., 2007, 897–977. DOI: 10.1016/S0167-3785(07)80055-8.

[24] Nienow, A. W. Fluidised bed granulation and coating: Applications to materials, agriculture and biotechnology. *Chemical Engineering Communications* 139(1) (1995), 233–253. DOI: 10.1080/00986449508936406.

[25] Bück, A., Tsotsas, E., and Sommer, K. Size enlargement. In: *Ullmann's Encyclopedia of Industrial Chemistry*. Weinheim: Wiley-VCH Verlag GmbH & Co. KGaA, 2014, 1–47. DOI: 10.1002/14356007.b02_07.pub2.

[26] Wan, L. S. and Lai, W. F. Factors affecting drug release from drug-coated granules prepared by fluidized-bed coating. *International Journal of Pharmaceutics* 72(2) (1991), 163–174. DOI: 10.1016/0378-5173(91)90055-S.

[27] Turton, R., Tardos, G. I., and Ennis, B. J. Fluidized bed coating and granulation. In: *Fluidization, solids handling, and processing*. Ed. by Yang, W.-C. Particle technology series. Westwood: Noyes Publications, 1999, 331–434. DOI: 10.1016/B978-081551427-5.50008-9.

[28] Albanez, R., Nitz, M., and Taranto, O. P. Influence of the type of enteric coating suspension, coating layer and process conditions on dissolution profile and stability of coated pellets of diclofenac sodium. *Powder Technology* 269 (2015), 185–192. DOI: 10.1016/j.powtec.2014.09.016.

[29] Capece, M. and Dave, R. Application of fluidized bed film coating for membrane encapsulation of catalysts. *Powder Technology* 211(2-3) (2011), 199–206. DOI: 10.1016/j.powtec.2011.04.015.

[30] Frey, C. Fluid bed coating-based microencapsulation. In: *Microencapsulation in the Food Industry*. Ed. by Gaonkar, A. G., Vasisht, N., Khare, A. R., and Sobel, R. San Diego: Academic Press, 2014, 65–79. DOI: 10.1016/B978-0-12-404568-2.00007-8.

[31] Kulah, G. and Kaya, O. Investigation and scale-up of hot-melt coating of pharmaceuticals in fluidized beds. *Powder Technology* 208(1) (2011), 175–184. DOI: 10.1016/j.powtec.2010.12.016.

[32] Jackson, L. S. and Lee, K. Microencapsulation and the food industry. *LWT - Food Science and Technology* 24(4) (1991), 289–297.

[33] Werner, S. R. L., Jones, J. R., Paterson, A. H. J., Archer, R. H., and Pearce, D. L. Air-suspension particle coating in the food industry: Part I - state of the art. *Powder Technology* 171(1) (2007), 25–33. DOI: 10.1016/j.powtec.2006.08.014.

[34] Hemati, M., Cherif, R., Saleh, K., and Pont, V. Fluidized bed coating and granulation: Influence of process-related variables and physicochemical properties on the growth kinetics. *Powder Technology* 130(1–3) (2003), 18–34. DOI: 10.1016/S0032-5910(02)00221-8.

[35] Blei, S., Schneider, K.-H., Fricke, H.-M., and Werner, A. Production of pesticide granulates in a spouted bed apparatus. Patent US20120263775. 2012.

[36] Cotabarren, I. M., Bertín, D. E., Moraga, S. V., Mirazú, L., Piña, J., and Bucalá, V. Production of granular urea as nitrogenous fertilizer. In: *Urea: Synthesis, Properties and Uses*. Ed. by Muñoz, C. M. and Fernández, A. M. New York: Nova Biomedical, 2012, 1–63.

[37] Moraga, S. V., Villa, M. P., Bertín, D. E., Cotabarren, I. M., Piña, J., Pedernera, M., and Bucalá, V. Fluidized-bed melt granulation: The effect of operating variables on process performance and granule properties. *Powder Technology* 286 (2015), 654–667. DOI: 10.1016/j.powtec.2015.09.006.

[38] Uemaki, O. and Mathur, K. B. Granulation of ammonium sulfate fertilizer in a spouted bed. *Industrial & Engineering Chemistry Process Design and Development* 15(4) (1976), 504–508. DOI: 10.1021/i260060a005.

[39] Wang, G., Yang, L., Lan, R., Wang, T., and Jin, Y. Granulation by spray coating aqueous solution of ammonium sulfate to produce large spherical granules in a fluidized bed. *Particuology* 11(5) (2013), 483–489. DOI: 10.1016/j.partic.2012.10.005.

[40] Rumpf, H. Grundlagen und Methoden des Granulierens. *Chemie Ingenieur Technik* 30(3) (1958), 144–158. DOI: 10.1002/cite.330300307.

[41] Schubert, H. Grundlagen des Agglomerierens. *Chemie Ingenieur Technik* 51(4) (1979), 266–277. DOI: 10.1002/cite.330510404.

[42] Palzer, S. Agglomeration of pharmaceutical, detergent, chemical and food powders: Similarities and differences of materials and processes. *Powder Technology* 206(1-2) (2011), 2–17. DOI: 10.1016/j.powtec.2010.05.006.

[43] Palzer, S. Agglomeration of dehydrated consumer foods. In: *Handbook of Powder Technology: Granulation*. Ed. by Salman, A. D., Hounslow, M. J., and Seville, J. P. K. Vol. 11. Amsterdam: Elsevier Science B.V., 2007, 591–671. DOI: 10.1016/S0167-3785(07)80048-0.

[44] Willart, J.-F. and Descamps, M. Solid state amorphization of pharmaceuticals. *Molecular Pharmaceutics* 5(6) (2008), 905–920. DOI: 10.1021/mp800092t.

[45] Dopfer, D., Palzer, S., Heinrich, S., Fries, L., Antonyuk, S., Haider, C., and Salman, A. D. Adhesion mechanisms between water soluble particles. *Powder Technology* 238 (2013), 35–49. DOI: 10.1016/j.powtec.2012.06.029.

[46] Iveson, S. M. and Litster, J. D. Growth regime map for liquid-bound granules. *AIChE Journal* 44(7) (1998), 1510–1518. DOI: 10.1002/aic.690440705.

[47] Iveson, S. M., Wauters, P. A. L., Forrest, S., Litster, J. D., Meesters, G. M., and Scarlett, B. Growth regime map for liquid-bound granules: Further development and experimental validation. *Powder Technology* 117(1-2) (2001), 83–97. DOI: 10.1016/S0032-5910(01)00317-5.

[48] Achanta, S. and Beimesch, W. E. Process for making a low density detergent composition by controlled agglomeration in a fluid bed dryer. Patent WO9903964. 1999.

[49] Wasserman, M. I., Ridyard, M. W., Capeci, S. W., Beimesch, W. E., and Mort III, P. R. Process for coating detergent granules in a fluidized bed. Patent WO0078912. 2000.

[50] Boerefijn, R., Dontula, P.-R., and Kohlus, R. Detergent granulation. In: *Handbook of Powder Technology: Granulation*. Ed. by Salman, A. D., Hounslow, M. J., and Seville, J. P. K. Amsterdam: Elsevier Science B.V., 2007, 673–703. DOI: 10.1016/S0167-3785(07)80049-2.

[51] Kristensen, H. G. and Schæfer, T. Granulation: A review on pharmaceutical wet-granulation. *Drug Development and Industrial Pharmacy* 13(4-5) (1987), 803–872. DOI: 10.3109/03639048709105217.

[52] Pitt, K. and Sinka, C. Tabletting. In: *Handbook of Powder Technology: Granulation*. Ed. by Salman, A. D., Hounslow, M. J., and Seville, J. P. K. Amsterdam: Elsevier Science B.V., 2007, 735–778. DOI: 10.1016/S0167-3785(07)80051-0.

[53] Kleinebudde, P. and Knop, K. Direct pelletization of pharmaceutical pellets in fluid-bed processes. In: *Handbook of Powder Technology: Granulation*. Ed. by Salman, A. D., Hounslow, M. J., and Seville, J. P. K. Amsterdam: Elsevier Science B.V., 2007, 779–811. DOI: 10.1016/S0167-3785(07)80052-2.

[54] Pfalzer, L., Bartusch, W., and Heiss, R. Untersuchungen über die physikalischen Eigenschaften agglomerierter Pulver. *Chemie Ingenieur Technik* 45(8) (1973), 510–516. DOI: 10.1002/cite.330450810.

[55] Westermarck, S., Juppo, A. M., Kervinen, L., and Yliruusi, J. Pore structure and surface area of mannitol powder, granules and tablets determined with mercury porosimetry and nitrogen adsorption. *European Journal of Pharmaceutics and Biopharmaceutics* 46(1) (1998), 61–68. DOI: 10.1016/S0939-6411(97)00169-0.

[56] Tsotsas, E. Influence of drying kinetics on particle formation: A personal perspective. *Drying Technology* 30(11-12) (2012), 1167–1175. DOI: 10.1080/07373937.2012.685139.

[57] Rieck, C., Hoffmann, T., Bück, A., Peglow, M., and Tsotsas, E. Influence of drying conditions on layer porosity in fluidized bed spray granulation. *Powder Technology* 272 (2015), 120–131. DOI: 10.1016/j.powtec.2014.11.019.

[58] Dadkhah, M. and Tsotsas, E. Influence of process variables on internal particle structure in spray fluidized bed agglomeration. *Powder Technology* 258 (2014), 165–173. DOI: 10.1016/j.powtec.2014.03.005.

[59] Dewettinck, K., Deroo, L., Messens, W., and Huyghebaert, A. Agglomeration tendency during top-spray fluidized bed coating with gums. *LWT - Food Science and Technology* 31(6) (1998), 576–584. DOI: 10.1006/fstl.1998.0421.

[60] Dewettinck, K., Messens, W., Deroo, L., and Huyghebaert, A. Agglomeration tendency during top-spray fluidized bed coating with gelatin and starch hydrolysate. *LWT - Food Science and Technology* 32(2) (1999), 102–106. DOI: 10.1006/fstl.1998.0507.

[61] Hede, P. D., Bach, P., and Jensen, A. D. Validation of the flux number as scaling parameter for top-spray fluidised bed systems. *Chemical Engineering Science* 63(3) (2008), 815–828. DOI: 10.1016/j.ces.2007.10.017.

[62] Hede, P. D., Bach, P., and Jensen, A. D. Top-spray fluid bed coating: Scale-up in terms of relative droplet size and drying force. *Powder Technology* 184(3) (2008), 318–332. DOI: 10.1016/j.powtec.2007.09.009.

[63] Akkermans, J. H. M., Edwards, M. F., Groot, A. T. J., Montanus, C. P. M., van Pomeren, R. W. J., and Yüregir, K. A. R. Production of detergent granulates. Patent WO9858046. 1998.

[64] Davis, R. H., Serayssol, J.-M., and Hinch, E. J. The elastohydrodynamic collision of two spheres. *Journal of Fluid Mechanics* 163 (1986), 479–497. DOI: 10.1017/S0022112086002392.

[65] Barnocky, G. and Davis, R. H. Elastohydrodynamic collision and rebound of spheres: Experimental verification. *Physics of Fluids* 31(6) (1988), 1324–1329. DOI: 10.1063/1.866725.

[66] Davis, R. H. Elastohydrodynamic collisions of particles. *Physicochemical Hydrodynamics* 9(1-2) (1987), 41–52.

[67] Tardos, G. I., Khan, M. I., and Mort, P. R. Critical parameters and limiting conditions in binder granulation of fine powders. *Powder Technology* 94(3) (1997), 245–258. DOI: 10.1016/S0032-5910(97)03321-4.

[68] Davis, R. H., Rager, D. A., and Good, B. T. Elastohydrodynamic rebound of spheres from coated surfaces. *Journal of Fluid Mechanics* 468 (2002), 107–119. DOI: 10.1017/S0022112002001489.

[69] Ennis, B. J., Tardos, G. I., and Pfeffer, R. A microlevel-based characterization of granulation phenomena. *Powder Technology* 65(1–3) (1991), 257–272. DOI: 10.1016/0032-5910(91)80189-P.

[70] Liu, L. X., Litster, J. D., Iveson, S. M., and Ennis, B. J. Coalescence of deformable granules in wet granulation processes. *AIChE Journal* 46(3) (2000), 529–539. DOI: 10.1002/aic.690460312.

[71] Donahue, C. M., Davis, R. H., Kantak, A. A., and Hrenya, C. M. Mechanisms for agglomeration and deagglomeration following oblique collisions of wet particles. *Physical Review E* 86 (2012), 021303. DOI: 10.1103/PhysRevE.86.021303.

[72] Donahue, C. M., Brewer, W. M., Davis, R. H., and Hrenya, C. M. Agglomeration and deagglomeration of rotating wet doublets. *Journal of Fluid Mechanics* 708 (2012), 128–148. DOI: 10.1017/jfm.2012.297.

[73] Villa, M. P., Bertín, D. E., Cotabarren, I. M., Piña, J., and Bucalá, V. Fluidized-bed melt granulation: Coating and agglomeration kinetics and growth regime prediction. *Powder Technology* 300 (2016), 61–72. DOI: 10.1016/j.powtec.2016.06.006.

[74] Ramkrishna, D. *Population balances: Theory and applications to particulate systems in engineering*. San Diego: Academic Press, 2000.

[75] Deutsches Institut für Normung e. V. *Darstellung der Ergebnisse von Partikelgrößenanalysen Teil 1: Grafische Darstellung*. DIN ISO 9276-1. 2004.

[76] Randolph, A. D. and Larson, M. A. *Theory of particulate processes*. New York: Academic Press, 1971.

[77] Deutsches Institut für Normung e. V. *Darstellung der Ergebnisse von Partikelgrößenanalysen Teil 2: Berechnung von mittleren Partikelgrößen/-durchmessern und Momenten aus Partikelgrößenverteilungen*. DIN ISO 9276-2. 2006.

[78] Hulburt, H. M. and Katz, S. Some problems in particle technology. *Chemical Engineering Science* 19(8) (1964), 555–574. DOI: 10.1016/0009-2509(64)85047-8.

[79] Gerstlauer, A., Gahn, C., Zhou, H., Rauls, M., and Schreiber, M. Application of population balances in the chemical industry: Current status and future needs. *Chemical Engineering Science* 61(1) (2006), 205–217. DOI: 10.1016/j.ces.2004.12.058.

[80] Heinrich, S., Peglow, M., Ihlow, M., Henneberg, M., and Mörl, L. Analysis of the start-up process in continuous fluidized bed spray granulation by population balance modelling. *Chemical Engineering Science* 57(20) (2002), 4369–4390. DOI: 10.1016/S0009-2509(02)00352-4.

[81] Vreman, A. W., van Lare, C. E., and Hounslow, M. J. A basic population balance model for fluid bed spray granulation. *Chemical Engineering Science* 64(21) (2009), 4389–4398. DOI: 10.1016/j.ces.2009.07.010.

[82] Silva, D. O., Tamiozzo, L. M., Duarte, C. R., Murata, V. V., and Barrozo, M. A. S. Modeling of seed coating in a spouted bed. *Drying Technology* 29(3) (2011), 286–294. DOI: 10.1080/07373937.2010.490892.

[83] Hounslow, M. J., Ryall, R. L., and Marshall, V. R. A discretized population balance for nucleation, growth, and aggregation. *AIChE Journal* 34(11) (1988), 1821–1832. DOI: 10.1002/aic.690341108.

[84] Kumar, J., Peglow, M., Warnecke, G., Heinrich, S., and Mörl, L. Improved accuracy and convergence of discretized population balance for aggregation: The cell average technique. *Chemical Engineering Science* 61(10) (2006), 3327–3342. DOI: 10.1016/j.ces.2005.12.014.

[85] Peglow, M., Kumar, J., Heinrich, S., Warnecke, G., Tsotsas, E., Mörl, L., and Wolf, B. A generic population balance model for simultaneous agglomeration and drying in fluidized beds. *Chemical Engineering Science* 62(1-2) (2007), 513–532. DOI: 10.1016/j.ces.2006.09.042.

[86] Burgschweiger, J. and Tsotsas, E. Experimental investigation and modelling of continuous fluidized bed drying under steady-state and dynamic conditions. *Chemical Engineering Science* 57(24) (2002), 5021–5038. DOI: 10.1016/S0009-2509(02)00424-4.

[87] Abberger, T. Population balance modelling of granulation. In: *Handbook of Powder Technology: Granulation*. Ed. by Salman, A. D., Hounslow, M. J., and Seville, J. P. K. Amsterdam: Elsevier Science B.V., 2007, 1109–1186. DOI: 10.1016/S0167-3785(07)80059-5.

[88] Peglow, M., Antonyuk, S., Jacob, M., Palzer, S., Heinrich, S., and Tsotsas, E. Particle formulation in spray fluidized beds. In: *Modern Drying Technology, Volume 3: Product Quality and Formulation*. Ed. by Tsotsas, E. and Mujumdar, A. S. Weinheim: Wiley-VCH Verlag GmbH & Co. KGaA, 2011, 295–378. DOI: 10.1002/9783527631728.ch20.

[89] Sherony, D. F. A model of surface renewal with application to fluid bed coating of particles. *Chemical Engineering Science* 36(5) (1981), 845–848. DOI: 10.1016/0009-2509(81)85037-3.

[90] Wnukowski, P. and Setterwall, F. The coating of particles in a fluidized bed (residence time distribution in a system of two coupled perfect mixers). *Chemical Engineering Science* 44(3) (1989), 493–505. DOI: 10.1016/0009-2509(89)85027-4.

[91] Li, J., Freireich, B., Wassgren, C., and Litster, J. D. A general compartment-based population balance model for particle coating and layered granulation. *AIChE Journal* 58(5) (2012), 1397–1408. DOI: 10.1002/aic.12678.

[92] Hampel, N., Bück, A., Peglow, M., and Tsotsas, E. Continuous pellet coating in a Wurster fluidized bed process. *Chemical Engineering Science* 86 (2013), 87–98. DOI: 10.1016/j.ces.2012.05.034.

[93] Neugebauer, C., Palis, S., Bück, A., Tsotsas, E., Heinrich, S., and Kienle, A. A dynamic two-zone model of continuous fluidized bed layering granulation with internal product classification. *Particuology* 31 (2017), 8–14. DOI: 10.1016/j.partic.2016.07.001.

[94] Maronga, S. J. and Wnukowski, P. Modelling of the three-domain fluidized-bed particulate coating process. *Chemical Engineering Science* 52(17) (1997), 2915–2925. DOI: 10.1016/S0009-2509(97)00112-7.

[95] Börner, M., Hagemeier, T., Ganzer, G., Peglow, M., and Tsotsas, E. Experimental spray zone characterization in top-spray fluidized bed granulation. *Chemical Engineering Science* 116 (2014), 317–330. DOI: 10.1016/j.ces.2014.05.007.

[96] Sastry, K. V. Similarity size distribution of agglomerates during their growth by coalescence in granulation or green pelletization. *International Journal of Mineral Processing* 2(2) (1975), 187–203. DOI: 10.1016/0301-7516(75)90021-6.

[97] Hussain, M. *Micro-macro transition from discrete modeling to population balances in spray fluidized bed agglomeration*. Ph.D. Thesis. Otto von Guericke University Magdeburg. Barleben: Docupoint-Verlag, 2014.

[98] Hussain, M., Kumar, J., Peglow, M., and Tsotsas, E. On two-compartment population balance modeling of spray fluidized bed agglomeration. *Computers & Chemical Engineering* 61 (2014), 185–202. DOI: 10.1016/j.compchemeng.2013.11.003.

[99] Hampel, R., Peglow, M., Tsotsas, E., and Heinrich, S. Study of fluidized bed spray agglomeration focussing the moisture content of the solid. *Proceedings of the 16th International Drying Symposium*. Ed. by Thorat, B. N. and Mujumdar, A. S. Vol. B. 2008, 1052–1059.

[100] Kapur, P. C. Kinetics of granulation by non-random coalescence mechanism. *Chemical Engineering Science* 27(10) (1972), 1863–1869. DOI: 10.1016/0009-2509(72)85048-6.

[101] Wang, F. Y. and Cameron, I. T. Review and future directions in the modelling and control of continuous drum granulation. *Powder Technology* 124(3) (2002), 238–253. DOI: 10.1016/S0032-5910(02)00020-7.

[102] Scott, W. T. Analytic studies of cloud droplet coalescence I. *Journal of the Atmospheric Sciences* 25(1) (1968), 54–65. DOI: 10.1175/1520-0469(1968)025<0054:ASOCDC>2.0.CO;2.

[103] Smoluchowski, M. von. Versuch einer mathematischen Theorie der Koagulationskinetik kolloider Lösungen. *Zeitschrift für Physikalische Chemie* 92(2) (1917).

[104] Reynolds, G. K., Sanders, C. F. W., Salman, A. D., and Hounslow, M. J. The kinetics of high-shear granulation. In: *Granular Materials: Fundamentals and Applications*. Ed. by Antony, S. J., Hoyle, W., and Ding, Y. Cambridge: The Royal Society of Chemistry, 2004, 296–318. DOI: 10.1039/9781847550996-00296.

[105] Golovin, A. M. The solution of the coagulation equation for cloud droplets in a rising air current. *Bulletin of the Academy of Sciences of the USSR / Geophysics series* 8 (1963), 482–487.

[106] Hounslow, M. J. The population balance as a tool for understanding particle rate processes. *KONA Powder and Particle Journal* 16(0) (1998), 179–193. DOI: 10.14356/kona.1998021.

[107] Hounslow, M. J., Pearson, J. M. K., and Instone, T. Tracer studies of high-shear granulation II: Population balance modeling. *AIChE Journal* 47(9) (2001), 1984–1999. DOI: 10.1002/aic.690470910.

[108] Hussain, M., Kumar, J., and Tsotsas, E. A new framework for population balance modeling of spray fluidized bed agglomeration. *Particuology* 19 (2015), 141–154. DOI: 10.1016/j.partic.2014.06.005.

[109] LeVeque, R. J. *Numerical methods for conservation laws*. 2nd ed. Basel: Birkhäuser Verlag, 1992.

[110] Bück, A., Klaunick, G., Kumar, J., Peglow, M., and Tsotsas, E. Numerical simulation of particulate processes for control and estimation by spectral methods. *AIChE Journal* 58(8) (2012), 2309–2319. DOI: 10.1002/aic.12757.

[111] Kumar, S. and Ramkrishna, D. On the solution of population balance equations by discretization I: A fixed pivot technique. *Chemical Engineering Science* 51(8) (1996), 1311–1332. DOI: 10.1016/0009-2509(96)88489-2.

[112] Kumar, S. and Ramkrishna, D. On the solution of population balance equations by discretization II: A moving pivot technique. *Chemical Engineering Science* 51(8) (1996), 1333–1342. DOI: 10.1016/0009-2509(95)00355-X.

[113] Marchisio, D. L., Pikturna, J. T., Fox, R. O., Vigil, R. D., and Barresi, A. A. Quadrature method of moments for population-balance equations. *AIChE Journal* 49(5) (2003), 1266–1276. DOI: 10.1002/aic.690490517.

[114] Marchisio, D. L. and Fox, R. O. Solution of population balance equations using the direct quadrature method of moments. *Journal of Aerosol Science* 36(1) (2005), 43–73. DOI: 10.1016/j.jaerosci.2004.07.009.

[115] Zhu, H. P., Zhou, Z. Y., Yang, R. Y., and Yu, A. B. Discrete particle simulation of particulate systems: Theoretical developments. *Chemical Engineering Science* 62(13) (2007), 3378–3396. DOI: 10.1016/j.ces.2006.12.089.

[116] van Annaland, M. S., Deen, N. G., and Kuipers, J. A. M. Multi-level computational fluid dynamics models for the description of particle mixing and granulation in fluidized beds. In: *Handbook of Powder Technology: Granulation*. Ed. by Salman, A. D., Hounslow, M. J., and Seville, J. P. K. Vol. 11. Amsterdam: Elsevier Science B.V., 2007, 1071–1107. DOI: 10.1016/S0167-3785(07)80058-3.

[117] Goldschmidt, M. J. V., Weijers, G. G. C., Boerefijn, R., and Kuipers, J. A. M. Discrete element modelling of fluidised bed spray granulation. *Powder Technology* 138(1) (2003), 39–45. DOI: 10.1016/j.powtec.2003.08.045.

[118] Fries, L. *Discrete particle modeling of a fluidized bed granulator*. Ph.D. Thesis. Hamburg University of Technology. Göttingen: Cuvillier Verlag, 2012.

[119] Metropolis, N. and Ulam, S. The Monte Carlo method. *Journal of the American Statistical Association* 44(247) (1949), 335–341. DOI: 10.1080/01621459.1949.10483310.

[120] Ramkrishna, D. Analysis of population balance IV: The precise connection between Monte Carlo simulation and population balances. *Chemical Engineering Science* 36(7) (1981), 1203–1209.

[121] Peborgh Gooch, J. R. van and Hounslow, M. J. Monte Carlo simulation of size-enlargement mechanisms in crystallization. *AIChE Journal* 42(7) (1996), 1864–1874. DOI: 10.1002/aic.690420708.

[122] Gillespie, D. T. An exact method for numerically simulating the stochastic coalescence process in a cloud. *Journal of the Atmospheric Sciences* 32 (1975), 1977–1989.

[123] Terrazas-Velarde, K., Peglow, M., and Tsotsas, E. Investigation of the kinetics of fluidized bed spray agglomeration based on stochastic methods. *AIChE Journal* 57(11) (2011), 3012–3026. DOI: 10.1002/aic.12506.

[124] Dernedde, M., Peglow, M., and Tsotsas, E. A novel, structure-tracking Monte Carlo algorithm for spray fluidized bed agglomeration. *AIChE Journal* 58(10) (2012), 3016–3029. DOI: 10.1002/aic.13709.

[125] McGuire, A. D., Mosbach, S., Lee, K. F., Reynolds, G., and Kraft, M. A high-dimensional, stochastic model for twin-screw granulation part 2: Numerical methodology. *Chemical Engineering Science* 188 (2018), 18–33. DOI: 10.1016/j.ces.2018.04.077.

[126] Oullion, M., Reynolds, G. K., and Hounslow, M. J. Simulating the early stage of high-shear granulation using a two-dimensional Monte-Carlo approach. *Chemical Engineering Science* 64(4) (2009), 673–685. DOI: 10.1016/j.ces.2008.08.014.

[127] KuShaari, K., Pandey, P., Song, Y., and Turton, R. Monte Carlo simulations to determine coating uniformity in a Wurster fluidized bed coating process. *Powder Technology* 166(2) (2006), 81–90. DOI: 10.1016/j.powtec.2006.05.001.

[128] Pandey, P., Katakdaunde, M., and Turton, R. Modeling weight variability in a pan coating process using Monte Carlo simulations. *AAPS PharmSciTech* 7(4) (2006), 83. DOI: 10.1208/pt070483.

[129] Barrasso, D. and Ramachandran, R. A comparison of model order reduction techniques for a four-dimensional population balance model describing multi-component wet granulation processes. *Chemical Engineering Science* 80 (2012), 380–392. DOI: 10.1016/j.ces.2012.06.039.

[130] Zhao, H., Maisels, A., Matsoukas, T., and Zheng, C. Analysis of four Monte Carlo methods for the solution of population balances in dispersed systems. *Powder Technology* 173(1) (2007), 38–50. DOI: 10.1016/j.powtec.2006.12.010.

[131] Smith, M. and Matsoukas, T. Constant-number Monte Carlo simulation of population balances. *Chemical Engineering Science* 53(9) (1998), 1777–1786. DOI: 10.1016/S0009-2509(98)00045-1.

[132] Dernedde, M. *Modellierung der Wirbelschicht-Sprühagglomeration unter Berücksichtigung der Partikelstrukturbildung*. Ph.D. Thesis. Otto von Guericke University Magdeburg, 2013.

[133] Roos, Y. H. and Karel, M. Phase transitions of mixtures of amorphous polysaccharides and sugars. *Biotechnology Progress* 7(1) (1991), 49–53. DOI: 10.1021/bp00007a008.

[134] Aguilera, J. M., Levi, G., and Karel, M. Effect of water content on the glass transition and caking of fish protein hydrolyzates. *Biotechnology Progress* 9(6) (1993), 651–654. DOI: 10.1021/bp00024a013.

[135] Descamps, N., Palzer, S., and Zuercher, U. The amorphous state of spray-dried maltodextrin: Sub-sub-Tg enthalpy relaxation and impact of temperature and water annealing. *Carbohydrate Research* 344(1) (2009), 85–90. DOI: 10.1016/j.carres.2008.06.033.

[136] Paterson, A. H. J., Ripberger, G. D., and Bridges, R. P. Measurement of the viscosity of freeze dried amorphous lactose near the glass transition temperature. *International Dairy Journal* 43 (2015), 27–32. DOI: 10.1016/j.idairyj.2014.11.005.

[137] Palzer, S. The effect of glass transition on the desired and undesired agglomeration of amorphous food powders. *Chemical Engineering Science* 60(14) (2005), 3959–3968. DOI: 10.1016/j.ces.2005.02.015.

[138] Avilés-Avilés, C., Dumoulin, E. D., and Turchiuli, C. Fluidised bed agglomeration of particles with different glass transition temperatures. *Powder Technology* 270 (2015), 445–452. DOI: 10.1016/j.powtec.2014.03.026.

[139] Blei, S. and Sommerfeld, M. CFD in drying technology: Spray-dryer simulation. In: *Modern Drying Technology, Volume 1: Computational Tools at Different Scales*. Ed. by Tsotsas, E. and Mujumdar, A. S. Weinheim: Wiley-VCH Verlag GmbH & Co. KGaA, 2007, 155–208. DOI: 10.1002/9783527631728.ch5.

[140] Burgschweiger, J., Groenewold, H., Hirschmann, C., and Tsotsas, E. From hygroscopic single particle to batch fluidized bed drying kinetics. *The Canadian Journal of Chemical Engineering* 77(2) (1999), 333–341. DOI: 10.1002/cjce.5450770220.

[141] Heinrich, S. and Mörl, L. Fluidized bed spray granulation: A new model for the description of particle wetting and of temperature and concentration distribution. *Chemical Engineering and Processing: Process Intensification* 38(4-6) (1999), 635–663. DOI: 10.1016/S0255-2701(99)00065-3.

[142] Ronsse, F., Pieters, J. G., and Dewettinck, K. Numerical spray model of the fluidized bed coating process. *Drying Technology* 25(9) (2007), 1491–1514. DOI: 10.1080/07373930701537245.

[143] Groenewold, H. and Tsotsas, E. Predicting apparent Sherwood numbers for fluidized beds. *Drying Technology* 17(7-8) (1999), 1557–1570. DOI: 10.1080/07373939908917635.

[144] van Meel, D. A. Adiabatic convection batch drying with recirculation of air. *Chemical Engineering Science* 9(1) (1958), 36–44. DOI: 10.1016/0009-2509(58)87005-0.

[145] Rieck, C., Bück, A., and Tsotsas, E. Monte Carlo modeling of fluidized bed coating and layering processes. *AIChE Journal* 62(8) (2016), 2670–2680. DOI: 10.1002/aic.15237.

[146] Rieck, C., Schmidt, M., Bück, A., and Tsotsas, E. Monte Carlo modeling of binder-less spray agglomeration in fluidized beds. *AIChE Journal* 64(10) (2018), 3582–3594. DOI: 10.1002/aic.16349.

[147] Terrazas-Velarde, K., Peglow, M., and Tsotsas, E. Stochastic simulation of agglomerate formation in fluidized bed spray drying: A micro-scale approach. *Chemical Engineering Science* 64(11) (2009), 2631–2643. DOI: 10.1016/j.ces.2009.02.041.

[148] Fichthorn, K. A. and Weinberg, W. H. Theoretical foundations of dynamical Monte Carlo simulations. *The Journal of Chemical Physics* 95(2) (1991), 1090–1096. DOI: 10.1063/1.461138.

[149] Gillespie, D. T. A general method for numerically simulating the stochastic time evolution of coupled chemical reactions. *Journal of Computational Physics* 22(4) (1976), 403–434. DOI: 10.1016/0021-9991(76)90041-3.

[150] Dadkhah, M., Peglow, M., and Tsotsas, E. Characterization of the internal morphology of agglomerates produced in a spray fluidized bed by X-ray tomography. *Powder Technology* 228 (2012), 349–358. DOI: 10.1016/j.powtec.2012.05.051.

[151] Meric, R. A. and Erbil, H. Y. Evaporation of sessile drops on solid surfaces: Pseudospherical cap geometry. *Langmuir* 14(7) (1998), 1915–1920. DOI: 10.1021/la970147c.

[152] Jiang, Z., Hagemeier, T., Bück, A., and Tsotsas, E. Experimental measurements of particle collision dynamics in a pseudo-2D gas-solid fluidized bed. *Chemical Engineering Science* 167 (2017), 297–316. DOI: 10.1016/j.ces.2017.04.024.

[153] Buffière, P. and Moletta, R. Collision frequency and collisional particle pressure in three-phase fluidized beds. *Chemical Engineering Science* 55(22) (2000), 5555–5563. DOI: 10.1016/S0009-2509(00)00186-X.

[154] Oesterle, B. and Petitjean, A. Simulation of particle-to-particle interactions in gas solid flows. *International Journal of Multiphase Flow* 19(1) (1993), 199–211. DOI: 10.1016/0301-9322(93)90033-Q.

[155] Sondej, F., Peglow, M., Bück, A., and Tsotsas, E. Experimental investigation of the morphology of salt deposits from drying sessile droplets by white-light interferometry. *AIChE Journal* 64(6) (2018), 2002–2016. DOI: 10.1002/aic.16085.

[156] Pashminehazar, R., Kharaghani, A., and Tsotsas, E. Three dimensional characterization of morphology and internal structure of soft material agglomerates produced in spray fluidized bed by X-ray tomography. *Powder Technology* 300 (2016), 46–60. DOI: 10.1016/j.powtec.2016.03.053.

[157] Freireich, B. and Wassgren, C. Intra-particle coating variability: Analysis and Monte-Carlo simulations. *Chemical Engineering Science* 65(3) (2010), 1117–1124. DOI: 10.1016/j.ces.2009.09.066.

[158] Gordon, M. and Taylor, J. S. Ideal copolymers and the second-order transitions of synthetic rubbers I: Non-crystalline copolymers. *Journal of Applied Chemistry* 2(9) (1952), 493–500. DOI: 10.1002/jctb.5010020901.

[159] Roos, Y. H. and Karel, M. Water and molecular weight effects on glass transitions in amorphous carbohydrates and carbohydrate solutions. *Journal of Food Science* 56(6) (1991), 1676–1681. DOI: 10.1111/j.1365-2621.1991.tb08669.x.

[160] Dokic, P., Jakovljevic, J., and Dokic-Baucal, L. Molecular characteristics of maltodextrins and rheological behaviour of diluted and concentrated solutions. *Colloids and Surfaces A: Physicochemical and Engineering Aspects* 141(3) (1998), 435–440. DOI: 10.1016/S0927-7757(97)00118-0.

[161] Castro, N., Durrieu, V., Raynaud, C., and Rouilly, A. Influence of DE-value on the physico-chemical properties of maltodextrin for melt extrusion processes. *Carbohydrate Polymers* 144 (2016), 464–473. DOI: 10.1016/j.carbpol.2016.03.004.

[162] Williams, M. L., Landel, R. F., and Ferry, J. D. The temperature dependence of relaxation mechanisms in amorphous polymers and other glass-forming liquids. *Journal of the American Chemical Society* 77(14) (1955), 3701–3707. DOI: 10.1021/ja01619a008.

[163] Sperling, L. H. *Introduction to physical polymer science*. 4th ed. Hoboken: John Wiley & Sons, 2006.

[164] Descamps, N., Palzer, S., Roos, Y. H., and Fitzpatrick, J. J. Glass transition and flowability/caking behaviour of maltodextrin DE 21. *Journal of Food Engineering* 119(4) (2013), 809–813. DOI: 10.1016/j.jfoodeng.2013.06.045.

[165] Kalbag, A. and Wassgren, C. Inter-tablet coating variability: Tablet residence time variability. *Chemical Engineering Science* 64(11) (2009), 2705–2717. DOI: 10.1016/j.ces.2009.02.037.

[166] Sondej, F., Bück, A., and Tsotsas, E. Comparative analysis of the coating thickness on single particles using X-ray micro-computed tomography and confocal laser-scanning microscopy. *Powder Technology* 287 (2016), 330–340. DOI: 10.1016/j.powtec.2015.09.039.

[167] Sondej, F., Bück, A., Koslowsky, K., Bachmann, P., Jacob, M., and Tsotsas, E. Investigation of coating layer morphology by micro-computed X-ray tomography. *Powder Technology* 273 (2015), 165–175. DOI: 10.1016/j.powtec.2014.12.050.

[168] Lefebvre, A. H. and McDonell, V. G. *Atomization and sprays*. 2nd ed. Boca Raton: CRC Press, 2017. DOI: 10.1201/9781315120911.

[169] Jiang, Z., Rieck, C., Bück, A., and Tsotsas, E. Estimation of coefficient of restitution of irregular shaped particles on horizontal substrates. *Proceedings of the 8th International Granulation Workshop*. Ed. by Salman, A. D., Palzer, S., and Hounslow, M. J. 2017.

[170] Takeiti, C. Y., Kieckbusch, T. G., and Collares-Queiroz, F. P. Morphological and physicochemical characterization of commercial maltodextrins with different degrees of dextrose-equivalent. *International Journal of Food Properties* 13(2) (2010), 411–425. DOI: 10.1080/10942910802181024.

[171] Peglow, M., Metzger, T., Lee, G., Schiffter, H., Hampel, R., Heinrich, S., and Tsotsas, E. Measurement of average moisture content and drying kinetics for single particles, droplets and dryers. In: *Modern Drying Technology, Volume 2: Experimental Techniques*. Ed. by Tsotsas, E. and Mujumdar, A. S. Weinheim: Wiley-VCH Verlag GmbH & Co. KGaA, 2009, 1–71. DOI: 10.1002/9783527631728.ch8.

[172] Rieck, C., Bück, A., and Tsotsas, E. Estimation of the dominant size enlargement mechanism in spray fluidized bed processes. *AIChE Journal* 66(5) (2020), 576. DOI: 10.1002/aic.16920.

[173] Rajniak, P., Stepanek, F., Dhanasekharan, K., Fan, R., Mancinelli, C., and Chern, R. T. A combined experimental and computational study of wet granulation in a Wurster fluid bed granulator. *Powder Technology* 189(2) (2009), 190–201. DOI: 10.1016/j.powtec.2008.04.027.

[174] Koren, B. A robust upwind discretization method for advection, diffusion and source terms. In: *Numerical methods for advection-diffusion problems*. Ed. by Vreugdenhil, C. B. and Koren, B. Notes on numerical fluid mechanics. Braunschweig: Vieweg, 1993, 117–138.

[175] Kuchling, H. *Taschenbuch der Physik*. 14th ed. Leipzig: Fachbuchverlag, 1994.

[176] Hampel, R. *Beitrag zur Analyse von kinetischen Einflüssen auf die Wirbelschicht-Sprühagglomeration*. Ph.D. Thesis. Otto von Guericke University Magdeburg, 2010.

[177] Jiménez, T., Turchiuli, C., and Dumoulin, E. D. Particles agglomeration in a conical fluidized bed in relation with air temperature profiles. *Chemical Engineering Science* 61(18) (2006), 5954–5961. DOI: 10.1016/j.ces.2006.05.007.

[178] Saleh, K., Cherif, R., and Hemati, M. An experimental study of fluidized-bed coating: Influence of operating conditions on growth rate and mechanism. *Advanced Powder Technology* 10(3) (1999), 255–277. DOI: 10.1163/156855299X00334.

[179] Saleh, K., Steinmetz, D., and Hemati, M. Experimental study and modeling of fluidized bed coating and agglomeration. *Powder Technology* 130(1-3) (2003), 116–123. DOI: 10.1016/S0032-5910(02)00254-1.

[180] Jiménez, T. *Agglomération de particules par voie humide en lit fluidisé*. Ph.D. Thesis. AgroParisTech, 2007.

[181] Derakhshani, S. M., Schott, D. L., and Lodewijks, G. Micro–macro properties of quartz sand: Experimental investigation and DEM simulation. *Powder Technology* 269 (2015), 127–138. DOI: 10.1016/j.powtec.2014.08.072.

[182] Zhang, H.-L. and Han, S.-J. Viscosity and density of water + sodium chloride + potassium chloride solutions at 298.15 K. *Journal of Chemical & Engineering Data* 41(3) (1996), 516–520. DOI: 10.1021/je9501402.

[183] Carl Roth GmbH + Co. KG. *Safety data sheet according to 1907/2006/EC, article 31: Gum arabic, spray dried*. 2014.

[184] Carl Roth GmbH + Co. KG. *Voluntary safety information following the safety data sheet format according to regulation (EC) No. 1907/2006: Sodium chloride > 99,8 %, with anticaking*. 2018.

[185] Jiang, Z., Rieck, C., Bück, A., and Tsotsas, E. Modeling of inter- and intra-particle coating uniformity in a Wurster fluidized bed by a coupled CFD-DEM-Monte Carlo approach. *Chemical Engineering Science* 211 (2020), 115289. DOI: 10.1016/j.ces.2019.115289.

[186] Singh, A. K. and Tsotsas, E. Stochastic model to simulate spray fluidized bed agglomeration: A morphological approach. *Powder Technology* 355 (2019), 449–460. DOI: 10.1016/j.powtec.2019.07.075.

[187] Glück, B. *Zustands- und Stoffwerte: Wasser, Dampf, Luft; Verbrennungsrechnung*. 2nd ed. Berlin: Verlag für Bauwesen, 1991.

[188] Poling, B. E., Prausnitz, J. M., and O'Connell, J. P. *The properties of gases and liquids*. 5th ed. New York: McGraw-Hill, 2001.

[189] Carl Roth GmbH + Co. KG. *Specification: Benzoic acid sodium salt*. 2017.

[190] Martin, H. Heat transfer in fluidized beds. In: *VDI Heat Atlas*. Ed. by VDI e.V. Berlin: Springer-Verlag, 2010, 1301–1309.

[191] Gnielinski, V. Fluid-particle heat transfer in flow through packed beds of solids. In: *VDI Heat Atlas*. Ed. by VDI e.V. Berlin: Springer-Verlag, 2010, 743–744.

[192] Patankar, S. V. *Numerical heat transfer and fluid flow*. New York: Hemisphere Publishing Corp., 1980.

[193] Weisstein, E. W. *CRC concise encyclopedia of mathematics*. 2nd ed. Boca Raton: Chapman & Hall/CRC, 2003.

[194] Heuser, H. *Lehrbuch der Analysis: Teil 2*. 10th ed. Stuttgart: Teubner, 1998.

Publications

Journal publications

[1] **Rieck**, **C.**, Hoffmann, T., Bück, A., Peglow, M., and Tsotsas, E. Influence of drying conditions on layer porosity in fluidized bed spray granulation. *Powder Technology* 272 (2015), 120–131. DOI: 10.1016/j.powtec.2014.11.019.

[2] Hoffmann, T., **Rieck**, **C.**, Schmidt, M., Bück, A., Peglow, M., and Tsotsas, E. Prediction of shell porosities in continuous fluidized bed spray layering. *Drying Technology* 33(13) (2015), 1662–1670. DOI: 10.1080/07373937.2015.1064943.

[3] Schmidt, M., **Rieck**, **C.**, Bück, A., and Tsotsas, E. Experimental investigation of process stability of continuous spray fluidized bed layering with external product separation. *Chemical Engineering Science* 137 (2015), 466–475. DOI: 10.1016/j.ces.2015.06.060.

[4] **Rieck**, **C.** and Bück, A. Mathematische Modellierung der Partikelformulierung in Trommelgranulatoren. *Chemie Ingenieur Technik* 88(7) (2016), 841–849. DOI: 10.1002/cite.201500016.

[5] **Rieck**, **C.**, Bück, A., and Tsotsas, E. Monte Carlo modeling of fluidized bed coating and layering processes. *AIChE Journal* 62(8) (2016), 2670–2680. DOI: 10.1002/aic.15237.

[6] **Rieck**, **C.**, Schmidt, M., Bück, A., and Tsotsas, E. Monte Carlo modeling of binder-less spray agglomeration in fluidized beds. *AIChE Journal* 64(10) (2018), 3582–3594. DOI: 10.1002/aic.16349.

[7] Jiang, Z., Du, J., **Rieck**, **C.**, Bück, A., and Tsotsas, E. PTV experiments and DEM simulations of the coefficient of restitution for irregular particles impacting on horizontal substrates. *Powder Technology* 360 (2020), 352–365. DOI: 10.1016/j.powtec.2019.10.072.

[8] Jiang, Z., **Rieck**, **C.**, Bück, A., and Tsotsas, E. Modeling of inter- and intra-particle coating uniformity in a Wurster fluidized bed by a coupled CFD-DEM-Monte Carlo approach. *Chemical Engineering Science* 211 (2020), 115289. DOI: 10.1016/j.ces.2019.115289.

[9] Mezhericher, M., **Rieck**, **C.**, Razorenov, N., and Tsotsas, E. Ultrathin coating of particles in fluidized bed using submicron droplet aerosol. *Particuology* (2020). In press.

[10] **Rieck**, **C.**, Bück, A., and Tsotsas, E. Estimation of the dominant size enlargement mechanism in spray fluidized bed processes. *AIChE Journal* 66(5) (2020), 576. DOI: 10.1002/aic.16920.

[11] **Rieck**, **C.**, Bück, A., and Tsotsas, E. Graded coating of particles in spray fluidized beds. *International Journal of Chemical Engineering* (2020). Submitted.

Proceedings

[1] **Rieck**, **C.**, Bück, A., and Tsotsas, E. Stochastic modelling of particle coating in fluidized beds. *Proceedings of the 7th World Congress on Particle Technology (WCPT7)*. Beijing, China, May 19–22, 2014. DOI: 10.1016/j.proeng.2015.01.222.

[2] **Rieck**, **C.**, Bück, A., and Tsotsas, E. Monte Carlo modelling of particle coating in fluidized beds. *Proceedings of the 19th International Drying Symposium (IDS 2014)*. Lyon, France, August 24–27, 2014.

[3] **Rieck**, **C.**, Bück, A., and Tsotsas, E. Modeling of layering growth processes using a Monte Carlo approach. *Proceedings of the 8th Vienna International Conference on Mathematical Modelling (MATHMOD 2015)*. Vienna, Austria, February 18–20, 2015. DOI: 10.1016/j.ifacol.2015.05.042.

[4] **Rieck**, **C.**, Bück, A., and Tsotsas, E. Stochastic modeling of layering growth processes in fluidized beds. *Proceedings of the 7th International Granulation Workshop*. Sheffield, UK, July 1–3, 2015.

[5] Sondej, F., **Rieck**, **C.**, Schmidt, M., Bück, A., and Tsotsas, E. Use of X-ray micro-computed tomography in pharmaceuticals and food industry. *Proceedings of the 6th Conference on Industrial Computed Tomography (iCT)*. Wels, Austria, February 9–12, 2016.

[6] Müller, D., **Rieck**, **C.**, Bück, A., and Tsotsas, E. Modelling of continuous spray-coating in fluidized bed with a vertical tube air classifier. *Proceedings of the 20th International Drying Symposium (IDS 2016)*. Gifu, Japan, August 7–10, 2016.

[7] **Rieck**, **C.**, Bück, A., and Tsotsas, E. Monte Carlo modeling of binder-less agglomeration in fluidized beds. *Proceedings of the 20th International Drying Symposium (IDS 2016)*. Gifu, Japan, August 7–10, 2016.

[8] Jiang, Z., **Rieck**, **C.**, Bück, A., and Tsotsas, E. Estimation of coefficient of restitution of irregular shaped particles on horizontal substrates. *Proceedings of the 8th International Granulation Workshop*. Sheffield, UK, June 28–30, 2017.

[9] **Rieck**, **C.**, Bück, A., and Tsotsas, E. Influence of contact liquid dispersion on fluidized bed spray agglomeration. *Proceedings of the 8th International Granulation Workshop*. Sheffield, UK, June 28–30, 2017.

[10] Jiang, Z., **Rieck**, **C.**, Bück, A., and Tsotsas, E. Modeling of particle behavior in a Wurster fluidized bed: Coupling CFD-DEM with Monte Carlo. *Proceedings of the 21st International Drying Symposium (IDS 2018)*. Ed. by Editorial Universitat Politècnica de València. València, Spain, September 11–14, 2018, 205–212.

[11] **Rieck**, **C.**, Müller, D., Bück, A., and Tsotsas, E. Modeling of undesired agglomeration in fluidized bed coating. *Proceedings of the 9th International Granulation Workshop*. Lausanne, Switzerland, June 26–28, 2019.

[12] Mezhericher, M., **Rieck**, **C.**, Razorenov, N., and Tsotsas, E. Ultrathin coating of particles in fluidized bed using aerosol of submicron droplets. *Proceedings of the 22nd International Drying Symposium (IDS 2021)*. Worcester, MA, USA, June 27–30, 2021.

[13] **Rieck**, **C.**, Bück, A., and Tsotsas, E. Estimation of the dominant size enlargement mechanism in spray fluidized beds. *Proceedings of the 22nd International Drying Symposium (IDS 2021)*. Worcester, MA, USA, June 27–30, 2021.

Oral and poster presentations

[1] Hoffmann, T., **Rieck**, **C.**, Bück, A., and Tsotsas, E. *Beeinflussung der Granulatporosität bei der Wirbelschicht-Sprühgranulation*. Poster presentation. Jahrestreffen der ProcessNet-Fachgruppen Trocknungstechnik und Mechanische Flüssigkeitsabtrennung. Karlsruhe, Germany, February 19–21, 2014.

[2] **Rieck**, **C.**, Bück, A., and Tsotsas, E. *Stochastische Modellierung des Schichtwachstums bei der Wirbelschicht-Sprühgranulation*. Poster presentation. Jahrestreffen Agglomerations und Schüttguttechnik mit Beteiligung der Fachgemeinschaft Anlagen- und Prozesssicherheit. Magdeburg, Germany, March 10–12, 2014.

[3] **Rieck**, **C.**, Hussain, M., Bück, A., and Tsotsas, E. *Stochastic modelling of particle coating in fluidized beds*. Oral presentation. 7th World Congress on Particle Technology (WCPT7). Beijing, China, May 19–22, 2014.

[4] **Rieck**, **C.**, Bück, A., and Tsotsas, E. *Monte Carlo modelling of particle coating in fluidized beds*. Oral presentation. 19th International Drying Symposium (IDS 2014). Lyon, France, August 24–27, 2014.

[5] **Rieck**, **C.**, Bück, A., and Tsotsas, E. *Monte-Carlo Simulation für das Partikelcoating in Wirbelschichten*. Oral presentation. ProcessNet-Jahrestagung. Aachen, Germany, September 30–October 2, 2014.

[6] **Rieck**, **C.**, Bück, A., and Tsotsas, E. *Modeling of layering growth processes using a Monte Carlo approach*. Oral presentation. 8th Vienna International Conference on Mathematical Modelling (MATHMOD 2015). Vienna, Austria, February 18–20, 2015.

[7] **Rieck**, **C.**, Bück, A., and Tsotsas, E. *Monte-Carlo-Modellierung von Schichtwachstumsprozessen in Wirbelschichten*. Poster presentation. Jahrestreffen der Fachgruppen Trocknungstechnik und Wärme- und Stoffübertragung. Leipzig, Germany, March 4–6, 2015.

[8] Bück, A. and **Rieck**, **C.** *Mathematische Modellierung der Partikelbildung in Trommelgranulatoren*. Oral presentation. Jahrestreffen der Fachgruppen Agglomerations- und Schüttguttechnik, Lebensmittelverfahrenstechnik mit Lebensmittelbiotechnologie, Grenzflächenbestimmte Systeme und Prozesse, mit Fachgemeinschaftstag Formulierung. Magdeburg, Germany, March 16–18, 2015.

[9] **Rieck**, **C.**, Bück, A., and Tsotsas, E. *Stochastic modeling of layering growth processes in fluidized beds*. Poster presentation. 7th International Granulation Workshop. Sheffield, UK, July 1–3, 2015.

[10] Sondej, F., **Rieck**, **C.**, Schmidt, M., Bück, A., and Tsotsas, E. *Use of X-ray micro-computed tomography in pharmaceuticals and food industry*. Poster presentation. 6th Conference on Industrial Computed Tomography (iCT). Wels, Austria, February 9–12, 2016.

[11] **Rieck**, **C.**, Bück, A., and Tsotsas, E. *Stochastische Modellierung der binderlosen Agglomeration durch Glasübergang in Wirbelschichten*. Poster presentation. Jahrestreffen der ProcessNet-Fachgruppe Lebensmittelverfahrenstechnik. Erlangen, Germany, March 10–11, 2016.

[12] **Rieck**, **C.**, Bück, A., and Tsotsas, E. *Stochastic modelling of binder-less agglomeration in fluidised beds*. Poster presentation. International Congress on Particle Technology. Nuremberg, Germany, April 19–21, 2016.

[13] Müller, D., **Rieck**, **C.**, Bück, A., and Tsotsas, E. *Modelling of continuous spray-coating in fluidized bed with a vertical tube air classifier*. Oral presentation. 20th International Drying Symposium (IDS 2016). Gifu, Japan, August 7–10, 2016.

[14] **Rieck**, **C.**, Bück, A., and Tsotsas, E. *Monte Carlo modeling of binder-less agglomeration in fluidized beds*. Oral presentation. 20th International Drying Symposium (IDS 2016). Gifu, Japan, August 7–10, 2016.

[15] Bück, A., **Rieck**, **C.**, and Tsotsas, E. *Trocknung partiell benetzter Partikeloberflächen*. Poster presentation. Jahrestreffen der ProcessNet-Fachgruppen Agglomerations- und Schüttguttechnik, Grenzflächenbestimmte Systeme und Prozesse, Trocknungstechnik, Lebensmittelverfahrenstechnik und Wärme- und Stoffübertragung. Bruchsal, Germany, February 13–17, 2017.

[16] Jiang, Z., **Rieck**, **C.**, Bück, A., and Tsotsas, E. *Measurements of the coefficient of restitution of group A particles on different horizontal substrates*. Poster presentation. Jahrestreffen der ProcessNet-Fachgruppen Agglomerations- und Schüttguttechnik, Grenzflächenbestimmte Systeme und Prozesse, Trocknungstechnik, Lebensmittelverfahrenstechnik und Wärme- und Stoffübertragung. Bruchsal, Germany, February 13–17, 2017.

[17] **Rieck**, **C.**, Bück, A., and Tsotsas, E. *Einfluss des Flüssigkeitstransports durch Partikelkollisionen auf die Wirbelschicht-Sprühagglomeration*. Oral presentation. Jahrestreffen der ProcessNet-Fachgruppen Agglomerations- und Schüttguttechnik, Grenzflächenbestimmte Systeme und Prozesse, Trocknungstechnik, Lebensmittelverfahrenstechnik und Wärme- und Stoffübertragung. Bruchsal, Germany, February 13–17, 2017.

[18] Jiang, Z., **Rieck**, **C.**, Bück, A., and Tsotsas, E. *Estimation of coefficient of restitution of irregular shaped particles on horizontal substrates*. Oral presentation. 8th International Granulation Workshop. Sheffield, UK, June 28–30, 2017.

[19] **Rieck**, **C.**, Bück, A., and Tsotsas, E. *Influence of contact liquid dispersion on fluidized bed spray agglomeration*. Poster presentation. 8th International Granulation Workshop. Sheffield, UK, June 28–30, 2017.

[20] **Rieck**, **C.**, Bück, A., and Tsotsas, E. *Impact of contact liquid dispersion on agglomeration in fluidized beds*. Oral presentation. 10th World Congress of Chemical Engineering (WCCE10). Barcelona, Spain, October 1–5, 2017.

[21] **Rieck**, **C.**, Bück, A., and Tsotsas, E. *Modellierung der binderlosen Agglomeration in Sprühwirbelschichten*. Poster presentation. Jahrestreffen der ProcessNet-Fachgruppen Zerkleinern und Klassieren und Agglomerations- und Schüttguttechnik. Neuss, Germany, March 13–15, 2018.

[22] **Rieck**, **C.**, Bück, A., and Tsotsas, E. *Monte Carlo modeling of binder-less agglomeration*. Poster presentation. 6th Population Balance Modelling Conference (PBM 2018). Ghent, Belgium, May 7–9, 2018.

[23] Jiang, Z., **Rieck**, **C.**, Bück, A., and Tsotsas, E. *Modeling of particle dynamics in a Wurster fluidized bed: Coupling CFD-DEM with Monte Carlo*. Poster presentation. 21st International Drying Symposium (IDS 2018). València, Spain, September 11–14, 2018.

[24] **Rieck**, **C.**, Bück, A., and Tsotsas, E. *Stochastic modeling of binder-less agglomeration in fluidized beds*. Poster presentation. 21st International Drying Symposium (IDS 2018). València, Spain, September 11–14, 2018.

[25] **Rieck**, **C.**, Bück, A., and Tsotsas, E. *Modeling of undesired agglomeration in spray fluidized bed coating*. Poster presentation. Jahrestreffen der ProceessNet-Fachgruppen Agglomerations- und Schüttguttechnik und Lebensmittelverfahrenstechnik. Lausanne, Switzerland, March 5–7, 2019.

[26] **Rieck**, **C.**, Bück, A., and Tsotsas, E. *Investigation of undesired agglomeration in a spray fluidized bed layering process*. Poster presentation. International Congress on Particle Technology. Nuremberg, Germany, April 9–11, 2019.

[27] Mezhericher, M., **Rieck**, **C.**, Zhang, R., Razorenov, N., and Tsotsas, E. *Ultrathin coating of particles in fluidized bed using submicron droplets*. Poster presentation. 9th International Granulation Workshop. Lausanne, Switzerland, June 26–28, 2019.

[28] **Rieck**, **C.**, Müller, D., Bück, A., and Tsotsas, E. *Modeling of undesired agglomeration in fluidized bed coating*. Oral presentation. 9th International Granulation Workshop. Lausanne, Switzerland, June 26–28, 2019.